SCUOLA
NORMALE
SUPERIORE

Classe di Scienze Matematiche e Naturali

Corso di perfezionamento in fisica
XXXV ciclo

Measurement of $D^0 - \overline{D}^0$ mixing parameters and search for CP violation in $D^0 \to K^+\pi^-$ decays with LHCb Run 2 data

Settore Scientifico Disciplinare **FIS/01**

Candidate:
Roberto Ribatti

Advisor:
Prof. Michael J. Morello

Phd. Coordinator:
Prof. Vittorio Giovannetti

Academic year 2023–2024

Abstract

This thesis presents the measurement of charm mixing and *CP*-violation parameters by comparing the decay-time dependent ratios of $D^0 \to K^+\pi^-$ to $\overline{D}^0 \to K^+\pi^-$ and $\overline{D}^0 \to K^-\pi^+$ to $D^0 \to K^-\pi^+$ decay rates in events where the charm meson flavour at the time of production is identified using promptly produced $D^{*\pm}$ decays. This measurement is performed on data from LHCb experiment with LHC proton-proton collision at a centre-of-mass energy of 13 TeV, corresponding to about 5.9 fb^{-1} of integrated luminosity recorded during the LHC Run 2, from 2015 to 2018. The measured parameter are

$$
\begin{aligned}
R_D &= (\ 343.1 \ \pm 2.0\ ) \times 10^{-5}, & A_D &= (\ -7.1 \ \pm 6.0\ ) \times 10^{-3}, \\
c_{K\pi} &= (\ 51.4 \ \pm 3.5\ ) \times 10^{-4}, & \Delta c_{K\pi} &= (\ 3.0 \ \pm 3.6\ ) \times 10^{-4}, \\
c'_{K\pi} &= (\ 13.1 \ \pm 3.7\ ) \times 10^{-6}, & \Delta c'_{K\pi} &= (\ -1.9 \ \pm 3.8\ ) \times 10^{-6}.
\end{aligned}
$$

A simultaneous fit between this and already published measurement using Run 1 data is performed returning the LHCb legacy results for these parameters, which improve the precision by a factor 1.6 with respect to the already published results. The result is statistically dominated and all the systematic uncertainties have been greatly reduced with respect to the previous iteration of this analysis, paving the road for the LHCb-Upgrade era.

Contents

Introduction

The phenomenon of *CP* violation (CPV), which is the non-invariance under the combined operations of charge conjugation (C) and parity (P), is described in the Standard Model (SM) through a single complex phase in the Cabibbo-Kobayashi-Maskawa (CKM) quark mixing matrix. The CPV produced through the CKM mechanism does not adequately account for the astrophysical observation of cosmological baryonic asymmetry in the Universe. On the other hand, the Standard Model predictions are in agreement with experimental measurements made at the particle accelerators. The precision of current experiments and theoretical predictions, however, is not sufficient to completely exclude the possibility of other mechanisms of *CP* violation beyond the Standard Model, which can be the key to understanding astrophysical observations. For instance, new interactions at energy scales higher than those currently probed, which could possess additional and more significant sources of CPV, might manifest at lower energies as slight deviations from SM predictions in the decay processes of well-known particles, potentially through contributions from higher-order loop diagrams.

In the systems of K- and B-mesons the CKM mechanism is well-established experimentally. Yet, the exploration of CPV in charm quark processes presents a unique opportunity, as charm mesons are the sole mesons containing up-type quarks where CPV can be measured. Within the Standard Model, CPV effects in charm meson decays are expected to be strongly suppressed, typically ranging from 10^{-4} to 10^{-3}. Nonetheless, there is potential for these effects to be amplified by new particles beyond the SM, which could distinctly influence CPV observables in down-type quarks. A recent milestone of the LHCb collaboration was the first observation of CPV in charm meson decay, via the measurement of the ΔA_{CP} observable [1], subsequently followed by the evidence of a non-null value of the $a^d_{\pi^+\pi^-}$ observable [2]. However, theoretical uncertainties related to low-energy quantum-chromodynamics effects make it unclear whether this result is consistent with the Standard Model or indicative of new dynamics in the up-quark sector [3, 4]. Investigating CPV in mixing and interference between mixing and decay is crucial. These tests, seeking even smaller SM-predicted effects, which lie one order of magnitude below the current experimental uncertainty, provide a complementary approach to direct CPV studies, potentially offering further insights into this complex field.

The mass eigenstates of neutral charmed mesons are linear combinations of the flavour

eigenstates, *i.e.* $|D_{1,2}\rangle = p|D^0\rangle \pm q|\overline{D}^0\rangle$, where p and q are complex coefficients. This leads to the phenomena of $D^0 - \overline{D}^0$ oscillations. Under *CP* symmetry, certain conditions hold: the magnitude ratio of q to p equals one ($|q/p| = 1$), and the weak phase ϕ is zero. The oscillations in this scenario are governed solely by the differences in mass and decay width between the *CP*-even (D_2) and *CP*-odd (D_1) mass eigenstates. These differences are quantified by the dimensionless mixing parameters $x \equiv \Delta m/\Gamma$ and $y \equiv \Delta\Gamma/2\Gamma$, where Γ denotes the average decay width of neutral D mesons. In cases where *CP* symmetry is violated, the oscillation probabilities for mesons initially produced as D^0 and $\overline{D}^0$ may vary, further enriching the phenomenology.

Due to the dominant influence of long-distance amplitudes, the oscillation dynamics of the D^0 meson stands apart from other flavoured neutral mesons like K^0, B^0, and B_s^0. Short-distance contributions involving a bottom quark loop are significantly CKM-suppressed and also suffer from the GIM mechanism, cancelling contributions from down and strange quarks. The theoretical challenge with long-distance amplitudes arises from the low-energy gluon exchange, which is complex to compute accurately. However short-distance amplitudes in D^0 mesons could include contributions from a wide variety of particles not foreseen in the Standard Model, altering the oscillation rates.

In 2009, the hypothesis of no oscillations was definitively dismissed by averaging results from *B*-factories [5]. Recently a measurement from the LHCb collaboration led to the first observation of a non-zero positive mass difference [6]. The current global fit [7] for the mixing parameters return $x = (0.40 \pm 0.05)\%$ and $y = (0.64 \pm 0.02)\%$. Regarding *CP* violation parameters, the world average is $|q/p| = 0.995 \pm 0.015$ and $\phi(^\circ) = (-2.5 \pm 1.2)^\circ$, with no evidence of *CP* asymmetry in the mixing or interference.

A highly sensitive method for determining mixing and *CPV* parameters involves the measurement of the decay-time-dependent ratios of $D^0 \to K^+\pi^-$ to $D^0 \to K^-\pi^+$ rates, and comparing them with the ratios for their respective charge-conjugated processes. To infer the flavour of the D^0 meson at its production, the strong flavour conserving decay $D^{*+} \to D^0\pi^+$ (and its charge conjugate $D^{*-} \to \overline{D}^0\pi^-$), can be exploited. Here the charge of the low-momentum pion (also referenced as soft pion, π_s) unequivocally determines the D^0 flavour. The processes of interest, along with their charge-conjugated counterparts, are right-sign (RS) decays, $D^{*+} \to D^0\,(\to K^-\pi^+)\,\pi_s^+$, and wrong-sign (WS) decays, $D^{*+} \to D^0\,(\to K^+\pi^-)\,\pi_s^+$. The RS decay rate is primarily determined by the amplitude of the Cabibbo-favoured $D^0 \to K^-\pi^+$ decay. In contrast, the WS decay rate arises from the interplay between the doubly Cabibbo-suppressed decay $D^0 \to K^+\pi^-$ and the D^0-$\overline{D}^0$ oscillations followed by the Cabibbo-favoured decay $\overline{D}^0 \to K^+\pi^-$. The time-dependent ratio of WS-to-RS decay rates of D neutral meson decaying to the $K^+\pi^-$ and $K^-\pi^+$ final states, $R'^+(t)$ and $R'^-(t)$, respectively, can be expanded as a function of mixing parameters, $|x|\Gamma t, |y|\Gamma t \ll 1$,

$$R^{\pm}(t) \simeq R_D(1 \pm A_D) + \sqrt{R_D(1 \pm A_D)}(c_{K\pi} \pm \Delta c_{K\pi})\Gamma t + (c'_{K\pi} \pm \Delta c'_{K\pi})(\Gamma t)^2, \tag{1}$$

where t is the D^0 decay time, R_D denotes the ratio of the decay rate of the doubly

Cabibbo-suppressed decay to that of the favoured decay,

$$c_{K\pi} \simeq y\cos\delta_{K\pi} - x\sin\delta_{K\pi} \quad \text{and} \quad c'_{K\pi} \simeq \frac{1}{4}(x^2+y^2), \tag{2}$$

are sensitive to mixing parameters, while A_D is the ratio asymmetry, sensitive to *CP* violation in the decay and

$$\begin{aligned}\Delta c_{K\pi} &\simeq (y\cos\delta_{K\pi} - x\sin\delta_{K\pi})\left(\left|\frac{q}{p}\right| - 1\right) - (x\cos\delta_{K\pi} + y\sin\delta_{K\pi})\,\phi^{\lambda}_{K\pi},\\ \Delta c'_{K\pi} &\simeq \frac{1}{2}(x^2+y^2)\left(\left|\frac{q}{p}\right| - 1\right),\end{aligned} \tag{3}$$

are sensitive to *CP* violation parameters. Assuming a negligible dependency on the final state, one can approximate $\phi^{\lambda}_{K\pi} \approx \phi$. Here, $\delta_{K\pi}$ is the phase difference between the decay amplitudes $\mathcal{A}(D^0 \to K^+\pi^-)$ and $\mathcal{A}(\overline{D}^0 \to K^+\pi^-)$. It is an external input for this measurement and it has been measured by the CLEO and BESIII experiments and recently also by the LHCb collaboration [7–9].

The LHCb collaboration, in 2018, published the most precise measurement of these observables [10], even if the used parametrization ($R_D^{\pm}$,$x'^{2\pm}$,$y'^{\pm}$) was different from that adopted here. This precision was obtained using the extensive dataset collected by the LHCb detector during the LHC Run 1 (2011-2012) and the first two years of LHC Run 2 (2015-2016), corresponding to an integrated luminosity of $3\,\text{fb}^{-1}$ of proton-proton (pp) collisions at $\sqrt{s}$ = 7-8 TeV, and $2\,\text{fb}^{-1}$ at $\sqrt{s}$ = 13 TeV, respectively. Considering that the most recent SM predictions of indirect *CPV* are still markedly below the current experimental uncertainties, enhancing sensitivity in these measurements is essential for a deeper understanding of charm quark dynamics and elucidating the post-ΔA_{CP} picture in charm physics.

The LHCb experiment, up to the conclusion of LHC Run 2, in 2017 and 2018, collected an additional data sample from pp collisions at $\sqrt{s}$ = 13 TeV, corresponding to an integrated luminosity of $4\,\text{fb}^{-1}$. This considerable increase in data effectively more than doubled the signal yields previously obtained. The work detailed in this thesis focuses on enhancing the statistical precision of R_D, the mixing parameters $c_{K\pi}$, $c'_{K\pi}$ and the *CPV* parameters A_D, $\Delta c_{K\pi}$, $\Delta c'_{K\pi}$. This improvement is achieved by extending the analysis to encompass the total data sample currently available from LHCb, including the newly acquired data from the latter half of LHC Run 2. Above all, a main component of this research is the substantial reduction of dominant systematic uncertainties and biases. This approach is not only relevant for the current phase of the analysis but also sets the stage for future measurements in the upcoming LHCb-Upgrade era (LHC Run 3 and beyond). In this forthcoming period, expectations are set for even higher statistical precision, potentially reaching or surpassing the levels of current systematic uncertainties. Such advancements will be crucial in furthering our understanding of charm quark dynamics and *CP* violation phenomena.

Chapter 1

Mixing and CPV in the SM

This chapter provides a brief introduction to the Standard Model of particle physics, followed by a focus on the formalism of the CKM matrix and how it allows experimentally accessing the quark mixing parameters and the violation of the CP symmetry in the weak interactions. A detailed description of the formalism of the neutral-flavoured meson mixing and the experimental manifestations of the CP violation concludes the chapter.

1.1 Fundamental principles of the Standard Model

The Standard Model (SM) of particle physics stands as a paradigm in quantum field theory, detailing the behaviour and interactions of elementary particles through three principal forces: the strong, electromagnetic, and weak forces. This model can be fundamentally characterized by three fundamental principles [11]:

- the intrinsic symmetries of the Lagrangian;
- the representations of fermions and scalars;
- the pattern of spontaneous symmetry breaking.

Lagrangian symmetry The Standard Model is a local gauge-invariant theory with a non-abelian gauge group of symmetry

$$G_{SM} = SU(3)_C \otimes SU(2)_L \otimes U(1)_Y. \tag{1.1}$$

Here, $SU(3)_C$ denotes the symmetry of Quantum Chromodynamics (QCD), representing the theory of the strong force, where the suffix C refer to the colour charge. Similarly, the composition $SU(2)_L \times U(1)_Y$ symbolizes the symmetry intrinsic to electroweak interactions, with reference to the Glashow-Weinberg-Salam model [12–14]. In this context, L delineates the inherent chirality of weak forces, whereas Y represents the hypercharge. Enforcing local gauge symmetry results in the emergence of associated boson gauge fields. Specifically, within the SM, these are all vectorial fields. The eight gluon boson fields, G^i, are intrinsically tied to the $SU(3)_C$ generators and mediate the strong force. In contrast, the three weak interaction boson fields W^i, connected to the

$SU(2)_L$ generators, and the hypercharge boson field B (linked to the $U(1)_Y$ generator) are not directly linked with observed physical particles. These ones emerge after the spontaneous symmetry breaking.

Particle representations In the Standard Model, there exist three generations of fermions. Each of these generations includes five distinct representations relative to the G_{SM} group:

$$Q^I_{Li}(3,2)_{+1/6}, \quad u^I_{Ri}(3,1)_{+2/3}, \quad d^I_{Ri}(3,1)_{-1/3}, \quad L^I_{Li}(1,2)_{-1/2}, \quad \ell^I_{Ri}(1,1)_{-1}. \tag{1.2}$$

Here, the index i denotes the specific generation, with L and R referring to left-handed and right-handed chiralities, respectively. The term I indicates the eigenstate of interaction. Following each field in this notation are two numbers in brackets, indicating the representation dimensions of the $SU(3)_C$ and $SU(2)_L$ groups, succeeded by a subscript indicating the associated hypercharge. Decomposing the $SU(2)_L$ doublets, one derives:

$$Q^I_{Li} = \begin{pmatrix} u^I_{Li} \\ d^I_{Li} \end{pmatrix}, \qquad L^I_{Li} = \begin{pmatrix} \nu^I_{Li} \\ \ell^I_{Li} \end{pmatrix}. \tag{1.3}$$

A summary of these representations can be found in Tab. 1.1. The electromagnetic charge, $U(1)_{em}$, is determined by $Q = I_3 + \frac{1}{2}Y$, where I_3 symbolizes the weak isospin and Y refers to the hypercharge.

Field	$SU(3)_C$	$SU(2)_L$	$U(1)_Y$	$U(1)_{em}$
$Q^I_{Li} = \begin{bmatrix} u^I_{Li} \\ d^I_{Li} \end{bmatrix}$	3	2	1/6	$\begin{bmatrix} 2/3 \\ -1/3 \end{bmatrix}$
u^I_{Ri}	3	1	2/3	2/3
d^I_{Ri}	3	1	-1/3	-1/3
$L^I_{Li} = \begin{bmatrix} \nu^I_{Li} \\ \ell^I_{Li} \end{bmatrix}$	1	2	-1/2	$\begin{bmatrix} 0 \\ -1 \end{bmatrix}$
ℓ^I_{Ri}	1	1	-1	-1

Table 1.1: Standard Model particles representations and their relative dimensions.

Particles that are singlets under a given representation are neutral to the corresponding force and do not couple to its gauge bosons. The categorisation can be elaborated as follows:

- **quarks** ($Q^I_{Li}, u^I_{Ri}, d^I_{Ri}$) are constituents of $SU(3)_C$ triplets, thereby participating in strong interactions;
- **leptons** (L^I_{Li}, ℓ^I_{Ri}) do not carry colour charge and are thus $SU(3)_C$ singlets, being inert to the strong force.

Furthermore, these particles can also be distinguished by their chirality:

- **left-handed** entities (Q^I_{Li}, L^I_{Li}) form $SU(2)_L$ doublets and are involved in interactions mediated by W^i bosons;

- **right-handed** counterparts ($u^I_{Ri}, d^I_{Ri}, \ell^I_{Ri}$) are $SU(2)_L$ singlets, and as such, they do not interact with W^i bosons.

The W^3 and B bosons undergo a mixing in order to yield the physically manifest Z^0 and A bosons after spontaneous symmetry breaking. Given that the B boson interacts with right-handed particles, the Z^0 boson does as well. This implies the chirality-based classification has limited significance. Apart from the fermionic content, the theory includes a unique scalar multiplet (spin 0): $\phi(1,2)_{+1/2}$.

Spontaneous symmetry breaking This singular scalar possesses a non-zero vacuum expectation value (VEV):

$$\langle \phi | 0 \rangle = \frac{1}{\sqrt{2}} \begin{pmatrix} 0 \\ v \end{pmatrix}. \tag{1.4}$$

This non-zero VEV induces the spontaneous breaking of the gauge symmetry as follows:

$$G_{SM} \to SU(3)_C \otimes U(1)_{em}, \tag{1.5}$$

in which $U(1)_{em}$ denotes the electromagnetic symmetry group. The scalar field ϕ is conveniently parametrised by

$$\phi(x) = \frac{1}{\sqrt{2}} \begin{pmatrix} 0 \\ v + H(x) \end{pmatrix} \tag{1.6}$$

wherein $H(x)$ represents the Higgs boson, a neutral scalar particle. Once the gauge symmetry is established as in Eq. 1.1, the representations as in Eq.1.2, and the spontaneous symmetry breaking mechanism is determined, the derivation of the Standard Model Lagrangian $\mathcal{L}_{SM}$ consequently follows. It is constructed to be the most general, renormalizable Lagrangian which obeys these stipulated conditions.

The Lagrangian of the Standard Model The Lagrangian of the Standard Model can be divided into three distinct components:

$$\mathcal{L}_{SM} = \mathcal{L}_{kinetic} + \mathcal{L}_{gauge} + \mathcal{L}_{Higgs} + \mathcal{L}_{Yukawa}. \tag{1.7}$$

The $\mathcal{L}_{kinetic}$ term aggregates the kinetic terms ($i\bar{\psi}\gamma_\mu \partial^\mu \psi$) of all fermions. Here, the standard derivative is supplanted by the covariant derivative encapsulated as:

$$D^\mu = \partial^\mu + i g_s G^\mu_a L_a + i g W^\mu_b T_b + i g' B^\mu Y. \tag{1.8}$$

L_a represents the generators of the $SU(3)_C$ group for the respective representations, being $\frac{1}{2}\lambda_a$ for triplets (with λ_a denoting the 3×3 Gell-Mann matrices) and 0 for singlets. T_b indicates the generators of the $SU(2)_L$ group, where $\frac{1}{2}\sigma_b$ is for doublets (with σ_b being the 2×2 Pauli matrices) and again 0 for singlets. Y is the hypercharge associated with the $U(1)_Y$ symmetry.

The $\mathcal{L}_{gauge}$ term grouped the kinetic terms of the gauge bosons

$$\mathcal{L}_{gauge} = -\frac{1}{4}(G^a_{\mu\nu}G^{\mu\nu}_a + W^b_{\mu\nu}W^{\mu\nu}_b + B_{\mu\nu}B^{\mu\nu}), \tag{1.9}$$

where $G^a_{\mu\nu} = \partial_\mu G^a_\nu - \partial_n u G^a_\mu - g_s f^{ajk} G^j_\mu G^k_\nu$, $W^b_{\mu\nu} = \partial_\mu W^b_\nu - \partial_n u W^b_\mu - g\epsilon^{bjk} W^j_\mu W^k_\nu$ and $B_{\mu\nu} = \partial_\mu B_\nu - \partial_\nu B_\mu$, are the field strenght tensors.
The term $\mathcal{L}_{Higgs}$ describes the self-interaction of the scalar field and takes the form:

$$\mathcal{L}_{Higgs} = -\mu^2\phi^\dagger\phi + \lambda(\phi^\dagger\phi)^2. \tag{1.10}$$

It is noteworthy that both the $\mathcal{L}_{kinetic}$ and $\mathcal{L}_{Higgs}$ terms in the Standard Model preserve *CP* symmetry. Lastly, the $\mathcal{L}_{Yukawa}$ component delineates the interaction between the fermions and the scalar field. This segment of the Lagrangian is generally non-conserving of *CP* symmetry and constitutes the sole source of *CP* violation as foretold by the Standard Model.

1.2 The CKM Matrix and CP Violation in the SM

In the Standard Model, quark masses and their mixings originate from Yukawa interactions between fermions and the scalar field. These interactions are represented as:

$$\mathcal{L}_{Yukawa} = -Y^d_{ij}\,\overline{Q^I_{Li}}\,\phi\,d^I_{Rj} \;-\; Y^u_{ij}\,\overline{Q^I_{Li}}\,\tilde{\phi}\,u^I_{Rj} \;- Y^\ell_{ij}\,\overline{L^I_{Li}}\,\phi\,\ell^I_{Rj} \;+\; \text{h.c.} \tag{1.11}$$

where $Y^{u,d,\ell}_{ij}$ are 3×3 complex matrices, with i and j indicating the generation indices, and $\tilde{\phi} = i\sigma^2\phi^\dagger$. Upon spontaneous symmetry breaking, the scalar field ϕ acquires a non-zero vacuum expectation value, as indicated in Eq. 1.4. By employing Eq. 1.6 and omitting the interaction terms, the mass term in the Lagrangian can be expressed as:

$$\mathcal{L}_M = -(M_d)_{ij}\overline{d^I_{Li}}d^I_{Rj} - (M_u)_{ij}\overline{u^I_{Li}}u^I_{Rj} - (M_\ell)_{ij}\overline{\ell^I_{Li}}\ell^I_{Rj} \tag{1.12}$$

where $M_f = \frac{v}{\sqrt{2}}Y^f$. The physically observable states correspond to the diagonalized mass matrices $M_{u,d,\ell}$, as the mass basis is defined by these diagonal matrices. The objective is to identify pairs of unitary matrices V_{fL} and V_{fR} that diagonalize these mass matrices:

$$V_{fL}M_f V^\dagger_{fR} = M^{diag}_f. \tag{1.13}$$

This process results in the mass eigenstates being represented as rotations from the weak interaction basis, as depicted in the left panel of Fig. 1.1:

$$\begin{aligned} d_{Li} &= (V_{dL})_{ij} d^I_{Lj}, \qquad & d_{Ri} &= (V_{dR})_{ij} d^I_{Rj}, \\ u_{Li} &= (V_{uL})_{ij} u^I_{Lj}, \qquad & u_{Ri} &= (V_{uR})_{ij} u^I_{Rj}, \\ \ell_{Li} &= (V_{\ell L})_{ij} \ell^I_{Lj}, \qquad & \ell_{Ri} &= (V_{\ell R})_{ij} \ell^I_{Rj}, \\ \nu_{Li} &= (V_{\nu L})_{ij} \nu^I_{Lj}. \end{aligned} \tag{1.14}$$

Mixing in weak charged current Within the kinetic term of the Lagrangian $\mathcal{L}_{kinetic}$, we scrutinise the interaction between the quarks and the charged gauge bosons of $SU(2)_L$, denoted as $W^{\pm}_{\mu} = \frac{1}{\sqrt{2}}(W\mu^1 \mp iW^2_{\mu})$. This interaction, when articulated in terms of weak interaction eigenstates, is given by:

$$\mathcal{L}_{W^{\pm}} = \frac{-g}{\sqrt{2}} \overline{Q^I_{Li}} \gamma^{\mu} W^+_{\mu} Q^I_{Li} + \text{h.c.} = \frac{-g}{\sqrt{2}} \overline{u^I_{Li}} \gamma^{\mu} W^+_{\mu} d^I_{Li} + \text{h.c.}\,. \tag{1.15}$$

This interaction exclusively involves left-handed quarks, as the $W^{\pm}$ bosons, in contrast to the Z^0 boson, interact solely with left-handed particles, preserving $SU(2)_L$ symmetry. Transitioning to the mass eigenstates as described in Eq. 1.14, we arrive at

$$\mathcal{L}_{W^{\pm}} = \frac{-g}{\sqrt{2}} \overline{u_{Li}} V_{uL} \gamma^{\mu} W^+_{\mu} V^{\dagger}_{dL} d^I_{Li} + \text{h.c.}\,. \tag{1.16}$$

By ordering the quarks within their respective generations by mass: $u_i \to (u, c, t)$ and $d_i \to (d, s, b)$, the Lagrangian can be expressed as:

$$\mathcal{L}_{W^{\pm}} = \frac{-g}{\sqrt{2}} (\overline{u_L}, \overline{c_L}, \overline{t_L}) \gamma^{\mu} W^+_{\mu} V_{CKM} \begin{pmatrix} d_L \\ s_L \\ b_L \end{pmatrix} + \text{h.c.}, \tag{1.17}$$

with

$$V_{CKM} \equiv V_{uL} V^{\dagger}_{dL} = \begin{pmatrix} V_{ud} & V_{us} & V_{ub} \\ V_{cd} & V_{cs} & V_{cb} \\ V_{td} & V_{ts} & V_{tb} \end{pmatrix}, \tag{1.18}$$

denoting the Cabibbo-Kobayashi-Maskawa matrix, a 3×3 unitary matrix arising from the product of unitary matrices [15, 16]. The general form of a 3×3 unitary matrix encompasses nine free parameters, but there is inherent flexibility in the definition of V_{CKM}. Consider the introduction of two arbitrary diagonal unitary matrices P_u and P_d:

$$P_u = \begin{pmatrix} e^{i\alpha_1} & 0 & 0 \\ 0 & e^{i\alpha_2} & 0 \\ 0 & 0 & e^{i\alpha_3} \end{pmatrix}, \qquad P_d = \begin{pmatrix} e^{i\beta_1} & 0 & 0 \\ 0 & e^{i\beta_2} & 0 \\ 0 & 0 & e^{i\beta_3} \end{pmatrix}, \tag{1.19}$$

used for transforming V_{uL} and V_{dL}:

$$\widetilde{V}_{uL} = P_u V_{uL}, \qquad \widetilde{V}_{dL} = P_d V_{dL}. \tag{1.20}$$

This modification does not affect the mass eigenstates as defined in Eq. 1.13:

$$P_f V_{fL} M_f V_{fR}^{\dagger} = P_f M_f^{diag}, \tag{1.21}$$

as P_f is diagonal and merely introduces a phase shift in each quark field. Consequently, the form of V_{CKM} is altered:

$$\tilde{V}_{CKM} = P_u V_{CKM} P_d^{\dagger} = \begin{pmatrix} V_{ud}\, e^{i(\alpha_1-\beta_1)} & V_{us}\, e^{i(\alpha_1-\beta_2)} & V_{ub}\, e^{i(\alpha_1-\beta_3)} \\ V_{cd}\, e^{i(\alpha_2-\beta_1)} & V_{cs}\, e^{i(\alpha_2-\beta_2)} & V_{cb}\, e^{i(\alpha_2-\beta_3)} \\ V_{td}\, e^{i(\alpha_3-\beta_1)} & V_{ts}\, e^{i(\alpha_3-\beta_2)} & V_{tb}\, e^{i(\alpha_3-\beta_3)} \end{pmatrix}. \tag{1.22}$$

With only five of these nine phase differences being independent, fixing them results in four free parameters: three mixing angles and a single CP-violating phase. The standard parametrization is given by [17]:

$$\begin{aligned} V_{CKM} &= \begin{pmatrix} 1 & 0 & 0 \\ 0 & c_{23} & s_{23} \\ 0 & -s_{23} & c_{23} \end{pmatrix} \begin{pmatrix} c_{13} & 0 & s_{13}e^{-i\delta} \\ 0 & 1 & 0 \\ -s_{13}e^{i\delta} & 0 & c_{13} \end{pmatrix} \begin{pmatrix} c_{12} & s_{12} & 0 \\ -s_{12} & c_{12} & 0 \\ 0 & 0 & 1 \end{pmatrix} \\ &= \begin{pmatrix} c_{12}c_{13} & s_{12}c_{13} & s_{13}e^{-i\delta} \\ -s_{12}c_{23} - c_{12}s_{23}s_{13}e^{i\delta} & c_{12}c_{23} - s_{12}s_{23}s_{13}e^{i\delta} & s_{23}c_{13} \\ s_{12}s_{23} - c_{12}c_{23}s_{13}e^{i\delta} & -c_{12}s_{23} - s_{12}c_{23}s_{13}e^{i\delta} & c_{23}c_{13} \end{pmatrix}, \end{aligned} \tag{1.23}$$

where $s_{ij} = \sin\theta_{ij}$, $c_{ij} = \cos\theta_{ij}$, and δ is the *CP* violating phase. The angles θ_{ij} are chosen to lie in the first quadrant, ensuring s_{ij}, $c_{ij} > 0$.

Mixing in lepton flavours Among the seven $V_{L,R}^{u,d,\ell,\nu}$, we considered only V_L^u and V_L^d, which contribute to the CKM matrix governing quark mixing and CP violation in charged current interactions. However, a mixing matrix for left-handed neutrinos and leptons can also be defined. In the Standard Model's original formulation, neutrinos are massless, and thus $V_{\nu L}$ can be chosen such that $V_{\nu_L} = V_{\ell L}$, making the mixing matrix effectively the identity matrix. Nonetheless, in extensions of the Standard Model that accommodate neutrino masses, the Pontecorvo–Maki–Nakagawa–Sakata (PMNS) matrix, denoted V_{PMNS}, emerges as a key player in lepton mixing and CP violation in interactions with $W^{\pm}$ bosons [18].

Mixing in weak neutral current The neutral weak boson Z^0 emerges from the mixing of the W_3 and B bosons. Although the Z^0 boson can couple to both left-handed and right-handed particles, it interacts with particles of the same chirality, coupling up-type quarks with up-type quarks and down-type quarks with down-type quarks. For instance, the Lagrangian describing the interaction of the Z^0 boson with down-type left-handed

quarks can be represented as:

$$\mathcal{L}_{Z^0} \propto \overline{d_{Li}}\gamma^{\mu}(V_{dL}^{\dagger}V_{dL})d_{Lj}Z_{\mu} + \dots. \tag{1.24}$$

In this framework, the flavour mixing matrices, such as V_{dL}, simplify due to their unitary nature. As a result, the weak neutral current interactions mediated by the Z^0 boson do not exhibit flavour mixing or CP violation phenomena.

Other sources of CP violation Apart from the well-established sources of CP violation in the weak interaction, another conceivable source within the Standard Model framework is linked to the strong interaction. This potential source is encapsulated by the θ_{QCD} parameter. The θ_{QCD} term could induce CP violation in strong interactions, a theoretical possibility within the Standard Model. However, empirical investigations, particularly those examining the electric dipole moment of the neutron, have imposed stringent constraints on the value of θ_{QCD}: $\theta_{QCD} < 10^{-9}$ and it is compatible with zero [19]. This observation has led to the so-called "strong CP problem", a notable puzzle in theoretical physics, given the natural expectation of a larger CP-violating effect in strong interactions.

In summary, within the current framework of the Standard Model, the CKM matrix remains the only mechanism for flavour changing and CP violation.

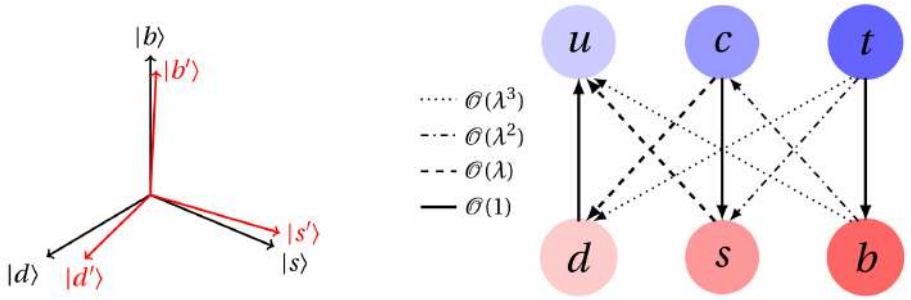

Figure 1.1: Graphical representation of CKM mechanism.

Wolfenstein parametrization The Wolfenstein parametrization offers a more intuitive representation of the CKM matrix, particularly in light of the experimental observation that in Eq. 1.23, $s_{13} \ll s_{23} \ll s_{12} \ll 1$. This parametrization replaces the parameters $(s_{12}, s_{23}, s_{13}, \delta)$ with four new parameters (λ, A, ρ, η), or alternatively $(\lambda, A, \bar{\rho}, \bar{\eta})$, defined as:

$$s_{12} = \lambda = \frac{|V_{us}|}{\sqrt{|V_{ud}|^2 + |V_{us}|^2}}, \qquad s_{23} = A\lambda^2 = \lambda\left|\frac{V_{cb}}{V_{us}}\right|, \tag{1.25}$$
$$s_{13}e^{i\delta} = V_{ub}^{*} = A\lambda^3(\rho + i\eta) = \frac{A\lambda^3(\bar{\rho} + i\bar{\eta})\sqrt{1 - A^2\lambda^4}}{\sqrt{1 - \lambda^2}[1 - A^2\lambda^4(\bar{\rho} + i\bar{\eta})]}.$$

In this parametrization, $\lambda = |V_{us}| \simeq 0.22$ is used as an expansion parameter and the η parameter is associated with the imaginary part of the CKM matrix, introducing the

CP-violating phase. The CKM matrix, up to $\mathcal{O}(\lambda^4)$, can then be expressed in terms of these new parameters [20]:

$$V_{CKM} = \begin{pmatrix} 1-\lambda^2/2 & \lambda & A\lambda^3(\rho - i\eta) \\ -\lambda & 1-\lambda^2/2 & A\lambda^2 \\ A\lambda^3(1-\rho-i\eta) & -A\lambda^2 & 1 \end{pmatrix} + \mathcal{O}(\lambda^4). \tag{1.26}$$

The right panel of Fig.1.1 graphically illustrates the strength of quark transitions, directly linked to the mixing rates.

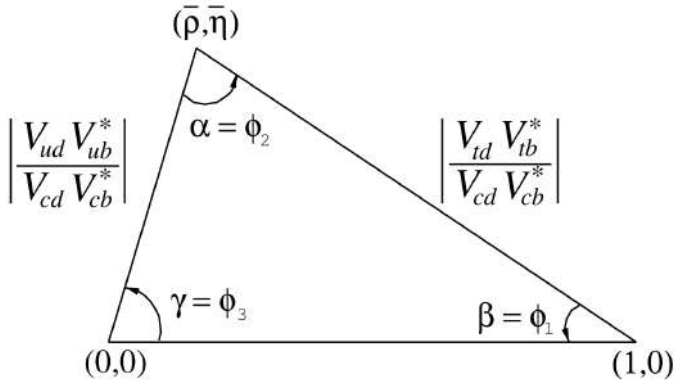

Figure 1.2: Sketch of the unitarity triangle.

The unitarity of the CKM matrix, which necessitates orthogonality among its rows and columns, leads to six constraints.

$$\sum_i V_{ij}V_{ik}^* = \delta_{jk}, \qquad \sum_j V_{ij}V_{kj}^* = \delta_{ik}. \tag{1.27}$$

These constraints can be visualized as triangles in the complex plane. The triangles formed by adjacent rows or columns are nearly degenerate, and all share the same area of $|J|/2$. The most commonly analysed unitarity triangle arises from the equation:

$$V_{ud}V_{ub}^* + V_{cd}V_{cb}^* + V_{td}V_{tb}^* = 0. \tag{1.28}$$

Dividing each term by $V_{cd}V_{cb}^*$, which is experimentally well-established, yields:

$$\frac{V_{ud}V_{ub}^*}{V_{cd}V_{cb}^*} + 1 + \frac{V_{td}V_{tb}^*}{V_{cd}V_{cb}^*} = 0, \tag{1.29}$$

This equation reveals that the vertices of this unitarity triangle correspond to the points $(0,0)$, $(1,0)$, and $(\bar{\rho},\bar{\eta})$. This particular unitarity triangle is depicted in Fig. 1.2.

The area of unitary triangles is a *CP*-violating quantity that remains invariant under different parametrizations, denoted as Jarlskog invariant, J, in the literature [21]. This parameter can be written as

$$\mathcal{I}m[V_{ij}V_{kl}V_{il}^*V_{kj}^*] = J\sum_{m,n}\epsilon_{ikm}\epsilon_{jln}. \tag{1.30}$$

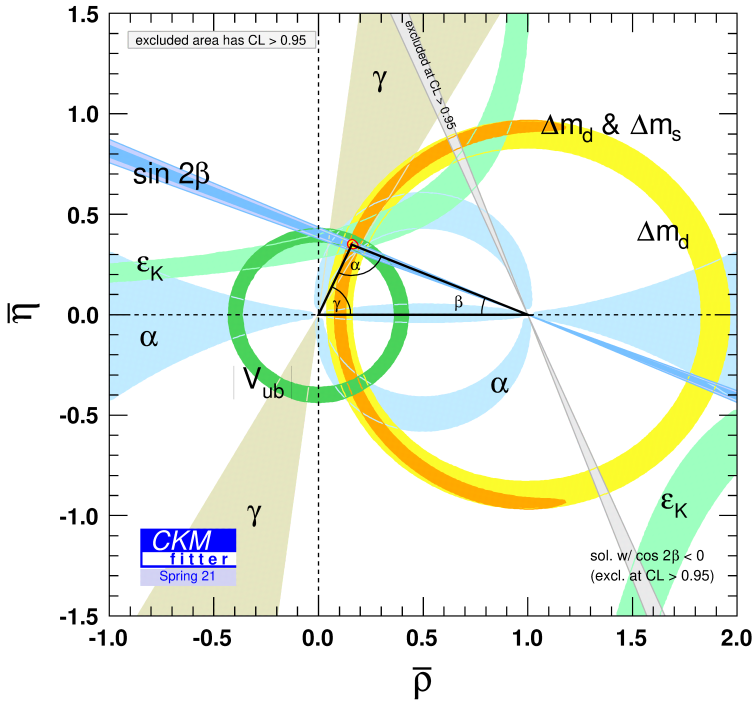

Figure 1.3: Current experimental status of the global fit to all available experimental measurements related to the unitarity triangle phenomenology [22]. The shaded areas have 95% CL.

Experimental measurement of CKM parameters The precision measurement of the CKM matrix elements is crucial for testing the predictions of the Standard Model and for constraining theories beyond the Standard Model. There are two primary methods for determining CKM parameters:

- **Direct measurements** involve observing tree-level processes to directly extract the magnitude of the CKM matrix elements, $|V_{ij}|$. However, certain elements like $|V_{tb}|$ and $|V_{cs}|$ are measured with less precision, while others such as $|V_{td}|$ and $|V_{ts}|$ are too suppressed for direct measurement.
- **Indirect measurements** that focus on higher-order processes to ascertain the values of products of CKM elements, like $|V_{tb}V_{td}|$.

The experimental results are often represented in the $\bar{\rho}$, $\bar{\eta}$ plane, as illustrated in Fig. 1.3. The shaded regions indicate the 95% confidence level areas, which show a consistent overlap around the global fit area. By combining data from both direct and indirect measurements and applying the CKM unitarity constraint (Eq. 1.27), the parameter space of the CKM elements can be tightly constrained. The global fit for the Wolfenstein

parameters returns [22]:

$$\lambda = 0.22500^{+0.00024}_{-0.00022}, \qquad A = 0.8132^{+0.0119}_{-0.0060},$$
$$\bar{\rho} = 0.1566^{+0.0085}_{-0.0048}, \qquad \bar{\eta} = 0.3475^{+0.0118}_{-0.0054}.$$

Furthermore, the fit results for the magnitudes of all nine CKM elements are given by:

$$|V_{CKM}| = \begin{pmatrix} 0.974353^{+0.000049}_{-0.000056} & 0.22500^{+0.00024}_{-0.00021} & 0.003667^{+0.000088}_{-0.000073} \\ 0.22487^{+0.00024}_{-0.00021} & 0.973521^{+0.000057}_{-0.000062} & 0.04145^{+0.00035}_{-0.00061} \\ 0.008519^{+0.000075}_{-0.000146} & 0.04065^{+0.00040}_{-0.00055} & 0.999142^{+0.000018}_{-0.000023} \end{pmatrix}.$$

1.3 Flavoured neutral mesons mixing

In the context of the Standard Model, there are exactly four flavoured neutral mesons that do not undergo decay via strong or electromagnetic interactions. These mesons are K^0 (composed of $d\bar{s}$ quarks), D^0 ($c\bar{u}$), B^0 ($d\bar{b}$), and B_s^0 ($s\bar{b}$). The term *flavoured* here refers to the presence of a non-zero flavour quantum number (strangeness, charmness, or bottomness). This differentiates them from neutral mesons like π^0, η, J/Ψ, etc., which decay through electromagnetic or strong interactions.
For these four flavoured neutral mesons, the interaction eigenstate in which they are produced is distinct from their mass eigenstate, which is the eigenstate of the free Hamiltonian governing their time evolution. Consequently, these mesons can oscillate between their particle and antiparticle states, changing their flavour quantum number by two units: a phenomenon known as *mixing*.

1.3.1 Time evolution of flavour eigenstates

The initial state of these mesons is a linear combination of the interaction eigenstates M^0 and $\overline{M}^0$ (where M^0 represents any of K^0, D^0, B^0, B_s^0):

$$|\psi(0)\rangle = a(0)|M^0\rangle + b(0)|\overline{M}^0\rangle. \tag{1.31}$$

The Schrödinger equation describes the time evolution of this state:

$$i\hbar\frac{\partial}{\partial t}|\psi\rangle = H_M|\psi(t)\rangle, \tag{1.32}$$

where H_M is the free Hamiltonian. The state $\psi(t)$ is a superposition of $|M^0\rangle$, $|\overline{M}^0\rangle$, and all possible final states $|f_k\rangle$ into which the two mesons can decay:

$$|\psi(t)\rangle = a(t)|M^0\rangle + b(t)|\overline{M}^0\rangle + \sum_k c_k(t)|f_k\rangle. \tag{1.33}$$

The Weisskopf-Wigner approximation [23] is applicable since time scale of mixing is much larger than the one of strong interaction. We can describe the $M^0 - \overline{M}^0$ subspace

evolution using a 2×2 effective Hamiltonian $\boldsymbol{\mathcal{H}}$:

$$i\frac{\partial}{\partial t}\begin{pmatrix} M^0(t) \\ \overline{M}^0(t) \end{pmatrix} = \begin{pmatrix} \mathcal{H}_{11} & \mathcal{H}_{12} \\ \mathcal{H}_{21} & \mathcal{H}_{22} \end{pmatrix}\begin{pmatrix} M^0(t) \\ \overline{M}^0(t) \end{pmatrix}. \tag{1.34}$$

This Hamiltonian can be decomposed into its Hermitian and anti-Hermitian components

$$\boldsymbol{\mathcal{H}} = \frac{1}{2}\left(\boldsymbol{\mathcal{H}} + \boldsymbol{\mathcal{H}}^\dagger\right) + \frac{1}{2}\left(\boldsymbol{\mathcal{H}} - \boldsymbol{\mathcal{H}}^\dagger\right) = \boldsymbol{\mathcal{M}} - \frac{i}{2}\boldsymbol{\Gamma}, \tag{1.35}$$

where we have conveniently defined the two Hermitian matrix

$$\boldsymbol{\mathcal{M}} = \begin{pmatrix} \mathcal{M}_{11} & \mathcal{R}e(\mathcal{M}_{12}) + i\mathcal{I}m(\mathcal{M}_{12}) \\ \mathcal{R}e(\mathcal{M}_{12}) - i\mathcal{I}m(\mathcal{M}_{12}) & \mathcal{M}_{22} \end{pmatrix} \equiv \frac{1}{2}\left(\boldsymbol{\mathcal{H}} + \boldsymbol{\mathcal{H}}^\dagger\right) \tag{1.36}$$

$$\boldsymbol{\Gamma} = \begin{pmatrix} \Gamma_{11} & \mathcal{R}e(\Gamma_{12}) + i\mathcal{I}m(\Gamma_{12}) \\ \mathcal{R}e(\Gamma_{12}) - i\mathcal{I}m(\Gamma_{12}) & \Gamma_{22} \end{pmatrix} \equiv i\left(\boldsymbol{\mathcal{H}} - \boldsymbol{\mathcal{H}}^\dagger\right). \tag{1.37}$$

The $\boldsymbol{\mathcal{M}}$ matrix is also known as the mass matrix, while $\boldsymbol{\Gamma}$, which controls the decay rate in the $M^0 - \overline{M}^0$ space, is also known as the decay matrix. The mass and decay matrix are related to the dispersive transitions through off-shell intermediate states, and absorptive transitions through on-shell intermediate states, respectively. In general $\boldsymbol{\mathcal{H}}$ possesses eight independent parameters, while each of $\boldsymbol{\mathcal{M}}$ and $\boldsymbol{\Gamma}$ have four, since these are Hermitian and we have $\mathcal{M}_{ij} = \mathcal{M}^*_{ji}$ and $\Gamma_{ij} = \Gamma^*_{ji}$. Some of these parameters can be constrained by enforcing invariance under discrete transformations like CPT, CP, or T, as detailed in Tab. 1.2. From now on we are going to assuming CPT invariance. Consequently, we can define the real parameters $\mathcal{M}$ and Γ as $\mathcal{M} \equiv \mathcal{M}_{11} = \mathcal{M}_{22}$ and $\Gamma \equiv \Gamma_{11} = \Gamma_{22}$, respectively.

Invariance	Constraints		
CPT	$\mathcal{M}_{11} = \mathcal{M}_{22}$	$\Gamma_{11} = \Gamma_{22}$	
CP	$\mathcal{M}_{11} = \mathcal{M}_{22}$	$\Gamma_{11} = \Gamma_{22}$	$\mathcal{I}m(\Gamma_{12}/\mathcal{M}_{12}) = 0$
T	$\mathcal{I}m(\Gamma_{12}/\mathcal{M}_{12}) = 0$		

Table 1.2: Constraints on $\boldsymbol{\mathcal{M}}$ and $\boldsymbol{\Gamma}$ depending on interaction invariance under different discrete transformations.

Now we want to determine the time-dependent probabilities for both M^0 and $\overline{M}^0$ mesons to oscillate (or not). Two equivalent formalisms are used in the literature for this purpose, which are known under the name of *Phenomenological* and *Theoretical* parametrisations.

Phenomenological parametrisation

Solving the eigenvalue problem gives

$$\lambda_{1,2} = \mathcal{H}_{11} \pm \sqrt{\mathcal{H}_{12}\mathcal{H}_{21}} = \mathcal{M} - i\Gamma/2 \pm \sqrt{\mathcal{H}_{12}\mathcal{H}_{21}}, \tag{1.38}$$

where λ_1 and λ_2 are the eigenvalue associated to the eigenstate $|M_1\rangle$ and $|M_2\rangle$, respectively. From the real and imaginary parts of λ_1 and λ_2,

$$m_{1,2} \equiv \mathcal{R}e\,(\lambda_{1,2}) = \mathcal{M} \pm \mathcal{R}e\left(\sqrt{\mathcal{H}_{12}\mathcal{H}_{21}}\right) \tag{1.39}$$

$$\Gamma_{1,2} \equiv -2\,\mathcal{I}m\,(\lambda_{1,2}) = \Gamma \mp 2\,\mathcal{I}m\left(\sqrt{\mathcal{H}_{12}\mathcal{H}_{21}}\right), \tag{1.40}$$

we can extract the mass and decay widths of $|M_{1,2}\rangle$.
Note that $\mathcal{M}$ and Γ, the values on the diagonal of the mass and decay matrix, respectively, are the average of the mass and decay width of the two eigenstates:

$$\mathcal{M} = \frac{m_1 + m_2}{2}, \qquad \Gamma = \frac{\Gamma_1 + \Gamma_2}{2}. \tag{1.41}$$

It is convenient to define also the differences

$$\Delta m \equiv m_2 - m_1 = -2\,\mathcal{R}e\left(\sqrt{\mathcal{H}_{12}\mathcal{H}_{21}}\right), \tag{1.42}$$

$$\Delta\Gamma \equiv \Gamma_2 - \Gamma_1 = 4\,\mathcal{I}m\left(\sqrt{\mathcal{H}_{12}\mathcal{H}_{21}}\right). \tag{1.43}$$

The time-dependency of these states is governed by

$$\begin{aligned} |M_{1,2}(t)\rangle &= \exp\left(-im_{1,2}t\right)\exp\left(-\Gamma_{1,2}t/2\right)|M_{1,2}(0)\rangle \\ &= \exp\left(-i\mathcal{M}t\right)\exp\left(-\Gamma t/2\right)\times \\ &\quad \times \exp\left(\mp i\mathcal{R}\sqrt{\mathcal{H}_{12}\mathcal{H}_{21}}t\right)\exp\left(\mp\mathcal{I}\sqrt{\mathcal{H}_{12}\mathcal{H}_{21}}t\right)|M_{1,2}(0)\rangle. \end{aligned} \tag{1.44}$$

Solving now for the normalized eigenvectors of the Hamiltonian $\boldsymbol{\mathcal{H}}$ we find[1]

$$\begin{aligned} |M_1\rangle &\equiv p|M^0\rangle + q|\overline{M}^0\rangle, \\ |M_2\rangle &\equiv p|M^0\rangle - q|\overline{M}^0\rangle, \end{aligned} \tag{1.45}$$

where

$$p = \frac{\sqrt{\mathcal{H}_{12}}}{\mathcal{H}_{12} + \mathcal{H}_{21}} = \frac{\sqrt{\mathcal{M}_{12} - i\Gamma_{12}/2}}{\mathcal{H}_{12} + \mathcal{H}_{21}} \tag{1.46}$$

$$q = \frac{\sqrt{\mathcal{H}_{21}}}{\mathcal{H}_{12} + \mathcal{H}_{21}} = \frac{\sqrt{\mathcal{M}_{21} - i\Gamma_{21}/2}}{\mathcal{H}_{12} + \mathcal{H}_{21}} = \frac{\sqrt{\mathcal{M}_{12}^* - i\Gamma_{12}^*/2}}{\mathcal{H}_{12} + \mathcal{H}_{21}} \tag{1.47}$$

Note that since $\boldsymbol{\mathcal{H}}$ is non-Hermitian, $|M_1\rangle$ and $|M_2\rangle$ may not be orthogonal.

The time evolution for a particle initially (*i.e.* at $t = 0$) in one of its flavour eigenstates

[1] Note that there is an ambiguity in the naming of the two eigenstates. Usually, this ambiguity is resolved by naming $|M_1\rangle$ the eigenstate with the longer decay time.

is given by substituting Eq. 1.44 into Eq. 1.45:

$$|M^0(t)\rangle = g_+(t)|M^0\rangle + \frac{q}{p}g_-(t)|\overline{M}^0\rangle, \tag{1.48}$$
$$|\overline{M}^0(t)\rangle = g_+(t)|\overline{M}^0\rangle + \frac{p}{q}g_-(t)|M^0\rangle,$$

where the coefficients $g_\pm(t)$ are defined as

$$g_\pm(t) \equiv \frac{\exp(-i\lambda_1 t) \pm \exp(-i\lambda_2 t)}{2} \tag{1.49}$$

Thus, from Eq. 1.48, we can determine the probabilities for oscillation,

$$\mathcal{P}(M^0(0) \to M^0(t)) = |\langle M^0(t)|M^0|\rangle|^2 = |g_+(t)|^2, \tag{1.50}$$
$$\mathcal{P}(\overline{M}^0(0) \to \overline{M}^0(t)) = |\langle \overline{M}^0(t)|\overline{M}^0|\rangle|^2 = |g_+(t)|^2, \tag{1.51}$$

and for non oscillation,

$$\mathcal{P}(M^0(0) \to \overline{M}^0(t)) = |\langle M^0(t)|\overline{M}^0|\rangle|^2 = \left|\frac{q}{p}\right|^2 \cdot |g_-(t)|^2, \tag{1.52}$$
$$\mathcal{P}(\overline{M}^0(0) \to M^0(t)) = |\langle \overline{M}^0(t)|M^0|\rangle|^2 = \left|\frac{p}{q}\right|^2 \cdot |g_-(t)|^2. \tag{1.53}$$

The probabilities for both M^0 and $\overline{M}^0$ mesons to not oscillate are identical. Instead, the probability of oscillation can be different, provided that $|q/p| \neq 1$. The linear coefficient $|g_\pm(t)|^2$ can be rewritten as

$$|g_\pm(t)|^2 = \frac{1}{2}\, e^{-\Gamma t}\left[\cosh\left(\frac{\Delta\Gamma t}{2}\right) \pm \cos(\Delta m\, t)\right]. \tag{1.54}$$

Finally, two adimensional mixing parameters can be defined:

$$x \equiv \Delta m/\Gamma, \qquad y \equiv \Delta\Gamma/2\Gamma, \tag{1.55}$$

and Eq. 1.54 can be rewritten in terms of these new parameters:

$$|g_\pm(t)|^2 = \frac{1}{2}\, e^{-\Gamma t}\left[\cosh(y\Gamma t) \pm \cos(x\Gamma t)\right]. \tag{1.56}$$

Theoretical parametrization

Another convention independent parametrization is also used to describe the mixing and *CPV* processes described before. This parametrization, known as *theoretical* parametrization was introduced in Ref. [24,25] and has the advantage of directly quantifying both the magnitudes and the phase difference between the dispersive and absorptive transition amplitudes. In particular the transition amplitudes between M^0 and $\overline{M}^0$ are described in

term of the mixing observable

$$x_{12} \equiv \frac{2|\mathcal{M}_{12}|}{\Gamma}, \quad y_{12} \equiv \frac{2|\Gamma_{12}|}{\Gamma}, \tag{1.57}$$

and the weak phase

$$\phi_{12} \equiv \arg\left(\frac{\mathcal{M}_{12}}{\Gamma_{12}}\right). \tag{1.58}$$

The first two parameter are *CP*-even, while the latter is *CP*-odd, which means that under *CP* operator (the combination of Charge Conjugation and Parity Transformation operators), they keep or change their sign, respectively. The two parametrizations are related by the following equation:

$$x^2 - y^2 = x_{12}^2 - y_{12}^2 \tag{1.59}$$

$$xy = x_{12}\, y_{12} \cos\phi_{12} \tag{1.60}$$

$$\left|\frac{q}{p}\right|^{\pm 2} (x^2 + y^2) = x_{12}^2 + y_{12}^2 \pm 2\, x_{12}\, y_{12} \sin\phi_{12}. \tag{1.61}$$

In the limit of small *CP* violation, $|q/p| - 1 \ll 1$, as experimentally verified for all the four neutral flavoured mesons, these approximations stand:

$$x_{12} \approx x, \tag{1.62}$$

$$y_{12} \approx y, \tag{1.63}$$

$$\left|\frac{q}{p}\right| - 1 \approx \frac{x_{12} y_{12}}{x_{12}^2 + y_{12}^2} \sin\phi_{12}. \tag{1.64}$$

The theoretical parameters, when fitted over global averages, offer the advantage of exhibiting a lesser degree of correlation compared to those observed between the phenomenological parameters.

1.3.2 Mixing phenomenology

In Eq. 1.56 the oscillation rate of neutral mesons, *i.e.* the cosine term, is determined by the parameter x, representing the mass difference between the two physical eigenstates. Exponential decay trends diverge due to the hyperbolic term, where instead the y parameter appears. These parameters, known as the *mixing parameters*, define the characteristic behaviour of neutral meson mixing.

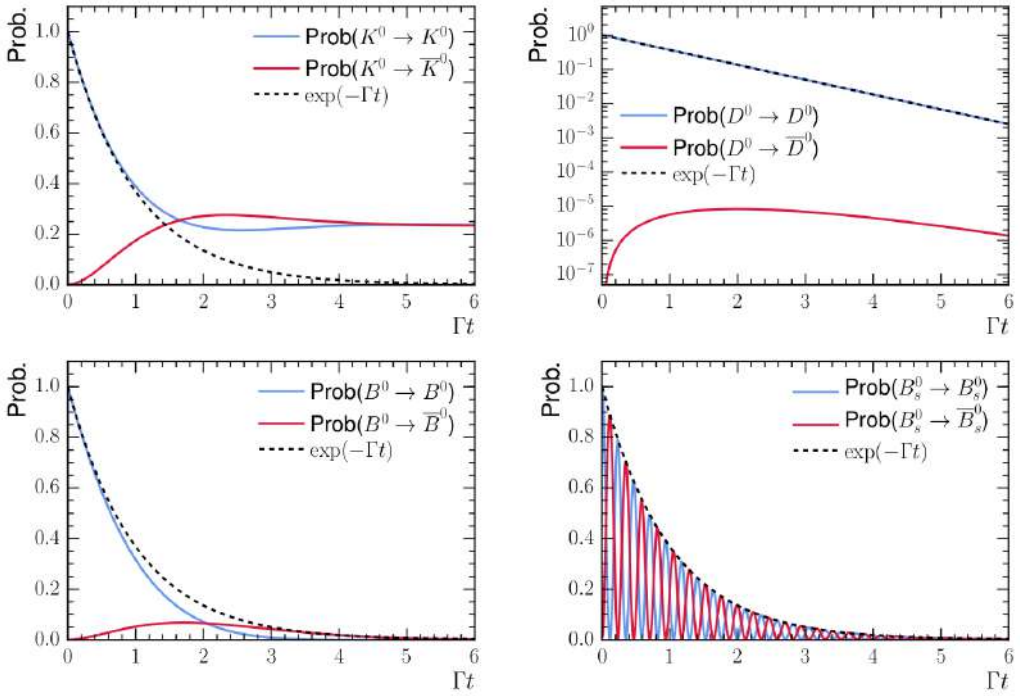

Figure 1.4: Flavour-changing (red) and flavour-unchanging (blue) PDFs for the four neutral meson systems.

Meson	⟨Mass⟩ $\mathcal{M}$ [MeV]	⟨Width⟩ Γ [ps^{-1}]	Lifetime [ps]	x	y
K^0	497.6	0.00559	89.5 52900	0.95	0.997
D^0	1864	2.43	0.410	0.004	0.007
B^0	5280	0.658	1.52	0.77	-0.001
B_s^0	5367	0.662	1.51	26.7	0.06

Table 1.3: Overview of approximate parameters relevant to meson mixing. Masses and widths are the average of the two physical eigenstates. Values taken from Ref. [26] and [27].

The distinct characteristics of the four flavoured neutral mesons (K^0, D^0, B^0, B_s^0) are summarized in Tab.1.3. The differences in their masses (x parameter) and decay widths (y parameter) significantly influence their oscillation behaviours, as depicted in Figs.1.4 and 1.5. As it is clear D^0 mesons mixing parameters are very different, compared to those of K^0, B^0 or B_s^0 mesons.

K^0 system In the kaon system, the y parameter is approximately 1, resulting in two mass eigenstates (K_S^0 and K_L^0) with drastically different lifetimes. For this reason at the time of their discovery, it was believed they were two completely different particles. The substantial mass difference, with $x \approx 1$, causes significant sinusoidal oscillation. This system allows for the study of relatively pure samples of K_S^0 or K_L^0 by analysing decays near the interaction point, where K_L^0 decays are just a small fraction, or at a distance,

where most K_S^0 have decayed.

B systems For both B^0 and B_s^0 mesons, the width difference (y) is small, but they exhibit significant values for the x parameter. The B_s^0 system, in particular, demonstrates fast oscillations requiring high spatial resolution for accurate measurements, which has only happened in recent times [28].

D^0 system The charm meson system is characterized by very small x and y parameters, necessitating large data samples for accurate statistical analysis. Evidence of charm mixing was first observed in 2007 [29, 30], and a high significance measurement was performed by the LHCb experiment only in 2012 [31].

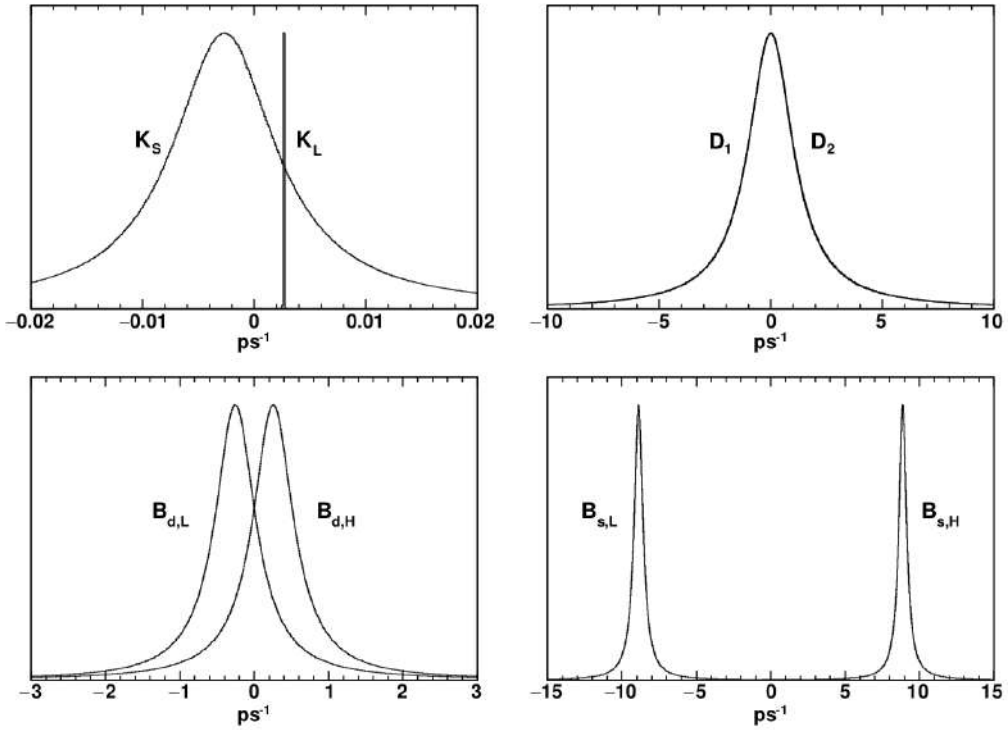

Figure 1.5: The widths and mass differences of the physical states of the flavoured neutral mesons. The width corresponds to the inverse lifetime while the mass difference determines the oscillation frequency.

Mixing amplitudes are influenced by two primary types of contributions: short distance and long distance.

Short distance contribution The short distance contribution primarily stems from the box diagram, as depicted in the left panel of Fig. 1.6 for the D^0 meson. This contribution is named for its characteristic smaller length scale relative to strong interactions since it involves only weak interaction vertices. In the systems of K^0 and B^0 mesons, this box diagram is the predominant component, whereas it is notably suppressed in the D^0 system. The suppression is due to the CKM suppression in the loop involving the

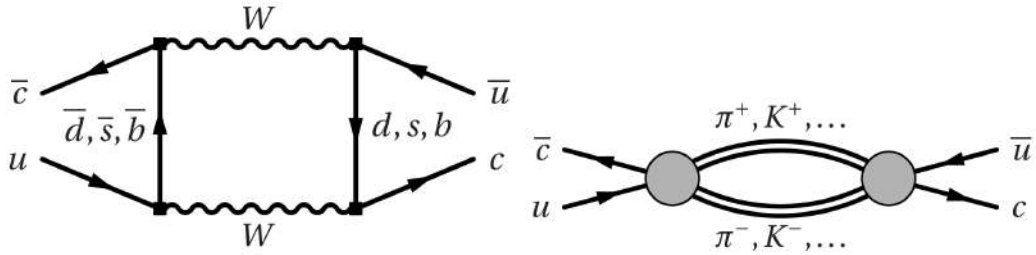

Figure 1.6: The two main diagrams contributing to the D^0-$\overline{D}^0$ mixing: (left) the box diagram and (right) the re-scattering diagram.

bottom quark, quantified by a factor of $|V_{ub}V_{cb}^*|^2/|V_{us}V_{cs}^*|^2 \approx 10^{-5}$. Additionally, the GIM mechanism [32] leads to the cancellation of contributions from down and strange quarks, as indicated by $V_{cd}^*V_{ud} + V_{cs}^*V_{us} \approx 10^{-5}$. Predictions for the x and y parameters in the D^0 system based solely on short distance contributions are around $\mathcal{O}(10^{-6})$, significantly lower than the experimentally observed values of about 0.5%. Hence, long-distance contributions play a major role in D^0 meson mixing.

Long distance contribution Long-distance contributions arise from intermediate on-shell states that are common to both the meson and its antiparticle. This mechanism, illustrated in the right panel of Fig 1.6 for the D^0 meson, can be conceptualized as the decay of the neutral meson into a common final state (like K^+K^- or $\pi^+\pi^-$ in the D^0 case), followed by the recombination of these final state particles into the anti-meson. Unlike the short-distance effect, long-distance contributions in charm meson mixing are not subject to the same level of suppression, making them the dominant factor in the mixing amplitude.

1.4 CP violation

CP violation is a phenomenon in particle physics where the symmetry between particles and antiparticles is not conserved. Under the CP operator, a state $|f\rangle$ transforms as $CP|f\rangle = \omega_f|\overline{f}\rangle$, where ω_f is a complex phase with a magnitude of 1. For antiparticles, the transformation is $CP|\overline{f}\rangle = \omega_f^*|f\rangle$. There are three experimentally observed types of CP violation [33]:

- CP violation in the decay;
- CP violation in the mixing;
- CP violation in the interference between decay and mixing.

CP violation in the decay For a particle X decaying into a final state f, the decay amplitude is defined as

$$\mathcal{A}(X \to f) \equiv \langle f|\boldsymbol{\mathcal{H}}|X\rangle, \tag{1.65}$$

where $\mathcal{H}$ is the decay Hamiltonian. Similarly, for the antiparticle $\overline{X}$ decaying into the C-conjugated final state $\overline{f}$, the amplitude is

$$\mathcal{A}(\overline{X} \to \overline{f}) \equiv \langle \overline{f}|\mathcal{H}|\overline{X}\rangle. \tag{1.66}$$

CP violation in decay occurs if the probability of X decaying into f differs from the probability of $\overline{X}$ decaying into $\overline{f}$. Generally, the computation of these amplitudes involves two kinds of phases.

Weak phases These are phases that arise from the weak interaction and are associated with the CKM matrix phase, the only source of *CP* violation in the Standard Model. They change sign under *CP* transformation.

Strong phases Also known as scattering phases, these are generated by strong interactions, particularly in processes involving hadrons. Unlike weak phases, strong phases do not change sign under *CP* transformation.
Considering a decay process with multiple amplitudes a_i, the total amplitude can be expressed as a sum of individual contributions, each with its own weak (ϕ_i) and strong (δ_i) phases:

$$\mathcal{A}(X \to f) = \sum_i |a_i| e^{i(\phi_i + \delta_i)}, \qquad \mathcal{A}(\overline{X} \to \overline{f}) = \sum_i |a_i| e^{i(-\phi_i + \delta_i)}, \tag{1.67}$$

The difference between the squared magnitudes of these amplitudes indicates *CP* violation:

$$|\mathcal{A}(X \to f)|^2 - \left|\mathcal{A}(\overline{X} \to \overline{f})\right|^2 = -2 \sum_{i,j} |a_i||a_j| \sin(\phi_i - \phi_j) \sin(\delta_i - \delta_j). \tag{1.68}$$

For observable *CP* violation, at least two amplitudes with different weak and strong phases are required. A key observable in this context is the *CP* asymmetry, defined as:

$$A^d_{CP}(f) = \frac{\Gamma(X \to f) - \Gamma(\overline{X} \to \overline{f})}{\Gamma(X \to f) + \Gamma(\overline{X} \to \overline{f})} \tag{1.69}$$

where Γ represents the time-integrated decay width. We can exploit that $\Gamma(X \to f) \propto |\mathcal{A}(X \to f)|^2$ and $\Gamma(\overline{X} \to \overline{f}) \propto |\mathcal{A}(\overline{X} \to \overline{f})|^2$, in order to rewrite Eq. 1.69:

$$A^d_{CP}(f) = \frac{|\mathcal{A}(X \to f)|^2 - |\mathcal{A}(\overline{X} \to \overline{f})||^2}{|\mathcal{A}(X \to f)|^2 + |\mathcal{A}(\overline{X} \to \overline{f})|^2} = \frac{1 - R_f^2}{1 + R_f^2}. \tag{1.70}$$

Here we introduce the ratio R_f, defines as:

$$R_f = \left|\frac{\mathcal{A}(\overline{X} \to \overline{f})}{\mathcal{A}(X \to f)}\right|. \tag{1.71}$$

This ratio, R_f, when different from one, is indicative of *CP* violation. For particles other

than the four flavoured neutral mesons, this is the only observable type of CP violation.

CP violation in the mixing CP violation in mixing occurs when the probability for a neutral meson M^0 to oscillate into its antiparticle $\overline{M}^0$ over time t is different from the probability of the reverse process, where $\overline{M}^0$ oscillates into M^0. This form of CP violation can be understood through the dynamics of meson mixing. From Eq. 1.52, we know that such a difference in oscillation probabilities is possible only if the magnitude of the ratio of the coefficients in the superposition of $|M^0\rangle$ and $|\overline{M}^0\rangle$ in the mass eigenstates (Eq. 1.45) is not equal to 1. This ratio is represented by R_m and is defined as:

$$R_m \equiv \left|\frac{q}{p}\right| \neq 1. \tag{1.72}$$

CP violation in the interference In cases where a final state is accessible from both M^0 (a neutral meson) and its antiparticle $\overline{M}^0$, CP violation can occur due to interference between the direct decay ($M^0 \to f$) and the decay involving mixing ($M^0 \to \overline{M}^0 \to f$). This type of CP violation is observable when the condition

$$\mathcal{I}m(\lambda_f) + \mathcal{I}m(\lambda_{\overline{f}}) \neq 0 \tag{1.73}$$

is satisfied, where λ_f and $\lambda_{\overline{f}}$ are defined as:

$$\lambda_f \equiv \frac{q\mathcal{A}(\overline{M}^0 \to f)}{p\mathcal{A}(M^0 \to f)} \qquad \text{and} \qquad \lambda_{\overline{f}} \equiv \frac{q\mathcal{A}(\overline{M}^0 \to \overline{f})}{p\mathcal{A}(M^0 \to \overline{f})}. \tag{1.74}$$

For CP-symmetric final states, λ_f can be expressed as:

$$\lambda_f = \left|\frac{q}{p}\right| \left|\frac{\mathcal{A}(\overline{M}^0 \to f)}{\mathcal{A}(M^0 \to f)}\right| \exp\left[i \arg\left(\frac{q\mathcal{A}(\overline{M}^0 \to f)}{p\mathcal{A}(M^0 \to f)}\right)\right] = R_m R_f e^{i\phi_f}, \tag{1.75}$$

whit

$$\phi_f \equiv \arg\left(\frac{q\mathcal{A}(\overline{M}^0 \to f)}{p\mathcal{A}(M^0 \to f)}\right). \tag{1.76}$$

1.4.1 CP violation in the D^0 system

The charm quark, part of the second generation of quarks, plays a significant role in the study of CP violation. It has a mass of about 1.3 GeV and an electric charge of $+\frac{2}{3}$. Like all quarks, the charm quark is not found in isolation but in bound states forming hadrons. These hadrons can be categorized as:

- **Open charm** mesons or baryons, containing one or more charm quarks bound to other quark types.
- **Charmonium** states, which are $c\bar{c}$ bound states with no net charm.

In the Standard Model, strong and electromagnetic interactions are flavour-conserving, meaning they do not change the flavour of quarks. Therefore, charm quarks can only decay through weak interactions mediated by $W^{\pm}$ bosons (in the case of open charm particles) or through annihilation with an anti-charm quark (as in charmonium states). Open charm particles are unique in that they provide an opportunity to study the decay of an up-type quark into a down-type quark within a bound state. This is not possible with up quarks, which are stable as the lightest quarks, or top quarks, which decay too rapidly for hadronization.

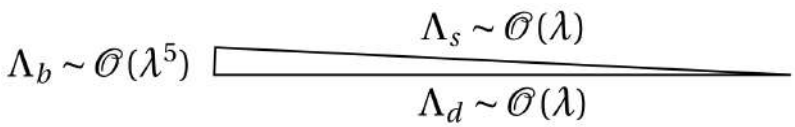

Figure 1.7: Sketch of the unitary triangle for charm meson decays. The figure is out of scale as the vertical direction is enlarged by a factor of twenty.

Charm unitary triangle The study of charmed meson decays focuses on specific elements of the CKM matrix, primarily those in the first two rows. The unitarity condition for these elements is given by:

$$V_{cd}^* V_{ud} + V_{cs}^* V_{us} + V_{cb}^* V_{ub} = 0. \tag{1.77}$$

Expanding each term using the Wolfenstein parametrization, we get:

$$V_{cd}^* V_{ud} = -\lambda + \frac{\lambda^3}{2} + \frac{\lambda^5}{8}(1+4A^2) - \lambda^5 A^2(\rho + i\eta) + \mathcal{O}(\lambda^7), \tag{1.78}$$

$$V_{cs}^* V_{us} = \lambda - \frac{\lambda^3}{2} - \frac{\lambda^5}{8}(1+4A^2) + \mathcal{O}(\lambda^7), \tag{1.79}$$

$$V_{cb}^* V_{ub} = \lambda^5 A^2(\rho + i\eta) + \mathcal{O}(\lambda^{11}), \tag{1.80}$$

resulting in a significantly distorted triangle, with one side of the order of λ^5, as depicted in Fig. 1.7, where $\Lambda_f = V_{cf}^* V_{uf}$.

Due to the influence of low-energy strong interaction effects, theoretical predictions for the magnitude of CP violation in charm decays are challenging to compute with high accuracy. The expected asymmetries are on the order of $10^{-3} - 10^{-4}$ for direct CPV [3,4,34]. For CPV in mixing and in the interference between mixing and decay, the expected asymmetries are even smaller [35].

Chapter 2

Measurement of mixing and CPV in the charm sector

This chapter gives a brief introduction to the varied experimental settings of charm physics and its techniques. It follows an overview of the main experimental observable in the field of charm mixing and CP violation, with an in-depth focus on the formalism and experimental state of the art of the measurement of the decay-time dependency of the $D^0 \to K\pi$ WS-to-RS ratio, which is the main subject of this thesis.

2.1 Charm production

Charm physics is explored in diverse experimental environments, including different types of accelerators, energy ranges, and production mechanisms, leading to a broad spectrum of cross sections. The primary distinction in experimental setups is between e^+e^- colliders and hadron colliders, each offering unique advantages:

- the e^+e^- **colliders** are characterized by cleaner interactions with known energy, fewer interaction vertices per event, almost hermetic detectors, minimal background, and high efficiency.
- the **hadron colliders** reach higher energies, leading to significantly higher cross sections. Though the event quality might be lower compared to e^+e^- colliders, the larger statistics compensate for this.

Within e^+e^- colliders, there are two main experimental setups used for studying charm physics.

"D-factories" Operating slightly above 3770 MeV, the $\Psi(3770)$ resonance is produced, decaying into quantum correlated $D^0\overline{D}^0$ or D^+D^- pairs. At this resonance, the cross section for $D\overline{D}$ pair production is about 8 nb. However, since $\Psi(3770)$ is produced at rest, measuring decay time and related observables is impossible. This setup has been utilized in the MARK III, CLEO and BESIII experiments.

B-factories These operate at a higher centre-of-mass energy of 10.6 GeV to produce $\Upsilon(4S)$, which predominantly decays into quantum-correlated $B^0\overline{B}^0$ or B^+B^- pairs. Those are the main focus of these experiments, and that is why they are known as B-factories. Charm particles are also produced as the result of the decay of $B\overline{B}$ pairs, still the cross section for producing at least one D^0 is smaller than at the $\Psi(3770)$ resonance: 1.45 nb. A comparable number of D mesons are produced in the continuum $e^+e^- \to c\bar{c}$. The BaBar and Belle experiments use this mechanism, benefiting from asymmetric colliders that enhance decay-time resolution. They compensate for the lower cross sections by achieving higher instantaneous luminosities[1], enabling them to collect extensive datasets over their operational lifetimes: about 500 fb^{-1} at the BaBar experiment, and about 1000 fb^{-1} at the Belle experiment, compared to the much lower 0.5 fb^{-1} and 3 fb^{-1} respectively collected by the CLEO and BESIII experiments.

Experiment	Year	beam	$\sqrt{s}$	$\sigma_{acc}(D^0)$	$\int \mathcal{L}\,\mathrm{d}t$	$\sim n(D^0)$
CLEO	2003-2008	e^+e^-	3.77 GeV	8 nb	0.5 fb^{-1}	4.0×10^6
BESIII *	2010-2024	e^+e^-	3.77 GeV	8 nb	20 fb^{-1}	1.6×10^8
BaBar	1999-2008	e^+e^-	10.6 GeV	1.45 nb	500 fb^{-1}	7.3×10^8
Belle	1999-2010	e^+e^-	10.6 GeV	1.45 nb	1000 fb^{-1}	1.5×10^9
Belle II *	2019-2026	e^+e^-	10.6 GeV	1.45 nb	50 ab^{-1}	7.5×10^{10}
CDF	2001-2011	$p\overline{p}$	2 TeV	13 μb	10 fb^{-1}	1.3×10^{11}
LHCb Run 1	2011-2011	pp	7-8 TeV	1.4-1.6 mb	1.1+2.1 fb^{-1}	4.6×10^{12}
LHCb Run 2	2015-2018	pp	13 TeV	2.7 mb	5.9 fb^{-1}	1.6×10^{13}
LHCb Run 3*	2022-2025	pp	13.6 TeV	2.7 mb	17 fb^{-1}	4.6×10^{13}

Table 2.1: Charm production values for different experiments with a focus on D^0 production in the respective detector acceptances. Ongoing experiments are marked with * and the planned integrated luminosities are reported.

Hadrons colliders Charm production cross sections at hadron colliders are significantly higher than at e^+e^- colliders. The asymmetric collisions lead to good time resolution due to the boost effect. For example, at the Tevatron ($p\overline{p}$ collider with $\sqrt{s}$ = 2 TeV), the CDF experiment collected an integrated luminosity of 10 fb^{-1} and measured a D^0 production cross section of 13 μb [36]. Similarly, at the LHC (pp collider), LHCb collected 1.1 fb^{-1}, 2.1 fb^{-1} and 5.9 fb^{-1}, respectively at $\sqrt{s}$ =7 TeV, $\sqrt{s}$ =8 TeV and $\sqrt{s}$ =13 TeV, measuring cross sections of 1.4 mb, 1.6 mb and 2.7 mb: six orders of magnitude larger than that at B-factories.

Table 2.1 summarizes the key features of major experiments focused on charm physics, highlighting the significant advances in data collection, especially at LHCb, which has the largest dataset of charm particles. This extensive dataset has enabled groundbreaking measurements in the charm sector, including the first observation of CP violation in charm particle decays on the 21^{st} of March 2019 [1].

[1]The present record for SuperKEKB is 4.7×10^{34} $\text{cm}^{-2}\text{s}^{-1}$.

2.2 Flavour tagging

Flavour tagging is a crucial technique in flavour physics, especially for measuring mixing. In our case, this process requires identifying the flavour of the D^0 at its production and at its decay time. Various methods are employed for flavour tagging.

D^* tagging One common method to tag the flavour at production involves the strong decay $D^{*+} \to D^0\pi^+$ and its charge-conjugate $D^{*-} \to \overline{D}^0\pi^-$. In this decay, the charge of the pion indicates the flavour of the D^0 meson. These pions have low kinetic energy and are often referred to as soft pions, π_s. Their trajectories are highly susceptible to being curved out of detector acceptance by the magnetic field, highly impacting their detection efficiency. For the same reason, they exhibit significant detection charge asymmetries that, if not properly accounted for, can lead to spurious physics asymmetries. Despite these challenges, the limited amount of free energy in D^* decays allows for better mass resolution and improved background rejection.

Semileptonic tagging Another approach utilizes flavour-specific decays of B mesons, particularly the process $B^0 \to D^0\mu X$ (where X represents a non-reconstructed portion of the final state). The advantages of this method include the high branching ratio of semileptonic decays and the efficient trigger response for muons, which compensates for the comparatively lower production rate against hadrons. Additionally, in this approach, the D^0 reconstruction efficiency is relatively independent of its flight distance, unlike with D^* tagging where D^0 mesons with decay vertices near the interaction point have lower trigger efficiency. Semileptonic tagging is often used alongside D^* tagging to enhance decay-time coverage and provides a more extended lever arm for measuring time-dependent effects.

Opposite side tagging At e^+e^- colliders, another effective technique involves reconstructing the opposite side charm meson in a flavour-specific decay. The underlying principle here is that quarks (or mesons) are always produced in pairs, so each charm meson is associated with a hadron containing an anti-charm quark. For instance, at colliders operating at the $\Psi(3770)$ resonant production energy, when quantum-entangled $D^0\overline{D}^0$ or D^+D^- pairs are produced, analysing one of the D mesons can yield information about its pair, providing valuable insights for flavour tagging. Tagging techniques based on opposite side tagging are also used at the Belle II experiment [37].

2.3 Measurement of $D^0 - \overline{D}^0$ mixing parameters

A wide variety of decay channels and methods are employed to measure D^0-$\overline{D}^0$ mixing parameters, each with its own set of challenges and advantages. In this section we will focus on these observables sensitive to mixing parameters, assuming *CP* symmetry. Under this assumption, the phenomenological and theoretical parameterization are equivalent, since $x_{12} = x$ and $y_{12} = y$, and *CP* violating phases are zero.

2.3.1 Mixing in $D^0 \to K^+\pi^-$ DCS decays

Historically, the first observation of D^0-$\overline{D}^0$ mixing [29,38] was based on studying the decay-time-dependence of the ratio between doubly Cabibbo-suppressed $D^0 \to K^+\pi^-$ decays and Cabibbo-favoured $D^0 \to K^-\pi^+$ decays. This method is among the most sensitive for detecting D^0-$\overline{D}^0$ mixing and forms the core subject of this thesis.

The $D^{*+} \to D^0\,(\to K^+\pi^-)\pi^+$ and $D^{*-} \to \overline{D}^0\,(\to K^-\pi^+)\pi^-$ decay chains are also known as wrong-sign (WS) decays, while the $D^{*+} \to D^0\,(\to K^-\pi^+)\pi^+$ and $D^{*-} \to \overline{D}^0\,(\to K^+\pi^-)\pi^-$ decay chains are also known as right-sign (RS) decays. This is because using the D^* tagging method to identify the flavour of the neutral D meson at production, the charge of the soft pion, produced in the $D^{*\pm}$ decay is opposite (or equal) to the charge of the pion coming from the D^0 (or $\overline{D}^0$) decay. Both $D^0 \to K^+\pi^-$ and $D^0 \to K^-\pi^+$ decays can occur through two different processes, as schematized in Fig. 2.1.

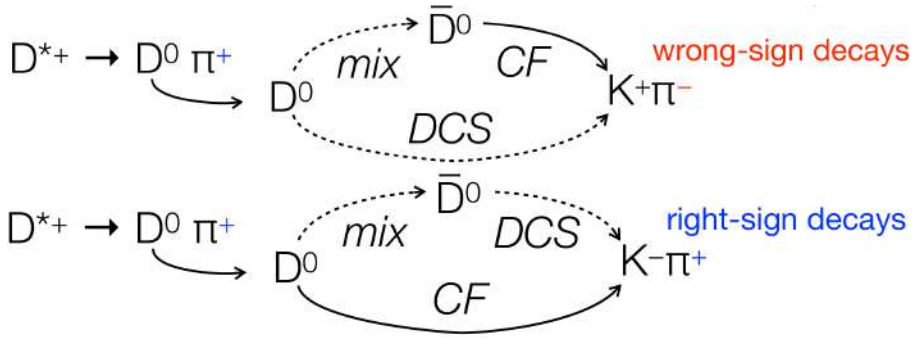

Figure 2.1: A sketch of wrong-sign (top) and right-sign (bottom) decays.

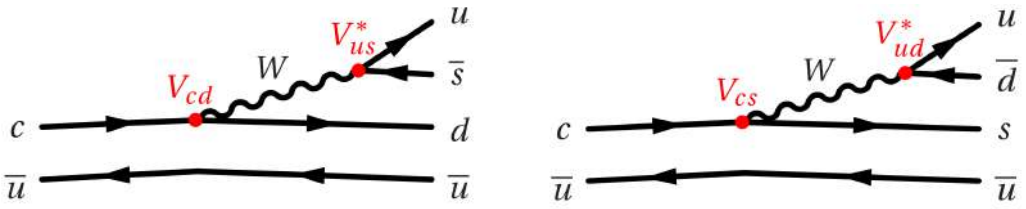

Figure 2.2: Leading tree-level diagrams for the doubly Cabibbo-suppressed $D^0 \to K^+\pi^-$ decay (left) and the Cabibbo-favoured $D^0 \to K^-\pi^+$ decay (right).

WS decay rate A D^0 that decays to a $K^+\pi^-$ final state (WS decay) may undergo

- direct decay $D^0 \to K^+\pi^-$ as shown in the left panel of Fig. 2.2. This process is referred to as doubly Cabibbo-suppressed (DCS) because the amplitude is CKM-suppressed by a factor $|V_{cd}V_{us}^*| \simeq \lambda^2 \sim 5\%$. It takes a λ suppression factor from both vertices;
- mixing to $\overline{D^0}$ followed by the Cabibbo-favoured (CF) decay $\overline{D}^0 \to K^+\pi^-$ as shown in the right panel of Fig. 2.2. Here no CKM suppression is present.

We want to determine the decay rate of WS decays under the assumption of no *CP* violation. We denote with f the final state $K^-\pi^+$, and correspondingly with $\overline{f}$ the charge conjugated, $K^+\pi^-$. The amplitudes of the decay of D^0 and $\overline{D}^0$ mesons into the $K^+\pi^-$ final state are

$$A_{\overline{f}} \equiv \langle \overline{f}|\mathcal{H}|D^0\rangle \quad \text{and} \quad \overline{A}_{\overline{f}} \equiv \langle \overline{f}|\mathcal{H}|\overline{D}^0\rangle. \tag{2.1}$$

Here $\mathcal{H}$ is the effective interaction Hamiltonian. From these we can compute the time-dependent decay rate of $D^0 \to K^+\pi^-$ decay:

$$\Gamma(D^0 \to \overline{f}, t) = \mathcal{N}_f \left|\langle \overline{f}|\mathcal{H}|D^0(t)\rangle\right|^2, \tag{2.2}$$

where $\mathcal{N}_f$ is a constant, accounting for phase space integration. Exploiting the already computed time-evolution of $|D^0(t)\rangle$ derived in Eq. 1.48 we obtain

$$\Gamma(D^0 \to \overline{f}, t) = \mathcal{N}_f \left|g_+(t)A_{\overline{f}} + g_-(t)\overline{A}_{\overline{f}}\right|^2. \tag{2.3}$$

Substituting the definition of $g_\pm(t)$ from Eq. 1.56 one get

$$\begin{aligned}\Gamma(D^0 \to \overline{f}, t) = \frac{\mathcal{N}_f}{2} e^{-\Gamma t} [&(1 + |\lambda_{\overline{f}}|^2)\cosh(y\Gamma t) + (1 - |\lambda_{\overline{f}}|^2)\cos(x\Gamma t) \\ &+ 2\,\mathcal{R}e(\lambda_{\overline{f}})\sinh(y\Gamma t) - 2\,\mathcal{I}m(\lambda_{\overline{f}})\sin(x\Gamma t)],\end{aligned} \tag{2.4}$$

where λ_f is the ratio defined in Eq. 1.74. For small values of mixing parameters x and y, ($x\Gamma t \ll 1$ and $y\Gamma t \ll 1$, as determined experimentally) the time-dependent decay rate can be expanded to quadratic order in the mixing parameters:

$$\begin{aligned}\Gamma(D^0 \to \overline{f}, t) \simeq \mathcal{N}_f\, e^{-\Gamma t} \left|A_{\overline{f}}\right|^2 \{1 + &\left[y\mathcal{R}e(\lambda_{\overline{f}}) - x\mathcal{I}m(\lambda_{\overline{f}})\right] \Gamma t \\ &+ \frac{1}{4}\left[y^2(1 + |\lambda_{\overline{f}}|^2) - x^2(1 - |\lambda_{\overline{f}}|^2)\right] (\Gamma t)^2\}.\end{aligned} \tag{2.5}$$

Till now this expression is completely general for any final state f and also in the presence of *CP* violation. For the $K\pi$ final state the typical parametrization (assuming *CP* symmetry) of the λ_f ratios are

$$\lambda_{K^-\pi^+} \equiv \frac{q}{p}\frac{\overline{A}_{K^-\pi^+}}{A_{K^-\pi^+}} \equiv \sqrt{R_D}\, e^{-i\delta_{K\pi}} \quad \text{and} \quad \lambda_{K^+\pi^-} \equiv \frac{q}{p}\frac{\overline{A}_{K^+\pi^-}}{A_{K^+\pi^-}} \equiv \sqrt{1/R_D}\, e^{i\delta_{K\pi}}, \tag{2.6}$$

where R_D is the ratio of the DCS to the CF rate,

$$R_D = \left|\frac{A_{K^+\pi^-}}{A_{K^-\pi^+}}\right|^2. \tag{2.7}$$

Here $\delta_{K\pi}$ is the strong phase difference between DCS and CF amplitude. The definition of the phase $\delta_{K\pi}$ follows the convention adopted by the HFLAV collaboration [27], and is related to those employed in refs. [7] and [39] as $\delta_{K\pi} = \delta_D^{K\pi} - \pi = -\Delta_{K^-\pi^+}$. Now we can

apply the $\lambda_{K^+\pi^-}$ parametrization defined in Eq. 2.6 in the quadratic expansion of Eq. 2.5, obtaining

$$\Gamma(D^0 \to K^+\pi^-, t) \simeq \mathcal{N}_{K\pi}\, e^{-\Gamma t} |A_{K^-\pi^+}|^2 \left(R_D + \sqrt{R_D} c_{\mathrm{W}} \Gamma t + c'_{\mathrm{W}} (\Gamma t)^2\right), \tag{2.8}$$

where the coefficient c_{W} and c'_{W} are equal to

$$c_{\mathrm{W}} = y \cos\delta_{K\pi} - x \sin\delta_{K\pi}, \tag{2.9}$$

$$c'_{\mathrm{W}} = \frac{1}{4}(y^2 + x^2) + \frac{1}{4} R_D (y^2 - x^2) \simeq \frac{1}{4}(y^2 + x^2), \tag{2.10}$$

where we can neglect the $R_D(y^2 - x^2)$ term at current level of precision ($R_D \sim 3.4 \times 10^{-3}$). In literature, these coefficients are often written as a function of

$$x' = x \cos\delta_{K\pi} + y \sin\delta_{K\pi} \tag{2.11}$$

$$y' = y \cos\delta_{K\pi} - x \sin\delta_{K\pi}, \tag{2.12}$$

that is a rotation of angle $\delta_{K\pi}$ of the mixing parameters x and y. Using this rotated parameter, Eq. 2.9 became

$$c_{\mathrm{W}} = y', \tag{2.13}$$

$$c'_{\mathrm{W}} \simeq \frac{1}{4}(y'^2 + x'^2). \tag{2.14}$$

If we were to measure the mixing parameters using the WS sample only (*i.e.* without using any other control channel), directly fitting Eq. 2.8, this would pose considerable challenges. In fact, the decay rate determined in Eq. 2.8 is highly biased by effects like lifetime acceptance and detection charge asymmetries which are very difficult to correct for.

RS decay rate A D^0 that goes to a $K^-\pi^+$ final state (RS decay chain) can proceed via two distinct mechanisms:

- direct Cabibbo-favoured decay $D^0 \to K^-\pi^+$;
- mixing to $\overline{D}^0$ followed by a doubly Cabibbo-suppressed decay $\overline{D}^0 \to K^-\pi^+$.

The RS process is much more common than the WS ones, in fact, the branching ratio of the Cabibbo-favoured decay $D^0 \to K^-\pi^+$ is about 4%, while the one of the doubly Cabibbo-suppressed $D^0 \to K^+\pi^-$ decay is about 290 times smaller [26]. Due to the much higher probability of direct Cabibbo-favoured decay, contributions from mixing are negligible at the current level of experimental uncertainties. The decay rate of RS decays can be derived as done with WS decays:

$$\Gamma(D^0 \to K^-\pi^+, t) \simeq \mathcal{N}_{K\pi}\, e^{-\Gamma t} |A_{K^-\pi^+}|^2 \left(1 + \sqrt{R_D} c_{\mathrm{R}} \Gamma t + c'_{\mathrm{R}} (\Gamma t)^2\right), \tag{2.15}$$

where the new coefficient c_{R} and c'_{R} are equal to

$$c_{\mathrm{R}} = y\cos\delta_{K\pi} + x\sin\delta_{K\pi}, \tag{2.16}$$

$$c'_{\mathrm{R}} = \frac{1}{4}(y^2 - x^2) + \frac{1}{4}R_D(y^2 + x^2) \simeq \frac{1}{4}(y^2 - x^2). \tag{2.17}$$

WS-to-RS ratio The RS sample has a significantly larger size compared to the WS sample and, therefore, allows it to function as a calibration reference. Modelling the time dependence of the efficiency due to trigger and reconstruction, production and most of the detection asymmetries, can be avoided by looking at $R(t)$, the WS-to-RS ratio of decay rates,

$$\begin{aligned} R(t) &= \frac{\Gamma(D^0(t) \to K^+\pi^-)}{\Gamma(D^0(t) \to K^-\pi^+)} \simeq \frac{R_D + \sqrt{R_D}\, c_{\mathrm{W}}\, \Gamma t + c'_{\mathrm{W}}(\Gamma t)^2}{1 + \sqrt{R_D}\, c_{\mathrm{R}}\, \Gamma t + c'_{\mathrm{R}}(\Gamma t)^2} \\ &\simeq \left[R_D + \sqrt{R_D}\, c_{\mathrm{W}}\, \Gamma t + c'_{\mathrm{W}}(\Gamma t)^2\right] \cdot \left[1 - \sqrt{R_D}\, c_{\mathrm{R}}\, \Gamma t - c'_{\mathrm{R}}(\Gamma t)^2\right] \\ &\simeq R_D + \sqrt{R_D}\,(c_{\mathrm{W}} - R_D c_{\mathrm{R}})\,\Gamma t + (c'_{\mathrm{W}} - R_D c'_{\mathrm{R}})(\Gamma t)^2. \end{aligned} \tag{2.18}$$

The contribution from RS decays to the ratio is suppressed by a factor R_D and can be neglected at the current level of precision, obtaining

$$\begin{aligned} R(t) &= \frac{\Gamma(D^0(t) \to K^+\pi^-)}{\Gamma(D^0(t) \to K^-\pi^+)} \simeq R_D + \sqrt{R_D}\, c_{\mathrm{W}}\, \Gamma t + c'_{\mathrm{W}}(\Gamma t)^2 \\ &\simeq R_D + \sqrt{R_D}\, y'\, \Gamma t + \frac{y'^2 + x'^2}{4}(\Gamma t)^2 \end{aligned} \tag{2.19}$$

Hence, measuring the time dependence of the WS-to-RS decay ratio allows us to access y' and x'. In order to gain insight into the mixing parameters x and y, we need the strong phase $\delta_{K\pi}$, which is not accessible with this experimental observable alone. This external input is crucial as its uncertainty limits the sensitivity to x and y. Measurements from CLEO and BESIII [8,40] provide constraints on $\delta_{K\pi}$, exploiting quantum-correlated D^0-$\overline{D}^0$ pairs produced at threshold. Moreover, recently a global fit to multiple $B \to Dh^+$ decays performed by the LHCb collaboration [7] allows us to further constrain this strong phase, increasing the sensitivity of this analysis. The result of the global fit [7] for this strong phase is a small value, even if significantly different from zero: $\delta_{K\pi} = (10.2^{+2.8}_{-2.8})^\circ$. It follows that $x' \approx x$ and $y' \approx y$, hence this measurement is much more sensitive to the y mixing parameter, which appears in the linear term, than x, that only appears in the quadratic term.

2.3.2 Mixing in $D^0 \to h^+h^-$ CS decays

The y^f_{CP} observable provides another probe for D^0-$\overline{D}^0$ mixing. Applying the approximation $1 - x \simeq e^{-x}$ to Eq. 2.5 we get

$$\begin{aligned}\Gamma(D^0 \to f, t) &\simeq \mathcal{N}_f \left|A_f\right|^2 e^{-\Gamma t}\{1 + \left[y\mathcal{R}e(\lambda_f) - x\mathcal{I}m(\lambda_f)\right] \Gamma t \\ &\simeq \mathcal{N}_f \left|A_f\right|^2 e^{-\hat{\Gamma}(D^0 \to f)t},\end{aligned} \tag{2.20}$$

where $\hat{\Gamma}(D^0 \to f)$ is known as effective decay time of the D neutral mesons to final states, f, defined as

$$\hat{\Gamma}(D^0 \to f) \equiv \Gamma \cdot \left[1 + \left(y\mathcal{R}e(\lambda_f) - x\mathcal{I}m(\lambda_f)\right)\right] \tag{2.21}$$

The observable y^f_{CP} is determine measuring this effective decay time:

$$y^f_{CP} \equiv \hat{\Gamma}(D^0 \to f) - \Gamma = y\mathcal{R}e(\lambda_f) - x\mathcal{I}m(\lambda_f). \tag{2.22}$$

In particular, we are interested in final states that are CP eigenstate (such as K^+K^- or $\pi^+\pi^-$). Starting from the general expression in Eq. 2.5, we take $f = \overline{f} = K^+K^-, \pi^+\pi^-$. Assuming CP symmetry the ratio $\lambda_{K^+K^-}$ and $\lambda_{\pi^+\pi^-}$ are conventionally set to -1. The reason for this convention will be clear in the next section when we generalise these expressions where CP is violated. Hence, under this assumption, y^{KK}_{CP} and $y^{\pi\pi}_{CP}$ are equivalent and can be combined in the single observable y_{CP} that allows to directly access the y mixing parameter: $y_{CP} = y$.

In contrast to the decay-time dependence of WS decays, where the quadratic term was enhanced by a factor $1/R_D \approx 290$, here for the final states $f = h^+h^-$, the quadratic term is negligible. In fact, the decay rate can be expanded as

$$\Gamma(D^0 \to h^+h^-, t) \simeq \mathcal{N}_{h^+h^-} e^{-\Gamma t}|A_{h^+h^-}|^2 \left(1 + c_{K,\pi}\Gamma t + c'_{K,\pi}(\Gamma t)^2\right), \tag{2.23}$$

where the coefficients $c_{K,\pi}$ and $c'_{K,\pi}$ are equal to

$$c_{K,\pi} = -y \tag{2.24}$$

$$c'_{K,\pi} = \frac{1}{2}y^2. \tag{2.25}$$

Exactly as with the WS decay channel, accessing the mixing parameters using only the K^+K^- or $\pi^+\pi^-$ decay channels is extremely challenging as within one experimental measurement the decay rates always appear multiplied by the instrumental and selection efficiencies, with their related time dependency, very difficult to model accurately. Again, it is useful to use the $D^0 \to K^-\pi^+$ (RS) decay as a reference channel. From Eq. 2.15 and 2.16 we derive that the observable $y^{K\pi}_{CP}$ is defines as

$$y^{K\pi}_{CP} \equiv -\sqrt{R_D}c_{\mathrm{R}} = \sqrt{R_D}y\cos\delta_{K\pi}. \tag{2.26}$$

The experimentally measured observable is the ratio $R^{hh}(t)$

$$R^{hh}(t) = \frac{\Gamma(D^0 \to h^+h^-, t)}{\Gamma(D^0 \to K^-\pi^+, t)} \simeq R^0 \, \frac{e^{-\hat{\Gamma}(D^0 \to h^+h^-)}}{e^{-\hat{\Gamma}(D^0 \to K^-\pi^+)}} = R^0 \, e^{-(y_{CP}^{hh} - y_{CP}^{K\pi})\Gamma t} \tag{2.27}$$

Fitting the decay-time dependency of this ratio one can measure the observable $y_{CP} - y_{CP}^{K\pi}$ while keeping the treatment of experimental efficiencies feasible. The global average for $y_{CP} - y_{CP}^{K\pi}$ is dominated by the recent LHCb measurement [41] using LHC Run 2 data:

$$y_{CP} - y_{CP}^{K\pi} = (6.96 \pm 0.26(\text{stat.}) \pm 0.13(\text{syst.})) \times 10^{-3}.$$

2.3.3 Mixing in $D^0 \to K^0_S h^+ h^-$ decays

Decays like $D^0 \to K^0_S\pi^+\pi^-$ and $D^0 \to K^0_S K^+ K^-$ provide direct access to the mixing parameters, particularly x, through simultaneous measurement of decay-time evolution and resonance amplitudes in the Dalitz plot. The two-body masses Dalitz plane ($m^2_\pm \equiv m^2(K^0_S h^\pm)$) can be divided into two sets of n bins, each symmetric about its principal bisector, as shown in Fig. 2.3. Bins are labelled with index $b = -n, .., -1, 1, ..n$, where positive indices refers to bins in the $m^2(K^0_S h^+) > m^2(K^0_S h^-)$ region. The decay rate expression from

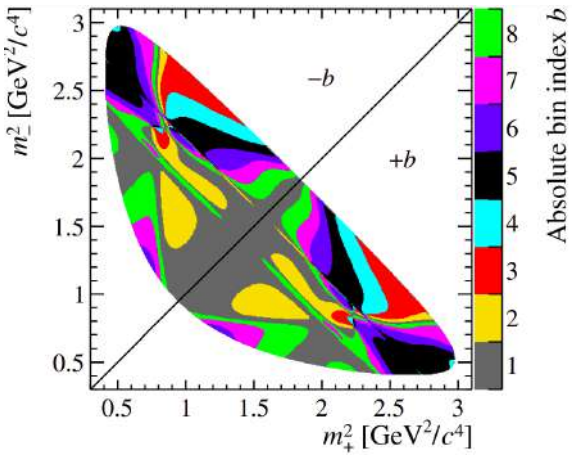

Figure 2.3: Iso-δ binning of the $D^0 \to K^0_S\pi^+\pi^-$ Dalitz plot, based on the BaBar 2008 amplitude model [42, 43]. The bins are symmetric with respect to the bisector. Positive indices refer to bins in the lower region. Colours indicate the absolute value of the bin index b.

Eq. 2.5 can be integrated over the kinematic regions delimited by the bins in the Dalitz

plane, obtaining

$$\begin{aligned}\Gamma_b(D^0 \to f, t) &\equiv \int_b \Gamma(D^0 \to f, t) \\ &\simeq \int_b \mathcal{N}_f \ |A_f|^2 \ e^{-\Gamma t}\{1 + \left[y\mathcal{R}e(\lambda_f) - x\mathcal{I}m(\lambda_f)\right] \Gamma t \\ &+ \frac{1}{4}\left[y^2(1+|\lambda_f|^2) - x^2(1-|\lambda_f|^2)\right] (\Gamma t)^2\} \\ &= \mathcal{N}_b \ |A_b|^2 \ e^{-\Gamma t}\{1 + \left[y\mathcal{R}e(\lambda_b) - x\mathcal{I}m(\lambda_b)\right] \Gamma t \\ &+ \frac{1}{4}\left[y^2(1+|\lambda_b|^2) - x^2(1-|\lambda_b|^2)\right] (\Gamma t)^2\},\end{aligned} \tag{2.28}$$

where the subscript b refers to the average value of each quantity in the Dalitz bin b. In particular, λ_b will be the average value of λ_f in the Dalitz bin b and, just like it is done for the WS decays, is conventionally expressed as

$$\lambda_b = r_b e^{-\delta^b_{K^0_S hh}}, \tag{2.29}$$

where

$$r_b \equiv \frac{\int_{-b} dm^2_+ dm^2_- |A_f(dm^2_+, dm^2_-)|^2}{\int_b dm^2_+ dm^2_- |A_f(dm^2_+, dm^2_-)|^2} \tag{2.30}$$

and $\delta^b_{K^0_S hh}$ is the average effective strong phase in the bin b, and $\cos_b \delta_{K^0_S hh}$ and $\sin_b \delta_{K^0_S hh}$ are the average value of cosine and sine of $\delta_{K^0_S hh}$ in each bin b. The experimental observable is the ratio of decay rate between opposite bins:

$$R_b(t) = \frac{\Gamma_{-b}(D^0 \to K^0_S h^+ h^-, t)}{\Gamma_b(D^0 \to K^0_S h^+ h^-, t)} \simeq \frac{r_b + \sqrt{r_b}\, c_{-b}\, \Gamma t + c'_{-b}(\Gamma t)^2}{1 + \sqrt{r_b}\, c_b\, \Gamma t + c'_b(\Gamma t)^2}, \tag{2.31}$$

where

$$c_{-b} = y \cos_b \delta_{K^0_S hh} - x \sin_b \delta_{K^0_S hh}, \tag{2.32}$$

$$c'_{-b} = \frac{1}{4}(y^2 + x^2) + \frac{1}{4} r_b (y^2 - x^2), \tag{2.33}$$

$$c_b = y \cos_b \delta_{K^0_S hh} + x \sin_b \delta_{K^0_S hh}, \tag{2.34}$$

$$c_b = \frac{1}{4}(y^2 - x^2) + \frac{1}{4} r_b (y^2 + x^2). \tag{2.35}$$

This expression is exactly equivalent to the WS-to-RS ratio one, however, in this case, r_b is $\mathcal{O}(0.1 - 1)$, hence quadratic terms can usually be dropped, leading to the approximation

$$R_b(t) \simeq r_b + \sqrt{r_b}\left[(1 - r_b) y \cos_b \delta_{K^0_S hh} - (1 + r_b) x \sin_b \delta_{K^0_S hh}\right] \Gamma t. \tag{2.36}$$

The ratios of multiple bins are fitted simultaneously, constraining the strong phases with external input allowing to access the mixing parameters x and y. The strong phase

$\delta_{K^0_S hh}$ varies moving in the Dalitz plot, spanning the whole range $[-\pi, \pi]$. The possible values of the strong phase can be divided into bins, and for each bin the contours of the corresponding one in the Dalitz plot can be determined, using an amplitude model. This is the optimal bin division since in this way the sensitivity to mixing parameters will vary from bin to bin, allowing to access both x and y in the linear term of the decay-time expansion. The accuracy of the amplitude model would impact the sensitivity of the measuring but would not bias it. However, just like the WS-to-RS ratio analysis, this measurement relies on external determination of the strong phases.

In literature, a different notation is used, where the mixing parameters are x_{CP} and y_{CP}, that under *CP* symmetry are equivalent to the previously defined mixing parameters x and y. In particular y_{CP} is theoretically equivalent to the y_{CP} observable described in the previous section. A recent LHCb measurement that exploits the full LHC Run 2 data reports on the measurements of these parameters in $D^0 \to K^0_S \pi^+ \pi^-$ decays [6]:

$$x_{CP} = (3.97 \pm 0.46(\text{stat.}) \pm 0.29(\text{syst.})) \times 10^{-3}$$
$$y_{CP} = (4.59 \pm 1.20(\text{stat.}) \pm 0.85(\text{syst.})) \times 10^{-3},$$

resulting in the first observation of a non-zero value for the x parameter.

2.3.4 Mixing in "forbidden" decay

A theoretically straightforward approach to measure mixing involves the rate of the "forbidden" decay $D^0 \to K^+ \mu^- \overline{\nu} \mu$, which is only possible through $D^0 - \overline{D}^0$ mixing. The time-integrated rate of these forbidden decays compared to their allowed counterparts, such as $D^0 \to K^- \mu^+ \nu \mu$, is given by:

$$R_m = \frac{\Gamma(D^0 \to K^+ \mu^- \overline{\nu}_\mu)}{\Gamma(D^0 \to K^- \mu^+ \nu_\mu)} \simeq \frac{x^2 + y^2}{2} \tag{2.37}$$

However, this measurement requires very large samples of D^0 mesons and it is more challenging at hadronic colliders due to the presence in the final state of a neutrino and the inability to measure the associated missing energy. Currently, there is still no evidence for D^0 mixing probing this experimental observable. The most precise measurement to date is from the Belle collaboration [44], reporting

$$R_m = (1.3 \pm 2.2(\text{stat.}) \pm 2.0(\text{syst.})) \times 10^{-4}.$$

2.4 Search for *CP* violation in charm decays

Differently from the previous section, here, we account for *CP* violation effects. Under this hypothesis, phenomenological and theoretical parametrization differ, hence observables will be described as a function of both parametrizations. As for measuring the mixing parameters, different decay channels and methods are used to measure *CP* violation effects, each with a different sensitivity.

In the previous section we derived the D^0 decay rate to final state f (see Eq. 2.5), similarly this can also be derived for the decay rate of $\overline{D}^0$:

$$\Gamma(D^0 \to f, t) \simeq \mathcal{N}_f\, e^{-\Gamma t}\, \left|A_f\right|^2 \{1 + \left[y\mathcal{R}e(\lambda_f) - x\mathcal{I}m(\lambda_f)\right]\, \Gamma t + \frac{1}{4}\left[y^2(1+|\lambda_f|^2) - x^2(1-|\lambda_f|^2)\right]\, (\Gamma t)^2\}, \tag{2.38}$$

$$\Gamma(\overline{D}^0 \to f, t) \simeq \mathcal{N}_f\, e^{-\Gamma t}\, \left|\overline{A}_f\right|^2 \{1 + \left[y\mathcal{R}e(\lambda_f^{-1}) - x\mathcal{I}m(\lambda_{\overline{f}}^{-1})\right]\, \Gamma t + \frac{1}{4}\left[y^2(1+|\lambda_f^{-1}|^2) - x^2(1-|\lambda_{\overline{f}}^{-1}|^2)\right]\, (\Gamma t)^2\}. \tag{2.39}$$

These expressions can be derived also in the theoretical parametrization framework, starting from the decay-time dependence of the decay rate:

$$\Gamma(D^0 \to f, t) \simeq \mathcal{N}_f\, e^{-\Gamma t}\, \left|A_f\right|^2 \{1 - \mathcal{R}e\left(y_{12}/\lambda_f^{\Gamma} + ix_{12}/\lambda_f^{M}\right)\, \Gamma t + \frac{1}{4}\left[y_{12}^2(1+|\lambda_f^{\Gamma}|^{-2}) + x^2(-1+|\lambda_f^{M}|^{-2}) + 2y_{12}x_{12}\mathcal{I}m(1/\lambda_f^{\Gamma}\lambda_f^{M*})\right]\, (\Gamma t)^2\}, \tag{2.40}$$

$$\Gamma(\overline{D}^0 \to f, t) \simeq \mathcal{N}_f\, e^{-\Gamma t}\, \left|A_f\right|^2 \{1 - \mathcal{R}e\left(y_{12}\lambda_f^{\Gamma} + ix_{12}\lambda_f^{M}\right)\, \Gamma t + \frac{1}{4}\left[y_{12}^2(1+|\lambda_f^{\Gamma}|^{2}) + x^2(-1+|\lambda_f^{M}|^{2}) + 2y_{12}x_{12}\mathcal{I}m(\lambda_f^{\Gamma}\lambda_f^{M*})\right]\, (\Gamma t)^2\}, \tag{2.41}$$

where the decay amplitude ratio λ_f^{Γ} and λ_f^{M} are introduced,

$$\lambda_f^{\Gamma} \equiv \frac{\Gamma_{12}}{|\Gamma_{12}|}\frac{A_f}{\overline{A}_f}, \quad \lambda_f^{M} \equiv \frac{\mathcal{M}_{12}}{|\mathcal{M}_{12}|}\frac{A_f}{\overline{A}_f}, \tag{2.42}$$

that corresponds to decay amplitudes proceeding through absorptive and dispersive mixing, respectively. Again, these expressions are completely general for any final state f, and the decay rate for the CP-conjugate final state $\overline{f}$ is obtained just by switching f with $\overline{f}$.

2.4.1 CP asymmetries in $D^0 \to K^+\pi^-$ DCS decays

The $D^0 \to K^+\pi^-$ decay mode, extensively discussed in this thesis, offers insights into all CPV types: in decay, mixing, and interference. It is useful to define the DCS to RS ratios of D^0 and $\overline{D}^0$ mesons and their average,

$$R_D^+ \equiv \left|\frac{A_{K^+\pi^-}}{A_{K^-\pi^+}}\right|^2, \quad R_D^- \equiv \left|\frac{\overline{A}_{K^+\pi^-}}{\overline{A}_{K^-\pi^+}}\right|^2, \quad R_D \equiv \frac{R_D^+ + R_D^-}{2}, \tag{2.43}$$

as well as the CP asymmetry in the decay of both DCS and CF decays:

$$a_{\mathrm{W}}^d \equiv \frac{|A_{K^+\pi^-}|^2 - |\overline{A}_{K^-\pi^+}|^2}{|A_{K^+\pi^-}|^2 + |\overline{A}_{K^-\pi^+}|^2} \quad \text{and} \quad a_{\mathrm{R}}^d \equiv \frac{|A_{K^-\pi^+}|^2 - |\overline{A}_{K^+\pi^-}|^2}{|A_{K^-\pi^+}|^2 + |\overline{A}_{K^+\pi^-}|^2}. \tag{2.44}$$

From these definitions, it follows that

$$R_D^{\pm} = R_D \frac{(1 \pm a_W^d)(1 \mp a_R^d)}{1 - 2a_W^d a_R^d} \simeq R_D[1 \pm (a_W^d - a_R^d)], \tag{2.45}$$

where, in the approximation, only terms at first order in a_W^d and a_R^d are retained. We can also define the *CPV* observable

$$A_D \equiv \frac{R_D^+ - R_D^-}{R_D^+ + R_D^-} \simeq a_W^d - a_R^d. \tag{2.46}$$

Phenomenological parametrization Accounting for *CPV* in the final states $K^{\pm}\pi^{\mp}$, the decay ratios λ_f and λ_f are conventionally written as

$$\lambda_{K^-\pi^+} \equiv \frac{q}{p}\frac{\overline{A}_{K^-\pi^+}}{A_{K^-\pi^+}} \equiv \sqrt{R_D^- \frac{1 - a_R^d}{1 + a_R^d}} \left|\frac{q}{p}\right| e^{i(\phi_{K\pi}^{\lambda} - \delta_{K\pi})}, \tag{2.47}$$

$$\lambda_{K^+\pi^-} \equiv \frac{q}{p}\frac{\overline{A}_{K^+\pi^-}}{A_{K^+\pi^-}} \equiv \sqrt{\frac{1}{R_D^+} \frac{1 - a_R^d}{1 + a_R^d}} \left|\frac{q}{p}\right| e^{i(\phi_{K\pi}^{\lambda} + \delta_{K\pi})}, \tag{2.48}$$

where $\phi_{K\pi}^{\lambda}$ is the *CP*-violating weak phase, which in general depends on the final state due to *CPV* contribution in the decay amplitude.
The WS time-dependent decay rates can be expanded as

$$\Gamma(D^0 \to K^+\pi^-, t) \simeq \mathcal{N}_{K\pi}\, e^{-\Gamma t} |A_{K^-\pi^+}|^2 \left(R_D^+ + \sqrt{R_D^+} c_W^+ \Gamma t + c_W'^+ (\Gamma t)^2\right), \tag{2.49}$$

$$\Gamma(\overline{D}^0 \to K^-\pi^+, t) \simeq \mathcal{N}_{K\pi}\, e^{-\Gamma t} |\overline{A}_{K^+\pi^-}|^2 \left(R_D^- + \sqrt{R_D^-} c_W^- \Gamma t + c_W'^- (\Gamma t)^2\right), \tag{2.50}$$

while for the RS we get

$$\Gamma(D^0 \to K^-\pi^+, t) \simeq \mathcal{N}_{K\pi}\, e^{-\Gamma t} |A_{K^-\pi^+}|^2 \left(1 + \sqrt{R_D^+} c_R^+ \Gamma t + c_R'^+ (\Gamma t)^2\right), \tag{2.51}$$

$$\Gamma(\overline{D}^0 \to K^+\pi^-, t) \simeq \mathcal{N}_{K\pi}\, e^{-\Gamma t} |\overline{A}_{K^+\pi^-}|^2 \left(1 + \sqrt{R_D^-} c_R^- \Gamma t + c_R'^- (\Gamma t)^2\right). \tag{2.52}$$

Accounting for *CPV* effects D^0 decay rates can differ from $\overline{D}^0$ ones, and we identify with the $+$ and $-$ superscript the coefficients in the decay-time expansion of the D^0 and $\overline{D}^0$

decay rate respectively:

$$c_{\mathrm{W}}^{\pm} = \left(\frac{1 \mp a_{\mathrm{R}}^{d}}{1 \pm a_{\mathrm{R}}^{d}}\right)^{1/2} \left|\frac{q}{p}\right|^{\pm 1} \left[y\cos\left(\pm\phi_{K\pi}^{\lambda} + \delta_{K\pi}\right) - x\sin\left(\pm\phi_{K\pi}^{\lambda} + \delta_{K\pi}\right)\right] \tag{2.53}$$
$$\simeq \left[1 \pm \left(\left|\frac{q}{p}\right| - 1\right) \mp a_{\mathrm{R}}^{d}\right] \left(y\cos\delta_{K\pi} - x\sin\delta_{K\pi}\right)\cos\phi_{K\pi}^{\lambda} \mp \left(x\cos\delta_{K\pi} + y\sin\delta_{K\pi}\right)\sin\phi_{K\pi}^{\lambda},$$
$$\simeq \left[1 \pm \left(\left|\frac{q}{p}\right| - 1\right) \mp a_{\mathrm{R}}^{d}\right] y' \mp x'\phi_{K\pi}^{\lambda},$$

$$c_{\mathrm{W}}'^{\pm} = \frac{1}{4}(y^2 + x^2)\left|\frac{q}{p}\right|^{\pm 2} \frac{1 \mp a_{\mathrm{R}}^{d}}{1 \pm a_{\mathrm{R}}^{d}} + \frac{1}{4}R_{D}^{\pm}(y^2 - x^2) \tag{2.54}$$
$$\simeq \frac{1}{4}\left[1 \pm 2\left(\left|\frac{q}{p}\right| - 1\right) \mp 2a_{\mathrm{R}}^{d}\right](x^2 + y^2) + \frac{1}{4}R_{D}\left[1 \pm \left(a_{\mathrm{W}}^{d} - a_{\mathrm{R}}^{d}\right)\right](y^2 - x^2),$$

$$c_{\mathrm{R}}^{\pm} = \left(\frac{1 \mp a_{\mathrm{W}}^{d}}{1 \pm a_{\mathrm{W}}^{d}}\right)^{1/2} \left|\frac{q}{p}\right|^{\pm 1} \left[y\cos\left(\pm\phi_{K\pi}^{\lambda} - \delta_{K\pi}\right) - x\sin\left(\pm\phi_{K\pi}^{\lambda} - \delta_{K\pi}\right)\right] \tag{2.55}$$
$$\simeq \left[1 \pm \left(\left|\frac{q}{p}\right| - 1\right) \mp a_{\mathrm{W}}^{d}\right] \left(y\cos\delta_{K\pi} + x\sin\delta_{K\pi}\right)\cos\phi_{K\pi}^{\lambda} \mp \left(x\cos\delta_{K\pi} - y\sin\delta_{K\pi}\right)\sin\phi_{K\pi}^{\lambda},$$

$$c_{\mathrm{R}}'^{\pm} = \frac{1}{4}(y^2 - x^2) + \frac{1}{4}R_{D}^{\pm}\left|\frac{q}{p}\right|^{\pm 2} \frac{1 \mp a_{\mathrm{W}}^{d}}{1 \pm a_{\mathrm{W}}^{d}}(y^2 + x^2) \tag{2.56}$$
$$\simeq \frac{1}{4}(x^2 - y^2) + \frac{1}{4}R_{D}\left[1 \pm 2\left(\left|\frac{q}{p}\right| - 1\right) \mp \left(a_{\mathrm{W}}^{d} + a_{\mathrm{R}}^{d}\right)\right](y^2 + x^2),$$

where only term at the first order on the CPV parameters (a_{W}^{d}, a_{R}^{d}, $\phi_{K\pi}^{\lambda}$, $\left|\frac{q}{p}\right| - 1$) are retained in the approximate expressions.

Theoretical parametrization The decay ratios λ_f^{Γ} and λ_f^{M} are conventionally written as

$$\lambda_{K^-\pi^+}^{\Gamma} \equiv \frac{\Gamma_{12}}{|\Gamma_{12}|}\frac{\overline{A}_{K^-\pi^+}}{A_{K^-\pi^+}} \equiv -\sqrt{R_{D}^{-}\frac{1 - a_{\mathrm{R}}^{d}}{1 + a_{\mathrm{R}}^{d}}}\, e^{i\left(\phi_{K\pi}^{\Gamma} + \delta_{K\pi}\right)}, \tag{2.57}$$

$$\lambda_{K^+\pi^-}^{\Gamma} \equiv \frac{\Gamma_{12}}{|\Gamma_{12}|}\frac{\overline{A}_{K^+\pi^-}}{A_{K^+\pi^-}} \equiv -\sqrt{\frac{1}{R_{D}^{+}}\frac{1 - a_{\mathrm{R}}^{d}}{1 + a_{\mathrm{R}}^{d}}}\, e^{i\left(\phi_{K\pi}^{\Gamma} - \delta_{K\pi}\right)}, \tag{2.58}$$

$$\lambda_{K^-\pi^+}^{M} \equiv \frac{\mathcal{M}_{12}}{|\mathcal{M}_{12}|}\frac{\overline{A}_{K^-\pi^+}}{A_{K^-\pi^+}} \equiv -\sqrt{R_{D}^{-}\frac{1 - a_{\mathrm{R}}^{d}}{1 + a_{\mathrm{R}}^{d}}}\, e^{i\left(\phi_{K\pi}^{M} + \delta_{K\pi}\right)}, \tag{2.59}$$

$$\lambda_{K^+\pi^-}^{M} \equiv \frac{\mathcal{M}_{12}}{|\mathcal{M}_{12}|}\frac{\overline{A}_{K^+\pi^-}}{A_{K^+\pi^-}} \equiv -\sqrt{\frac{1}{R_{D}^{+}}\frac{1 - a_{\mathrm{R}}^{d}}{1 + a_{\mathrm{R}}^{d}}}\, e^{i\left(\phi_{K\pi}^{M} - \delta_{K\pi}\right)}, \tag{2.60}$$

where the CP-violating weak phases $\phi_{K\pi}^{M}$ and $\phi_{K\pi}^{\Gamma}$ satisfy the relation $\phi_{K\pi}^{M} - \phi_{K\pi}^{\Gamma} = \phi_{12}$.
The decay rate of WS and RS can be expanded as in Eq. 2.49 and 2.51, where the

parameters $c_{\rm W}^{\pm}$, $c_{\rm W}^{\prime\pm}$, $c_{\rm R}^{\pm}$ and $c_{\rm R}^{\prime\pm}$ are equal to

$$c_{\rm W}^{\pm} = \left(\frac{1\mp a_{\rm R}^{d}}{1\pm a_{\rm R}^{d}}\right)^{1/2}\left[y_{12}\cos\left(\mp\phi_{K\pi}^{\Gamma}+\delta_{K\pi}\right)-x_{12}\sin\left(\mp\phi_{K\pi}^{M}+\delta_{K\pi}\right)\right] \tag{2.61}$$

$$\simeq \left(1\mp a_{\rm R}^{d}\right)\left(y_{12}\cos\phi_{K\pi}^{\Gamma}\cos\delta_{K\pi}-x_{12}\cos\phi_{K\pi}^{M}\sin\delta_{K\pi}\right) \pm\left(x_{12}\sin\phi_{K\pi}^{M}\cos\delta_{K\pi}+y_{12}\sin\phi_{K\pi}^{\Gamma}\sin\delta_{K\pi}\right)$$

$$c_{\rm W}^{\prime\pm} = \frac{1}{4}(y_{12}^{2}+x_{12}^{2}\pm 2x_{12}y_{12}\sin\phi_{12})\frac{1\mp a_{\rm R}^{d}}{1\pm a_{\rm R}^{d}}+\frac{1}{4}R_{D}^{\pm}(y_{12}^{2}-x_{12}^{2}) \tag{2.62}$$

$$\simeq \frac{1}{4}\left[\left(1\mp 2a_{\rm R}^{d}\right)(x_{12}^{2}+y_{12}^{2})\pm 2x_{12}y_{12}\sin\phi_{12}\right]+\frac{1}{4}R_{D}\left[1\pm(a_{\rm W}^{d}-a_{\rm R}^{d})\right](y_{12}^{2}-x_{12}^{2}),$$

$$c_{\rm R}^{\pm} = \left(\frac{1\mp a_{\rm W}^{d}}{1\pm a_{\rm W}^{d}}\right)^{1/2}\left[y_{12}\cos\left(\pm\phi_{K\pi}^{\Gamma}+\delta_{K\pi}\right)+x_{12}\sin\left(\pm\phi_{K\pi}^{M}+\delta_{K\pi}\right)\right] \tag{2.63}$$

$$\simeq \left(1\pm\mp a_{\rm W}^{d}\right)\left(y_{12}\cos\phi_{K\pi}^{\Gamma}\cos\delta_{K\pi}+x_{12}\cos\phi_{K\pi}^{M}\sin\delta_{K\pi}\right) \pm\left(x_{12}\sin\phi_{K\pi}^{M}\cos\delta_{K\pi}-y_{12}\sin\phi_{K\pi}^{\Gamma}\sin\delta_{K\pi}\right),$$

$$c_{\rm R}^{\prime\pm} = \frac{1}{4}(y_{12}^{2}-x_{12}^{2})+\frac{1}{4}R_{D}^{\pm}\frac{1\mp a_{\rm W}^{d}}{1\pm a_{\rm W}^{d}}(y_{12}^{2}+x_{12}^{2}\pm 2x_{12}y_{12}\sin\phi_{12}) \tag{2.64}$$

$$\simeq \frac{1}{4}(y_{12}^{2}-x_{12}^{2})+\frac{1}{4}R_{D}\left[1\mp(a_{\rm W}^{d}+a_{\rm R}^{d})\right](y_{12}^{2}+x_{12}^{2})\pm\frac{1}{2}R_{D}x_{12}y_{12}\sin\phi_{12},$$

Standard observable To measure the mixing and CPV parameters, while removing the dependence from most of the instrumental and selection efficiency, the WS-to-RS decay ratio is used. It can be computed in different ways. The most widely used approach exploits the WS-to-RS decay ratios where both WS and RS have the same initial D^0 flavour (D^0 or $\overline{D}^0$)

$$R^{+}(t)\equiv\frac{\Gamma(D^{0}\to K^{+}\pi^{-},t)}{\Gamma(D^{0}\to K^{-}\pi^{+},t)}\quad\text{and}\quad R^{-}(t)\equiv\frac{\Gamma(\overline{D}^{0}\to K^{-}\pi^{+},t)}{\Gamma(\overline{D}^{0}\to K^{+}\pi^{-},t)}. \tag{2.65}$$

The decay-time dependency of these two pairs of ratios is

$$R^{\pm}(t) = \frac{R_{D}^{\pm}+\sqrt{R_{D}^{\pm}}\,c_{\rm W}^{\pm}\,\Gamma t+c_{\rm W}^{\prime\pm}(\Gamma t)^{2}}{1+\sqrt{R_{D}^{\pm}}\,c_{\rm R}^{\pm}\,\Gamma t+c_{\rm R}^{\prime\pm}(\Gamma t)^{2}} \tag{2.66}$$

$$\simeq R_{D}^{\pm}+\sqrt{R_{D}^{\pm}}\,(c_{\rm W}^{\pm}-R_{D}^{\pm}c_{\rm R}^{\pm})\,\Gamma t+(c_{\rm W}^{\prime\pm}-R_{D}c_{\rm R}^{\prime\pm})(\Gamma t)^{2}.$$

This is the experimental observable commonly found in literature and the one that has been previously used in the measurements from BaBar, Belle and LHCb experiments.

Alternative observable The WS-to-RS decay ratios can also be evaluated by requiring both WS and RS to decay into the same final state ($K^+\pi^-$ or $K^-\pi^+$)

$$R'^{+}(t) \equiv \frac{\Gamma(D^0 \to K^+\pi^-, t)}{\Gamma(\bar{D}^0 \to K^+\pi^-, t)} \quad \text{and} \quad R'^{-}(t) \equiv \frac{\Gamma(\bar{D}^0 \to K^-\pi^+, t)}{\Gamma(D^0 \to K^-\pi^+, t)}. \tag{2.67}$$

The decay-time dependency of these two pairs of ratios is

$$\begin{aligned} R'^{\pm}(t) &= \frac{1 \pm a^d_{\mathrm{R}}}{1 \mp a^d_{\mathrm{R}}} \frac{R^{\pm}_D + \sqrt{R^{\pm}_D}\, c^{\pm}_{\mathrm{W}}\, \Gamma t + c'^{\pm}_{\mathrm{W}} (\Gamma t)^2}{1 + \sqrt{R^{\mp}_D}\, c^{\mp}_{\mathrm{R}}\, \Gamma t + c'^{\mp}_{\mathrm{R}} (\Gamma t)^2} \\ &\simeq (1 \pm 2a^d_{\mathrm{R}}) \left[R^{\pm}_D + \left(\sqrt{R^{\pm}_D} c^{\pm}_{\mathrm{W}} - R^{\pm}_D \sqrt{R^{\mp}_D} c^{\mp}_{\mathrm{R}} \right) \Gamma t + (c'^{\pm}_{\mathrm{W}} - R^{\mp}_D c'^{\mp}_{\mathrm{R}}) (\Gamma t)^2 \right]. \end{aligned} \tag{2.68}$$

Contributions from RS decays to the linear and quadratic term are negligible at the current level of precision in both Eq. 2.66 and 2.68, being suppressed by an additional R_D factor. In the future upgrades of the LHCb experiment, these corrections might become relevant, but only for the *CP*-even observables. Hence, the two pairs of ratios, $R^{\pm}(t)$ and $R'^{\pm}(t)$, are experimentally indistinguishable up to the factor $1 - 2a^d_{\mathrm{R}}$. Moreover, the direct *CP*-violating asymmetry in the Cabibbo-Favoured decays is expected to be extremely small in the Standard Model and in any BSM scenarios, therefore, this alternative observable is fully equivalent to the standard one if a^d_{R} is assumed to be equal to zero. This assumption is, however, already in place, since the treatment of the bias from the instrumental charge asymmetries developed in this thesis uses an external measurement that already makes this assumption (see Sec. 7.2). This new correction procedure is much simpler and more robust than that used in the past iteration of this analysis [10], and, therefore the alternative observable is preferred, and it is adopted here.

Experimental parametrizations In the previous iteration of this measurement [10] the two sets of mixing parameters, (R^+_D, y'^+, x'^{2+}) and (R^-_D, y'^-, x'^{2+}), are used, closely linked to phenomenological parametrization. These parameters adhere to WS-to-RS decay ratios:

$$R(t)^{\pm} \simeq R^{\pm}_D + \sqrt{R^{\pm}_D} y'^{\pm}\, \Gamma t + \frac{x'^{2\pm} + y'^{2\pm}}{4} (\Gamma t)^2, \tag{2.69}$$

with

$$x'^{\pm} = \left| \frac{q}{p} \right|^{\pm} (x' \cos\phi^{\lambda}_{K\pi} \pm y' \sin\phi^{\lambda}_{K\pi}), \tag{2.70}$$

$$y'^{\pm} = \left| \frac{q}{p} \right|^{\pm} (y' \cos\phi^{\lambda}_{K\pi} \mp x' \sin\phi^{\lambda}_{K\pi}). \tag{2.71}$$

Discrepancies between R^+_D and R^-_D indicate *CP* violation in the decay. Conversely, differences in (x'^{2+}, y'^{+}) and (x'^{2-}, y'^{-}) signify *CP* violation in mixing and interference between mixing and decay. From the observables $x'^{2\pm}$ and $y'^{\pm}$ one can directly access *CPV* parameters $\left|\frac{q}{p}\right|$ and $\phi^{\lambda}_{K\pi}$.

Another common parametrization of mixing and *CPV* parameters, used in other charm mixing and *CPV* measurements is [6]

$$y^f_{CP} = y_{12}\,\cos\phi^M_f \simeq y_{12}, \tag{2.72}$$
$$x^f_{CP} = x_{12}\,\cos\phi^\Gamma_f \simeq x_{12}, \tag{2.73}$$
$$\Delta y_f = x_{12}\,\sin\phi^M_f, \tag{2.74}$$
$$\Delta x_f = -y_{12}\,\sin\phi^\Gamma_f. \tag{2.75}$$

Here, y_{CP} and x_{CP} are the mixing observable already defined in the previous section, with explicit corrections for *CPV* effects. Notably, these corrections are only quadratic in $\phi^M_{K\pi}$ and $\phi^\Gamma_{K\pi}$, hence their dependence from *CPV* parameter is negligible and consequently also their final state dependence.

For the measurement described in this thesis, we decided to adopt a new model-independent experimental parametrization, that can be easily linked to both the phenomenological and theoretical parametrization. It is mainly driven by experimental considerations, aiming at fully decorrelating the statistical and systematic uncertainties of mixing parameters from those of *CP*-violating ones. The parameter in the linear term of the ratio has some similarities with the parametrization used in Ref. [6], described above. The time-dependence of the WS-to-RS ratio is described by three *CP*-even parameters, R_D, $c_{K\pi}$ and $c'_{K\pi}$, and three *CP*-odd parameters A'_D, $\Delta c_{K\pi}$ and $\Delta c'_{K\pi}$, as

$$R'^{\pm}(t) = R_D(1 \pm 2A'_D) + \sqrt{R_D(1 \pm 2A'_D)}\,(c_{K\pi} \pm \Delta c_{K\pi})\,\Gamma t + (c'_{K\pi} \pm \Delta c'_{K\pi})(\Gamma t)^2. \tag{2.76}$$

The relationship between these new experimental parameters and the physics observables in both phenomenological a theoretical parametrizations, as well as their link with the other experimental parametrizations, is reported here:

$$A'_D \simeq a^d_{\rm W} + a^d_{\rm R}, \tag{2.77}$$

$$\begin{aligned} c_{K\pi} &\simeq y\cos\delta_{K\pi} - x\sin\delta_{K\pi} \\ &\simeq y_{12}\cos\phi^\Gamma_{K\pi}\cos\delta_{K\pi} - x_{12}\cos\phi^M_{K\pi}\sin\delta_{K\pi} \\ &\simeq y_{CP}\cos\delta_{K\pi} - x_{CP}\sin\delta_{K\pi} \\ &\simeq \frac{1}{2}(y'^{+} + y'^{-}), \end{aligned} \tag{2.78}$$

$$\begin{aligned} \Delta c_{K\pi} &\simeq (y\cos\delta_{K\pi} - x\sin\delta_{K\pi})\left(\left|\frac{q}{p}\right| - 1\right) - (x\cos\delta_{K\pi} + y\sin\delta_{K\pi})\,\phi^\lambda_{K\pi} \\ &\simeq x_{12}\phi^M_{K\pi}\cos\delta_{K\pi} + y_{12}\phi^\Gamma_{K\pi}\sin\delta_{K\pi} \\ &\simeq \Delta y\cos\delta_{K\pi} - \Delta x\sin\delta_{K\pi}, \\ &\simeq \frac{1}{2}(y'^{+} - y'^{-}), \end{aligned} \tag{2.79}$$

$$
\begin{aligned}
c'_{K\pi} &\simeq \frac{1}{4}\left(x^2+y^2\right) \\
&\simeq \frac{1}{4}\left(x_{12}^2+y_{12}^2\right) \\
&\simeq \frac{1}{4}(y_{CP}^2+x_{CP}^2) \\
&\simeq \frac{1}{8}(y'^{2+}+x'^{2+}+y'^{2-}+x'^{2-}),
\end{aligned}
\tag{2.80}
$$

$$
\begin{aligned}
\Delta c'_{K\pi} &\simeq \frac{1}{2}(x^2+y^2)\left(\left|\frac{q}{p}\right|-1\right) \\
&\simeq \frac{1}{2}x_{12}y_{12}(\phi^M_{K\pi}-\phi^\Gamma_{K\pi}) \\
&\simeq \frac{1}{2}(y_{CP}\Delta y_{K\pi}+x_{CP}\Delta x_{K\pi}) \\
&\simeq \frac{1}{8}(y'^{2+}+x'^{2+})-\frac{1}{8}(y'^{2-}-x'^{2-}).
\end{aligned}
\tag{2.81}
$$

Here, the coefficients are expressed up to quadratic order in the mixing parameters and to linear order in the CPV parameters, neglecting terms proportional to CPV parameters and R_D. These corrections are so small, that they might be even negligible at the end of the LHCb Upgrade II experiment. Terms proportional to the mixing parameters and R_D are also not displayed. They are very small and therefore can be neglected at the current level of precision. These terms come from the RS time dependence and affect only the $c_{K\pi}$ coefficient. They will become relevant at the end of the LHCb Upgrade II:

$$
c_{K\pi} \simeq y\cos\delta_{K\pi}(1-R_D)-x\sin\delta_{K\pi}(1+R_D). \tag{2.82}
$$

As we have seen, the asymmetry of same final state ratios (alternative observable), $A'_D \simeq a^d_{\mathrm{W}}+a^d_{\mathrm{R}}$, differ from the asymmetry of same D^0 flavour ratios (standard observable), $A_D \simeq a^d_{\mathrm{W}}-a^d_{\mathrm{R}}$, however, the direct CP asymmetry in the CF decay (a^d_{R}) can be neglected, making the two asymmetries indistinguishable. For this reason, in the following, we will omit the $'$ subscript to simplify the notation: $A'_D \equiv A_D \simeq a^d_{\mathrm{W}}$.

2.4.2 CP asymmetries in $D^0 \to h^+h^-$ CS decays

A key method for detecting CP violation in charm decays involves analysing the time-dependent asymmetry of the decay rates of D^0 and $\overline{D}^0$ mesons into CP eigenstates, such as K^+K^- and $\pi^+\pi^-$:

$$
A_{CP}(h^+h^-;t)=\frac{\Gamma(D^0(t)\to h^+h^-)-\Gamma(\overline{D}^0(t)\to h^+h^-)}{\Gamma(D^0(t)\to h^+h^-)+\Gamma(\overline{D}^0(t)\to h^+h^-)} \simeq a^d_{h^+h^-}+\Delta Y_{h^+h^-}\,\Gamma\,t, \tag{2.83}
$$

The constant terms, $a^d_{h^+h^-}$, are the *CP*-violating violating asymmetries in the decay (or direct), and are defined as:

$$a^d_{K^+K^-} \equiv \frac{|A_{K^+K^-}|^2 - |\overline{A}_{K^+K^-}|^2}{|A_{K^+K^-}|^2 + |\overline{A}_{K^+K^-}|^2} \quad \text{and} \quad a^d_{\pi^+\pi^-} \equiv \frac{|A_{\pi^+\pi^-}|^2 - |\overline{A}_{\pi^+\pi^-}|^2}{|A_{\pi^+\pi^-}|^2 + |\overline{A}_{\pi^+\pi^-}|^2}. \tag{2.84}$$

The experimental measurement of these quantities, at very high precision, requires overcoming several challenges, such as an accurate determination of both production and detection asymmetries. These individual asymmetries in CS decay have been recently measured using the full dataset collected by the LHCb experiment during LHC Run 1 and 2, by showing for the first time evidence for *CP* violation in a single decay mode [2]:

$$a^d_{K^+K^-} = (7.7 \pm 5.7) \times 10^{-4},$$
$$a^d_{\pi^+\pi^-} = (23.2 \pm 6.1) \times 10^{-4}.$$

Experimental methods can identify key observables capable of mitigating the challenges related to the measurement of an individual asymmetry, and which allow achieving much higher precision. For instance, one of these golden observables is ΔA_{CP}, defined as:

$$\Delta A_{CP} = a^d_{K^+K^-} - a^d_{\pi^+\pi^-}. \tag{2.85}$$

From a pure experimental point of view, this observable allows us to effectively cancel out both production and detection asymmetries in a very robust and reliable way, and consequently, to exploit the full size of the available data samples of CS decay modes. In the limit of U-spin symmetry, the direct *CP* asymmetry is equal in magnitude and opposite in sign for K^+K^- and $\pi^+\pi^-$, though the size of U-spin-breaking effects at play is still very uncertain [45]. A LHCb collaboration's measurement revealed the first evidence of *CP* violation in charm decays by measuring a significant non-zero value in the measurement of this observable published in 2019 [1]:

$$\Delta A_{CP} = (-15.4 \pm 2.9) \times 10^{-4}.$$

The results of the measurements of the direct CPV in the CS decays of the the D^0 mesons are illustrated in Fig. 2.4

The slope of the linear expansion, the $\Delta Y_{h^+h^-}$ parameter, of Eq. 2.83 is another golden observable and it can be expressed as a function of physics observables as

$$\Delta Y_{h^+h^-} \simeq -x\phi^{\lambda}_{h^+h^-} + y\left(\left|\frac{q}{p}\right| - 1\right) - ya^d_{h^+h^-} \simeq -x_{12}\phi^M_{h^+h^-} + y_{12}a^d_{h^+h^-} \simeq -\Delta y_{h^+h^-} + y_{CP}a^d_{h^+h^-}. \tag{2.86}$$

The final state dependence can be neglected at the current level of precision [46], hence $\Delta Y_{K^+K^-}$ and $\Delta Y_{\pi^+\pi^-}$ can be combined to obtain a single observable ΔY probing CPV in mixing and interference. The latest measurement performed by the LHCb collaboration

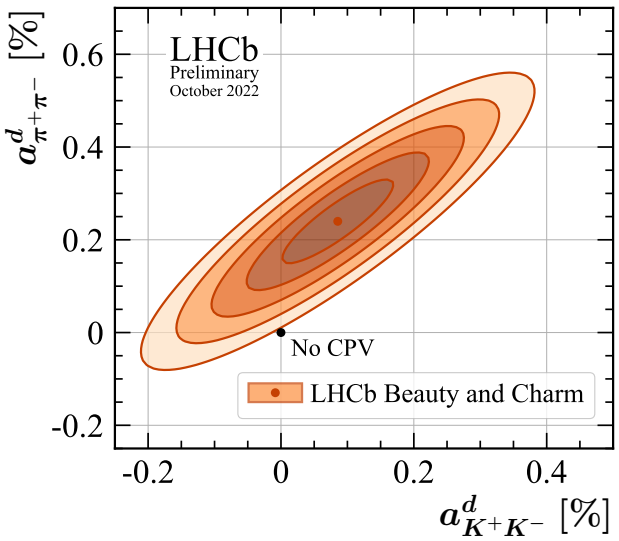

Figure 2.4: Two-dimensional profile likelihood contours for the CP asymmetries in the decay of the $D^0 \to K^+K^-$ and $D^0 \to \pi^+\pi^-$ channels [7]. Contours are drawn out to 5σ and contain 68.3%, 95.4%, 99.7%, etc. of the distribution.

dominates the world average of ΔY, indicating no evidence for CP violation [46]:

$$\Delta Y = (-2.7 \pm 1.3(\text{stat.}) \pm 0.3(\text{syst.})) \times 10^{-4}.$$

2.4.3 CP asymmetries in $D^0 \to K^0_S h^+h^-$ decays

Measuring the time-dependence of the ratio of $\overleftrightarrow{D^0} \to K^0_S\pi^+\pi^-$ or $\overleftrightarrow{D^0} \to K^0_S K^+K^-$ between opposite bin in the Dalitz plot, allows measuring the CPV parameters Δx and Δy [47]

$$R^{\pm}_b(t) = \frac{\Gamma_{-b}(D^0 \to K^0_S h^+h^-, t)}{\Gamma_b(D^0 \to K^0_S h^+h^-, t)} \left[\frac{\Gamma_{-b}(\overline{D}^0 \to K^0_S h^+h^-, t)}{\Gamma_b(\overline{D}^0 \to K^0_S h^+h^-, t)}\right] \tag{2.87}$$

$$\simeq r_b + \sqrt{r_b}\left[(1-r_b)(y_{CP} \pm \Delta y_f)\cos_b \delta_{K^0_S hh} - (1+r_b)(x_{CP} \pm \Delta x_f)\sin_b \delta_{K^0_S hh}\right]\Gamma t. \tag{2.88}$$

Since $\cos_b \delta_{K^0_S hh}$ and $\sin_b \delta_{K^0_S hh}$ span the whole $[-1,1]$ range, this observable is particularly sensitive to Δx, since this appear in the linear term when $\delta_{K^0_S hh} \approx \pm\pi/2$. A recent measurement from the LHCb collaboration, which uses the full LHC Run 2 data sample, reports [6] :

$$\Delta x_{K^0_S\pi\pi} = (-0.27 \pm 0.18(\text{stat.}) \pm 0.01(\text{syst.})) \times 10^{-3},$$
$$\Delta y_{K^0_S\pi\pi} = (0.20 \pm 0.36(\text{stat.}) \pm 0.13(\text{syst.})) \times 10^{-3},$$

resulting in no evidence of CPV in mixing or interference.

2.5 Theoretical predictions and final-state dependence

The measurements of the mixing parameters have prompted discussions about potential implications for physics beyond the Standard Model [48–50]. However, a major challenge in addressing this issue is the absence of precise predictions within the Standard Model. Accurate calculations of long-distance effects, especially for the D^0 meson, are fraught with large uncertainties due to the charm quark's intermediate mass scale. As a consequence, theoretical predictions for the D^0-$\overline{D}^0$ mixing and *CP* violation parameters are very challenging. Precise measurement of these mixing parameters is thus essential for improving theoretical models and improving our knowledge of the dynamics of the charm sector. Despite the absence of exact Standard Model predictions, the notably small magnitude of the D^0 mixing parameters could be used to establish strong constraints on models introducing novel interactions beyond the SM. These limits tend to be more stringent compared to those derived from the measurement of B-meson mixing [51].

As shown in Eq. 1.68 in the SM in order to observe *CP* violation in the decay at least two amplitudes with different weak and strong phases are required. In CF and DCS decays this requirement does not hold, since these decays are not sensitive to QCD electroweak-loop and chromomagnetic dipole operators, hence the CPV in the decay is expected to be negligible in these decays. On the other hand, this requirement applies to CS decay. The predictions for the magnitude of $a^d_{K^+K^-}$ and $a^d_{\pi^+\pi^-}$ are in the range between 10^{-4} and 10^{-3} and assuming U-spin symmetry it follows that $a^d_{K^+K^-}$ and $a^d_{\pi^+\pi^-}$ are approximately equal in magnitude and opposite in sign.

The phases ϕ_f^M and ϕ_f^Γ, defined in Eq. 2.57 are approximately equal to the intrinsic mixing phases, ϕ^M and ϕ^Γ, except for a small correction. The SM prediction for ϕ^M and ϕ^Γ are of the same order of magnitude and it is about 2 mrad [39]. The correction, $\delta\phi_f$, depends on the final state but is shared by both ϕ_f^M and ϕ_f^Γ: $\delta\phi_f = \phi_f^M - \phi^M = \phi_f^\Gamma - \phi^\Gamma$. This correction is predicted to be extremely small for WS and RS decays, $\mathcal{O}(10^{-6})$. On the other hand, these corrections are less suppressed in CS decays, where their magnitude is expected in the range between 10^{-5} and 10^{-4}. Correspondingly, the same considerations apply in the phenomenological parametrization for ϕ_f^λ and the intrinsic mixing phase ϕ. At the current level of experimental precision, final state corrections are negligible, allowing to average together phases measured in different decay channels. For this reason, from now on the subscript f for the final state dependence will be omitted.

The superweak approximation [52] states that the exclusive origin of *CP* violation in D^0-meson decays arises from *CP*-violating interactions involving new particles with a mass scale significantly higher than D^0 mass. From this approximation, it follows that the only parameter sensitive to *CP* violation would be the weak angle ϕ^M, and ϕ^Γ (or equivalently Δx) is zero. While the superweak scenario has been experimentally invalidated for all the other neutral mesons, it can be still used, in the study of D^0 mesons, to constrain new interactions beyond the SM, since *CP* violation in time-dependent measurements of D^0-meson decays remains beneath the threshold of their experimental precision.

2.6 Overview of present experimental context

LHCb results vastly dominate the world average for mixing and CPV parameters. The LHCb collaboration performed a global fit [7] to all LHCb measurements sensitive to mixing and CPV parameters, including[2] the measurement of numerous $B^{\pm} \to D^0 h^{\pm}$ decay rates, that have sensitivity to the strong phase $\delta_{K\pi}$. Figure. 2.5 shows a breakdown of the sensitivity on the strong phase $\delta_{K\pi}$ amongst different sub-combinations of modes. The addiction of beauty modes to the global fit actually improves the estimate of $\delta_{K\pi}$ by more than a factor 3 compared to the only measurement of CLEO and BESIII.

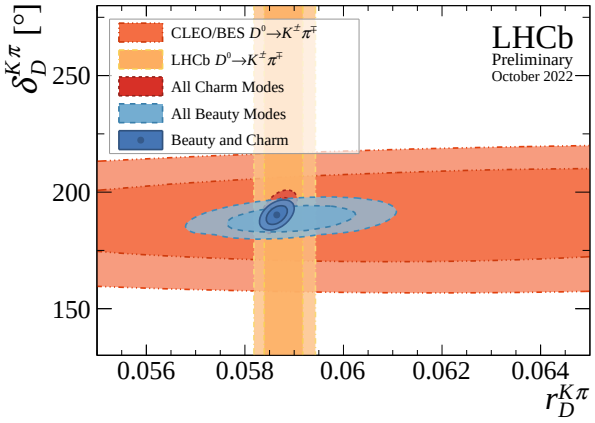

Figure 2.5: Profile likelihood contours for the $\delta_{K\pi}$ and R_D parameters, showing the breakdown of sensitivity amongst different sub-combinations of modes. The contours indicate the 68.3% and 95.4% confidence regions. Fig. from Ref. [7].

The fit result for the mixing and CPV parameter is [7]:

$$x = 0.398^{+0.050}_{-0.049}\,\%, \qquad y = 0.636^{+0.020}_{-0.019}\,\%,$$
$$\left|\frac{q}{p}\right| = 0.995^{+0.015}_{-0.016}, \qquad \phi = -2.5^{+1.2}_{-1.2}\,^{\circ},$$

with no measured evidence for CP violation. Figures 2.6 and 2.7 show the confidence intervals returned by the global fit in the x,y and $\left|\frac{q}{p}\right|$, ϕ parameters space, and breakdown of sensitivity between multiple combinations of charm and beauty observable.

[2] External measurements of $\delta_{K\pi}$ from CLEO [8] and BESIII [40] are also included in this global fit.

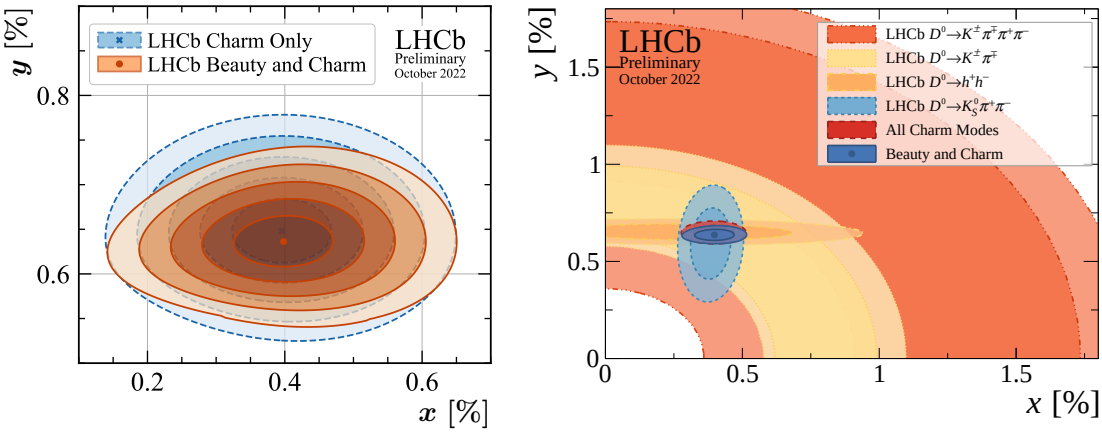

Figure 2.6: Profile likelihood contours for the x and y parameters (right) and a breakdown of sensitivity amongst different sub-combinations of modes (left). The contours indicate the 68.3% and 95.4% confidence regions. Fig. from Ref. [7].

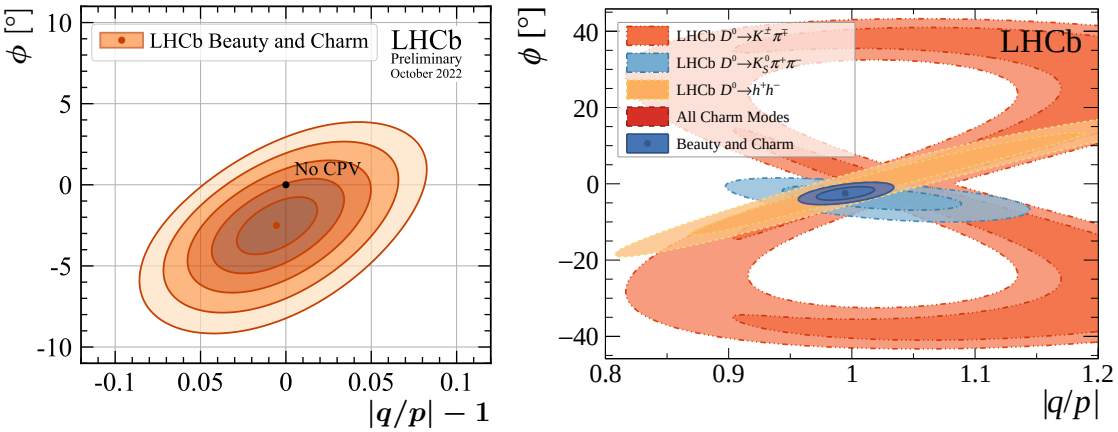

Figure 2.7: Profile likelihood contours for the $\left|\frac{q}{p}\right|$ and ϕ parameters (right) and a breakdown of sensitivity amongst different sub-combinations of modes (left). The contours indicate the 68.3% and 95.4% confidence regions. Fig. from Ref. [7].

2.6.1 State of the art of WS-to-RS ratio measurement

A significant contribution to the global fit comes from the measurement of the decay-time-dependent ratio of WS $D^0 \to K^+\pi^-$ to RS $D^0 \to K^-\pi^+$ decay rates. The present state of experimental insights into the parameters R_D, y' and x'^2 is encapsulated in Tab. 2.2, measured using the WS-to-RS ratio and assuming negligible CP violation. Additionally, Tab. 2.3 lists the most recent evaluations of indirect CPV indicators $x'^{2\pm}$, $y'^{\pm}$ alongside the direct CPV observable A_D.

Experiment	R_D [$\times 10^{-5}$]	x'^2 [$\times 10^{-5}$]	y' [$\times 10^{-4}$]
BaBar [29]	303 ± 19	-22 ± 37	97 ± 54
Belle [53]	353 ± 13	9 ± 22	46 ± 34
CDF [54]	351 ± 35	8 ± 18	43 ± 43
LHCb [10]	345.4 ± 3.1	3.9 ± 1.9	52.8 ± 5.3

Table 2.2: Summary of the measurement of D^0 mixing parameter R_D, x'^2, y', performed using the WS-to-RS ratio assuming no CPV.

Experiment	A_D [10^{-3}]	x'^{2+} [10^{-5}]	x'^{2-} [10^{-5}]	y'^{+} [10^{-4}]	y'^{-} [10^{-4}]
BaBar [29]	-21 ± 54	-24 ± 52	-20 ± 50	98 ± 78	96 ± 75
Belle [30]	23 ± 47	32 ± 37	6 ± 34	12 ± 58	43 ± 43
LHCb [10]	-0.1 ± 9.1	6.1 ± 3.7	1.6 ± 3.9	51.1 ± 7.4	55.4 ± 7.4

Table 2.3: Summary of the measurements of the CP-violating observables A_D, $x'^{2\pm}$, $y'^{\pm}$, performed using the WS-to-RS ratio.

The most recent measurement from the LHCb collaboration of the $(R_D^{\pm}, x'^{2\pm}, y'^{\pm})$ parameters dates back to 2018 and it is published in the Phys. Rev. D journal. [10]. This is the most precise measurement of such parameters, and it has employed a data sample of 3 fb^{-1} of pp collisions at 7 and 8 TeV centre-of-mass energies, recorded during the LHC Run 1 (2011-2012) and 2 fb^{-1} from pp collisions at 13 TeV collected during the first two years of LHC Run 2 (2015-2016). During this time, the LHCb experiment gathered a sample of approximately 177 million of $D^0 \to K^-\pi^+$ decays and around 722 thousand suppressed $D^0 \to K^+\pi^-$ WS decays. The measured WS-to-RS yields and their decay-time dependency fit are shown in Fig. 2.8. The study identified four dominant sources of systematic uncertainty, contributing to the total uncertainty, and outlined in Tables 2.4 and 2.5 for CP-averaged and CP-violating mixing parameters, respectively. Statistical uncertainties and central values are also reported for each observable.
The "instrumental asymmetry" uncertainty relates to the systematic error in measuring the detection efficiency ratio $\epsilon(K^{\pm}\pi^{\mp})/\epsilon(K^{\mp}\pi^{\pm})$, determined using D^+ control decay channels. The "peaking background" uncertainty originates from RS candidates misidentified as WS, showing a reconstructed D^* mass peaking at the nominal D^* mass value. The "secondary D decays" uncertainty addresses the bias from residual contamination of D^* mesons from weak decays of B-hadrons (secondary decays), not originating from the pp primary vertex. Lastly, the "ghost soft pions" uncertainty arises from incorrectly reconstructed tracks that combine correctly identified clusters in the VELO detector (upstream of the magnet) with clusters from different particles in the T-stations (downstream of the magnet), resulting in D^* candidates peaking in D^* mass due to the accurate reconstruction of pion direction, despite incorrect momentum. Contamination of secondary D^* decays is the dominant source of systematic uncertainty. The uncertainty due to the ghost soft pion contamination is also not negligible, however, it is assessed using a conservative approach.

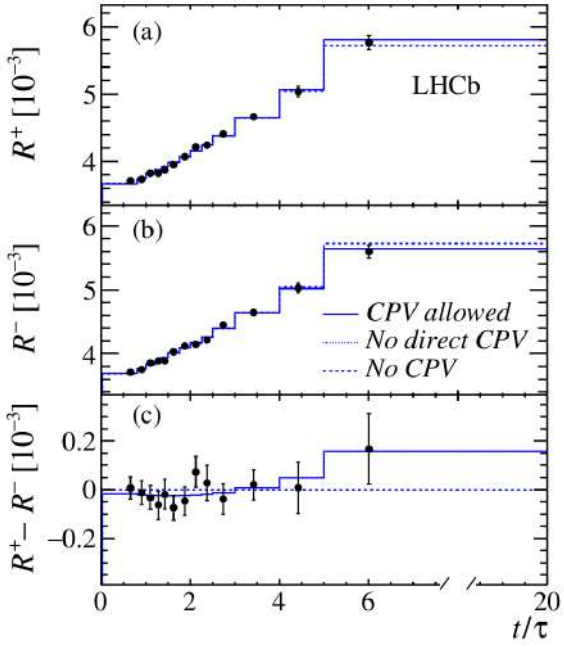

Figure 2.8: Efficiency-corrected ratios of WS-to-RS yields, as measured in Ref. [10], for (a) D^{*+} decays, (b) D^{*-} decays, and (c) their differences as functions of decay time in units of D^0 lifetime. Projections of fits allowing for (dashed line) no *CP* violation, (dotted line) no direct *CP* violation, and (solid line) direct and indirect *CP* violations are overlaid. The last two curves overlap. The abscissa of each data point corresponds to the average decay time over the bin. The error bars indicate the statistical uncertainties.

No CP violation			
Source	R_D [10^{-5}]	y' [10^{-4}]	x'^2 [10^{-5}]
Instrumental asymm.	<0.1	<0.1	<0.1
Peaking background	0.3	0.4	0.2
Secondary D decays	1.0	2.1	1.1
Ghost soft pions	0.8	1.5	0.8
Total syst. uncertainty	1.4	2.7	1.4
Statistical uncertainty	2.8	4.5	2.3
Total uncertainty	3.1	5.3	2.7

Table 2.4: Summary of statistical and systematic uncertainties in the mixing parameter fit not allowing for CPV, as reported in the previously published measurement [10].

CP violation in the decay, in the mixing and in the interference						
Source	R_D^+ $[10^{-5}]$	R_D^- $[10^{-5}]$	y'^+ $[10^{-4}]$	y'^- $[10^{-4}]$	x'^{2+} $[10^{-5}]$	x'^{2-} $[10^{-5}]$
Instrumental asymm.	0.6	0.6	0.4	0.3	0.2	0.1
Peaking background	0.3	0.3	0.4	0.4	0.2	0.2
Secondary D decays	1.4	1.4	2.9	2.9	1.5	1.5
Ghost soft pions	1.2	1.2	2.1	2.1	1.1	$\pm$ 1.1
Total syst. uncertainty	2.0	2.0	3.8	3.8	1.9	2.0
Statistical uncertainty	4.0	4.0	6.4	6.4	3.2	3.3
Total uncertainty	4.4	4.4	7.4	7.4	3.8	3.8

Table 2.5: Summary of statistical and systematic uncertainties in the mixing parameter fit allowing for CPV in the decay, in the mixing and in the interference, as reported in the previously published measurement [10].

Chapter 3

The LHCb experiment at the LHC

The measurement performed in this thesis uses a dataset of pp collisions collected by the LHCb detector, which is one of the four major experiments installed at the Large Hadron Collider (LHC). This chapter delves into the details of the diverse subsystems of the LHCb detector, with a particular emphasis on those that are more relevant for this measurement. For a more detailed and comprehensive explanation of the experimental setup, readers are directed to the various references cited throughout the chapter.

3.1 The Large Hadron Collider

The Large Hadron Collider at CERN, straddling the Swiss-French border near Geneva, functions both as a proton-proton (pp) and heavy ion collider. This remarkable facility is situated in a circular tunnel 27 kilometres in circumference, buried approximately 100 meters underground [55]. The process of proton acceleration at the LHC is a multi-stage process, outlined in Fig. 3.1:

- initially, protons, extracted from hydrogen gas, are propelled in the Linear Accelerator (**LINAC 2**) to an energy of 50 MeV;
- following this, they advance to the Proton Synchrotron Booster (**BOOSTER**), boosting their energy to 1.5 GeV;
- next, the Proton Synchrotron (**PS**) further accelerates them to 25 GeV;
- finally, they enter the Super Proton Synchrotron (**SPS**), where they attain 450 GeV, the necessary energy for injection into the LHC.

In the final stage within the LHC, two proton beams are directed in opposite trajectories, accelerated by superconducting radio-frequency (RF) cavities and guided by superconducting NbTi dipole magnets. In its first operational phase, known as Run 1, the LHC operated at energies below its designed maximum of 14 TeV: 7 TeV in 2011, and an increased 8 TeV in 2012. Post a two-year shut-down for upgrades and magnet system checks, the collider restarted operations at 13 TeV, maintaining this energy throughout Run 2, spanning 2015 to the end of 2018. At their peak energy, these protons collide at

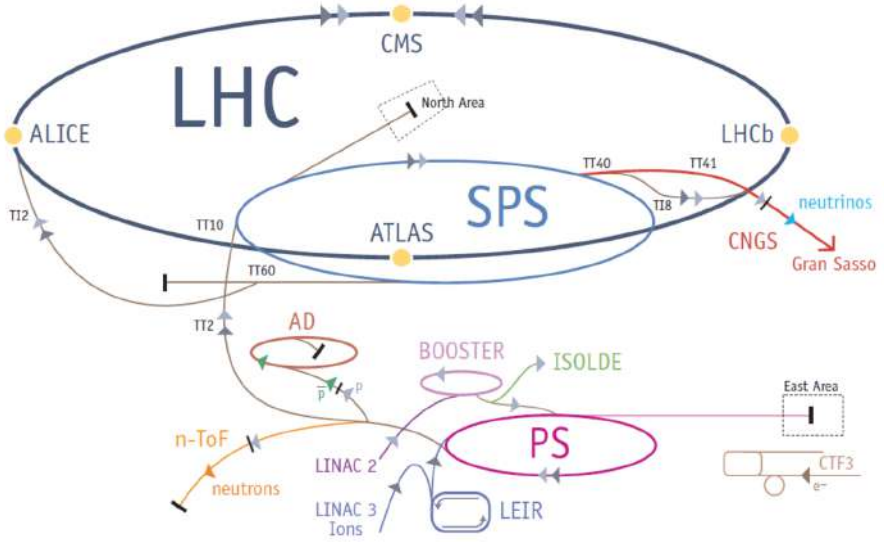

Figure 3.1: Depiction of the CERN accelerator complex. Figure from Ref. [56].

four interaction points. The particles produced are detected by four major experiments: ATLAS, CMS, LHCb and ALICE.

3.1.1 Luminosity at the LHC

The LHC organizes protons into groups or 'bunches', each containing approximately 10^{11} protons. The spacing between these bunches was altered from Run 1's 50 ns to 25 ns in Run 2. This change resulted in bunch-crossing rates of 20 MHz and 40 MHz, respectively. However, practical operational necessities such as gaps between bunches for injection and dumping processes result in a reduced average bunch crossing rate, approximately 15 MHz for Run 1 and 30 MHz for Run 2. The calculation of the event rate is expressed as follows:

$$\frac{\mathrm{d}N}{\mathrm{d}t} = \mathcal{L} \cdot \sigma, \tag{3.1}$$

where σ represents the cross section of the process under study and $\mathcal{L}$ denotes the instantaneous luminosity of the collider. For bunches distributed in a Gaussian manner, a suitable approximation at the LHC, the luminosity is given by

$$\mathcal{L} = \frac{k f n_1 n_2}{4\pi\sigma_x\sigma_y} \cdot \frac{1}{\sqrt{1 + \left(\frac{\sigma_z}{\sigma_x}\tan\frac{\phi}{2}\right)^2}}, \tag{3.2}$$

where

- k: the number of bunches per beam, approximately 2500 during Run 2;
- f: the revolution frequency, which can be estimated based on ultra-relativistic particles and a collider length of approximately 27 km, yielding $f \sim 11\,\mathrm{kHz}$;

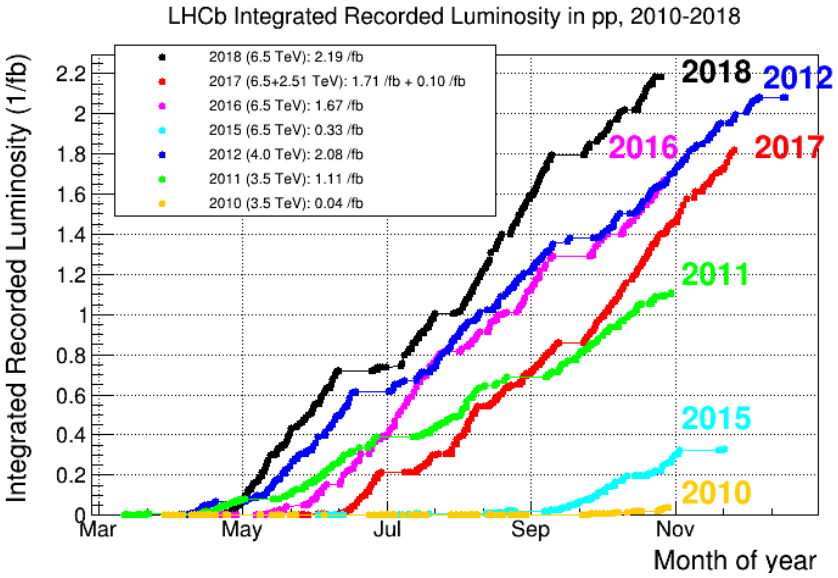

Figure 3.2: Integrated LHCb luminosity year by year from 2010 to 2018.

- n_1 and n_2: the number of protons in each beam, with equal quantities at the LHC, $n_1 = n_2 \simeq 1 \times 10^{11}$;
- σ_x, σ_y, and σ_z: the standard deviations of the spatial distribution along the three axes, with $\sigma_x = \sigma_y \simeq 16\mu$m, while σ_z is significantly greater than $\sigma_{x,y}$;
- ϕ: the angle at which the two beams interSec.

While CMS and ATLAS are designed to reach a peak luminosity of approximately 10^{34} cm^{-2}s^{-1}, LHCb operates at a significantly lower luminosity of 2×10^{32} cm^{-2}s^{-1}. Therefore, in the LHCb experiment, the luminosity is maintained constant by dynamically adjusting the intersection angle ϕ. In 2012, a decision was made to elevate the luminosity to 4×10^{32} cm^{-2}s^{-1}. The total number of events produced is determined by the integrated luminosity, $L = \int \mathcal{L} dt$, multiplied by the cross section of interest. The year-by-year recorded integrated luminosity at LHCb is depicted in Fig. 3.2.

3.2 LHCb Detector

The LHCb experiment features a unique single-arm forward spectrometer design, offering an angular acceptance ranging from 10 mrad to 300 mrad in the horizontal plane and 250 mrad in the vertical plane. This corresponds to a pseudorapidity ($\eta = -\log\theta/2$) range approximately between 2 and 5. This specific design is motivated by the primary research goal of the experiment: the analysis of b- and c-hadron properties. In hadron colliders, bottom and charm quarks are predominantly produced through the strong production of $b\bar{b}$ and $c\bar{c}$ pairs. These pairs are usually emitted along the beam axis, as illustrated in Fig. 3.3. By focusing exclusively on the forward direction, the LHCb detector efficiently collects 27% of the total produced $b\bar{b}$ pairs. This is achieved with a considerably smaller solid angle coverage compared to general-purpose detectors like CMS and ATLAS, which cover $|\eta| < 2.4$, providing a more cost-effective and accessible

design for sub-detector maintenance and construction. The components of the LHCb

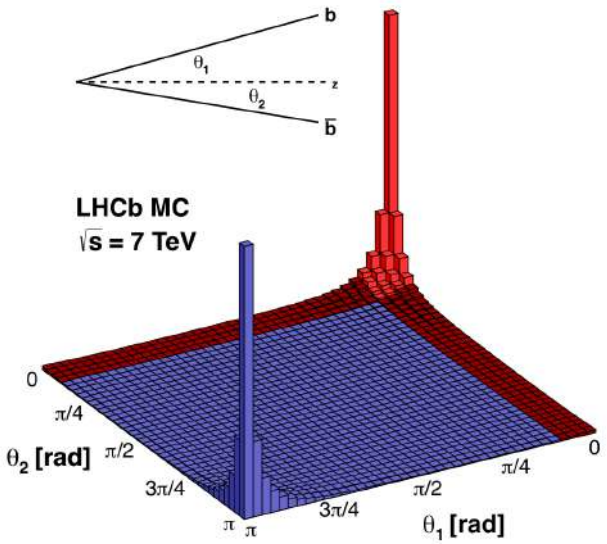

Figure 3.3: The $b\bar{b}$ angular production distribution at $s = \sqrt{7}$ TeV from PYTHIA [57]. Figure from Ref. [58].

detector, depicted in Fig. 3.4, are as follows:

- **VELO**, the Vertex Locator, is a silicon strip detector positioned around the pp interaction vertex for precise decay vertex reconstruction;
- **RICH1**, situated near the VELO, is the Ring Imaging Cherenkov used for particle identification (PID) within the 1-60 GeV/c momentum range;
- A warm dipole **magnet** that produces a 4 Tm bending power for particle momentum measurement;
- **TT**, the Tracker Turicensis, a silicon strip detector located just before the magnet;
- **T1-3**, three tracking stations positioned after the magnet, made up of silicon strips in the region closest to the beam pipe and straw drift tubes in the outer one;
- **RICH2**, the second Ring Imaging Cherenkov detector, covering a different momentum range (15-100 GeV/c) than RICH1;
- **SPD/PS**, the Scintillating Pad and Preshower detectors, enhance electron identification;
- **ECAL**, the electromagnetic calorimeter, which identifies electrons and photons and contributes to the trigger system;
- **HCAL**, the hadronic calorimeter, designed for hadron identification and triggering;
- **M1-5**, five muon stations, consisting of multi-wire proportional chambers and iron layers, dedicated to identifying and triggering muons, the only particles that can penetrate to this part of the detector.

3.2.1 Coordinate system

The LHCb coordinate system serves as the reference framework for the LHCb experiment and is defined as follows:

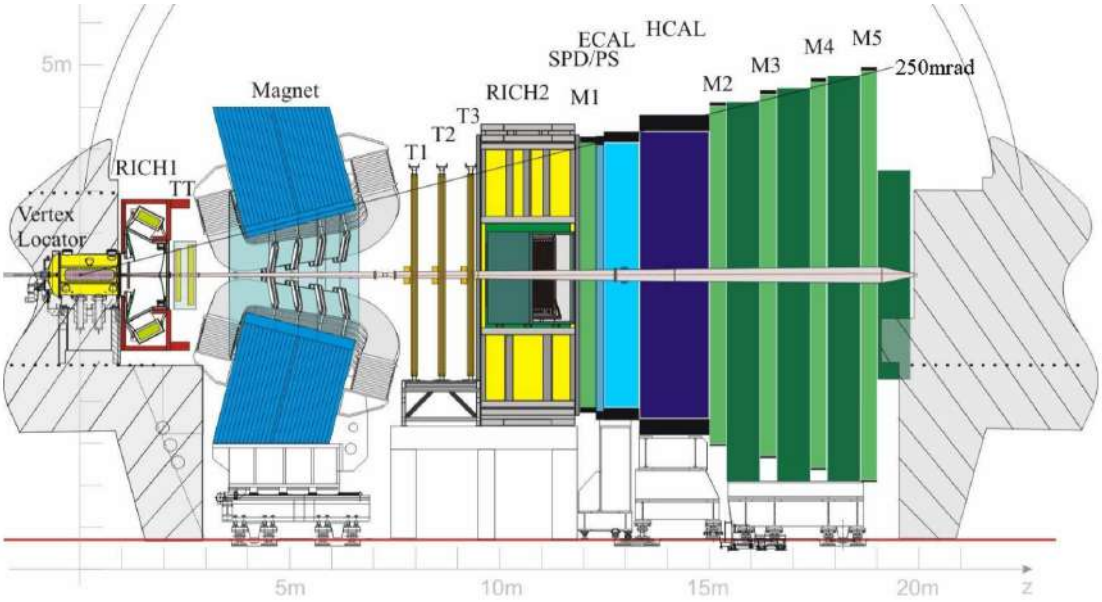

Figure 3.4: Layout of LHCb detector. Figure from Ref. [59].

- The origin of the coordinate system, denoted as $\vec{O}$, is positioned at the nominal interaction vertex;
- The x-axis is horizontal, extending from the interaction point outward, away from the LHC ring.
- The y-axis, perpendicular to both the x-axis and the beam line, points upwards, inclined at 3.601 mrad relative to the vertical.
- The z-axis extends from the interaction point towards the LHCb detector, aligning with the beam direction to form a right-handed Cartesian coordinate system (x, y, z).

Unless otherwise specified, all vector positions discussed in subsequent sections are assumed to be in the LHCb coordinate system.

3.2.2 Tracking systems

The dipole magnet

The warm dipole magnet of LHCb is strategically positioned between the TT and T-stations. Its design, featuring two saddle-shaped coils angled slightly relative to the beam axis, is shown in the right panel of Fig. 3.5. This arrangement is tailored to optimize the acceptance of LHCb. The magnetic field, oriented in the y direction, causes particle trajectories to curve within the $x - z$ plane. The field's peak intensity is about 1.1 T, with an integral of $\int B\mathrm{d}l = 4$ Tm. A detailed map of the magnetic field, essential for accurate momentum resolution, is measured before data collection using Hall probes.

This magnet design inherently creates a charge asymmetry in detection. The vertical field bends particles depending on their charge, hence particles of a certain sign will preferably interact with different parts of the detector, generating a detection charge

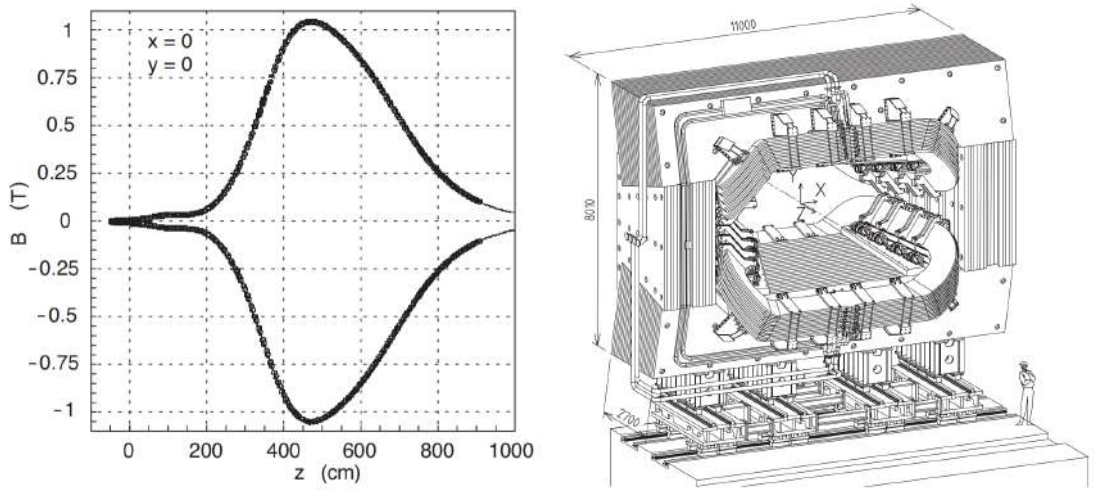

Figure 3.5: (Left) y component of the magnetic field measured along the z axis both polarities. (Right) View of the LHCb dipole magnet (lengths in mm). Figures from Ref. **??**.

asymmetry. This is particularly notable for low-momentum particles heavily affected by the vertical field.

A unique aspect of the LHCb magnet is the ability to reverse its polarity (*MagUp* or *MagDown*). This feature can be useful in reducing detector charge asymmetry. In fact, by alternating the magnet polarity approximately every two weeks between two data sets of similar size and conditions, it is possible to partially cancel the effects of this asymmetry. In the precision analysis carried out in this thesis work, the compatibility of the *MagUp* and *MagDown* period is first verified, and then in the nominal analysis workflow, we integrate data from both polarities in order to benefit from further instrumental asymmetry cancellation.

Vertex locator

The VErtex LOcator (VELO) [60], a silicon strip detector encircling the nominal pp interaction vertex, serves two main purposes: measuring particle momenta by comparing track directions in the VELO (pre-magnet) and T stations (post-magnet), and reconstructing primary pp interaction vertices and displaced secondary vertices. These secondary vertices are indicative of b- and c-hadron decays, typically occurring around 1 cm from the primary vertex. High-resolution vertex reconstruction is crucial for minimizing the background from promptly produced particles.

The VELO consists of 42 semicircular silicon modules arrayed perpendicularly to the beam axis, divided equally on both sides and grouped into 21 tracking stations. Each station comprises two slightly overlapping modules, ensuring that tracks within the LHCb acceptance intersect at least four modules (see Fig. 3.6). Each module features two sub-modules that independently measure R and ϕ coordinates (illustrated in Fig. 3.7). The sensitive area of both sub-modules is 300 μm thick, extending from $R = 8.2$ mm to $R = 41.9$ mm. The R sensor includes concentric semicircular strips, segmented into four 45° sectors to manage occupancy. The strip pitch varies linearly from 38 μm at the inner

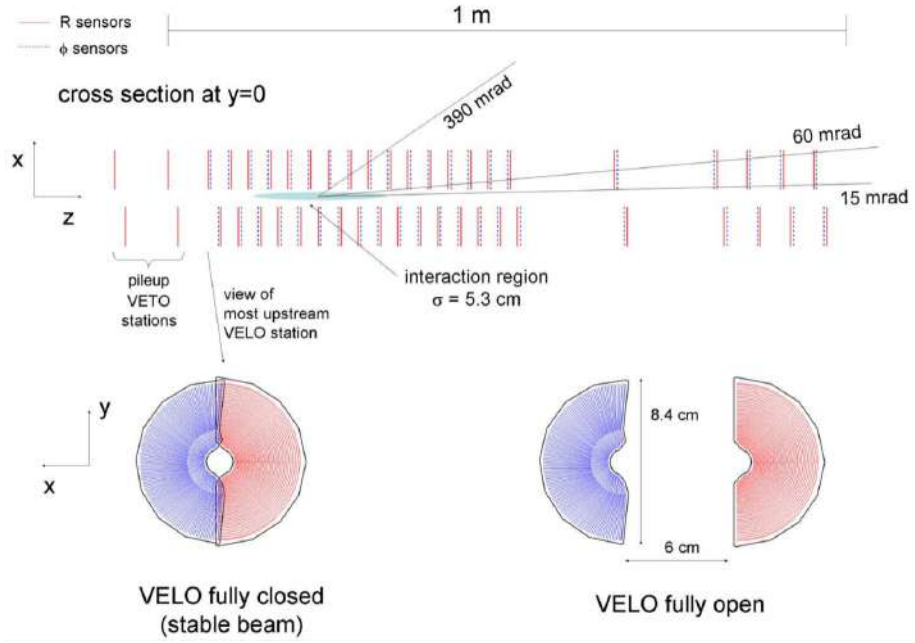

Figure 3.6: (Top) Schematic view of the VELO modules along the beam axis in the $x - z$ plane. (Bottom) Front view of a single station in both closed (left) and open (right) configuration. Figure from Ref. [61].

radius to 101.6 μm at the outer radius. The ϕ sensor split into two sub-sectors to deal with high occupancy. The inner section comprises 683 strips angled at approximately 20° to the radial direction up to R =17.25 mm. The outer section, with 1365 strips angled at roughly 10°, covers the remaining area. Consequently, the pitch in the ϕ direction varies based on radial distance, ranging from 38 μm to 78 μm in the inner section and 39 μm to 97 μm in the outer section. The modules are arranged such that adjacent ϕ sensors have oppositely tilted strips, enhancing background rejection. A schematic of the tracking station geometry is presented in Fig. 3.7.

During the injection phase at the LHC, the size of the beam-hole of the VELO is too small to prevent sensor damage. As a precautionary measure, the two halves of the VELO are retracted by 3 cm until the beam stabilizes. Additionally, to safeguard against damage from beam-induced currents and to segregate the VELO vacuum from the LHC vacuum, each half is encased in a shielding box. The innermost part of this shielding, known as RF-foils, is constructed from a 300 μm thick alloy of aluminium and magnesium for radio-frequency shielding. This section is distinctively corrugated, as shown in Fig. 3.7, allowing for the overlapping of modules.

Tracker Turicensis

The Tracker Turicensis (TT), a silicon micro-strip detector, is situated just before the magnet. It plays a critical role in detecting low-momentum particles that could be deflected by the magnetic field and in reconstructing long-lived particles such as K^0_S and Λ. The TT comprises four layers, each measuring 150 cm by 130 cm, arranged in two stations 30 cm apart along the beam line. These layers are organized in an "x-u-v-x"

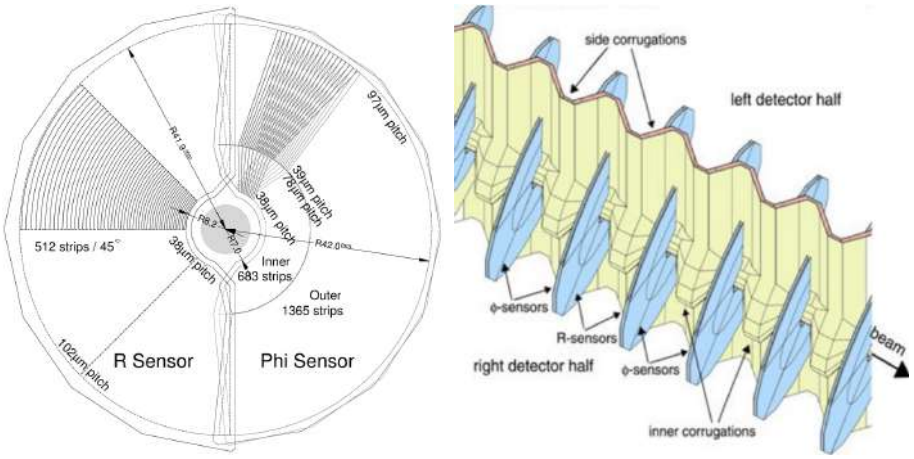

Figure 3.7: (Left) $R - \phi$ geometry of the VELO modules. (Right) Illustration of the RF-foils in the closed configuration. Figures from Ref. **??**

configuration as depicted in Fig. 3.8. This means that the outer layers consist of vertical strips ("x" configuration), while the intermediate layers are tilted by $\pm 5^\circ$ from the vertical ("u" and "v" configurations), aiding in the measurement of the y-direction. This design leads to lower resolution along the y direction, which is not critical for momentum measurements (particles bend along x direction), but is sufficient to easier path-finding and to reduce background. Each sensor module is 500 μm thick, with a 9.6 cm by 9.4 cm sensitive region, and contains 512 strips with a 183 μm pitch.

T-stations

The T-stations (T1, T2, T3) are three tracking stations located immediately after the magnet, with the task of measuring the momentum of charged particles. Spanning an area of about 6 m by 5 m, they are segmented into two components: a smaller Inner Tracker (IT) made of silicon micro-strip and a larger Outer Tracker (OT) composed of straw tubes.

Inner Tracker The Inner Tracker [62] is a silicon micro-strip detector positioned in the internal region of each T-station. It extends horizontally, as illustrated in Fig. 3.9, forming a cross shape about 125 cm wide and 40 cm high. Similar to the TT, the IT consists of four layers in an "x-u-v-x" arrangement. The silicon micro-strip modules resemble those in the TT, with a 198 μm pitch and a sensitive area of 7.6 cm by 11 cm.

Outer Tracker The Outer Tracker [63], a gaseous ionization detector, is installed in the outer areas of each T-station. Comprising straw tubes functioning as proportional counters, the OT also features four detection planes in an "x-u-v-x" layout, as shown in the left panel of Fig. 3.10. The drift tubes, 2.4 m in length with a 4.9 mm inner diameter, are arranged in two staggered rows per plane, as depicted in the right panel of Fig. 3.10. Filled with an $Ar/CO_2/O_2$ gas mixture (70%/28.5%/1.5%), the tubes are characterized

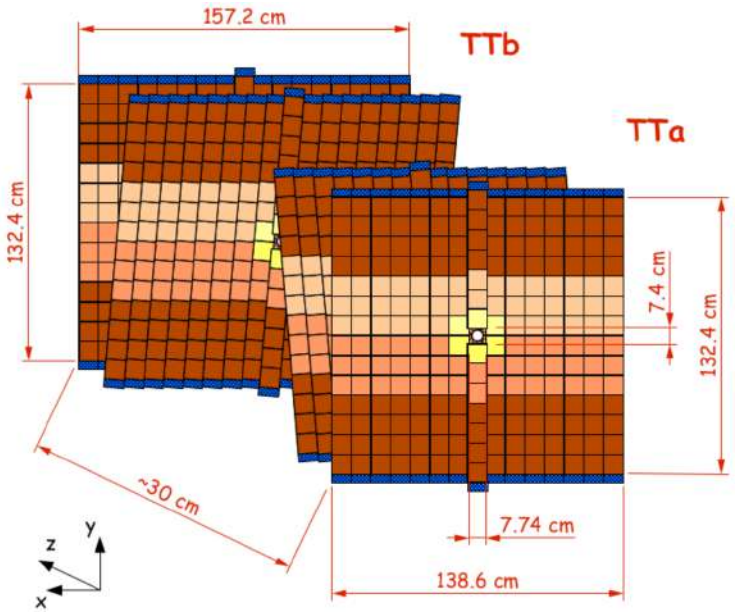

Figure 3.8: Schematic representation of the TT detector geometry. Figures from Ref. **??**.

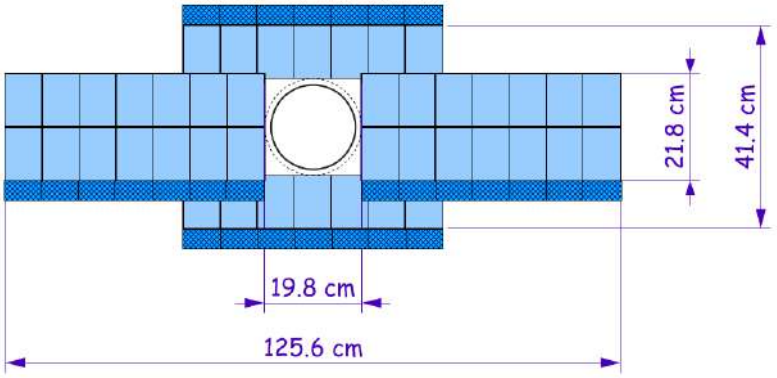

Figure 3.9: Front view of a single IT layer. Figures from Ref. **??**.

by a 50 ns drift time. Occupancies typically hover around 10%, with hit efficiencies exceeding 99% for tracks near a tube's centre.

3.2.3 Particle Identification Systems

The Ring Cherenkov Detectors

The LHCb experiment utilizes two Ring Cherenkov detectors (RICH1 and RICH2) as essential components for particle identification, particularly in distinguishing pions from kaons over a momentum range from 1 GeV/c to 100 GeV/c, using the Cherenkov effect [64]. When a particle with velocity v travels through a medium with a refractive index n at a speed exceeding the medium's light speed, it emits Cherenkov photons in a

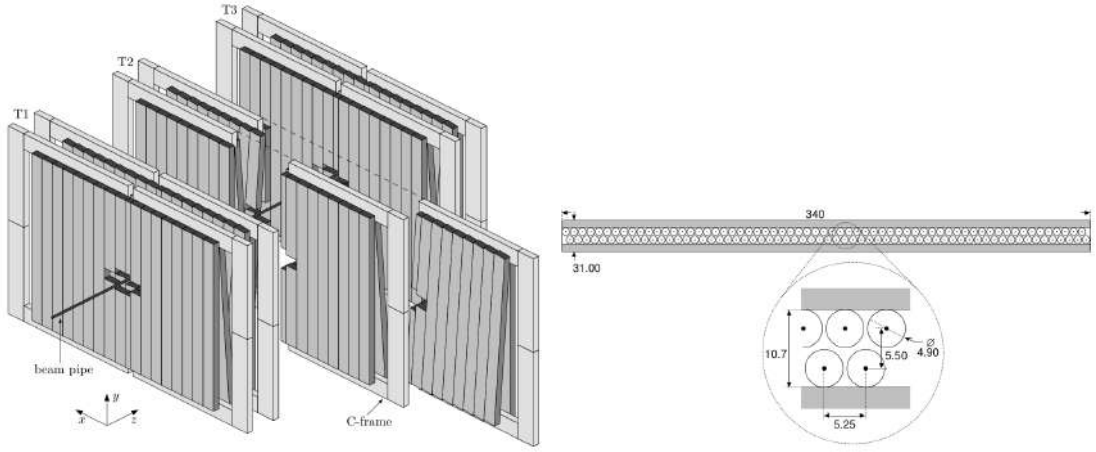

Figure 3.10: (Left) Geometry of the OT detector planes. (Right) Section of a single OT detection plane. Figures from Ref. [63].

cone with an opening angle θ_C, defined as

$$\theta_C = \frac{1}{\beta n}, \tag{3.3}$$

where $\beta = v/c$ and c is the speed of light. Notably, Cherenkov radiation is emitted only if $\beta > 1/n$. Given the momentum p of the particle, determined by the tracking system, the Cherenkov angle can be related to the particle's mass as

$$\theta_C = \arccos\left(\frac{1}{n}\sqrt{1+\left(\frac{mc}{p}\right)^2}\right). \tag{3.4}$$

The relationship between the Cherenkov angle and the particle momenta, for the radiation media used at LHCb, is depicted in Fig.3.11. Achieving optimal separation between pion and kaon mass hypotheses, especially at high momenta, requires a small refractive index (close to 1). However, a lower refractive index also means higher threshold momenta below which Cherenkov light is not emitted, necessitating a balance between these two factors.

LHCb employs two RICH detectors with different refractive indices to span a wide momentum range. RICH1 targets the lower momentum range (1-60 GeV/c) using air (in Run 1 aerogel (n =1.03) was used instead) and C_4F_{10}(n =1.0014) as radiation media, yielding maximum Cherenkov angles of 242 mrad and 53 mrad, respectively. Positioned before the magnet (between VELO and TT), RICH1 identifies particles deflected out of the LHCb acceptance by the magnetic field. RICH2, located after T3, is designed for the higher momentum range (15-100 GeV/c) and uses CF_4 ($n = 1.0005$) as its radiation medium, producing a maximum Cherenkov angle of 32 mrad. Both RICH detectors utilize a sophisticated system of mirrors to reflect the emitted photons outside the LHCb acceptance towards hybrid photon detectors (HPDs). This design allows the HPDs to be shielded from the magnetic field and minimizes the material budget. The geometries of

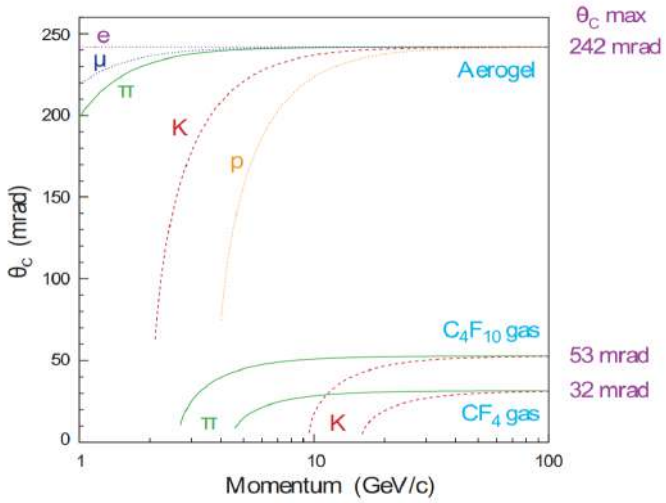

Figure 3.11: Cherenkov angles plotted against particle momentum for different radiation media used at LHCb. Figure from Ref. [59].

the two RICH detectors are illustrated in Fig. 3.12.

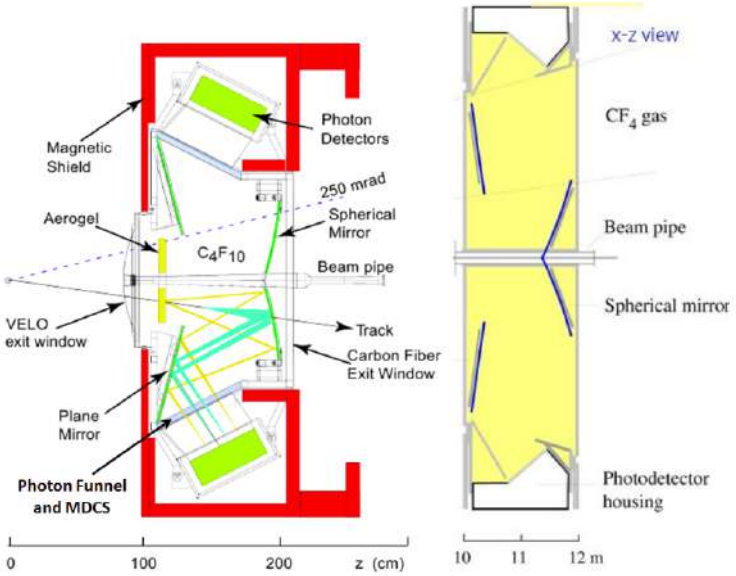

Figure 3.12: RICH1 (left) and RICH2 (right) geometry. Figure from Ref. [64].

Calorimeter detectors

The calorimetric system of the LHCb experiment comprises four sub-detectors: the Scintillator Pad (SPD), the PreShower (PS), the Electromagnetic Calorimeter (ECAL), and the Hadron Calorimeter (HCAL). These components are crucial for differentiating between electrons, photons and hadrons, providing rapid estimates of their energies and positions, and are part of the low-level trigger system.

SPD and PS The SPD and PS [65] are primarily utilized in the low-level electron trigger to eliminate background noise from charged and neutral pions. The SPD, functioning similarly to a tracking detector, detects only charged particles. Positioned after the SPD, the PS is separated by a 15 mm lead absorber, equivalent to about 2.5 radiation lengths for electrons. In this setup, electrons and photons initiate showers, generating significantly larger signals on the PS compared to pions. Thus, electrons are uniquely identifiable as they produce signals in both the SPD and PS, as depicted in Fig. 3.13. Additionally, the SPD plays a role in the low-level trigger by counting the number of tracks per event, enabling a veto on overly crowded events.

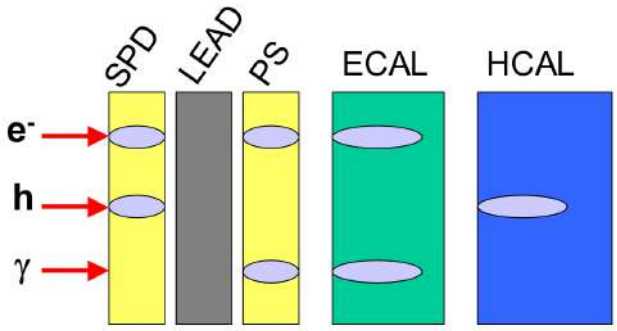

Figure 3.13: A schematic representation of energy deposit in each sub-detector of the calorimeter system. Figures from Ref. [65].

ECAL The ECAL [66] is constructed with alternating layers of 4 mm thick scintillator tiles and 2 mm thick lead plates, amounting to about 25 radiation lengths. This design ensures almost complete containment of electromagnetic showers, yielding a resolution of $0.9\% \oplus 10\%/\sqrt{E/GeV}$ [67].

HCAL Composed of alternating 4 mm thick scintillator tiles and 16 mm thick iron slabs, the HCAL [66] spans approximately 5.6 interaction lengths. This thickness is insufficient to fully contain hadronic showers, resulting in a resolution of $9\% \oplus 69\%/\sqrt{E/GeV}$ [67]. Therefore, the HCAL's primary function is to quickly estimate hadron energy for use in the hardware trigger.

The SPD, PS, and ECAL share a common layout, depicted in Fig. 3.14 (left). These detectors are divided into three sections with varying tile sizes: 4×4 cm in the inner region, 6×6 cm in the middle, and 12×12 cm in the outer region. This segmentation addresses the increasing occupancy near the beam line. The HCAL follows a similar design, as shown in Fig. 3.14 (right), but is split into two sections with tile sizes of 13×13 cm and 26×26 cm, respectively. All these detectors employ a common read-out system, where scintillation light is transmitted to photomultipliers using wavelength-shifting fibres.

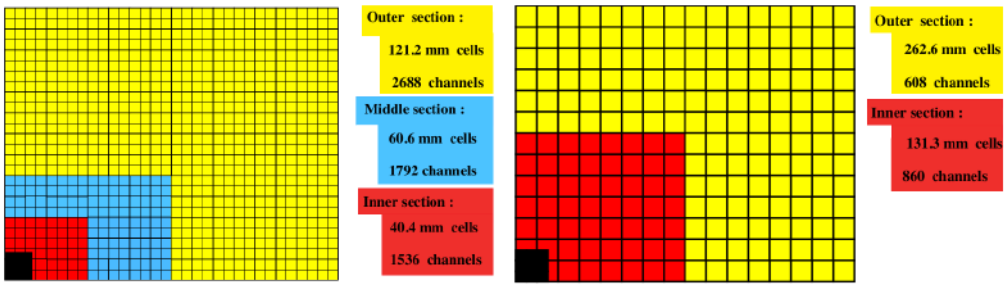

Figure 3.14: Segmentation of one quadrant of the PS, SPD, ECAL (left) and HCAL (right). Figure from Ref. [59].

Muon detectors

The muon system of LHCb, comprising stations M1 through M5 [68] and illustrated in Fig. 3.15, is engineered to identify muons and rapidly estimate their momenta for the low-level trigger. Station M1, positioned before the calorimeter system, plays a crucial role in refining the transverse momentum (p_T) measurement for the trigger. The presence of the calorimeters, with their substantial material composition, can lead to multiple scattering errors, which M1 helps to mitigate. Stations M2 to M5, located downstream of the calorimeters, are interspersed with iron absorbers, each 80 cm thick. This arrangement ensures that only muons with sufficient penetrating power, typically requiring a minimum momentum of about 6 GeV/c, can traverse the entire system. The cumulative thickness of these absorbers, along with the calorimeters, equates to around 20 interaction lengths.

Each muon station is divided into four distinct regions (R1–R4), featuring increasingly finer segmentation nearer to the beam pipe to accommodate higher particle multiplicity in these areas. While multiwire proportional chamber detectors are used across all stations, an exception is made for the innermost region (R1) of the first station (M1). Here, triple gas electron multiplier detectors (triple-GEM) are employed, catering to the high particle density and necessitating radiation-tolerant detectors.

In the trigger process, muon reconstruction is exclusively handled by the muon system, achieving an average transverse momentum resolution of approximately 20%.

3.3 LHCb Trigger

The LHCb trigger system, designed to manage the flow of data from the LHC's bunch structure and the interaction point's low luminosity, faces a unique challenge. Although the frequency of visible interactions, *i.e.* events with at least two charged particles within LHCb's acceptance, is about 10 MHz (in Run 2), only a limited rate of events can be stored: 5 kHz during Run 1 and 12.5 kHz in Run 2. Given that a small fraction of the 10 MHz rate comprises events of interest, a two-level trigger system is employed: the Level-0 (L0) hardware trigger and the High Level Trigger (HLT) running on a dedicated computing farm.

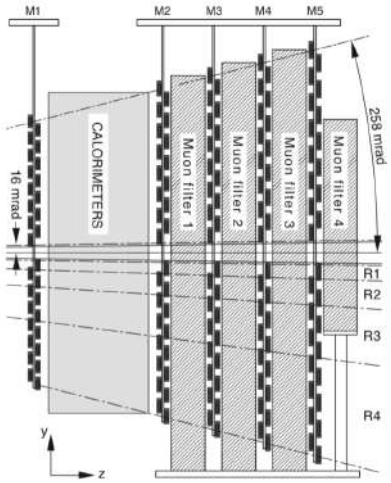

Figure 3.15: Illustration of the muon system from a side view. Figure from Ref. [68].

3.3.1 Level-0 trigger

The L0 trigger must reduce the event rate to about 1 MHz. It relies on quickly accessible and computationally light information from the calorimeters and muon stations, as pattern recognition at this stage is too resource-intensive. The L0 trigger comprises three independent triggers running in parallel and exploiting the information from different sub-detectors.

L0Hadron Utilizing data from the HCAL, this trigger is designed to enrich the sample with b- and c-hadron events, exploiting the fact that final states of such particles have higher transverse momenta than light quark processes. It identifies hadronic showers in 2×2 clusters and calculates their transverse energy as

$$E_T = \sum_i^4 E_i \sin\theta_i, \tag{3.5}$$

where E_i is the energy in the i^{th} cell, and θ_i is the angle relative to the beam line from the nominal interaction point. An event is triggered if at least one cluster exceeds a specific transverse energy threshold, typically around 3.6 GeV, with an estimated trigger output rate of 450 kHz.

L0Photon/Electron This trigger, using information from the SPD, PS and ECAL identifies electrons and photons. Events with at least one cluster exceeding a transverse energy threshold of about 2.4 GeV for electrons and 2.8 GeV for photons are selected. Its estimated output rate is 150 kHz.

L0Muon/Dimuon Drawing data from the muon stations, this trigger identifies muons and estimates their momentum. Events with either a single muon exceeding a momentum threshold (around 1.5 GeV) or a pair of muons where $\sqrt{p_T(\mu_1) \cdot p_T(\mu_2)}$ surpasses a given

threshold (typically 1.3 GeV) are selected. The estimated output rate for this trigger is 400 kHz.

3.3.2 High Level trigger

Events passing the L0 are processed by the Event Filter Farm (EFF) where the High Level Trigger, a C++ executable, performs full event reconstruction, running in parallel on thousands of machines, and decides whether to save each event on disk or to discharge it. The HLT is divided into two successive stages, HLT1 and HLT2.

HLT1 This stage processes the full 1 MHz event rate from L0, conducting partial reconstruction to reduce it to about 80 kHz. It involves full reconstruction of VELO tracks and identification of pp interaction vertices. Only tracks with significant impact parameters and minimum transverse momentum are fully reconstructed using TT and T-station information. An event is selected if it contains at least one or two well-reconstructed tracks meeting specific impact parameters and momentum criteria.

HLT2 The HLT2 performs a full reconstruction, similar to offline processing but with some approximations, to achieve the final output rate. It consists of inclusive and exclusive selections, with different decay types selected according to specific algorithms and trigger lines.

3.3.3 Turbo stream in LHCb Run 2

A significant challenge for LHCb, especially in charm physics, is managing the vast data volume. The event rate written to disk is constrained by storage capacity. From Run 1 to Run 2, advancements in processing power and buffer storage enabled an improvement in the quality of reconstruction carried out by HLT2, making it comparable to offline reprocessing in Run 2. This led to the introduction of the "Turbo" stream [69], a strategy where, instead of saving entire raw events (averaging 70 kb), only data related to relevant particles for each trigger line are stored, reducing the event size to about 5 kb. This approach allowed for an increase in the event rate saved to disk. In Run 2 the final trigger rate is about 12 kHz, among those triggered events about 5 kHz are triggered by lines in the Turbo stream and notably the data used in this analysis comes from such a trigger line. A schematic view of Run 1 and Run 2 trigger is shown in Fig. 3.16.

3.4 Event reconstruction and performances

3.4.1 Track reconstruction

The initial step in track reconstruction at LHCb is pattern recognition, where hits created by the same charged particle are grouped together. Various types of tracks are distinguished based on the sub-detectors they traverse (as illustrated in Fig.3.17):

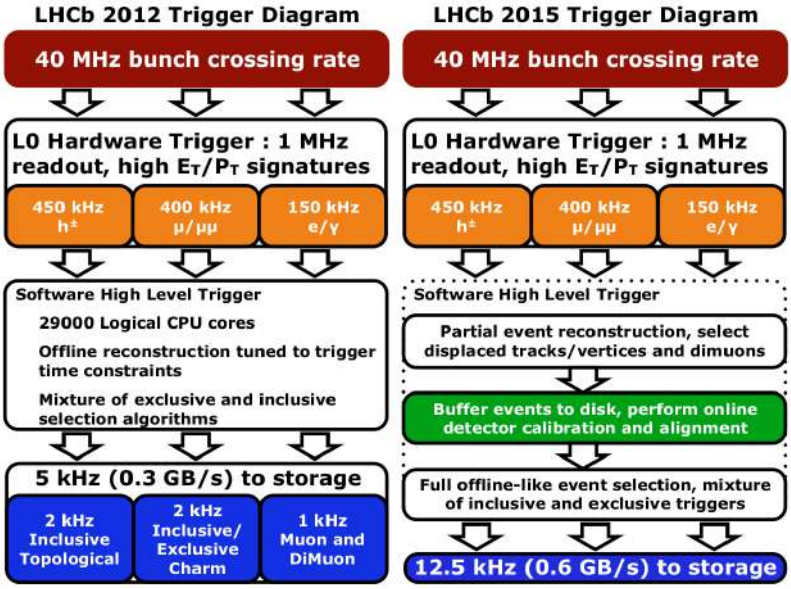

Figure 3.16: Illustration of the LHCb trigger system during Run 1 (left) and Run 2 (right).

- **VELO tracks**, formed solely from VELO hits, are crucial for primary vertex reconstruction and serve as seeds for long and upstream track reconstruction;
- **Upstream tracks**, comprising hits in both the VELO and TT, these tracks correspond to low-momentum particles deflected by the magnetic field.
- **T tracks**, formed from hits in the T-stations, these tracks are used as seeds for downstream and long track reconstructions.
- **Downstream tracks**, utilizing hits from the TT and T-stations, downstream tracks are linked to long-lived particles like K_S^0 that decay outside the VELO.
- **Long tracks**, combining hits from the VELO, TT, and T-stations, offer the best momentum resolution and are the primary focus of this analysis.

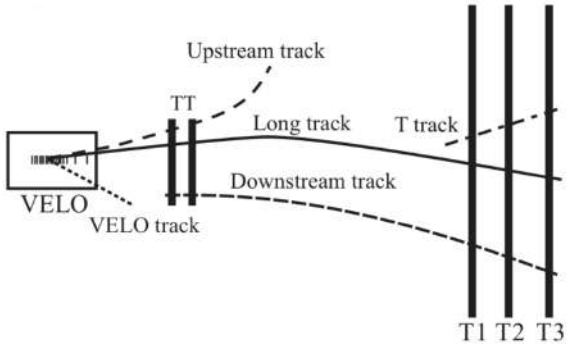

Figure 3.17: Diagram showing the classification of tracks at LHCb based on crossed sub-detectors. Figure from

The resolution for long tracks is approximately $\sigma_p/p = 0.5\%$ for momenta below 20 GeV/c, rising linearly to 0.8% at 100 GeV/c. This leads to a mass resolution of about

$\sigma_m / m \simeq 0.5\%$ up to the Y mass. The primary vertex (PV) resolution is heavily influenced by the number of tracks originating from the vertex (as shown in Fig.3.18), with an average PV resolution in our data of about 10 μm in the x and y directions, and about 70 μm in the z direction.

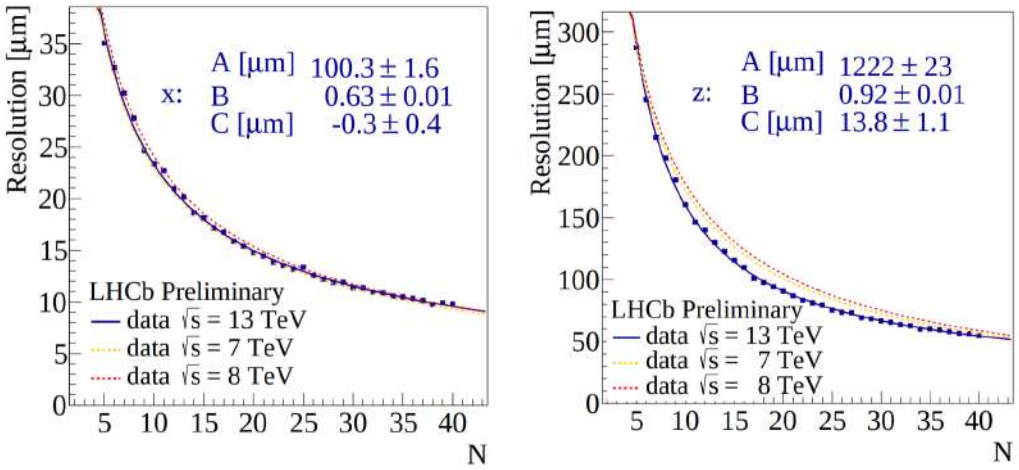

Figure 3.18: Resolution of the primary vertex in the x (left) and z (right) directions as a function of the number of particles in the vertex fit for various center-of-mass energies. Figures from Ref [60].

3.4.2 Particle identification

Particle identification at LHCb leverages different sub-detectors. The measured Cherenkov angle from the RICH detectors, combined with momentum data from the tracking system, aids in deducing particle mass (refer to Eq. (3.4)). Muon track reconstruction involves identifying tracks in the tracking system and associating hits around their extrapolated paths in the muon system. For identifying photons, electrons, and π^0 candidates, the calorimeter system is utilized. Neutral particles are differentiated from charged ones by examining the presence or absence of tracks in front of the energy deposits. The distinction between photons and π^0 mesons is made by analyzing the cluster shape. The particle identification (PID) data from the muon, RICH, and calorimeter systems are integrated to provide a more powerful identification. Each subsystem contributes likelihood information for specific particle hypotheses, cumulatively contributing to a combined likelihood, $\mathcal{L}(X)$. This likelihood is often calculated against the pion hypothesis, $\mathcal{L}(\pi)$, as pions are the most abundantly produced and detected particles at LHCb. The difference in the logarithms of two likelihoods for the X and π hypotheses is calculated as PID$X = DLL_{X\pi} \equiv \log \mathcal{L}(X) - \log \mathcal{L}(\pi)$. Higher PID$X$ values indicate a higher likelihood of the particle being of type X rather than a pion. To select pions, small or negative values are typically required. Performance metrics for $K - \pi$ separation are depicted in Fig. 3.19 [70].

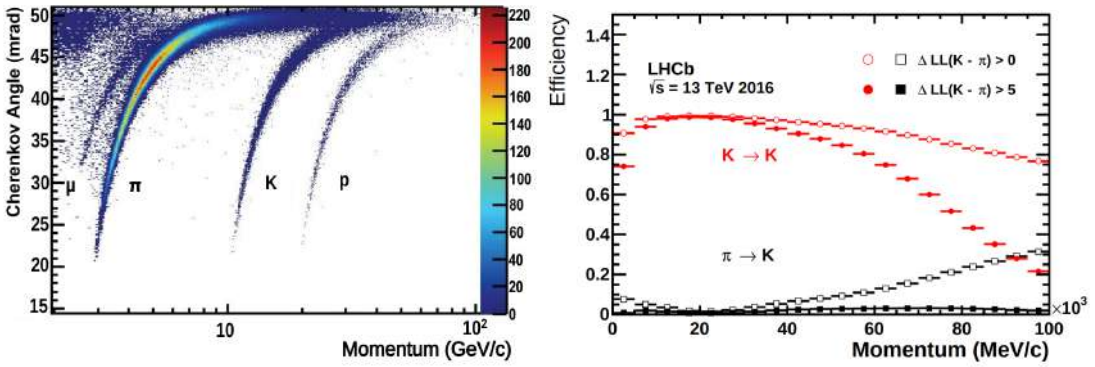

Figure 3.19: (Left) Reconstructed Cerenkov angle for isolated tracks, as a function of track momentum in the C_4F_{10} radiator. (Right) Kaon identification efficiency (red) and pion misidentification rate (black) as a function of track momentum for two different requirements on $DLL_{K\pi}$. Figures from Ref. [64].

Chapter 4

Overview of the analysis strategy

This chapter provides a concise outline of the entire analysis strategy to provide guidance for reading this document. Everything that follows is the result of my original contribution during the course of this thesis work.

The LHCb experiment continued to take data until the end of the LHC Run 2, in 2017 and 2018, collecting an additional sample corresponding to an integrated luminosity of $4\,\text{fb}^{-1}$ from pp collisions at 13 TeV, more than doubling the signal yields compared to 2015-2016 data sample. The work described in this thesis has therefore the main purpose of improving the statistical precision of mixing and CPV parameters, detailed in Sec. 2.4.1 extending their measurement to the total currently available LHCb data sample, including the new data, collected during the second half of LHC Run 2. Furthermore, it aims at a significant reduction of the dominant systematic uncertainties, paving the way for future measurements, in the LHCb-Upgrade era (LHC Run 3 and beyond), where still higher statistical precision, comparable or even lesser than the current systematic one, is expected.

Data sample The flavour of the neutral D^0 meson at production is determined from the charge of the low-momentum pion in the flavour-conserving strong-interaction decay $D^{*+} \to D^0 \pi_s^+$. The pion from the decay of the D^* meson is often referred to as *soft pion*, π_s. As already defined in the Chap. 2, the $D^{*+} \to D^0\,(\to K^-\pi^+)\,\pi_s^+$ process is denoted as right-sign (RS), while the $D^{*+} \to D^0\,(\to K^+\pi^-)\,\pi_s^+$ as wrong-sign (WS).
Applying triggers and offline selections (described in Sec. 5) to the LHCb dataset collected during the full LHC Run 2, we extract a huge sample of about 413 million extremely clean $D^0 \to K^-\pi^+$ RS decays, and an unprecedented abundant sample of 1.6 million suppressed $D^0 \to K^+\pi^-$ WS decays. The final signal yields, for each data-taking period and separately for RS and WS, are illustrated in Tab. 4.1. This sample is much larger than the one collected during the LHC Run 1 [31], corresponding to about 54 million RS and 230 thousand WS decays. Due to the limited impact on the precision of the

	2016	2017	2018	total
RS yield ($\times 10^6$)	135	131	147	413
WS yield ($\times 10^3$)	540	520	584	1644

Table 4.1: Fitted RS and WS yields, year by year, after the offline selection.

final measurement (about 7% of the total uncertainties), Run 1 data are not reanalysed. The measurement described in this thesis, therefore, focuses on the extension of the analysis to the full data sample collected during the LHC Run 2, including both the reanalysis of the 2015 and 2016 data samples, and the brand new analysis of 2017 and 2018 data samples. During this period running conditions (including trigger configurations) remained almost unchanged. Any improvement and optimization of the analysis of new data is automatically extended to the full Run 2 data sample making the work easier and more powerful owing to a better uniformity across different years. An average is ultimately performed with the results of the measurement detailed in this thesis and the measurement already published using data collected during the LHC Run 1 [10], resulting in a legacy LHCb measurement of these golden observables for mixing and CPV in the charm mesons sector.
Together with the main data sample of $D^{*\pm} \to D^0(\overline{D}^0)[\to K\pi]\pi_s^\pm$, other data and simulated samples are used to study and measure sources of systematic effects. The data sample of $D^{*\pm} \to D^0(\overline{D}^0)[\to K^+K^-]\pi_s^\pm$ decays is used as a calibration channel to correct for instrumental asymmetry bias. A small dataset of $B \to D^*(\to D^0\pi_s)\mu X$ is used to study the background from secondary D^* decays, together with simulated samples of a cocktail of $B \to D^*(\to D^0\pi_s)X$ decays.

General strategy The general strategy of the analysis follows that of the previous one based on data collected during Run 1 and the first two years (2015-2016) of Run 2 [10]. Candidates belonging to the $D^{*+} \to D^0\ (\to K^\pm\pi^\mp)\ \pi_s^+$ decay chain are then reconstructed and selected to improve as much as possible the purity of WS signal decays, as described in Sec. 5. The RS decays are already very clean and abundant. The final data set is then divided into different disjointed sub-samples on the basis of the D^0 decay-time (decay-time bin), which are utilized to determine the decay-time dependency of the WS-to-RS ratio, separately for the two D^0 final states ($K^+\pi^-$ and $K^-\pi^+$). In order to do so, we need to evaluate the WS-to-RS yield ratio r_i' and the average of the D^0 (squared) decay time distribution, $\langle t\rangle_i$ ($\langle t^2\rangle_i$) in each decay-time bin i. Here, $\langle\rangle_i$ represents the average of a certain quantity over the decay-time bin i. These first raw determinations, of both the ratios and average decay times, need to be corrected for the known sources of bias. Subsequently, the dependency of the corrected ratios on the corrected average decay times, both for $D^0(\overline{D}^0) \to K^+\pi^-$ and $D^0(\overline{D}^0) \to K^-\pi^+$ is fitted in order to infer the mixing and CPV parameters of interest.
The data set is divided into 18 bins, approximately equipopulated[1], of reconstructed D^0 decay time, in a range from $0.4\,\tau_{D^0}$ to $8\,\tau_{D^0}$. This binning scheme differs from the one used

[1]The last four bins have half of the statistics of the other ones.

in this analysis's previous iteration, which was chosen to have 13 equipopulated bins as in Run 1 data. The choice of bin number is determined by a compromise. By increasing the number of bins, the statistical power increases asymptotically: by going from 13 to 30 bins, the final uncertainty is reduced by 3%. However, decreasing the statistic in each bin makes it more complicated to measure the smallest background component consistently. The Q-value of the $D^{*+} \to D^0\pi_s^+$ decay, approximately 6 MeV/c^2, is much lesser than the known value of the mass of both the D^0 meson and the pion. Consequently, they are both produced nearly at rest in the D^{*+} reference frame. Furthermore, the mass of the π_s^+ is much smaller than that of the D^0 meson, then its momentum is typically much less than that of the D^0 daughter particles. An effect of the tiny Q-value of the D^{*+} decay is that the D^0 and the π_s^+ are produced with nearly collinear momenta in the laboratory frame. As a consequence, the resolution of the position of the D^{*+} decay vertex along its momentum direction is very poor, approximately 1.5 cm, comparable with the average value of the D^0 flight distance, approximately 1 cm. This translates into a very poor decay-time resolution which would dilute and bias the decay-time dependence of the WS-to-RS ratio. The decay-time resolution greatly improves, down to the level of 0.1 τ_{D^0}, if the flight distance is calculated from the primary pp collision vertex (PV) instead of the reconstructed D^{*+} decay vertex[2]. This employs the fact that most D^{*+} are produced in the PV and that D^{*+} has an extremely short lifetime. As a consequence, the production points of the D^{*+} and the D^0 mesons are indistinguishable.

Backgrounds in the D^* invariant mass The prominent background from genuine, properly reconstructed D^0 decays associated with a random pion, commonly called *combinatorial background*, is indistinguishable from the signal in looking at the $K\pi$ invariant mass, $m(K\pi)$. This is the two-body invariant mass computed with the $K\pi$ mass hypothesis, in which the pion mass is assigned to the particle having the same (opposite) charge of the tagging pion, in order to reconstruct RS (WS) candidates. On the other hand, this combinatorial background features a smoothly growing, square-root-like shape in $m(D^0\pi_s)$: the invariant mass of D^0 and π_s, computed constraining the D^0 mass to the PDG value. Random three-track combinations that accidentally meet the selection requirements show a smooth distribution in $m(K\pi)$ and the same square-root-like shape in the D^* mass distribution.
An other potentially dangerous background in the D^* invariant mass distribution arises from `ghost soft pions` that are built from the combinations of correctly identified hits in the VELO and hits from different particles in the T-stations. The $D^{*\pm}$ candidates reconstructed using these ghost soft pions produce a peak in the $m(D^0\pi_s)$ distribution because the direction of these soft pions is correctly measured even if their momentum is wrong. The charge of the pion is also random, as a consequence, the very abundant genuine RS decays seed the production of RS and WS ghost candidates, biasing the WS signal yield. The mass line shape of this ghost background is modelled starting from a pure subsample of this background, selected as illustrated in Sec. 5.4.

[2]Any residual bias due to the decay-time resolution is small and is subtracted together with the other sources of decay-time bias as shown in Sec. 8

WS-to-RS ratio and average decay time measurement The WS-to-RS yield ratios are determined in each decay-time bin, discriminating the signal from the combinatorial and ghost backgrounds thanks to the distinctive shape of each component in the D^* invariant mass distribution. A global fit is performed to the $D^* \to D^0\,(\to K\pi)\,\pi_s$ decay chain, requiring the production vertex of the D^0 to coincide with its pp primary vertex. This allows us to improve the $m(D^0\pi_s)$ resolution, bringing it from about $0.8\,\mathrm{MeV}/c^2$ to about $0.3\,\mathrm{MeV}/c^2$. The corresponding fitting algorithm [71] is often referenced to as `DecayTreeFitter` (DTF) and is performed, including the momentum scale correction. Whenever a kinematic quantity used in this analysis is calculated using the output variables of this fit, it will be made explicit by adding the DTF subscript. In particular, our discriminating variable, used for yield extraction is $m(D^0\pi_s)_{\mathrm{DTF}}$: the $m(D^0\pi_s)$ invariant mass computed using momenta resulted from the DTF fit.
Signal and backgrounds are modelled with empirical pdfs, fitted independently in each decay-time bin and for each D^0 final state ($K^+\pi^-$ and $K^-\pi^+$). We simultaneously fit the selected subsample of pure ghost background, together with WS and RS samples, assuming the same $m(D^0\pi_s)_{\mathrm{DTF}}$ distribution for the WS and RS signal. The fit model and strategy are detailed in Sec. 6.
The raw average decay time (and its square) for each decay time bin is evaluated, removing combinatorial background through a sideband subtraction in the $m(D^0\pi_s)$ distribution, as described in Sec. 6.2

Ratio biases The assumptions under the D^* mass fit model are tested and justified in Sec. 7.1, with data-driven techniques and pseudo-experiments.

Experimental effects such as different efficiencies for reconstructing WS or RS decays may bias the observed ratio of reconstructed candidates and the corresponding measurement of mixing parameters. Assuming that the efficiency for detecting the three final-state particles factorizes as the product of efficiencies of the D^0 decay products, $\epsilon(K^\mp\pi^\pm)$, and the efficiency for reconstructing the charged soft pion, $\epsilon(\pi_s^\pm)$, the charge-specific observed WS-to-RS yield ratios, in any sub-sample, can be written as

$$R'^{\mathrm{obs}\pm} = \frac{N^{\mathrm{obs}}_{WS\pm}}{N^{\mathrm{obs}}_{RS\mp}} = \frac{\int R'^{\pm}\epsilon(K^\pm\pi^\mp)\epsilon(\pi_s^\pm)(1 \pm A_P)}{\int \epsilon(K^\pm\pi^\mp)\epsilon(\pi_s^\mp)(1 \mp A_P)} \simeq R'^{\pm}\left[1 \pm 2\left(A_D(\pi_s) + A_P\right)\right], \quad (4.1)$$

where the integrals run over the kinematics of the K, π and π_s in that subsample. The production asymmetry, A_P, between D^{*+} and D^{*-} and the detection asymmetry of soft pions of different charge, $A_D(\pi_s)$, are the only relevant instrumental nuisances since kaon-pion detection efficiency cancels out at first order when fiducial cuts are in place. Appendix B provides an in-depth description of how these cancellations work. The net effect of these nuisance asymmetries, which we note as $A_{D^*\pi_s}$, is determined on data measuring the raw asymmetry of the control samples of prompt $D^0 \to K^-K^+$ decays as described in Sec. 7.2. This is a Single Cabibbo-Suppressed decay, hence it could be affected by a non-negligible *CP*-violating asymmetry, which is measured in Ref. [72] and used as an external input.

The WS and RS yields are extracted from a fit to the D^* invariant mass observable,

where the D^0 mass is constrained to the PDG value. Due to this constraint, if a hadron from a $D^0 \to h^+h^-$ decays ($h = K, \pi$) is misidentified, the $m(D^0\pi_s)_{\rm DTF}$ distribution of this background is almost indistinguishable from the signal, producing a bias to the fitted ratio. We only fit the $m(D^0\pi_s)_{\rm DTF}$ distribution for candidates restricted to a narrow signal region in the D^0 invariant mass distribution to reduce the contamination from misidentified $D^0 \to K^+K^-$ and $D^0 \to \pi^+\pi^-$ decays to a negligible level and minimize the contribution from hard-to-model physics backgrounds from other mis-reconstructed charm decays. The D^0 decays that are reconstructed as the result of a double misidentification (the kaon is identified as a pion, and the pion is identified as a kaon) show a broad structure in the D^0 mass observable but are very similar to the signal in the D^* mass distribution, $m(D^0\pi_s)_{\rm DTF}$. This peaking background is strongly reduced by the offline selection and the residual bias is estimated in Sec. 7.

There are some D^0 candidates which are simultaneously associated with a pair of soft pions with opposite charges. They generate two different D^* candidates (also indicated as multiple candidates), that are classified as a RS and a WS candidate, and therefore saved, at HLT2 level, in the two different data ntuples. When the D^* invariant mass of the RS candidate is near the D^* peak (within 3σ from the D^* peak), this is with high probability a genuine candidate, while the associated WS candidate is either combinatorial background or ghost background. Thus, these WS candidates are removed from the data sample, increasing the signal-to-background ratio (see Sec. 5.3.5). However, a small fraction of these RS candidates comes from a real RS background, while the corresponding WS candidate is genuine. Therefore, the removal of these common candidates from the WS data sample implies rejecting a very small fraction of WS real candidates, that must be accurately accounted for in the final measurement. In general, any trigger or offline requirement with a different efficiency for WS and RS is absorbed in the $A_{D^*\pi_s}$ correction and properly accounted for with the $D^0 \to K^+K^-$ sample. However, in this case, the removal of the common candidates cannot be applied, for obvious reasons, thus, the bias is evaluated and corrected separately, as described in Sec. 7.4.

Decay-time bias As previously mentioned, we use the constraint that the D^{*+} decay vertex coincides with the PV both in the D^0 decay-time estimate and the $m(D^0\pi_s)_{\rm DTF}$ calculation, since most D^{*+} are produced in the PV (*prompt decays*). However, a minor fraction of candidates comes from the decay of long-lived b-hadrons (*secondary decays*). The measurement of their decay time is biased to higher values because the D^0 flight distance is calculated starting from the PV, diluting the mixing effects. A known (minor) bias also affects the measurement of the D^0 decay vertex z position, consequently biasing the decay time. These decay-time biases are further discussed and precisely determined using a simulated sample as shown in Sec. 8.

Time-dependent fit After correcting the raw WS-to-RS ratios and raw average decay time for the known biases, these are fitted with the expected time-dependent function:

$$\begin{aligned} R_i'^{\pm} \equiv \langle R'^{\pm}(t)\rangle_i = \;& R_D(1 \pm A_D) \\ & + \sqrt{R_D(1 \pm A_D)}\,(c_{K\pi} \pm \Delta c_{K\pi})\,\langle t/\tau_{D^0}\rangle_i \\ & + (c'_{K\pi} \pm \Delta c'_{K\pi})\langle t^2/\tau^2_{D^0}\rangle_i, \end{aligned} \tag{4.2}$$

where R_D is the Doubly Cabibbo Suppressed to Cabibbo Favoured ratio, $c_{K\pi}$ and $c'_{K\pi}$ are *CP*-even observables linked to the mixing parameters, while A_D, $\Delta c_{K\pi}$ and $\Delta c'_{K\pi}$ are *CP* observables related to the *CP* violation in the decay, interference between decay and mixing, and mixing, respectively. The fit is also performed using the parametrization employed in the previous iteration of this measurement:

$$R_i'^{\pm} = R_D^{\pm} + \sqrt{R_D^{\pm}}\,y'^{\pm}\langle t/\tau_{D^0}\rangle_i + \frac{y'^{2\pm} + x'^{2\pm}}{4}\langle t^2/\tau^2_{D^0}\rangle_i. \tag{4.3}$$

The time-dependent fit minimizes a χ^2 expression appropriately modified to include the effect of instrumental asymmetries, background contamination, and any other systematic effects included in the form of nuisance parameters, as described in Sec. 9.
The data set is divided into two or more sub-samples and the full measurement is performed independently in the disjointed sub-samples. The compatibility between the different sets of results is assessed to accurately check the robustness and reliability of the analysis strategy. The observables and the criteria to divide the data sample are chosen based on their high sensitivity to target the sources of bias studied and determined in this work. This procedure is repeated multiple times for various observables, as described in Sec. 9.2.

Results and conclusion The final results are outlined in Sec. 10 for different scenarios where *CP* violation is fully allowed, not allowed, and partially allowed, with a detailed decomposition of the contributions of all the systematic sources. The impact of this measurement on the global average of charm mixing and CPV parameters is evaluated in Sec. 10.4.

Chapter 5

Data sample and event selection

This chapter describes the trigger and offline requirements used to reduce as much as possible the main backgrounds while keeping a high efficiency on signal $D \to K\pi$ candidates. It follows with the description of all control data samples and simulated samples utilized throughout the measurement described in this thesis.

The measurement is performed using the data collected in pp collisions during 2015–2018 (Run 2) at $\sqrt{s} = 13\,\text{TeV}$. About half of the data were collected each year with the magnetic field pointing upwards (*MagUp*) and the other half with the opposite polarity (*MagDown*). The dataset is divided into three sub-samples that are independently analysed. These sub-samples correspond to the data-taking periods of 2015–2016, 2017, and 2018, amounting to an integrated luminosity of 1.9, 1.7 and 2.1 fb^{-1}, respectively. The dataset collected in 2015 is small ($0.3\,\text{fb}^{-1}$), hence we decided to treat it together with the 2016 dataset. Hereafter, for simplicity, we refer to the whole 2015–2016 data-taking period as the 2016 sample.

5.1 Definitions of main variables

Before delving into the specifics of the selection process, it is useful to define various variables and concepts utilized in the LHCb trigger system and the offline selection presented in this thesis. The topology of our signal decays is sketched in Fig. 5.1 and briefly described in Sec. 4 (data-sample).

Primary vertex (PV) The PV represents the vectorial location (with respect to the LHCb coordinate system) of the reconstructed primary pp interaction. When emphasizing its vectorial nature, it is denoted as $\overrightarrow{\text{PV}}$. Multiple primary vertices may be produced in a pp collision, but single interaction events are the most common at the LHCb interaction point during Run 2. Particles are assigned to the PV that minimizes χ^2_{IP} (explained

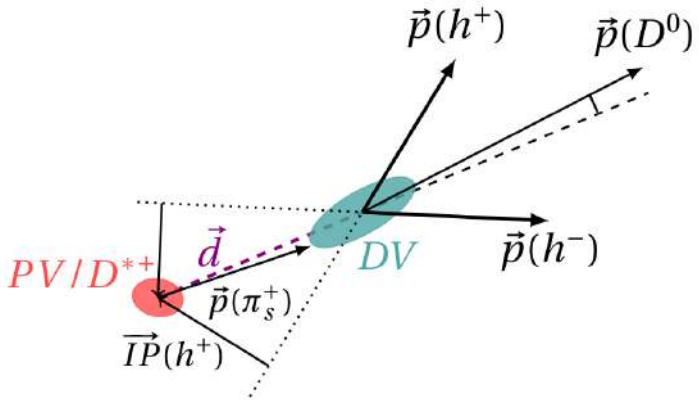

Figure 5.1: A sketch of the topology of a $D^{*+} \to D^0(\to h^+h'^-)\pi_s^+$ decay, with some key trigger variable highlighted.

later on in this section). When referring to the primary vertex associated with a specific particle P, it's denoted as $\overrightarrow{\mathrm{PV}}(P)$. Typically, PV indicates the primary vertex linked with the decay chain of interest, so the P dependency is often omitted.

Decay vertex (DV) The $\overrightarrow{\mathrm{DV}}$ is the vectorial position where a particle decays. In this analysis, the focus is on the D^0 decay vertex $\overrightarrow{\mathrm{DV}}(D^0)$, commonly referred to simply as $\overrightarrow{\mathrm{DV}}$.

Flight Distance (FD) The displacement vector, or flight distance vector, ($\overrightarrow{\mathrm{FD}}$) connects the production vertex to the decay vertex. For a D^0 the displacement vector is:

$$\overrightarrow{\mathrm{FD}}(D^0) = \overrightarrow{\mathrm{DV}}(D^0) - \overrightarrow{\mathrm{DV}}(D^*). \tag{5.1}$$

However, due to the low resolution of the reconstructed D^* vertex $\overrightarrow{\mathrm{DV}}(D^*)$ and the smallness of $\overrightarrow{\mathrm{FD}}(D^*)$, the primary vertex is used instead:

$$\vec{d}(D^0) = |\overrightarrow{\mathrm{DV}}(D^0) - \overrightarrow{\mathrm{PV}}|. \tag{5.2}$$

Thus, the displacement vector can be viewed as the position of the decay vertex in a new reference system, oriented like the LHCb system, but with the origin at the primary vertex. With flight distance (FD) we refer to the magnitude of the displacement vector. For the D^0 meson, given its average momentum of about 60 GeV/c at LHCb, this translates to a γ factor of approximately 40. Consequently, the average flight distance of a D^0 is about 0.5 cm.

Proper decay time Proper decay time is calculated from the relation:

$$\mathrm{FD} = \gamma\vec{\beta}ct = \frac{|\vec{p}|}{m}ct \tag{5.3}$$

Here, c is the speed of light, $|\vec{p}|$ is the particle momentum, m is its mass, and t is its proper decay time. As already mentioned and as will be detailed afterwards, in this analysis the calculation assumes the D^0 is produced at the PV. The proper decay time is often measured in units of τ, the particle's mean lifetime. For the D^0, $\tau \simeq 0.41\,\text{ps}$.

Direction Angle (DIRA) The DIRA is defined as the angle between the particle's momentum vector and its displacement vector, represented mathematically as:

$$\cos\theta_{\text{DIRA}} \equiv \frac{\vec{p}}{|\vec{p}|} \cdot \frac{\overrightarrow{\text{FD}}}{|\overrightarrow{\text{FD}}|} = \hat{p} \cdot \hat{\text{FD}}, \tag{5.4}$$

where the hat symbol (ˆ) denotes a unit vector.

Impact Parameter (IP) The $\text{IP}_r(P)$ is the shortest distance between the trajectory of the particle P and the reference point $\vec{r}$. If a particle originates from that point, then its IP will be zero, neglecting the experimental resolution. Conversely, the IP is generally non-zero for particles not coming from the reference point. This thesis will primarily focus on IPs relative to the primary vertex, and for simplicity, we omit the reference point in the notation. Additional insights on the IP are provided in Sec. 8.3.3.

Distance of Closest Approach (DOCA) The term DOCA refers to the minimum distance between two particle tracks. If two particles originate from the same spatial point, such as a decay vertex, their DOCA will be zero, neglecting experimental resolution.

Impact parameter χ^2 (χ^2_{IP}) For a given particle th χ^2_{IP} represents the difference in the χ^2 of the fit to the primary vertex with and without the inclusion of that particle. Particles not originating from the PV generally exhibit a larger χ^2_{IP} compared to prompt particles (*i.e.*, particles coming from the PV).

χ^2 distance This term refers to the significance of the separation between two spatial points. Given the estimated position of two spatial points, indicated with $\vec{x}_1$, and $\vec{x}_2$ and their respective covariance matrices, $\boldsymbol{cov}_1$ and $\boldsymbol{cov}_2$, the χ^2 distance between these two points is defined as:

$$(\vec{x}_1 - \vec{x}_2)^T (\boldsymbol{cov}_1 + \boldsymbol{cov}_2)^{-1} (\vec{x}_1 - \vec{x}_2). \tag{5.5}$$

Flight Distance χ^2 (χ^2_{FD}) This is the χ^2 distance calculated between the primary vertex, $\overrightarrow{\text{PV}}$, and the decay vertex, $\overrightarrow{\text{DV}}$, associated with a given particle. Essentially, it measures the significance of the displacement vector being non-zero.

PIDK Also known as $\text{DLL}_{K\pi}$, the PIDK represents the difference between the logarithms of likelihoods for the kaon and pion hypotheses. A higher PIDK value suggests a greater likelihood of the particle being a kaon. More detail on this can be found in Sec. 3.4.2.

Track χ^2/ndf This is the normalized χ^2 of the track trajectory fit, where ndf stands for the number of degrees of freedom. It is employed to assess the quality of the track fit and helps to reject fake tracks, and therefore combinatorial background.

Track Ghost Probability ($\mathcal{P}_{\text{ghost}}$) This metric is derived from a multivariate classifier trained to differentiate between genuine tracks and spurious ones that do not correspond to an actual particle [73]. The primary cause of such *ghost* tracks is the erroneous association of hits from different tracks. These tracks, especially those formed by incorrectly associating segments in the VELO and T-stations from different particles, are significant sources of background in this analysis. Another minor cause of ghost tracks is the lingering detector signal from real tracks of past events, known as *spillover*.

Decay Tree Fitter (DTF) The DTF is an algorithm that refits candidates' trajectories offline [71]. Specifically, it is applied in this analysis to constrain the D^0 meson and the soft pion to originate from the primary vertex, enhancing mass resolution and aiding in better background rejection. Variables derived from this constrained refit are indicated with the DTF subscript. If the refit is unsuccessful, the candidate is excluded from the offline selection.

Δm The Δm observable is the mass difference between $m(D^*)$ and $m(D^0)$, where

$$\begin{aligned} m(D^*) &= m(K\pi\pi_s) \\ &= \sqrt{E_{D^*}^2 - |\vec{p}_{D^*}|^2} \\ &= \sqrt{(E_K + E_\pi + E_{\pi_s})^2 - |\vec{p}_K + \vec{p}_\pi + \vec{p}_{\pi_s}|^2} \\ &= \sqrt{\left(\sqrt{m_K^2 + |\vec{p}_K|^2} + \sqrt{m_\pi^2 + |\vec{p}_\pi|^2} + \sqrt{m_\pi^2 + |\vec{p}_{\pi_s}|^2}\right)^2 - |\vec{p}_K + \vec{p}_\pi + \vec{p}_{\pi_s}|^2}, \end{aligned} \tag{5.6}$$

and

$$\begin{aligned} m(D^0) = m(K\pi) &= \sqrt{E_D^2 - |\vec{p}_D|^2} \\ &= \sqrt{(E_K + E_\pi)^2 - |\vec{p}_K + \vec{p}_\pi|^2} \\ &= \sqrt{\left(\sqrt{m_K^2 + |\vec{p}_K|^2} + \sqrt{m_\pi^2 + |\vec{p}_\pi|^2}\right)^2 - |\vec{p}_K + \vec{p}_\pi|^2}. \end{aligned} \tag{5.7}$$

A portion of the uncertainties on the D^0 mass cancels out in the difference, allowing the Δm observable to have a much better mass resolution than $m(D^*)$. For further discussions see Sec. 6.1.1.

Corrected mass (m_{corr}) It is defined as

$$m_{\text{corr}}(h^+, h^-) \equiv \sqrt{m^2 + p_{Tmis}^2} + |p_{Tmis}|, \tag{5.8}$$

where p_{Tmis} is the missing momentum in the transverse plane to the displacement vector. This variable is designed for decays with undetected (*e.g.* out of the acceptance) or undetectable (*e.g.* semileptonic decay) particles, in order to be a better proxy of the mass of the mother particle. In the $D^0 \to K^{\pm}\pi^{\mp}$ case m_{corr} will be equivalent to the invariant mass, within the experimental resolution, hence the requirement on the corrected mass ($m_{corr} > 1\,\text{GeV}/c^2$) applied at the HLT1 level, always holds because the D^0 mass ($\sim 1.8\,\text{GeV}/c^2$) is greater than the value of the chosen threshold.

Trigger On Signal (TOS) TOS events are those where the trigger activation is caused by a particle within the signal decay chain itself. In other words, the trigger is fired due to one of the particles involved in the decay process. An illustrative example of TOS is provided in Fig. 5.2, where a pion fires the `L0Hadron` trigger.

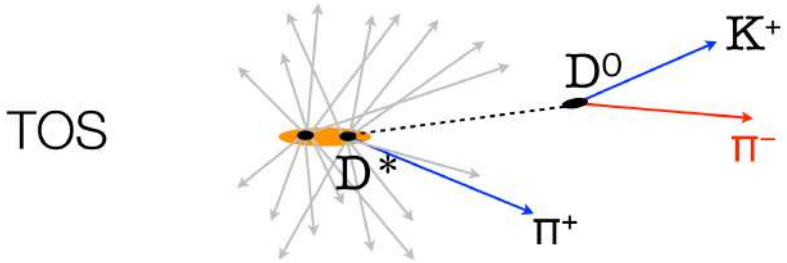

Figure 5.2: Illustration of a TOS events: the π^- (shown in red) triggers the `L0Hadron` trigger line.

Trigger Independent of Signal (TIS) In contrast, TIS refers to events where the trigger is activated independently of the signal decay chain. This means that the trigger is set off by particles unrelated to the signal of interest. An example is depicted in Fig. 5.3, where a muon from a different decay process activates the `L0Muon` trigger line, unrelated of the presence of the $D^{*+} \to D(\to K^+\pi^-)\pi^+$ signal.

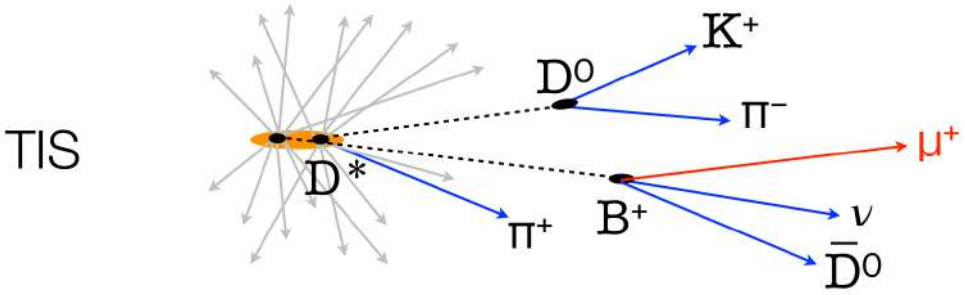

Figure 5.3: Illustration of a TIS events: a muon (shown in red), coming from a decay chain different from the signal one, triggers the `L0Muon` trigger line.

5.2 Trigger selection

This section describes the trigger requirements at the hardware level (L0) and at the software level (HLT).

5.2.1 Hardware trigger (L0)

The thresholds for the main L0 physics trigger lines are outlined in Tab. 5.1. The L0 hadronic trigger line (`L0Hadron`) is designed to select b- and c-hadron events, and its decisions are based on the transverse energy of reconstructed clusters. The threshold for transverse energy ($E_T \gtrsim 3.7\,\text{GeV}$) is significantly higher than the HLT2 requirement for the D^0 meson's transverse momentum ($p_\text{T}(D^0) > 1\,\text{GeV}/c$). Due to the approximate method used to calculate the transverse energy of hadrons at the L0 level, a considerable number of events with D^0 mesons having transverse energy above the threshold still do not get selected by the `L0Hadron` line. Consequently, only about 42% of the $D^0 \to K^\pm\pi^\mp$ decays reconstructed by the HLT fired the L0 hadronic trigger. All the other are triggered by other particles in the events. Only a very loose selection is imposed at the L0 level to prevent a significant loss of signal yields. This approach is viable as the measurement is based on the yield ratio of two nearly identical final states. The robustness of the measurement against the L0 selection is examined in Sec. 9.2. The used criteria at the L0 level include:

$$\texttt{Dst\_L0AllPhysLines\_TIS} \,||\, \texttt{D0\_L0Hadron\_TOS},$$

where `Dst_L0AllPhysLines_TIS` is defined as the logical `OR` of all the L0 Level physics lines. After all offline selection about 42% of the events are triggered on signal using calorimeter information (`D0_L0Hadron_TOS`), 69% are triggered independently of signal (`Dst_L0AllPhysLines_TIS`), and 11% of the events are triggered simultaneously on signal and independently. Thresholds of the L0 requirements for the main physics lines are shown in Tab. 5.1.

5.2.2 First-stage software trigger (HLT1)

In Run 2, it is required that one of the particles coming from the decay of the D^0 fired `Hlt1TrackMVA` trigger line or that the combination of the two particles fired the `Hlt1TwoTrackMVA` trigger line. Four sets of thresholds were used for the two lines during Run 2. These sets are labelled by the following letters and correspond to:

(a) about 30% of the 2016 sample;

(b) about 5% of the 2016 sample;

(c) about 25% of the 2016 sample;

(d) about 40% of the 2016 sample and the full 2017–2018 sample.

The requirements of the two lines are listed in Tab. 5.2.

TCK	0x00a2	0x00a3	0x00a8	0x1603	0x1604	0x1605	0x1609	0x160e
L0Hadron E_T [MeV]	3600	3096	4008	3216	3552	3696	3696	3696
L0Photon E_T [MeV]	2688	2280	2688	2304	2784	2976	2832	2976
L0Electron E_T [MeV]	2688	2280	2688	2112	2256	2592	2352	2592
L0Muon p_T [MeV/c]	2800	2400	2800	1100	1300	1500	1300	1500
L0DiMuon $\sqrt{p_{T1}p_{T2}}$ [MeV/c]	1300	1300	1300	1000	1200	1300	1300	1300
SumEtPrev E_T [GeV]	—	—	—	—	—	—	—	—
Fraction of events [%]	2.5	1.4	1.1	0.8	0.5	1.3	12.4	0.9

TCK	0x160f	0x1611	0x1612	0x1702	0x1703	0x1704	0x1705	0x1706
L0Hadron E_T [MeV]	3744	3888	3888	2976	3216	3552	3696	3888
L0Photon E_T [MeV]	2784	2976	2974	2112	2304	2784	2976	3072
L0Electron E_T [MeV]	2400	2616	2616	1872	2112	2256	2592	2688
L0Muon p_T [MeV/c]	1800	1500	1600	700	1100	1300	1500	1900
L0DiMuon $\sqrt{p_{T1}p_{T2}}$ [MeV/c]	1500	1400	1500	900	1000	1200	1300	1800
SumEtPrev E_T [GeV]	—	—	—	24	24	24	24	24
Fraction of events [%]	10.0	0.7	1.5	0.1	0.6	0.5	2.1	0.4

TCK	0x1707	0x1708	0x1709	0x17a7	0x1801	0x18a1	0x18a2	0x18a4
L0Hadron E_T [MeV]	3720	3216	3456	3720	3792	3792	3792	3792
L0Photon E_T [MeV]	2712	2304	2472	2712	2952	2952	2952	2952
L0Electron E_T [MeV]	2304	2112	2112	2304	2376	2376	2376	2376
L0Muon p_T [MeV/c]	1700	1100	1400	1700	1750	1750	1750	1750
L0DiMuon $\sqrt{p_{T1}p_{T2}}$ [MeV/c]	1800	1000	1300	1800	1800	1800	1800	1800
SumEtPrev E_T [GeV]	24	24	24	24	24	24	24	24
Fraction of events [%]	10.8	5.4	11.5	0.1	14.8	>0.1	14.2	6.4

Table 5.1: Thresholds of the L0 requirements for the main physics lines. For every configuration of the thresholds, identified by the *Trigger Configuration Key* (TCK) and represented as a column, the selected fraction of signal events with respect to the whole sample (after the full event selection) is displayed as well. Additional requirement on the number of SPD hits to avoid events with a high number of tracks and high ghost rate: $n_{SPD} < 900$ for the L0DiMuon line, $n_{SPD} < 450$ for the other ones. The requirement on SumEtPrev, defined as the sum of the transverse energy of all HCAL L0 clusters in the previous bunch crossing, is applied to all lines other than L0DiMuon.

Single track HLT1 line The HLT1TrackMVA trigger line selects a single detached, high momentum, good quality, long track that could identify an heavy flavour hadron. The quality of the tracks is ensured by:

- requiring tracks to be long tracks with a minimum number (9) of hits on VELO;
- requirement on the track fit $\chi^2/\text{ndf} < 2.5$;
- requirement on ghost probability: the threshold of this cut has varied in data acquisition time, however for most of the data-set $\mathcal{P}_{\text{ghost}}(h^\pm) < 0.2$, where $h^\pm$ identifies the decay product of the D^0 (either $K^\pm$ or $\pi^\pm$).

Momentum requirement also has been varying during data acquisition time, but most of the dataset is selected with $p(h^\pm) > 5\,\text{GeV}/c^2$.
In order to ensure the displacement from the PV (the D^0 decay product must come from a DV) and to further ask for higher momenta a multivariate request, involving $p_T(h^\pm)$

and $\chi^2_{\rm IP}(h^\pm)$, is done:

$$\{p_{\rm T} > 25. \wedge \chi^2_{\rm IP} > 7.4\} \vee \left\{[1. < p_{\rm T} < 25.] \wedge \left[\ln\chi^2_{\rm IP} > \ln 7.4 + \frac{1}{(p_{\rm T} - 1.)^2} + \alpha\left(1. - \frac{p_{\rm T}}{25.}\right)\right]\right\}, \tag{5.9}$$

where $\chi^2_{\rm IP}$ designates the minimum $\chi^2_{\rm IP}$ concerning any of the primary vertices, the momentum is expressed in GeV/c units, and α is a constant equal to 1.1, 1.6 and 2.3 for (a,d), (b) and (c) sub-samples, respectively. The region of the $\chi^2_{\rm IP}$–$p_{\rm T}$ plane selected by Eq. 5.9 is represented in Fig. 5.4. A D^0 candidate is considered TOS on the `Hlt1TrackMVA` trigger line if at least one of the decay products (either $K^\pm$ or $\pi^\pm$) fires the trigger.

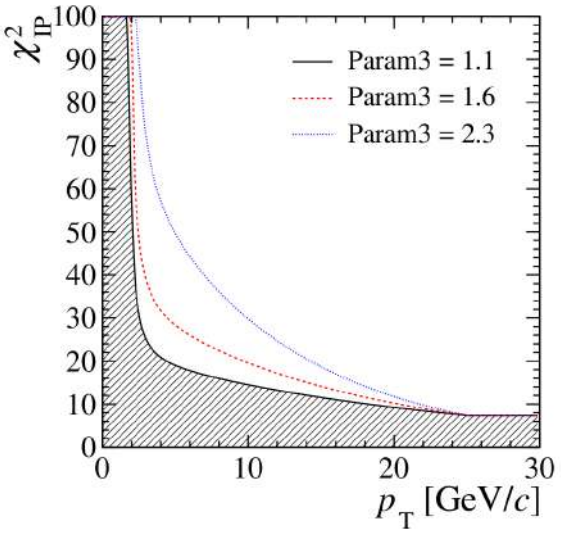

Figure 5.4: Boundary of the region of the track $\chi^2_{\rm IP}$ *vs.* $p_{\rm T}$ plane selected by the `Hlt1TrackMVA` line, for the three different values of α. The shaded area is excluded when $\alpha = 1.1$.

Two tracks HLT1 line The `Hlt1TrackMVA` trigger line is designed to select a combination of two good-quality long tracks compatible with the hypothesis of having originated in the same vertex. Quality and momentum cuts are the same of the single tracks trigger `Hlt1TrackMVA`. In contrast, the requirements on $p_{\rm T}$ and $\chi^2_{\rm IP}$ are loosened: this corresponds to a rectangular cut with $\chi^2_{\rm IP}(h^\pm) > 4$ and $p_{\rm T}(h^\pm) > 500 - 600$ MeV/c, with the threshold that has been changed during the data-taking.
In addition to those requests on the decay products, other constraints on their combinations are added, in particular, the two tracks should originate from the same decay vertex, enforced requiring the two tracks vertex fit $\chi^2/{\rm ndf} < 10$ and a cut is applied to the output of a bonsai boosted decision tree [74] that takes as input the following variables:

1. χ^2 distance between the PV and the two-tracks vertex (abbreviated as flight distance χ^2, or $\chi^2_{\rm FD}$);
2. sum of the $p_{\rm T}$ of the two tracks, $p_{\rm T}$ (h^+) + $p_{\rm T}$ (h^-);

3. number of tracks with $\chi^2_{\text{IP}} < 16$;
4. χ^2 of the vertex fit of the two tracks.

5.2.3 Second-stage software trigger (HLT2)

At the HLT2 level, $D^{*+} \to D^0$ ($\to h^\pm h^\mp$) π_s^+ decays are selected by the `Hlt2CharmHadDstp2D0PipD02xxTurbo` lines, where `xx` stands for `KpPim`, `KmPip` or `KmKp`, corresponding to the RS, WS and KK[1] decay channels, respectively. These are exclusive trigger lines that target $D^{*\pm} \to D^0(\to h^+h'^-)\pi^\pm$ decay chain, where h and h' are either kaons or pions. All lines share the exact requirements, except those on the particle identification (PIDK) information of the hadrons coming from the D^0 meson decay. The list of HLT2 requirements is reported in Tab. 5.2.
The requirements include finding three long tracks of good quality, each with track fit χ^2/ndf < 3. The D^0 candidates are constructed by pairing particles that meet the following conditions:

- not originating from the PV: $\chi^2_{IP} > 4$;
- high momentum and transverse momentum: $p > 5\,\text{GeV}/c$ and $p_T > 800\,\text{MeV}/c$;
- identified as pions or kaons based on PIDK: considered as pions if PIDK < 5, and as kaons otherwise;
- high-quality vertex: D^0 vertex fit $\chi^2/\text{ndf} < 10$, $\chi^2_{\text{FD}} < 25$ and DOCA< 0.1 mm;
- the reconstructed D^0 should come from the PV: $\theta_{\text{DIRA}} < 17.3$ mrad[2];
- the invariant mass of the reconstructed D^0 meson ($m(K\pi)$) must be close to the known D^0 mass (1863.83 MeV/c^2)): $m(K\pi) \in [1712, 2015]\,\text{MeV}/c^2$.

Additional criteria are applied to the third track (π_s), primarily concerning its momenta: $p(\pi_s) > 1\,\text{GeV}/c$ and $p_T(\pi_s) > 100 - 200\,\text{MeV}/c$. The threshold for the latter was set at 100 MeV/c in 2015-2016 and increased to 200 MeV/c in 2017-2018. This cut significantly reduces background, as detailed in Sec. 5.3.
Minimal requirements are also placed on the combination of the three tracks:

- the reconstructed D^* vertex must be of high quality: D^* vertex fit $\chi^2/\text{ndf} < 25$;
- the invariant mass of the reconstructed D^* ($m(K\pi\pi_s)$) should be near the known D^* mass (2010.27 GeV/c^2). Rather than setting a direct limit on $m(K\pi\pi_s)$, a constraint on Δm is preferred due to its superior mass resolution: $\Delta m \in [130, 160]\,\text{MeV}/c^2$.

5.3 Offline selection

Additional requirements are imposed offline to further increase the purity of the data sample. Each requirement is designed to reduce as much as possible the contribution from one (or more than one) known background or to diminish the impact of sources of

[1] This decay channel will be used for the subtraction of the instrumental asymmetry bias. More details can be found in Sec. 7.2.
[2] This requirement significantly reduces contamination from secondary decays while having minimal impact on signal prompt decays.

systematic uncertainties while keeping high signal efficiency. This section motivates and details all the requirements, which are finally summarized in Table 5.2.

5.3.1 Secondary D^{*+} decays

Secondary D^* decays, which are not promptly generated in the primary pp interaction vertex, but in the decay of a b-hadron, are reduced to a few per cent by requiring $\mathrm{IP}(D^0) < 60\,\mu\mathrm{m}$, while keeping a very high efficiency on the signal (about 99%, estimated with simulated sample). This requirement takes advantage of the fact that promptly produced D^* have a zero impact parameter (neglecting the measurement resolution), while secondary D^* generally have a non-zero impact parameter. Figure. 5.5 shows the D^0 impact parameter distribution of a data sample subset where it is easy to identify the prompt D^* component bulk around 0, and the long secondary D^* tail. This selection is applied in order to reduce the bias on the D^0 decay time and the deformation of the $m(D^0\pi_\mathrm{s})_\mathrm{DTF}$ distribution. The removal of the bias associated with this background is a complex subject that is described in detail in Sec. 8.

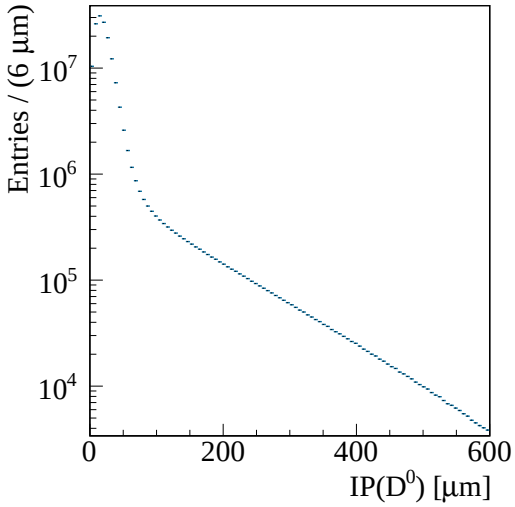

Figure 5.5: Distribution of the reconstructed D^0 impact parameter $\mathrm{IP}(D^0)$ for a subset RS candidates.

5.3.2 Hadrons from interactions with RF foil

The following fiducial requirement

$$R_{xy} < 5\,\mathrm{mm} \quad \text{and} \quad |z(\mathrm{DV})| < 200\,\mathrm{mm}, \tag{5.10}$$

where $z(\mathrm{DV})$ is the z coordinate of the DV of the D^0 meson and

$$R_{xy} \equiv \sqrt{(x_\mathrm{DV} - x_\mathrm{PV})^2 + (y_\mathrm{DV} - y_\mathrm{PV})^2} \tag{5.11}$$

is the distance between its DV and PV in the plane transverse to the beam, is used to reject a very small contamination (about 0.02% of RS sample) of D^0 candidates that are produced in the interaction of other hadrons with the RF foil that protects the VELO, and which decayed soon after that. Such a requirement also rejects the D^0 candidates that originated in the two oval regions on the right and the left of the nominal collision point of the proton bunches in Fig. 5.6.

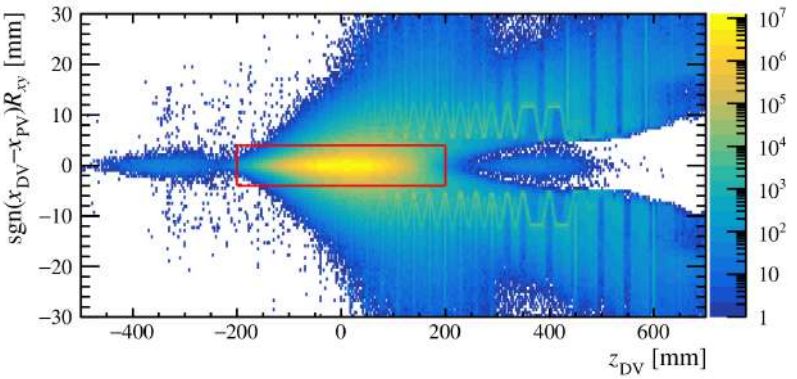

Figure 5.6: Signed radial distance of the DV of the D^0 meson to its PV, as defined in Eq. 5.11, *vs.* its z coordinate. Vertical lines corresponding to VELO sensors and the wavy shape of the shielding RF foil are visible in the region $R_{xy} > 5\,\mathrm{mm}$. Only the candidates within the red rectangle are selected. This is the distribution of an unfiltered subsample of RS candidates. Applying all the offline requirements already removes most of the background outside the red box.

5.3.3 Misidentified decays

The PID requirement for the pions coming from the D^0 decay is tightened from $\mathrm{PID}K(\pi^\pm) < 5$ to $\mathrm{PID}K(\pi^\pm) < -5$, to reduce the background from misidentified $D^0 \to K^+K^-$ decays. The same requirement for kaons is instead left unchanged compared to the HLT2 value, $\mathrm{PID}K(K^\pm) > 5$ (see Tab.5.2). In addition to PID requirements, the D^0 reconstructed invariant mass, $m(K\pi)$, must lie within $24\,\mathrm{MeV}/c^2$ ($\sim 3\sigma$) from the D^0 mass. All these requirements are standard and are used in many charm measurements with two-body h^+h^- decay modes.

In addition to them, however, the analysis of highly suppressed WS decays requires particular attention to a 'peaking background' from $D^0 \to K\pi$ decay where the identification of the two hadrons is swapped (double misidentification). In order to suppress this type of background we require the D^0 mass computed with the swapped K/π mass assignment, $m(K\pi)_{\mathrm{swap}}$, not to lie within $16\,\mathrm{MeV}/c^2$ ($\sim 1.5\sigma$) from the nominal D^0 mass. This requirement removes 11% of the signal sample while removing more than 80% of the double mis-ID background, making the residual background negligible, as shown in Sec. 7.3. Figure 5.7 shows the 2D distribution of the D^0 mass of WS candidates with the correct mass assignment *vs.* with the inverted mass assignment, when offline selection (except for the requirement on the D^0 mass) is applied to D^{*+} sideband subtracted candidates.

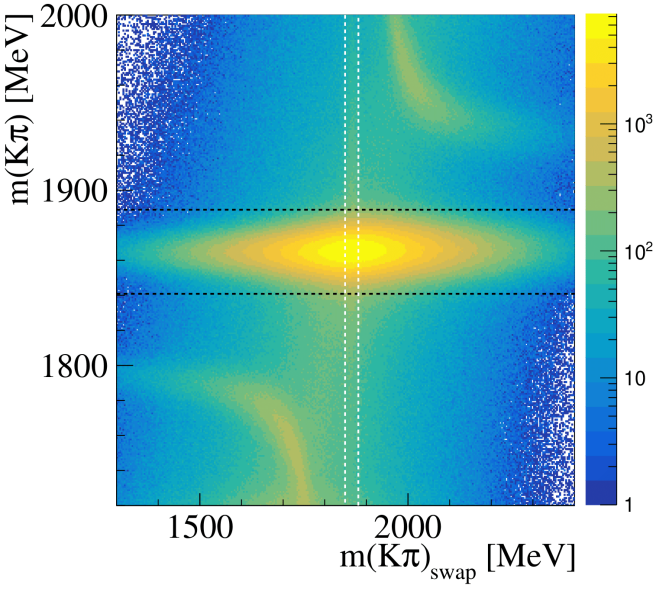

Figure 5.7: D^0 mass distribution with the standard K/π mass assignment versus the D^0 mass distribution with the swapped K/π mass assignment for the WS candidates. Offline selection (except requirement on $m(K\pi)$ and $m(K\pi)_{\text{swap}}$) are applied to D^{*+} sideband subtracted candidates. The black and white dashed lines show the border of the excluded region.

5.3.4 Misreconstructed and clone tracks

A track is defined as a 'clone track' if it is a sub-track or a copy of another track. A small number (about 0.25% of RS candidates) of clone tracks are removed with a selection based on the Kullback–Liebler distance [75]:

$$\texttt{TRACK\_CloneDist}(K, \pi, \pi_s) > 5000. \tag{5.12}$$

This distance gives a measure of the difference in information content between two tracks: if this distance is small then two tracks are likely to be clones. The estimated signal inefficiency of this requirement for the RS signal is 0.08%[3].

In addition to the requirement above, different types of clone tracks are suppressed by looking at the track directions in the 3D space, and at the values of reconstructed momenta. For instance, we have found a tiny fraction (about 0.001% of RS candidates) of clone tracks that share the same VELO-track segment and are reconstructed simultaneously as a kaon, a pion or a π_s. As shown in Fig. 5.8, they form a sharp peak at zero in the angle between their directions and therefore can be easily rejected by requiring

$$\theta[\vec{p}(p_1), \vec{p}(p_2)] > 0.001\,\text{rad}. \tag{5.13}$$

Another small sample of clone tracks (about 0.05% of RS candidates) that share the same

[3]The final uncertainty on the direct asymmetry A_D is about 0.6%, Hence even if this requirement would turn up to be very charge asymmetric, this would produce a negligible bias.

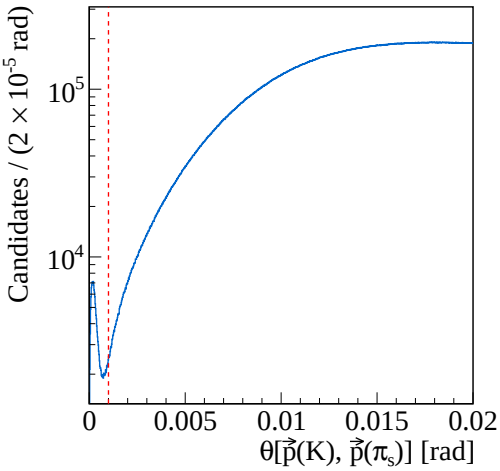

Figure 5.8: Angle between the momenta of the kaon and the π_s. The cut of Eq. 5.13, which rejects the clones concentrated near zero, is displayed.

T-track segment and are reconstructed both as a kaon and as a π_s is found in the space of the asymmetry of their momenta *vs.* the angle between their directions (Fig. 5.9). This sample is rejected by requiring,

$$0.026 \cdot \frac{p(\pi_s^+) - p(K^\pm)}{p(\pi_s^+) + p(K^\pm)} < -0.01976 + \theta[\vec{p}(\pi_s^+), \vec{p}(K^\pm)]. \tag{5.14}$$

5.3.5 Multiple candidates

When a single D^0 ($\to K^-\pi^+$) candidate is associated with two (or more) soft pions in order to build multiple D^* candidates, those are called *multiple candidates*. We distinguish between two different types of multiple candidates. If the two (or more) soft pions share the same charge, the D^* candidates will be triggered by the same HLT2 line (either WS or RS). Instead, if the soft pions have opposite charges, the same D^0 will appear both in the WS and RS dataset.

Multiple candidates in the same HLT2 line

The `totCandxD0` variable returns for each D^0 candidate, the number of D^* candidates in a given HLT2 line (hence separately for WS and RS) that are built using that D^0. The sub-set of $D^{*\pm}$ candidates with `totCandxD0` > 1 has a worse signal-to-noise ratio, as shown in Fig. 5.10, because at most one of the D^{*+} candidates come from a real signal event. Moreover, the sub-sample of RS candidates with `totCandxD0` > 1 is also enriched of ghost candidates: D^0 mesons from true RS decays associated with fake pion tracks which share the VELO track segment with the true soft pion[4]. Thus, candidates with

[4]Also a tiny fraction of the sub-sample of WS candidates with `totCandxD0` > 1 is due to ghost soft pions. However, WS decays are much rarer, and most of this sub-sample is made of combinatorial background.

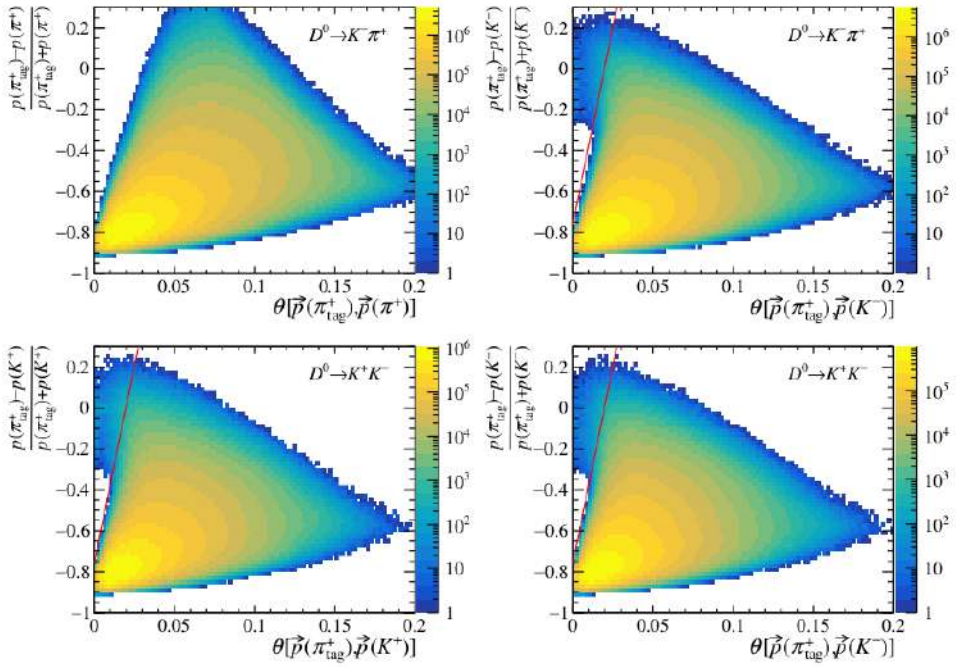

Figure 5.9: Asymmetry and angle between the momenta of one of the two hadrons coming from the decay of the D^0 and π_s for (top) RS and (bottom) KK D^0 decays. The cut of Eq. 5.14, which rejects the clones concentrated near the point (0,0), is displayed wherever applied. Figure from LHCb internal Ref. [76].

`totCandxD0` > 1 are removed from both WS and RS samples. They constitute 9.5% of all the WS candidates and 6.5% of all the RS candidates. The total number of candidates consists of both signal and background. The signal-to-background ratio is different for WS and RS and the previous requirement has different efficiency for signal and background, explaining the different fractions.

Any requirement of the analysis, in general, might have a different efficiency for RS and WS decays. All these effects are collectively included in the instrumental asymmetries, which are corrected in Sec. 7.2.

Multiple candidates in different HLT2 lines

A D^0 meson candidate can be simultaneously used in the reconstruction of a RS and a WS D^* candidate, and this is likely due to the simultaneous association of a genuine D^0 with its true soft pion and with a random or ghost soft pion. Figure 5.11 (Left) shows the 2D distribution of D^* mass computed using WS versus RS soft pion associated to those D^0 candidates that are reconstructed both in the WS and RS HLT2 lines. Due to the abundance of RS decays compared to WS ones, those are likely to be genuine RS candidates instead of WS ones. They are, therefore, removed from the WS sample if the value of $m(D^0\pi_s)_{\rm DTF}$ of the reconstructed RS candidates is within 0.9 MeV/c^2 (3σ) from the D^* mass. This sub-sample is called "common" sample, and it is shown in Fig. 5.11 (Right) and accounts for about 15.8% of the WS sample. From this subsample, we can disentangle the component of ghost soft pions and the one of combinatorial background.

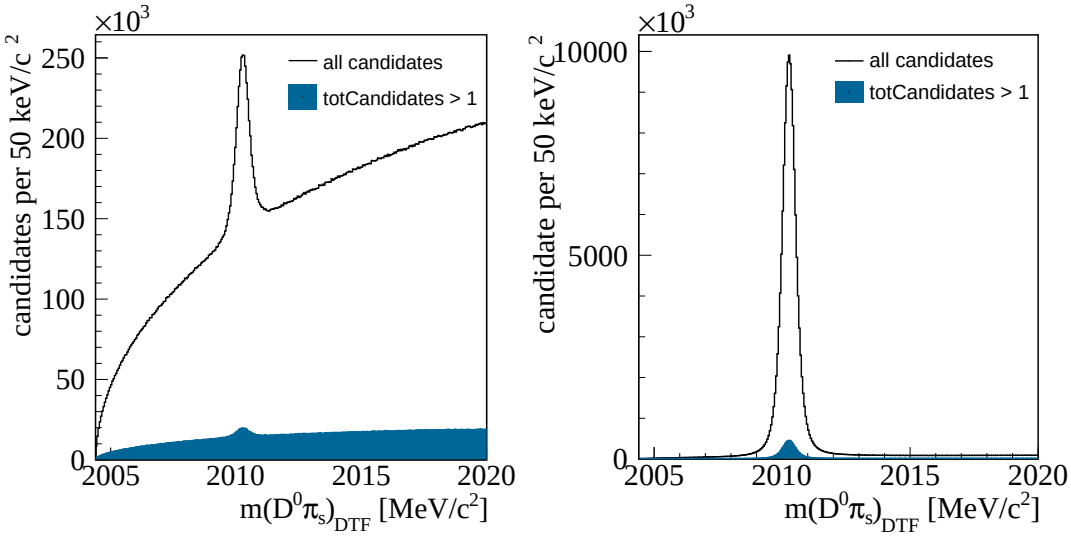

Figure 5.10: Distribution of $m(D^0\pi_s)_{\rm DTF}$ for WS (Left) and RS (Right) candidates (satisfying all offline selection) with `totCandidates` ≥ 1 (open) and `totCandidates` > 1 (filled).

The first one is then used in the WS-to-RS ratio fit to over-constrain the mass shapes of this background. More detail on this sub-sample can be found in Sec. 5.4.

5.3.6 Ghost soft pions background

Soft pions that, after crossing the VELO, go outside the T-station acceptance, can be wrongly reconstructed by associating a genuine VELO segment with a 'wrong' T-track to form a fake 'ghost' long track. The removal of the "common" sample, described in the previous sub-section, unfortunately, does not reject these ghost soft pions, which contaminate our WS signal sample. The D^* (or Δm) mass distribution of D^* candidates reconstructed with these ghost soft pions (combined with genuine D^0 mesons) peaks as the WS signal decays, even if it is much wider, making this background potentially very dangerous. A relevant fraction of this residual ghost background, about 40%, can be, however, removed by requiring high-quality reconstructed soft pions, requiring lower values of the track-based ghost probability variable:

$$\texttt{track-based ghost probability}(\pi_s^+) < 0.1. \tag{5.15}$$

It is possible to further suppress this background by removing soft pions kinematic regions displaying large detection charge asymmetries. After the removal of the common sample, the residual soft ghost pions populate, with very high probability, kinematic regions close to the borders of the LHCb tracking acceptance, which are the same regions where the soft pions generate very large charge asymmetries, up to values of 100%. In analogy with ΔA_{CP} measurement [1], the soft pion is required to be within the fiducial

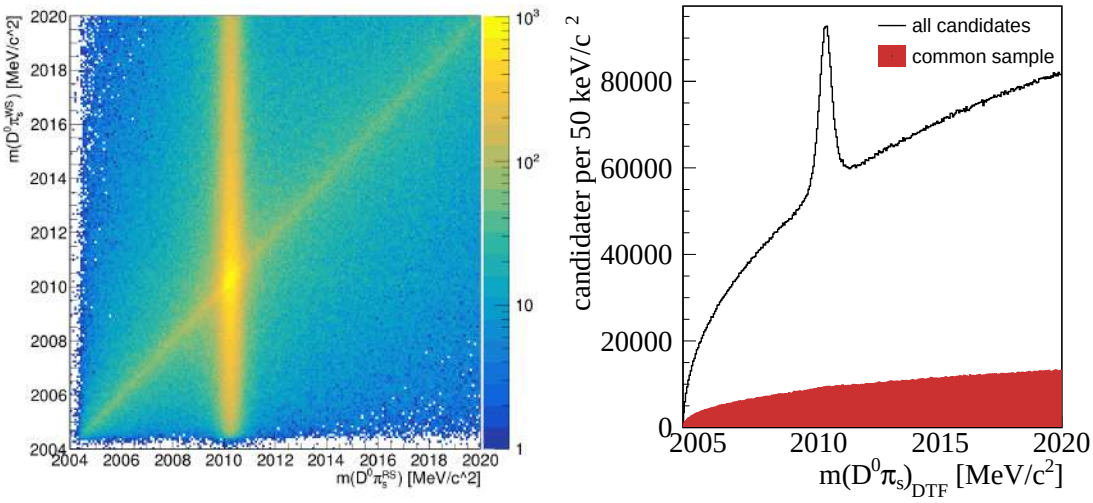

Figure 5.11: (Left) 2D distribution of D^* mass computed using WS versus RS soft pion, for those candidates reconstructed both in the WS and RS HLT2 lines. In this sample, one can identify true RS candidates, true WS candidates (this component here is very faint, Fig. 7.10 show this component in a clearer way), the peak of ghost candidates and combinatorial background. (Right) Distribution of $m(D^0\pi_s)_{\rm DTF}$ for a subset of WS candidates (satisfying all offline selections) with all candidates (open) and the common removed sample (filled).

regions shown in Fig. 5.12 and defined by the following expression,

$$|p_x| < 0.317 \cdot (|p| - 2000) \wedge \left[\left|\frac{p_y}{p_z}\right| > 0.015 \vee |p_x| < 470 - 0.01397 \cdot p_z \vee |p_x| > 430 + 0.01605 \cdot p_z\right], \quad (5.16)$$

where momenta are expressed in MeV/c. An additional relative fraction of about 20% of the ghost soft pions is so removed. This requirement is less stringent than the one utilized in Ref. [1], to avoid rejecting too many signal candidates. Although it has the advantage of removing ghost soft pions, it is also driven by its capacity to remove any possible residual bias from the subtraction of the detection charge asymmetries (see more details in App. B).

Despite the selection optimization process, described above, to reduce as much as possible the fraction of ghost soft pions, a residual contamination of about 1% remains in our final data sample. The size of this contamination is, unfortunately, comparable to the final statistical uncertainty on the R_D parameter, so it must be properly and carefully treated, to avoid having a systematic uncertainty of the same order or greater than the statistical uncertainty on this parameter (see App. A.2).

5.3.7 Combinatorial background

The common sub-sample of RS and WS candidates, described in sec. 5.3.5 and in sec. 5.4, is a pure sample of background (mostly combinatorial background) with extremely similar features of the combinatorial background under WS signal decays. Therefore, by

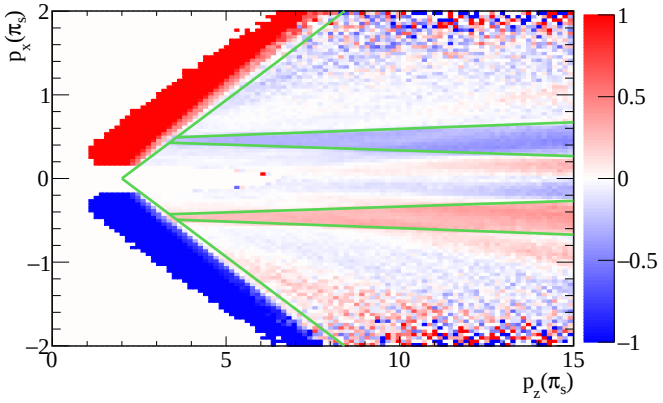

Figure 5.12: Distribution of the raw asymmetry in the (p_x, p_z) plane of soft pions with $\left|\frac{p_y}{p_z}\right| < 0.03$, for the magnet-up polarity for RS candidates reconstructed in 2018 data, as an example. The green lines show the boundaries of the large-asymmetry regions excluded by the fiducial cuts.

comparing distributions of background candidates, belonging to this sub-sample, to the ones of RS candidates selected around the signal peak (almost pure signal), as shown in Fig. 5.13, we added extra requirements on some observables of the soft pion to reject as much as possible background candidates, by keeping very high signal efficiency. They are simple rectangular cuts:

$$p_T(\pi_s) > 200\,\text{MeV}/c, \quad \text{PID}e(\pi_s) < 2, \quad \text{PID}K(\pi_s) < 5, \quad \eta(\pi_s) < 4.3. \tag{5.17}$$

We deliberately avoided using more sophisticated and/or multivariate approaches for two main reasons. The signal-to-background ratio of our sample is very good already at the trigger level, so any further optimization process would not have provided a significant gain in terms of sample purity. Furthermore, the soft pion is a low-momentum reconstructed track and any stringent requirement on it could introduce dangerous and subtle biases, very difficult to keep under control at the desired level of accuracy. This is especially true for biases related to detector-induced charge asymmetries, such as those introduced by requirements on PID variables.

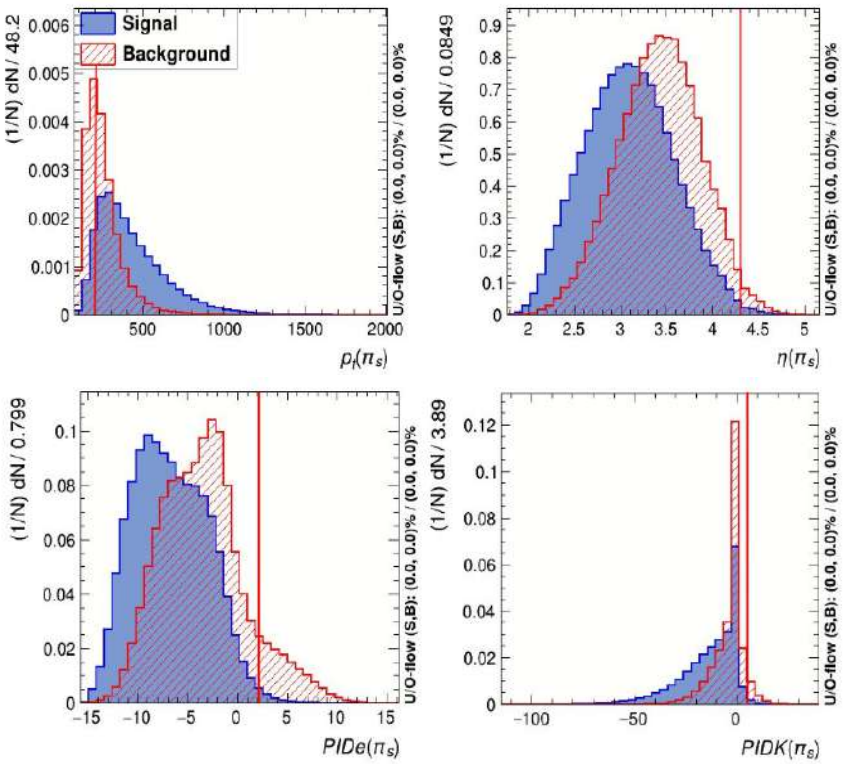

Figure 5.13: Distributions of the selected variables with high separation power for (blue) RS candidates 3σ within the nominal D^{*+} mass (very pure signal sample) and (red) common sample (very pure ghost and combinatorial background). The red lines show the border of the excluded region.

Candidate	Quantity	HLT1TrackMVA	HLT1TwoTrackMVA	HLT2	Offline	Unit
$h^{\pm}$	track χ^2/ndf($h^{\pm}$)	< 2.5	< 2.5	< 3	—	—
	track-based ghost probability ($h^{\pm}$)	$< 0.4^{(a)} - 0.2^{(b,c,d)}$	$< 0.4^{(a)} - 0.2^{(b,c,d)}$	—	—	—
	TRACK_CloneDist($h^{\pm}$)	—	—	—	> 5000	
	$p(h^{\pm})$	$> 3^{(a,b)}$,$5^{c,d}$	$> 3^{(a,b)}$–$5^{(c,d)}$	> 5	-	GeV/c
	$p_{\mathrm{T}}(h^{\pm})$	see Eq. (5.9)	$> 0.5^{(a,b)}$–$0.6^{(c,d)}$	> 0.8	—	GeV/c
	$\chi^2_{\mathrm{IP}}(h^{\pm})$	see Eq. (5.9)	> 4	> 4	—	—
	PID$K(K^{\pm})$	—	—	> 5	> 5	—
	PID$K(\pi^{\pm})$	—	—	< 5	< -5	—
D^0	η(DV − PV)	—	$\in [2, 5]$	—	—	—
	$m_{corr}(h^+, h^-)$	—	> 1	—	—	GeV/c
	Yandex classifier	—	$> 0.95^{(a,b,d)}$,$0.97^{(c)}$	—	—	—
	max[$p_{\mathrm{T}}(h^+)$, $p_{\mathrm{T}}(h^-)$]	—	—	> 1.5	-	GeV/c
	p_{T} (D^0)	—	> 2	> 1	—	GeV/c
	$m(K\pi)$	—	—	$\in [1715, 2015]$	$\in [1840.84, 1888.84]$	MeV/c^2
	$m(K\pi)_{\mathrm{swap}}$	—	—	—	$\notin [1848.84, 1882.84]$	MeV/c^2
	DOCA(h^+h^-)	—	—	< 100	-	µm
	D^0 vertex-fit χ^2/ndf	—	< 10	< 10	—	—
	$\theta_{\mathrm{DIRA}}(D^0)$	—	$\in [0, \pi/2]$	$>$ arccos (0.00173)	—	rad
	$\chi^2_{FD}(D^0)$	—	—	> 25	—	—
	R_{xy}	—	—	—	< 5	mm
	$\lvert z(DV) \rvert$	—	—	—	< 200	mm
	IP (D^0)	—	—	—	< 60	µm
	D^0 decay time	—	—	—	$\in [0.4, 8]$	$\tau(D)$
	D^0 Hlt1*Track*_TOS	—	—	True	—	—
	D^0 Hlt1TrackMVA_TOS || Hlt1TwoTrackMVA_TOS	—	—	—	True	—
π_{s}^+	track χ^2/ndf(π_{s}^+)	—	—	< 3	—	—
	track-based ghost probability (π_{s}^+)	—	—	$< 0.4^{16}, 0.25^{17,18}$	< 0.1	—
	TRACK_CloneDist(π_s)	—	—	—	> 5000	
	p_{T} (π_{s}^+)	—	—	$> 0.1^{16}, 0.2^{17,18}$	> 0.2	GeV/c
	$p(\pi_{\mathrm{s}}^+)$	—	—	> 1	—	GeV/c
	$\lvert p_x/p_z \rvert$, $\lvert p_y/p_z \rvert$	—	—	—	see Eq. 5.16	
	$\eta(\pi_{\mathrm{s}}^+)$	—	—	—	< 4.3	
	PIDe (π_{s})	—	—	—	< 2	
	PIDK (π_{s})	—	—	—	< 5	
D^{*+}	D^{*+} vertex-fit χ^2/ndf	—	—	< 25	—	—
	Δm	—	—	$\in [130, 160]$	—	MeV/c^2
	totCandsD0	—	—	—	$== 1$	—
	DTF χ^2/ndf	—	—	—	> 0	—
	D^{*+} L0AllPhysLines_TIS || D^0 L0Hadron_TOS	—	—	—	True	—
	D^{*+} Hlt2CharmHadD02KPi_TOS	—	—	—	True	—
	$m(D^0\pi_{\mathrm{s}})^{\mathrm{RS}}_{\mathrm{DTF}}$ WS common candidates	—	—	—	∈[2009.37,2011.17]	MeV/c^2

Table 5.2: Selection requirements. The labels “16" and “17,18" refer to different thresholds in the 2016 and 2017–2018 sub-sample. The L0 requirements are described in Sec. 5.2.1

5.4 WS-RS common sample

The sample of WS-RS common candidates, removed from the final data sample, is composed of WS candidates that have the D^0 candidate simultaneously reconstructed as a RS candidate, and with the $m(D^0\pi_s)_{\rm DTF}$ of the RS candidates to be within a 3σ mass window centred around the D^{*+} nominal mass value. The sample of RS candidates selected in this mass window is a very pure sample of $D^{*\pm}$ signal decays,[5] while the WS candidates are reconstructed by associating a D^0 meson candidate with a ghost or random soft pion. For this reason, this sample of WS common candidates is used to model the ghost pion background (see Sec.6.1.5) and to study the shape of $m(D^0\pi_s)_{\rm DTF}$ combinatorial background (see App. A.2). A fraction of the removed sample comprises correctly reconstructed WS decays associated with ghost soft pions. However, this fraction is tiny, as shown in Sec. 7.

The angle formed by the directions of the soft pions of common WS and RS candidates, $\theta(\pi_s^{\rm RS}, \pi_s^{\rm WS})$, easily allows the two different sources of backgrounds to be disentangled, as shown in Fig. 5.14. The ghost soft pions form a narrow peak close to zero, while the random slow pions have a much wider distribution centred at higher angle values. The requirement $\theta(\pi_s^{\rm RS}, \pi_s^{\rm WS}) < 1 \times 10^{-3}$ rad is, therefore, used to select a pure

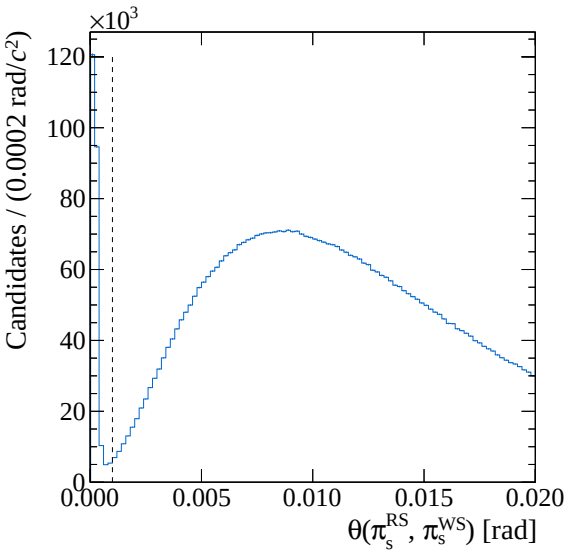

Figure 5.14: Distribution of the angle between common WS and RS soft pions, $\theta(\pi_s^{\rm RS}, \pi_s^{\rm WS})$, in the common candidates of the 2018 sub-sample. The 1×10^{-3} rad threshold is marked by a dashed line.

sample of WS candidates associated with ghost soft pions. This subsample's time-integrated $m(D^0\pi_s)_{\rm DTF}$ distribution is shown in Fig. 5.15 (left). We will refer to this subsample as *common ghost candidates* (CG). The complementary requirement on the angle, $\theta(\pi_s^{\rm RS}, \pi_s^{\rm WS}) > 5 \times 10^{-4}$ rad is, instead, used to select a pure sample of WS candidates associated with random slow pions. This subsample's time-integrated $m(D^0\pi_s)_{\rm DTF}$

[5]The RS candidates are reconstructed by associating a true soft pion with a D^0 meson.

distribution is shown in Fig. 5.15 (right). In the following, we will refer to this sub-sample as *common combinatorial candidates* (CC).

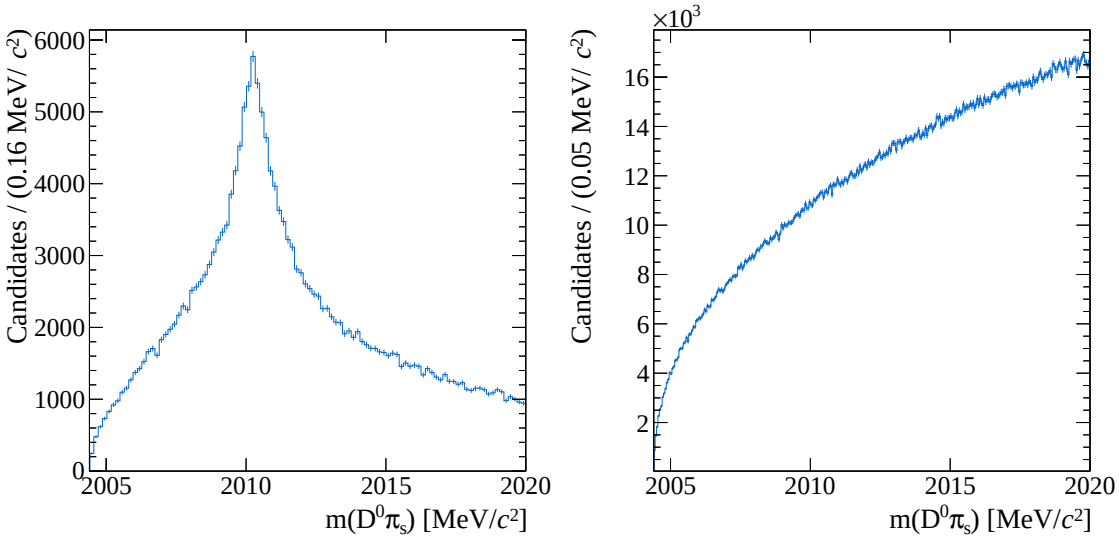

Figure 5.15: Distribution of $m(D^0\pi_s)_{\mathrm{DTF}}$ of the common ghost candidates (left) and common combinatorial candidates (right).

The common ghost candidates, isolated with the procedure described above, can be used as a reliable proxy of the residual ghost candidates. The residual ghost candidates, still present in the final data sample, differ from the common ghost candidates only because the genuine associated RS candidate is not reconstructed. A soft pion that goes through the VELO detector cannot be fully reconstructed either because it goes out of the acceptance due to the magnetic field (T-track is not available) or because it does not pass the HLT2 trigger requirements ($p_{\mathrm{T}}(\pi_s) > 200\,\mathrm{MeV}/c$). The former will be spatially distributed at the border of the geometrical acceptance in the highly asymmetrical regions of the soft pion kinematics. Hence this background is highly reduced by the application of fiducial cuts, as previously explained. Instead, the latter does not constitute a peaking background because the transverse momentum of the ghost soft pion, and consequently its momentum, will necessarily be greater than those of the genuine soft pion. Ghost soft pions producing a peaking D^* mass are those with transverse momentum close to one of the genuine pions. The main difference between common and residual ghost candidates is, therefore, only related to the kinematics: common ghost candidates mainly populate the low-asymmetry region, while residual ghost candidates mainly populate the high-asymmetry region close to the border of the geometrical acceptance. This can produce differences in D^0 decay time correlated with the soft pions kinematics. More studies on residual ghost candidates can be found in App A.

5.5 $D^{*+}\mu^-$ sample

The removal of the residual contamination of secondary D^* decays originating from a b-hadron decay is one the most difficult challenges of the measurement described in this thesis. It is, therefore, very important to have various control data samples (in addition to reliable simulated samples) where secondary decays can be accurately studied. The Turbo Stream allows to *persist*[6] the presence of a muon with opposite electric charge (opposite-sign pair) in the vicinity of the D^* candidate, forming a good vertex originating from the $\bar{B}^0 \to D^{*+}\mu^-\bar{\nu}_\mu X$ decay process. This allows the selection of an almost pure sub-sample of secondary decays, which is used to check the agreement of simulated secondary decays with real data. In addition to the requirements in Tab. 5.2, some extra requests are used to select this sample of semimuonic b-hadron decays and they are reported in Tab. 5.3.

Candidate	Quantity	Online	Offline	Unit
μ^-	track χ^2/ndf	< 4	—	—
	track-based ghost probability	< 0.4	—	—
	$p_T(\mu^-)$	$> 2^{16}, > 0.8^{17,18}$	> 2	GeV/c
	$p(\mu^-)$	> 3	—	GeV/c
	$\chi^2_{IP}(\mu^-)$	> 4	—	—
$D^{*+}\mu^-$	$\cos\theta_{\text{DIRA}}(D^{*+})$	> 0.999	—	—
	$D^{*+}\mu^-$ vertex χ^2/ndf	—	< 6	—
	$m(D^{*+}\mu^-)$	—	$\in [3,5]$	GeV/c^2

Table 5.3: Selection requirements for the secondary decays obtained combining a D^{*+} meson with a `PersistReco` μ^-. the labels "16" and "17,18" refer to different thresholds in the 2016 and 2017–2018 sub-sample, respectively.

This sub-sample is not background-free. A residual combinatorial background of D^{*+} mesons combined with an unrelated μ^-, or another misidentified particle, is removed based on the distribution of the reconstructed invariant mass of the combinations of D^{*+} mesons with muons with the same electric charge (same-sign pairs), $m(D^{*+}\mu^+)$. The ratio of the $m(D^{*\pm}\mu^\pm)$ distribution of opposite-sign pairs to that of same-sign pairs is fitted in the sideband $[5.5 - 8.0]\,\text{GeV/c}^2$ with a linear function. The function is then extrapolated to the signal region. The same-sign pairs in the signal region are assigned a weight equal to the negative of its value to remove the combinatorial background.

[6]This feature is referred to as `PersistReco` and it is used to permanently save on disk extra information to the reconstructed candidate.

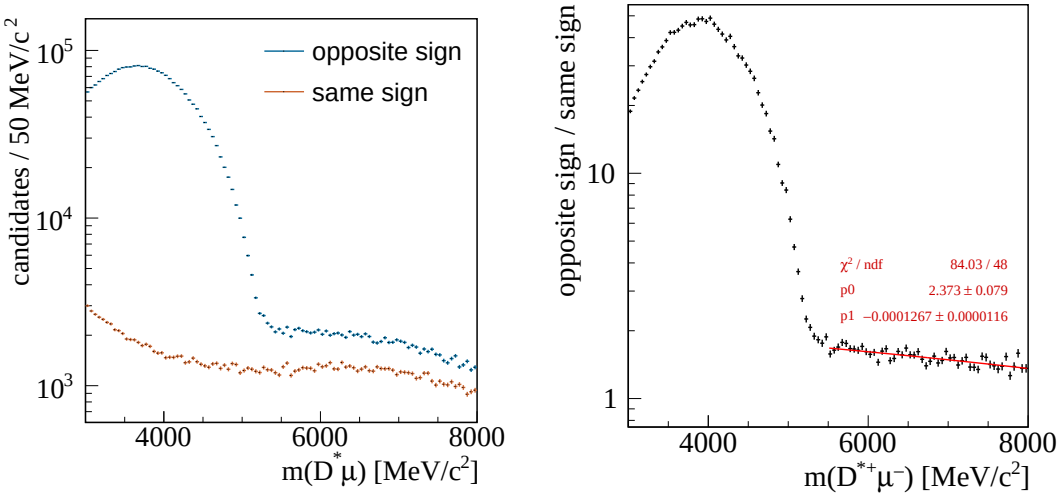

Figure 5.16: Invariant mass distribution of the combination of the D^{*+} meson with a muon with opposite and equal electric charge (left). The ratio between the combination of the D^{*+} meson with a muon with opposite and equal electric charge and the χ^2 fit in the range [5.5, 8] GeV/c^2 of a linear function (right).

5.6 Simulated samples

Simulation is utilized for estimating the magnitude of decay-time bias, determined in Sec. 8. The GAUSS software [77] serves as the LHCb simulation framework, overseeing the generation of simulated events through interactions with various external applications. The event creation follows a specific sequence:

- PYTHIA software [57] generates an event containing the requisite signal particle. This is achieved either by generating minimum bias pp collision events until a corresponding particle is located or by ensuring its production in every event. The resultant event comprises stable or unstable particles.
- The signal particle undergoes decay exploiting the `EvtGen` software [78], leading to the desired final state, while all remaining unstable particles decay independently. In this stage the generation of final-state radiation is incorporated via PHOTOS [79].
- Criteria might be applied to ensure that the signal and its decay products meet generator-level cuts.
- Particle transport through the detector simulation is implemented in GEANT 4 software [80], representing the most time-consuming phase (minutes compared to seconds for the rest).

An unfiltered (i.e. without HLT1 and HLT2 selection) full simulation with adequate statistics demands substantial computational resources and is not currently available for this thesis or future analyses. To expedite the generation of realistic simulated samples, a `ParticleGun` simulation method is employed. Rather than generating a complete PYTHIA event, a single particle is generated, its kinematics tailored to a specified input momentum distribution, and subsequently compelled to decay into the desired final state. This approach increases the speed by approximately a factor of 50. However, the detector resolutions and efficiencies often prove slightly superior compared to those of the full simulation due to the considerably lower detector occupancy.
Four `ParticleGun` simulated samples are produced with the aim of studying the secondary D^* background and decay time biases in the prompt decay reconstruction.

- prompt D^* decays: $D^{*+} \to D^0 \pi_s^+$;
- secondary B^0 decays: $B^0 \to D^{*\pm} (\to D^0 \pi_s^\pm)\ X$;
- secondary B^+ decays: $B^+ \to D^{*\pm} (\to D^0 \pi_s^\pm)\ X$;
- secondary B^0 decays with a persisted muon: $B^0 \to D^{*+} (\to D^0 \pi_s^+)\ \mu^-\ \nu_\mu$;

where the D^0 decays in RS $K\pi$ pair.

The simulation of D^* meson decay consistently applies the VSS model, whereas the decay of D^0 mesons utilizes a phase-space model, directing the decay towards the $K\pi$ final state. The decay channels, branching ratios and decay models used in the simulation of B^0 and B^+ inclusive decays into $D^{*\pm}$ mesons are listed in Tabs. 5.4 and 5.5, respectively. At present time the known Λ_b^0 and B_s^0 decays to $D^{*\pm}$ have negligible branching ratios. However, the presence of unknown processes will be absorbed by an effective correction applied in Sec. 8.5.5. The momentum distribution of the particle at the head of the decay chain is taken from a PYTHIA 8 simulation for $D^{*\pm}$ decays at $\sqrt{s} = 8\,\text{TeV}$ instead of 13 TeV,

to limit computational resource utilization, leveraging the pre-existing availability of the former at the start of this measurement. Subsequently, kinematic weighting techniques are employed to mitigate disparities between simulation outcomes and experimental data, as explained later in this document. This reweighting is still necessary even using the $\sqrt{s} = 13\,\text{TeV}$ spectrum. Instead, both B^0 and B^+ mesons are generated using the B^+ Pythia 8 distribution at $\sqrt{s} = 13$ TeV. After the truth matching procedure and the application of the selection requirements described in the previous sections, the number of selected events is about 130k, 130k, 130k and 40k for each data-taking period, for the prompt sample, the B^0 and B^+ inclusive secondary samples and $D^{*+}\mu^-$ sample, respectively.

The samples of B^+ and B^0 decays are merged, weighting the B^+ events with a factor of 0.19 to account for different generator-level efficiencies and branching ratios. The weight is the product of three factors:

- the B^+-to-B^0 ratio of production cross section in LHCb acceptance[7]

$$\frac{\sigma(pp \to B^+X)}{\sigma(pp \to B^0X)} \sim 1; \tag{5.18}$$

- the B^+-to-B^0 ratio of the inclusive branching fraction

$$\frac{\mathcal{B}(B^+ \to D^*X)}{\mathcal{B}(B^0 \to D^*X)} = \frac{(5.5 \pm 1.2)\%}{(30.0 \pm 1.5)\%} = 0.182 \pm 0.040; \tag{5.19}$$

- the B^0-to-B^+ ratio of generator-level cut efficiencies[8]

$$\frac{\epsilon_{gen}(B^0)}{\epsilon_{gen}(B^+)} = \frac{0.2772 \pm 0.0001}{0.2604 \pm 0.0001} = 1.0645 \pm 0.0006. \tag{5.20}$$

It follows that the applied weight is

$$w(B^+) = \frac{\sigma(pp \to B^+X)}{\sigma(pp \to B^0X)} \times \frac{\mathcal{B}(B^+ \to D^*X)}{\mathcal{B}(B^0 \to D^*X)} \times \frac{\epsilon_{gen}(B^0)}{\epsilon_{gen}(B^+)} = 0.19 \pm 0.04. \tag{5.21}$$

We will refer to this joint sample as *inclusive secondaries simulation* in the following.

In order to improve the agreement between data and simulation, some corrections have been applied (see Sec. 8 for a detailed description):

- injection of realistic primary vertex resolution;
- tuning of decay vertex resolution;
- injection of VELO misalignment as estimated from data;
- tuning of the secondaries' cocktail composition;
- kinematics weighting in the six dimensional observable space: $p_{\text{T}}(D^0)$, $\eta(D^0)$, $\phi(D^0)$, $p_{\text{T}}(\pi_{\text{s}})$, $\eta(\pi_{\text{s}})$ and $\phi(\pi_{\text{s}})$.

[7]Since no measurements of the B^0 cross-section at $\sqrt{s} = 13$ TeV are available to date, it is assumed to be equal to that of the B^+ meson, similarly to what is measured at $\sqrt{s} = 7$ TeV.
[8]The number of saved events is the same for the secondary B^0 and B^+ simulations.

A filtered full simulation of the decays of interest is also available. These simulated events include the full underlying event, however, since the HLT selection is already applied, these samples are not versatile for the tuning that we need to apply.

Decay channel	$\mathcal{B}$ [$\times 10^{-3}$]	EvtGen Model
$B^0 \to D^{*-} e^+ \nu_e$	50.5 ± 1.4	HQET2 1.205 0.908 1.404 0.854
$B^0 \to D^{*-} \mu^+ \nu_\mu$	50.5 ± 1.4	HQET2 1.205 0.908 1.404 0.854
$B^0 \to D^{*-} D_s^{*+}$	17.7 ± 1.4	SVV_HELAMP 0.4904 0. 0.7204 0. 0.4904 0.
$B^0 \to D^{*-} 2\pi^+ \pi^- \pi^0$	17.6 ± 2.7	PHSP
$B^0 \to D^{*-} \tau^+ \nu_\tau$	15.7 ± 0.9	ISGW2
$B^0 \to D^{*-} \pi^+ \pi^0$	15 ± 5	PHSP
$B^0 \to D^{*-} a_1(1260)^+$	13.0 ± 2.7	SVV_HELAMP 0.200 0. 0.866 0. 0.458 0.
$B^0 \to D^{*-} D^*(2007)^0 K^+$	10.6 ± 0.9	PHSP
$B^0 \to D^{*-} D_{sJ}(2457)^+$	9.3 ± 2.2	SVV_HELAMP 0.4904 0. 0.7204 0. 0.4904 0.
$B^0 \to D^{*-} D^{*+} K^0$	(2×) 8.1 ± 0.7	PHSP
$B^0 \to D^{*-} D_s^+$	8.0 ± 2.4	SVS
$B^0 \to D^{*-} 2\pi^+ \pi^-$	7.21 ± 0.29	PHSP
$B^0 \to D^{*-} \rho^+$	6.8 ± 0.9	SVV_HELAMP 0.317 0.19 0.936 0. 0.152 1.47
$B^0 \to D^{*-} \rho^0 \pi^+$	5.7 ± 3.2	PHSP
$B^0 \to D^{*-} D^{*+} K^{*0}$	(2×) 5.0*	PHSP
$B^0 \to D^{*-} D^{*0} K^{*+}$	5.0*	PHSP
$B^0 \to D^{*+} D^- K^0$	4.7 ± 0.4	PHSP
$B^0 \to D^{*-} 3\pi^- 2\pi^+$	4.7 ± 0.9	PHSP
$B^0 \to D^{*-} \pi^-$	2.74 ± 0.13	SVS
$B^0 \to D^{*+} D^0 K^{*+}$	2.5*	PHSP
$B^0 \to D^{*+} D^+ K^{*0}$	2.5*	PHSP
$B^0 \to D^{*+} D^- K^{*0}$	2.5*	PHSP
$B^0 \to D^{*-} D^0 K^+$	2.47 ± 0.21	PHSP
$B^0 \to D^{*-} \omega(782) \pi^+$	2.46 ± 0.18	PHSP
$B^0 \to D^{*-} D^+ K^0$	1.8 ± 0.2	PHSP
$B^0 \to D^{*-} D_{s0}^*(2317)^+$	1.5 ± 0.6	SVS
$B^0 \to D^{*-} p \overline{n}$	1.4 ± 0.4	PHSP
$B^0 \to D^{*-} \pi^+ \pi^- e^+ \nu_e$	1.4 ± 0.5	PHOTOS GOITY_ROBERTS
$B^0 \to D^{*-} \pi^+ \pi^- \mu^+ \nu_\mu$	1.4 ± 0.5	PHOTOS GOITY_ROBERTS
$B^0 \to D^{*-} K^+ \bar{K}^{*0}$	1.29 ± 0.33	PHSP
$B^0 \to D^{*-} \rho^+ \pi^0$	1*	PHSP
$B^0 \to D^{*-} 2\pi^0 \pi^+$	1*	PHSP
$B^0 \to D^{*-} D_{s1}(2536)^+$	0.83 ± 0.20	PHSP
$B^0 \to D^{*-} D^{*+}$	(2×) 0.80 ± 0.06	SVV_HELAMP 0.56 0. 0.96 0. 0.47 0.
$B^0 \to D^{*-} D^-$	0.61 ± 0.16	SVS
$B^0 \to D^{*-} K^+ \pi^- \pi^+$	0.47 ± 0.04	PHSP
$B^0 \to D^{*-} p \overline{p} \pi^+$	0.47 ± 0.05	PHSP
$B^0 \to D^{*-} \pi^0 e^+ \nu_e$	0.4*	PHOTOS GOITY_ROBERTS
$B^0 \to D^{*-} \pi^0 \mu^+ \nu_\mu$	0.4*	PHOTOS GOITY_ROBERTS
$B^0 \to D^{*-} K^{*+}$	0.33 ± 0.06	SVV_HELAMP 0.283 0. 0.932 0. 0.228 0.
$B^0 \to D^{*-} K^0 \pi^+$	0.30 ± 0.08	PHSP
$B^0 \to D^{*-} D^+$	0.3*	PHSP
$B^0 \to D^{*-} K^+$	0.212 ± 0.15	SVS

Table 5.4: Cocktail of decays used to generate the simulated sample of inclusive secondary $B^0 \to D^{*-} X$ decays. The values of the branching ratios are taken from Ref. [26], except for the values marked with *, which lack measurements and are taken from the EvtGen decay list.

Decay channel	$\mathcal{B}$ [$\times 10^{-3}$]	EvtGen Model
$B^+ \to D^{*-} 2\pi^+ \pi^0$	15 ± 7	PHSP
$B^+ \to D^{*+} \overline{D}^{*}(2007)^0 K^0$	9.2 ± 1.2	PHSP
$B^+ \to D^{*-} \pi^+ e^+ \nu_e$	6.1*	PHOTOS GOITY_ROBERTS
$B^+ \to D^{*-} \pi^+ \mu^+ \nu_\mu$	6.1*	PHOTOS GOITY_ROBERTS
$B^+ \to D^{*+} \overline{D}^0 K^0$	3.8 ± 0.4	PHSP
$B^+ \to D^{*-} 3\pi^+ \pi^-$	2.6 ± 0.4	PHSP
$B^+ \to D^{*-} \overline{D}^0 K^{*0}$	2.5*	PHSP
$B^+ \to D^{*-} 2\pi^+$	1.35 ± 0.22	PHSP
$B^+ \to D^{*-} D^{*+} K^+$	$(2\times)$ 1.32 ± 0.18	PHSP
$B^+ \to D^{*-} D^{*+} K^{*+}$	$(2\times)$ 1*	PHSP
$B^+ \to D^{*+} \overline{D}^{*}(2007)^0$	0.81 ± 0.17	SVV_HELAMP 0.56 0. 0.96 0. 0.47 0.
$B^+ \to D^{*+} D^- K^+$	0.63 ± 0.13	PHSP
$B^+ \to D^{*-} D^+ K^+$	0.6 ± 0.13	PHSP
$B^+ \to D^{*+} D^- K^{*+}$	0.5	PHSP
$B^+ \to D^{*-} D^+ K^{*+}$	0.5	PHSP
$B^+ \to D^{*+} \overline{D}$	0.39 ± 0.05	SVS

Table 5.5: Cocktail of decays used to generate the simulated sample of inclusive secondary $B^+ \to D^{*-} X$ decays. The values of the branching ratios are taken from Ref. [26], except for the values marked with *, which lack measurements and are taken from the EvtGen decay list.

Chapter 6

Raw ratio and average decay-time determination

This chapter describes the measurement of the raw WS-to-RS ratio in each D^0 decay-time bin and data-taking period through a fit to the D^* invariant mass. The choice of the $m(D^0\pi_s)_{DTF}$ observable as a discriminating variable is motivated, followed by a detailed description of the fitting model and fitting results. Finally, the methodology used to determine the average D^0 decay time in each bin is described.

The next sections are exclusively dedicated to the technical description of the procedure adopted to determine the numerical values and the associated uncertainties of both the raw WS-to-RS ratio and the average decay time in each decay-time bin. Since this is already a very complex task, we decided to go through the procedure without going deep into the motivation and explanation of the choices and assumptions made, and provide the raw results at the end of the chapter. These aspects of the procedure will be discussed and motivated in depth in the next chapters, as well as the determination of the biases and the corrections that will serve to correct these raw quantities, in order to perform the final measurement of the physics observables of interest.

6.1 Raw WS-to-RS ratio determination

6.1.1 Signal discriminating variables

To disentangle signal from combinatorial and ghost backgrounds and to determine the signal yields, one needs to identify variables with a great separation power between these two classes of candidates. The combinatorial background is mainly due to the association of a true D^0 track with a random slow pion or, less often, to the combination of three

random tracks. Usually, the invariant masses are the best candidates for this task since backgrounds typically do not peak under the signal distribution.

The $m(D^0\pi_s^+)$ and Δm observables Two observables, $m(D^0\pi_s^+)$ and Δm, are usually used at LHCb to separate signal from the combinatorial background. The invariant mass $m(D^0\pi_s^+)$ is computed using imposing the nominal mass value $\overline{m}(D^0)$ and $\overline{m}_\pi$ [26] of the D^0 meson and pion, respectively. It is defined as

$$\begin{aligned} m(D^0\pi_s^+) &\equiv \sqrt{E^2_{D^{*+}} - |\vec{p}_{D^{*+}}|^2} \\ &= \sqrt{(E_{D^0} + E_{\pi_s})^2 - |\vec{p}_{D^0} + \vec{p}_{\pi_s}|^2} \\ &= \sqrt{\left(\sqrt{\overline{m}^2_{D^0} + |\vec{p}_K + \vec{p}_\pi|^2} + \sqrt{\overline{m}^2_\pi + |\vec{p}_{\pi_s}|^2}\right)^2 - |\vec{p}_K + \vec{p}_\pi + \vec{p}_{\pi_s}|^2}. \end{aligned} \tag{6.1}$$

The Δm observable, instead, is defined as

$$\Delta m \equiv m(K\pi\pi_s) - m(K\pi), \tag{6.2}$$

where a large part of D^0 mass resolution cancels out in the difference.

In both observables, signal distribution appears as a Gaussian-like peak with a similar resolution of about 0.8 MeV/c^2. The only difference between the two is related to the shapes of misidentified two-body decays compared to the shape of signal decays. The value of $m(D^0\pi_s)$ is determined using the nominal mass value of the D^0 meson and only information from the momenta of the two decay products. All two-body D^0 decays (for instance $D^0 \to K^\pm\pi^\mp$, $D^0 \to K^+K^+$ and $D^0 \to \pi^+\pi^-$) exhibit, therefore, the same mass shape, independently of what is considered signal or background. There is no way to distinguish them using only this observable. The determination of Δm implies a mass assignment of the D^0 decay products ($K^+\pi^-$ and $K^-\pi^+$ for signal decays). Instead, the presence of contamination of other two-body decays (K^+K^- and $\pi^+\pi^-$), bumps appear in the tails. The shape of these bumps is difficult to model without a full Monte Carlo simulation. Therefore, we prefer to use $m(D^0\pi_s)$, evaluating the background from misidentified D^0 mesons as described in Sec. 7.

The $m(D^0\pi_s^+)_{\mathbf{DTF}}$ observable The dependence of $m(D^0\pi_s^+)$ on the angle $\theta_{D^0\pi_s^+}$ between the direction of the D^0 momentum and that of the π_s is displayed in the following equation:

$$\begin{aligned} m(D^0\pi_s) &= \sqrt{\left(\sqrt{\overline{m}^2_{D^0} + |\vec{p}_{D^0}|^2} + \sqrt{\overline{m}^2_\pi + |\vec{p}_{\pi_s}|^2}\right)^2 - |\vec{p}_{D^0} + \vec{p}_{\pi_s}|^2} = \\ &= \sqrt{\overline{m}^2_{D^0} + |\vec{p}_{D^0}|^2 + \overline{m}^2_\pi + |\vec{p}_{\pi_s}|^2 + 2E_{D^0}E_{\pi_s} - \left(|\vec{p}_{D^0}|^2 + |\vec{p}_{\pi_s}|^2 + 2|\vec{p}_{D^0}||\vec{p}_{\pi_s}|\cos\theta_{D^0\pi_s^+}\right)} = \\ &= \sqrt{\overline{m}^2_{D^0} + \overline{m}^2_\pi + 2E_{D^0}E_{\pi_s} - 2|\vec{p}_{D^0}||\vec{p}_{\pi_s}|\cos\theta_{D^0\pi_s^+}}. \end{aligned} \tag{6.3}$$

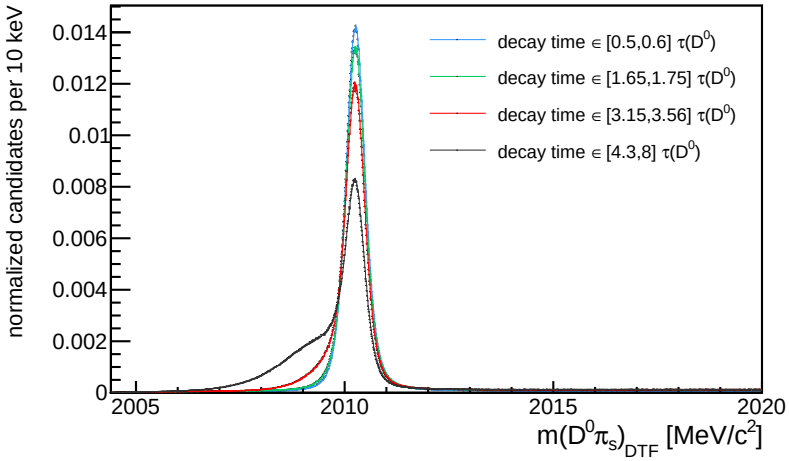

Figure 6.1: Distribution of $m(D^0\pi_s)_{\rm DTF}$ in a RS sub-sample for four decay-time bins. The requirement IP $< 60\,\mu$m is removed from the selection to enhance the effect in the figure.

The determination of this small angle is highly improved by refitting the D^{*+} candidates with the `Decay Tree Fitter` algorithm [71]. This algorithm constraints the D^{*+} meson to come from the PV within the tracking uncertainties to take advantage of the fact the PV position is known more precisely than the one of the DV(D^{*+}). Therefore, $m(D^0\pi_s^+)_{\rm DTF}$ shows an improved resolution of about 0.3 MeV/c^2.

Mass line-shape deformation The constraint to the D^{*+} to be produced in the PV, when applied to a secondary D^0 decays, produces a bias in the $m(D^0\pi_s)_{\rm DTF}$ distribution. Although the magnitude of the momenta (and consequently of the energies) is almost unchanged by this constraint, the small angle $\theta_{D^0\pi_s^+}$ between the D^0 momentum, $\vec{p}_{D^0}$, and the π_s momentum, $\vec{p}_{\pi_s}$, is highly influenced by the D^* vertex fit. In particular, for the secondary decays, the size of $\theta_{D^0\pi_s^+}$ is reduced by the D^* vertex constraint. Therefore, any artificial reduction of the value of the $\theta_{D^0\pi_s^+}$ variable leads to an underestimation of $m(D^0\pi_s)_{\rm DTF}$, as seen from Eq. 6.3. This effect is shown in Fig. 6.1, where a clear second peak appears on the left of the main one at high decay time due to the contamination of secondary decays. To correctly fit the signal yields, it is better to limit as much as possible the deformation of the mass distribution due to the secondary contamination, as described in Sec. 8.

6.1.2 Fitting strategy

To determine the D^0 decay-time dependence of the WS-to-RS ratio, the sample is divided into decay-time bins. The signal yields are determined independently for each decay-time bin, the three data-taking periods and $D^{*\pm}$ flavours. We perform simultaneous χ^2 fits to the $m(D^0\pi_s^+)_{\rm DTF}$ distributions of three data samples: WS, RS, and CG (common ghost candidates). The fit models of signal, combinatorial and ghost background components are empirical functions. There are 18 decay-time bins ranging from 0.4 τ_{D^0} to 8 τ_{D^0},

chosen in such a way that they have the same WS yield, except for the last four, which have a yield equal to half the others. To get an idea of the decay-time distribution of these candidates and the effects of trigger selections on it, Fig. 6.2 shows the decay-time distribution of a subsample of RS decays. The chosen binning scheme is the following:

$$t(D^0)/\tau_{D^0} \in [0.40, 0.64, 0.77, 0.88, 0.99, 1.10, 1.21, 1.33, 1.46, 1.61, \\ 1.77, 1.97, 2.21, 2.51, 2.93, 3.23, 3.65, 4.36, 8.00]. \tag{6.4}$$

Less than 1% of the sample is removed by rejecting candidates in the region below 0.4 τ_{D^0}, where the dependence of the acceptance is very steep and difficult to reproduce in simulation accurately. Decay times above 8 τ are also removed because secondary D^{*+} candidates heavily contaminate this region, while only a few promptly-produced signal candidates are present. The $m(D^0\pi_s^+)_{\mathrm{DTF}}$ binning scheme is 312 bins for WS and RS decays and 26 bins for CG background, from 2004.4 MeV/c^2 to 2020.0 MeV/c^2.

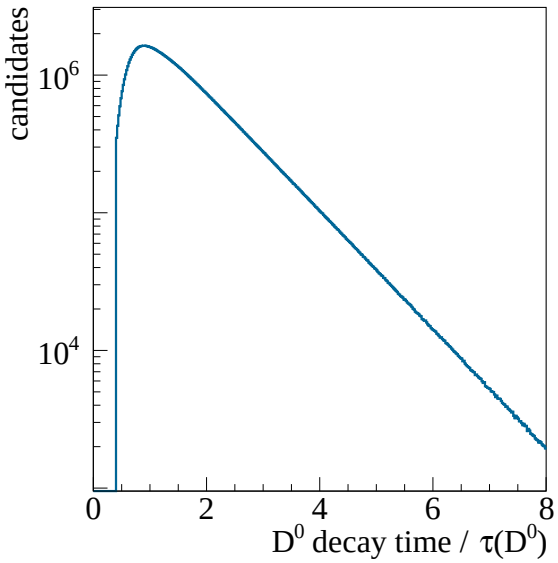

Figure 6.2: The D^0 decay-time distribution of a subsample of RS candidates after all the selections described in this section. The selected decay-time range is $t(D^0) \in [0.4, 8]\tau_{D^0}$.

6.1.3 Signal model

The signal pdf is described by

$$\mathcal{P}_{\mathrm{sgn}}(m\,|\mu, \Delta m_0, \boldsymbol{\theta}_{\mathrm{sgn}}) = C_{\mathrm{sgn}} \cdot \mathcal{H}(m - \overline{m_0} + \Delta m_0) \cdot (m - \overline{m_0} + \Delta m_0)^{1+\rho} \cdot \{\mathcal{L}(m\,|\,\Gamma) \circledast \\ [f\,\mathcal{J}(m\,|\overline{m}_{D^*} + \mu + \Delta\mu, \sigma_1, \delta_1, \gamma_1) + (1-f)\,\mathcal{J}(m\,|\overline{m}_{D^*} + \mu - \Delta\mu, \sigma_2, \delta_2, \gamma_2)]\}. \tag{6.5}$$

The term C_{sgn} is the normalization of the pdf in the fitting range, 2004.4–2020.0 MeV/c^2. The term, $\mathcal{H}(m - \overline{m_0} + \Delta m_0) \cdot (m - \overline{m_0} + \Delta m_0)^{1+\rho}$, forces the kinematics limit of the distribution and accounts for resolution effects near the threshold ($\mathcal{H}$ is a Heaviside step

function); $\overline{m_0}$ is a constant term equal to $\overline{m}_{D^0} + \overline{m}_\pi = 2004.41\,\mathrm{MeV}/c^2$, according to PDG values [26]. We consider a possible offset Δm_0 free to float to account for possible small inaccuracies from momentum calibration.
The Johnson SU function [81]

$$\mathcal{J}(x \mid \mu, \sigma, \delta, \gamma) = \frac{|\delta|}{\sigma\sqrt{2\pi}} \frac{e^{-\frac{1}{2}\left[\gamma + \delta \sinh^{-1}\left(\frac{x-\mu}{\sigma}\right)\right]^2}}{\sqrt{1 + \left(\frac{x-\mu}{\sigma}\right)^2}}, \tag{6.6}$$

aims to model the mass resolution of prompt and secondaries candidates. Mass resolution is not the same for all candidates in the sample but depends on various factors, most notably the daughter tracks' momentum, pseudorapidity and opening angle. We can therefore imagine the resolution of the entire sample as a weighted sum of many Gaussians. The final result is a resolution with a standard deviation equal to the average standard deviation of the Gaussians, which is no longer Gaussian; in fact, it shows a significantly higher kurtosis. The final-state radiation (together with the kinematic limit) contributes to the asymmetry of the curve. This distribution can be well approximated by a Johnson SU function: a 4-parameter function that can have any given mean, standard deviation, asymmetry and kurtosis. The simulated sample of prompt candidates shows that the bulk of their resolution is well-fitted by a Johnson SU function with low asymmetry. The simulated sample of secondary candidates shows a deformed and highly asymmetrical resolution distribution, so an independent Johnson SU function is needed. The combined resolution function is convoluted ($\circledast$) with a Lorentz distribution

$$\mathcal{L}(m \mid \Gamma) = \frac{1}{\pi}\left(\frac{\frac{1}{2}\Gamma}{m^2 + \left(\frac{1}{2}\Gamma\right)^2}\right), \tag{6.7}$$

which is needed to reproduce $(m - m_{D^*})^{-2}$ tail behaviour, due to multiple scattering and the natural width of the D^{*+}, approximately 80 keV/c^2, which becomes relevant in comparison to resolution width, approximately $300\,\mathrm{keV}/c^2$, at mass values far from the signal peak. This convolution, which is performed numerically, allows us to obtain much more stable and physically sound tails behaviour.
With the term $\boldsymbol{\theta}_{\mathrm{sgn}}$, we refer to all the parameters of the signal pdf that are shared between WS and RS:

- the parameter $\Delta\mu$, which determines the separation between the two Johnson components;
- the relative fraction between the two Johnson components, f;
- the parameters $\sigma_{1,2}, \delta_{1,2}$ and $\gamma_{1,2}$ that determine variance, asymmetry and kurtosis of the Johnson distributions;
- the parameter Γ, related to the natural D^{*+} width;
- the parameter ρ, a small correction to the linear kinematic constraint.

6.1.4 Combinatorial background model

The combinatorial background is modelled using a simplified two-body phase-space model

$$\mathcal{P}_{\text{bkg}}(m\,|\Delta m_0, \boldsymbol{\theta}_{\text{bkg}}) = C_{\text{bkg}} \left[(m - \overline{m_0} + \Delta m_0)^{\frac{1}{2}} + \alpha (m - \overline{m_0} + \Delta m_0)^{\frac{3}{2}} + \beta (m - \overline{m_0} + \Delta m_0)^{\frac{5}{2}} \right]. \tag{6.8}$$

Here C_{bkg} is the normalization of the pdf in the fitting range, $\overline{m}_0$, is the constant kinematic threshold (2004.41 MeV/c^2), that is allowed to float by Δm_0 (this parameter is shared with signal pdf) and the α and β parameter are the coefficients of the small higher order correction to the square root behaviour. With the term $\boldsymbol{\theta}_{\text{bkg}}$, we refer to all the parameters of the combinatorial background pdf that are shared between WS and RS, *i.e.* α and β.

6.1.5 Ghost background model

The ghost background pdf is

$$\mathcal{P}_{\text{gst}}(m \,|\, \boldsymbol{\theta}_{\text{sgn}}) = C_{\text{gst}} \cdot \left[f\, C_c + (1 - f)\, C_J\, \mathcal{J}(m \,|\, \mu_g, \sigma_g, \delta_g, \gamma_g) \right] \cdot \mathcal{T}(m \,|\, \omega). \tag{6.9}$$

The term C_{gst} normalizes the pdf to 1 in the fitting range. The constant term models the widespread tails, while the Johnson SU function accounts for the peaking bulk of the distribution. Both components are normalized to 1 by the constant terms C_c and C_J. The $\mathcal{T}$ function

$$\mathcal{T}(m \,|\, \omega) = \mathcal{H}(m - \overline{m_0}) \left[1 - \left(\frac{\overline{m_0}}{m} \right)^{\omega} \right], \tag{6.10}$$

is 0 at the threshold $\overline{m_0}$ and asymptotically goes to 1. Its purpose is to force the kinematics limit of the distribution.
The ghost background parameters $\boldsymbol{\theta}_{\text{gst}}$ include:

- the shift from the known D^{*+} mass of the Johnson distribution's core, μ_g;
- the widths of the Johnson distribution's core, σ_g;
- the parameters δ_g and γ_g determine the asymmetric tails of the Johnson distribution's tails;
- the parameter ω that determines the steepness of the threshold function.

6.1.6 Fitting model

We have three data samples to fit simultaneously: WS, RS, and CG. Here is the full model for the three samples:

$$\begin{aligned}\mathcal{P}_{\rm WS}(m) &= \mathcal{P}_{\rm sgn}(m|\mu^{\rm WS}, \Delta m_0^{\rm WS}, \theta_{\rm sgn}) \cdot N_{\rm sgn}^{\rm RS} \cdot \widetilde{r}' \\ &+ \mathcal{P}_{\rm bkg}(m|\Delta m_0^{\rm WS}, \theta_{\rm bkg}^{\rm WS}) \cdot N_{\rm bkg}^{\rm WS} \\ &+ \mathcal{P}_{\rm gst}(m|\theta_{\rm gst}) \cdot N_{\rm gst}^{\rm RS} \cdot R_{\rm gst} \end{aligned} \tag{6.11}$$

$$\begin{aligned}\mathcal{P}_{\rm RS}(m) &= \mathcal{P}_{\rm sgn}(m|\mu^{\rm RS}, \Delta m_0^{\rm RS}, \theta_{\rm sgn}) \cdot N_{\rm sgn}^{\rm RS} \\ &+ \mathcal{P}_{\rm bkg}(m|\Delta m_0^{\rm RS}, \theta_{\rm bkg}^{\rm RS}) \cdot N_{\rm bkg}^{\rm RS} \\ &+ \mathcal{P}_{\rm gst}(m|\theta_{\rm gst}) \cdot N_{\rm gst}^{\rm RS} \end{aligned} \tag{6.12}$$

$$\mathcal{P}_{\rm CG}(m) = \mathcal{P}_{\rm gst}(m|\theta_{\rm gst}) \cdot N_{\rm gst}^{\rm CG} \tag{6.13}$$

Here $\widetilde{r}'$ is the parameter of interest, the raw WS-to-RS signal yield ratio. Hereafter we will use $\sim$ to indicate raw observables (biased and to be corrected). The signal shape parameters are shared between WS and RS, except for μ and Δm_0, to account for differences in momentum calibration of charged soft pions. This assumption is reasonable because signal WS and RS candidates have the same kinematics, and the only difference is the charge of the soft pions that, at most, could produce a small mass shift due to asymmetry in momentum calibration. This approach exploits the much larger RS sample to determine the signal shape precisely and how it varies as a function of decay time to fit precisely the WS sample while automatically considering correlations between the RS signal yield and the WS one, which is not negligible.

The combinatorial background shape parameters are independent among WS and RS. The signal and combinatorial background share the Δm_0 parameter. We expect the combinatorial background to be almost identical between WS and RS. However, some small non-peaking physical backgrounds have different yields between the decay modes. Hence they are conservatively allowed to vary independently.

The ghost background shape parameters are shared among the three samples. This assumption is reasonable, as explained in Sec. 5.4: the $m(D^0\pi_{\rm s})_{\rm DTF}$ distribution of ghosts background weakly depends on the direction of the soft pion (hence $\theta_{gst}^{WS} \simeq \theta_{gst}^{RS} \simeq \theta_{gst}^{CG}$). The assumption $R_{\rm gst} = 1$ derived in App. A is used. This assumption has no visible effect on the parameter of interest $R_{\rm sgn}$ while it improves fit stability and convergence. Ghost's background shape weakly depends also on the D^0 decay time. Hence some parameters (σ_g, δ_g and γ_g) are fixed to the result of a fit to the time-integrated sample. The validity of these assumptions will be discussed in depth in Sec. 7.1.3.

6.1.7 Fit results

Figure 6.3 shows a typical simultaneous fit, in a given decay-time bin, to the $m(D^0\pi_{\rm s})_{\rm DTF}$ invariant mass distribution of the RS, WS, and CG decays. The fit projections are overlaid, as well as the returned goodness-of-fit (χ^2/ndof), and the distributions of pulls for each fitted mass line shape. For RS and WS decays, different contributions from signal,

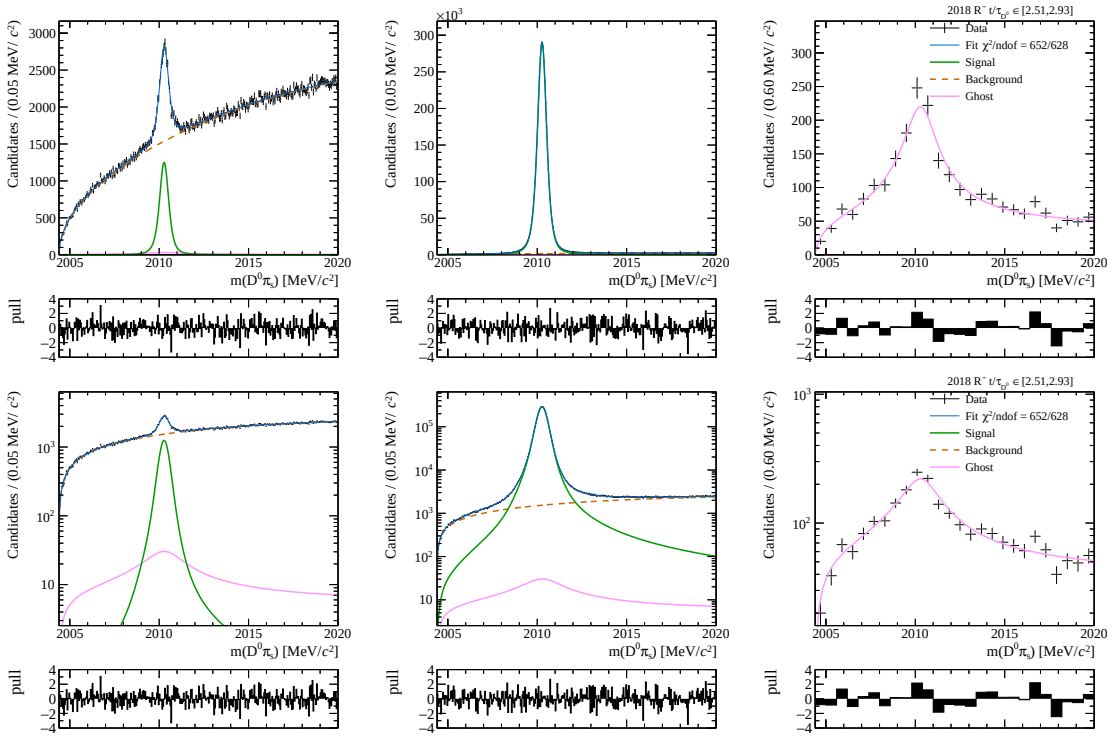

Figure 6.3: An example of the $m(D^0\pi_s)_{\rm DTF}$ distributions in linear (Up) and logarithmic (Bottom) scale of WS (Left), RS (Center), and CG (Right) in the 2018 $K^+\pi^-$ sample in the $t \in [2.51, 2.93]$ decay-time bin. The fit results are superimposed.

combinatorial background, and CG decays are also displayed. As previously explained in the text, the signal component, both for RS and WS decays, also includes the contribution of secondary decays originating from a b-hadron decay.

The distribution of all mass fits with the corresponding fit projections overlaid, in each decay-time bin and for each data-taking period, can be found and reviewed in App. C. They are too many to be reported in the main body of the thesis, therefore, all the returned values of χ^2/ndof are reported in a single distribution, shown in Fig. 6.4. This allows a direct visualization of the global agreement of data to the fit functions. The mean value of this distribution is about 1.06, while its standard deviation equals about 0.07, to be compared with the expected values of 1 and $\sqrt{2/\text{ndof}} \approx 0.056$, respectively. Although the agreement with the expected values is not perfect, this can be considered very satisfactory considering that the size of the data sample is very large and that most of the used pdfs are pure empirical functions with a limited number of free parameters. Furthermore, many checks and studies on both the reliability and robustness of the adopted fit strategy of the D^* invariant mass are described in depth in Sec. 7. However, an inflation factor of $\sqrt{1.06}$ will be applied in Sec. 9 to the uncertainty of the measured raw ratio, $r'^{\pm}$ in order to account for possible small effect of mismodeling of the empirical functions of signal and backgrounds.

Finally, Tab. 6.1 reports the WS-to-RS yield raw ratios, $\widetilde{r}'^{+}$ and $\widetilde{r}'^{-}$, with their corresponding decay-time bin, for each data-taking period.

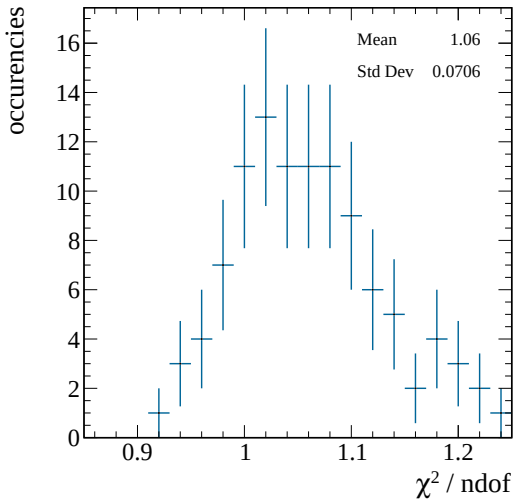

Figure 6.4: The distribution of χ^2/ndf for all the 108 ratio mass fits. The number of degrees of freedom for each mass fit is 628.

decay-time bin	$\widetilde{r}'^{+} \times 10^5$			$\widetilde{r}'^{-} \times 10^5$		
	16	17	18	16	17	18
0.40 - 0.64	358.5 ± 5.3	352.1 ± 4.7	356.2 ± 4.4	370.8 ± 5.3	365.3 ± 4.9	372.7 ± 4.5
0.64 - 0.77	362.4 ± 5.4	362.3 ± 5.2	355.9 ± 4.9	370.8 ± 5.5	367.5 ± 5.3	367.0 ± 5.0
0.77 - 0.88	366.4 ± 5.5	361.3 ± 5.5	363.0 ± 5.2	365.9 ± 5.6	380.0 ± 5.7	372.4 ± 5.3
0.88 - 0.99	355.4 ± 5.5	373.5 ± 5.5	368.9 ± 5.2	376.0 ± 5.6	368.3 ± 5.7	380.0 ± 5.4
0.99 - 1.10	366.3 ± 5.6	357.6 ± 5.7	367.3 ± 5.4	381.1 ± 5.8	386.7 ± 6.0	384.8 ± 5.5
1.10 - 1.21	375.9 ± 5.8	380.8 ± 5.9	366.3 ± 5.6	375.6 ± 5.9	376.2 ± 6.1	384.7 ± 5.7
1.21 - 1.33	372.9 ± 5.8	373.7 ± 5.9	371.6 ± 5.6	390.0 ± 5.9	387.4 ± 6.1	385.1 ± 5.7
1.33 - 1.46	375.5 ± 5.8	372.1 ± 6.0	387.0 ± 5.7	389.9 ± 5.9	385.9 ± 6.3	400.2 ± 5.8
1.46 - 1.61	383.9 ± 5.8	377.9 ± 5.9	378.1 ± 5.6	393.6 ± 5.9	396.3 ± 6.2	394.7 ± 5.8
1.61 - 1.77	389.5 ± 6.0	393.6 ± 6.2	390.7 ± 5.9	395.9 ± 6.1	397.3 ± 6.4	402.0 ± 6.0
1.77 - 1.97	397.5 ± 5.9	398.7 ± 6.1	397.8 ± 5.8	405.8 ± 6.0	419.3 ± 6.4	410.3 ± 5.9
1.97 - 2.21	401.6 ± 6.1	409.0 ± 6.2	400.3 ± 5.9	420.8 ± 6.1	419.0 ± 6.6	399.0 ± 6.0
2.21 - 2.51	408.6 ± 6.9	421.2 ± 6.4	416.2 ± 6.0	411.0 ± 6.4	431.9 ± 6.8	430.5 ± 6.3
2.51 - 2.93	429.6 ± 6.6	418.8 ± 6.5	431.7 ± 6.2	434.8 ± 6.3	437.9 ± 7.5	428.7 ± 6.3
2.93 - 3.23	436.1 ± 9.0	443.8 ± 9.2	441.0 ± 8.7	449.3 ± 8.9	466.2 ± 9.7	464.6 ± 9.0
3.23 - 3.65	449.8 ± 9.3	452.3 ± 9.4	462.0 ± 8.9	467.5 ± 9.2	458.4 ± 9.7	467.5 ± 9.1
3.65 - 4.36	481.6 ± 9.6	469.1 ± 9.6	476.4 ± 9.1	496.3 ± 9.4	489.7 ± 10.1	480.7 ± 9.3
4.36 - 8.00	522.0 ± 10.0	536.6 ± 10.4	538.8 ± 9.9	541.6 ± 10.0	537.9 ± 10.8	553.4 ± 10.1

Table 6.1: WS-to-RS signal yields ratio resulting from mass fits in each decay-time bin, data-taking period and D^0 flavour. A random shift parabolic in decay time is applied to the raw ratio, with independent parameters for the two flavours.

6.2 Raw average decay-time determination

For each decay-time bin i, we need to know the raw average decay time $\langle \tilde{t} \rangle_i$ and the raw average squared decay time $\langle \tilde{t}^2 \rangle_i$ for the signal candidates. Hereafter, the notation is simplified with $\tilde{t}_i$ and $\tilde{t}_i^2$, respectively. To remove the contribution from the combinatorial background, which has a slightly different decay-time distribution, we perform a sideband subtraction on $m(D^0\pi_s)$ distribution (without DTF constraint) in each decay-time bin. Weighted candidates will give the resulting decay-time distribution:

- in the signal region ($|m(D^0\pi_s^+) - m_{D^{*+}}| < 1.8\,\mathrm{MeV}/c^2$) with weight equal to 1;
- in the sideband ($m(D^0\pi_s^+) \in [2014, 2020]\,\mathrm{MeV}/c^2$) with weight equal to $-s(i)$.

Here, $s(i)$ is the ratio, in the i^{th} decay-time bin, between the background in the signal region and the sideband, computed by performing a mass fit to the RS candidates, with the same model previously described but neglecting the ghost background component. This signal region is only used for this sideband subtraction. In the raw ratio determination, the $m(D^0\pi_s)_{\mathrm{DTF}}$ observable is used to disentangle the signal yields and no requirements are applied on $m(D^0\pi_s)_{\mathrm{DTF}}$ or $m(D^0\pi_s)$ in the offline selection. Here, in the measurement of the average decay time, we prefer to use $m(D^0\pi_s)$ instead of $m(D^0\pi_s)_{\mathrm{DTF}}$ because, as already seen in Fig. 6.1, the $m(D^0\pi_s)_{\mathrm{DTF}}$ distribution of the background from secondary D^{*+} decays differs from that of the signal, showing a larger tail at low values of $m(D^0\pi_s)_{\mathrm{DTF}}$. Therefore, if the sideband subtraction is applied cutting on $m(D^0\pi_s)_{\mathrm{DTF}}$, this would select a different fraction of prompt and secondary candidates compared to the one present in the measured signal yield in Sec. 6.1. In particular, it would select a smaller fraction of secondary decays, thus biasing the fraction of secondary decays determined in Sec. 8. The values of $\tilde{t}_i$ and $\tilde{t}_i^2$ are computed for each decay-time bin i, separately for both D^{*+}, D^{*-} candidates and for each data-taking year. These values have negligible statistical uncertainties, so they are taken as constants in the mixing parameters fit.

decay-time bin	$\tilde{t}$ / $\tau(D^0)$						$\tilde{t}^2$ / $\tau^2(D^0)$					
	D^{*+}			D^{*-}			D^{*+}			D^{*-}		
	16	17	18	16	17	18	16	17	18	16	17	18
0.40 - 0.64	0.549	0.545	0.544	0.549	0.545	0.544	0.305	0.301	0.300	0.305	0.301	0.300
0.64 - 0.77	0.708	0.707	0.707	0.708	0.707	0.707	0.503	0.502	0.501	0.503	0.502	0.502
0.77 - 0.88	0.826	0.825	0.825	0.826	0.825	0.825	0.683	0.682	0.682	0.683	0.682	0.682
0.88 - 0.99	0.935	0.935	0.935	0.935	0.935	0.935	0.876	0.875	0.875	0.876	0.875	0.875
0.99 - 1.10	1.045	1.045	1.045	1.045	1.045	1.045	1.093	1.092	1.092	1.093	1.092	1.092
1.10 - 1.21	1.155	1.154	1.154	1.155	1.154	1.154	1.334	1.334	1.334	1.334	1.334	1.334
1.21 - 1.33	1.269	1.269	1.269	1.269	1.269	1.269	1.613	1.612	1.612	1.612	1.612	1.612
1.33 - 1.46	1.394	1.394	1.394	1.394	1.394	1.394	1.945	1.945	1.945	1.945	1.945	1.945
1.46 - 1.61	1.534	1.534	1.534	1.534	1.533	1.534	2.354	2.354	2.354	2.354	2.353	2.354
1.61 - 1.77	1.688	1.688	1.688	1.688	1.688	1.688	2.853	2.852	2.852	2.853	2.852	2.852
1.77 - 1.97	1.867	1.867	1.867	1.867	1.867	1.867	3.490	3.490	3.489	3.490	3.490	3.489
1.97 - 2.21	2.086	2.086	2.086	2.086	2.086	2.086	4.355	4.355	4.355	4.356	4.355	4.355
2.21 - 2.51	2.353	2.353	2.353	2.353	2.353	2.353	5.546	5.545	5.546	5.546	5.546	5.546
2.51 - 2.93	2.707	2.707	2.707	2.707	2.707	2.707	7.343	7.342	7.343	7.344	7.342	7.342
2.93 - 3.23	3.073	3.073	3.074	3.074	3.074	3.073	9.453	9.454	9.454	9.454	9.454	9.453
3.23 - 3.65	3.428	3.427	3.427	3.428	3.427	3.428	11.76	11.76	11.76	11.76	11.76	11.76
3.65 - 4.36	3.971	3.971	3.971	3.971	3.971	3.971	15.81	15.81	15.81	15.81	15.81	15.81
4.36 - 8.00	5.517	5.516	5.521	5.516	5.515	5.518	31.32	31.31	31.37	31.31	31.30	31.33

Table 6.2: Raw average values of the D^0 decay time, and its square, in each decay-time bin, data-taking period and D^0 flavour after the combinatorial background subtraction.

Chapter 7

Ratio biases

This chapter details the experimental methodologies used to identify and quantify all the known sources of bias to the previously measured raw WS-to-RS ratios. The D^* mass fit model is extensively studied to assess the reliability of the used empirical models, as well as that of the used assumptions and constraints. The charge asymmetries from detection and production mechanisms are conveniently removed by exploiting the $D^0 \to K^+K^-$ control sample. The bias from misreconstructed or misidentified physics backgrounds is subsequently evaluated, as well as that generated by the removal of the WS-RS common subsample.

7.1 Modeling of the D^* invariant mass

The purpose of this section is to clarify, motivate, and check the assumptions of the empirical model adopted to fit the D^* invariant mass distributions in each decay-time bin, as described in Sec. 6.1.6, and verify that the fit model is unbiased whereby no correction to the measured raw ratio WS-to-RS ratio is assigned because of the mass modelling.

7.1.1 Signal pdf

The signal pdf is an empirical function and it is designed to accommodate two categories of events with quite different resolution curves, corresponding to the prompt and secondary decays. It mainly aims at correctly describing the Gaussian-like bulk of the distribution, the non-Gaussian tails, and the small time-dependent left tail due to DTF constraint to secondary decays. Although an attempt has been made to make this function as simple as possible and physics-sounded in order to avoid over-fitting, it still consists of numerous free parameters. However, if the combinatorial background, and the ghost soft pions background, are modelled accurately within the assigned uncertainties, as it is checked in the next sections, it is sufficient that the signal parameterization is capable of describing all features of the signal line shape. A good quality of the mass fits, as we find, ensures that our model is accurate and capable of describing the parent mass distribution of our RS and WS signal candidates (see App. C).

Parameters constraints The signal pdf used in the mass fits is the same for RS and WS signal candidates. The two functions share all the free parameters, except their absolute normalization and the $\delta\mu$ parameter. In the simultaneous mass fits, WS and RS candidates decay to almost identical final states. Thus all resolution and momentum calibration effects that determine the D^* mass line shape are almost the same. The only difference between WS and RS candidates comes from the charge of the soft pion. A slight difference in the momentum calibration for π_s^+ and π_s^- could determine a small shift in the bulk of the D^* mass distribution between WS and RS, which is correctly taken into account with the $\delta\mu$ parameter. All other effects are second-order corrections and can be neglected.

7.1.2 Combinatorial background pdf

The parametric expression describing the combinatorial background is very simple, and it is just a square root function with power corrections at higher order. The main features of this shape can be directly derived from the formula used to compute the D^* invariant mass,

$$m(D^0\pi_s) = \sqrt{\left(\sqrt{\overline{m}_{D^0}^2 + |\vec{p}_{D^0}|^2} + \sqrt{\overline{m}_\pi^2 + |\vec{p}_{\pi_s}|^2}\right)^2 - |\vec{p}_{D^0} + \vec{p}_{\pi_s}|^2}, \tag{7.1}$$

where the D^0 and π mass hypotheses are assigned and their PDG mass values are used. Let us place ourselves in the D^0 reference system. Here the previous equation becomes

$$m(D^0\pi_s) = \sqrt{\left(\overline{m}_{D^0} + \sqrt{\overline{m}_\pi^2 + |\vec{p}^{\,*}_{\pi_s}|^2}\right)^2 - \left|\vec{p}^{\,*}_{\pi_s}\right|^2}, \tag{7.2}$$

where the $*$ subscript indicates that the quantity is evaluated in the D^0 reference system. The typical energy in this system is of the order of magnitude of the Q-value of the D^* decay (6 MeV/c^2), hence we can expand this expression at the first order in the parameters $|\vec{p}^{\,*}_{\pi_s}|/\overline{m}_\pi, |\vec{p}^{\,*}_{\pi_s}|/\overline{m}_{D^0} \ll 1$:

$$\begin{aligned}
m(D^0\pi_s) &= \sqrt{\left(\overline{m}_{D^0} + \sqrt{\overline{m}_\pi^2 + |\vec{p}^{\,*}_{\pi_s}|^2}\right)^2 - \left|\vec{p}^{\,*}_{\pi_s}\right|^2} \\
&\simeq \sqrt{\left(\overline{m}_{D^0} + \overline{m}_\pi + \frac{|\vec{p}^{\,*}_{\pi_s}|^2}{2\overline{m}_\pi}\right)^2 - \left|\vec{p}^{\,*}_{\pi_s}\right|^2} \\
&\simeq \sqrt{\overline{m}_{D^0}^2 + \overline{m}_\pi^2 + 2\overline{m}_{D^0}\overline{m}_\pi + \frac{|\vec{p}^{\,*}_{\pi_s}|^2\overline{m}_{D^0}}{\overline{m}_\pi} + |\vec{p}^{\,*}_{\pi_s}|^2|\vec{p}^{\,*}_{\pi_s}|^2} \\
&\simeq \sqrt{(\overline{m}_{D^0} + \overline{m}_\pi)^2 + \frac{|\vec{p}^{\,*}_{\pi_s}|^2\overline{m}_{D^0}}{\overline{m}_\pi}} \\
&\simeq \overline{m}_{D^0} + \overline{m}_\pi + |\vec{p}^{\,*}_{\pi_s}|^2 \frac{\overline{m}_{D^0}}{2\overline{m}_\pi(\overline{m}_{D^0} + \overline{m}_\pi)}.
\end{aligned} \tag{7.3}$$

Given the pdf of the π_s momentum magnitude, $f_{|p^*_{\pi_s}|}$, we can change the variable to obtain the pdf of $m(D^0\pi_s)$. Inverting Eq. 7.3 and computing its derivative gives:

$$|\vec{p}^{\,*}_{\pi_s}| \propto \sqrt{m(D^0\pi_s) - \overline{m}_{D^0} + \overline{m}_\pi}, \tag{7.4}$$

$$\frac{d\sqrt{m(D^0\pi_s) - \overline{m}_{D^0} + \overline{m}_\pi}}{dm(D^0\pi_s)} = \frac{1}{\sqrt{m(D^0\pi_s) - \overline{m}_{D^0} + \overline{m}_\pi}} \tag{7.5}$$

Hence the pdf for $m(D^0\pi_s)$ is

$$f_{m(D^0\pi_s)}(m(D^0\pi_s)) \propto \frac{1}{\sqrt{m(D^0\pi_s) - \overline{m}_{D^0} + \overline{m}_\pi}} f_{p^{*x}_{\pi_s}}\left(\sqrt{m(D^0\pi_s) - \overline{m}_{D^0} + \overline{m}_\pi}\right). \tag{7.6}$$

Assuming spherical symmetry for the probability distribution of $\vec{p}^{\,*}_{\pi_s}$, and given the pdf of one component of the π_s momentum, $f_{p^{*x}_{\pi_s}}$, we can switch to spherical variables and integrate over ϕ and η to obtain:

$$f_{|\vec{p}^{\,*}_{\pi_s}|}(|\vec{p}^{\,*}_{\pi_s}|) \propto |\vec{p}^{\,*}_{\pi_s}|^2 f_{p^{*x}_{\pi_s}}(|\vec{p}^{\,*}_{\pi_s}|). \tag{7.7}$$

The distribution of $f_{p^{*x}_{\pi_s}}$ is not null in zero and it can be expanded as a series, producing higher-order corrections to the first-order behaviour, which results in being proportional to

$$\sqrt{m(D^0\pi_s) - \overline{m}_{D^0} + \overline{m}_\pi}. \tag{7.8}$$

Kinematic threshold A kinematic threshold characterizes the distribution: no D^* candidates can have a mass value under $\overline{m}_{D^0} + \overline{m}_\pi$ mass, corresponding to the limit of zero energy in the centre of mass of the (D^0, π_s) reference system. A degree of freedom is allowed to this threshold adding the nuisance parameter δm_0 in order to account for a slight shift due to the π_s momentum calibration and its asymmetry.

Parameters constraints The combinatorial background is described by the same parametric function both in WS and RS samples, but the two sets of parameters are independent. This allows us to take into account differences in the backgrounds of RS and WS decays, such as small discrepancies in physics backgrounds. Despite the parameters for the RS and WS combinatorial background returned by the simultaneous fit being very similar, they are not compatible and sharing a subset of those parameters would end up producing a significant difference in the fitted signal ratio. For this reason, we chose to stick to the most general assumption.

Data driven test of goodness We have checked the level of accuracy of the chosen combinatorial background model with a data-driven technique. We artificially built a pure combinatorial background using a weighted data subsample, very similar to the real background under our signal and verified that our model is accurately able to reproduce all observed features. The main constituents of the combinatorial backgrounds are:

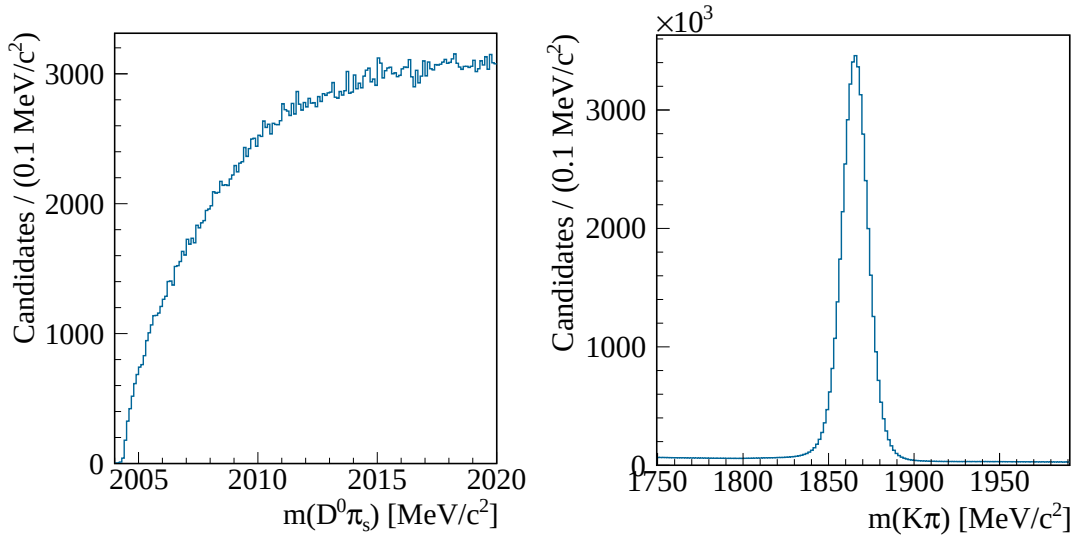

Figure 7.1: (Left) The $m(D^0\pi_s)$ distribution of a data subsample of three random tracks extracted selecting a sideband in the $m(K\pi)_{swapp}$ *vs.* $m(K\pi)$ observable space. (Right) The $m(K\pi)$ distribution of the $m(D^0\pi_s)$ sideband.

- prompt D^0 associated with a random soft pion (this is the most abundant component);
- fake D^0 generated from two random pions, associated with a random soft pion (this is expected to be suppressed due to good D^0 purity in the D^0 mass requirement range.);
- multibody and/or misreconstructed D^0 decay, that is expected to be very small as stated in Sec. 7.3.

A subsample of a very pure combinatorial background from real D^0 associated with random soft pions can be extracted from the WS-RS common sample (described in Sec. 5.4). These are WS D^* candidates, where the associated D^0 is also used to build a RS D^* candidate (using an opposite charge soft pion) within 3σ from the D^* nominal peak. These events are, with very high probability, RS decays, and the reconstructed WS candidates are either combinatorial or ghost background. The ghost background in this subsample is removed requiring a separation angle between the WS and RS soft pions larger than 10^{-3} rad. After this requirement, we have a subsample of pure combinatorial background with prompt D^0. The D^* mass distribution of this subsample, shown in the left panel of Fig. 5.11 closely resembles the one of the combinatorial background in WS and RS samples.

A subsample of combinatorial background from three random pions can be extracted by selecting the upper-left sideband in the $m(K\pi)_{swapp}$ *vs.* $m(K\pi)$ observable space ($m(K\pi)_{swapp} < 1800\,\text{MeV}$ and $m(K\pi) > 1915\,\text{MeV}$), as shown in Fig. 5.7. This region is free from real $D^0 \to h^+h^-$ decays and it is a pure subsample of a combinatorial background with fake D^0 built from random tracks.

The relative fraction of these two categories of combinatorial background is fitted by looking at the $m(K\pi)$ distribution in the right sideband of the $m(D^0\pi_s)$ distribution

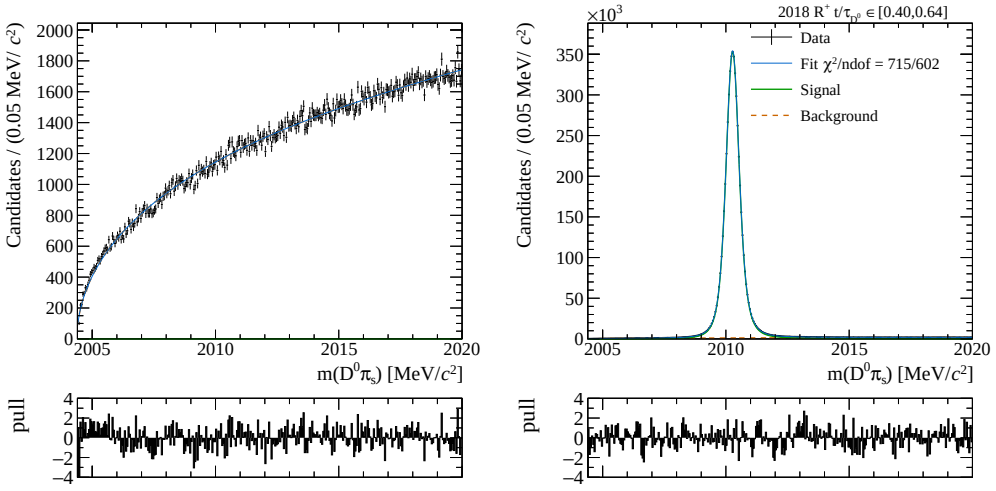

Figure 7.2: The $m(D^0\pi_s)$ distributions of data-driven combinatorial background (Left) and a subsample of RS decay (Right). The fit results are superimposed.

($m(D^0\pi_s) > 2014\,\text{MeV}$). This sideband is composed of a pure combinatorial background. Looking at the $m(K\pi)$ distribution of this subsample we can disentangle the two components: the background from true prompt D^0 constitutes the peaking bulk, while the one from three random tracks forms the flat distribution. The relative fraction is determined with a simplified fit where true prompt D^0 are modelled with two Gaussian and the three random tracks with a linear distribution. We find that the three random track backgrounds account for about 3% of the total combinatorial background.

The relative fraction is used to weight the two data subsamples in order to create an artificial combinatorial sample. This is a realistic subsample of combinatorial background and it has very similar features to the real background under our signal. However, some small discrepancies are present because it is selected differently, and any attempt to reweight kinematic distributions does not produce a satisfactory agreement because of the vicinity of the kinematic threshold.

However, even if this subsample cannot be directly used to model the combinatorial component of our background, it can be used to check that our parametric model is capable of accurately modelling a real sub-sample of combinatorial background. This artificial sample, with no presence of signal, is used to generate a fake WS sample that is paired with a real subsample of RS candidates. We simultaneously fit these two samples, modelling the mass distributions with the same pdfs as in the central analysis, except for the ghost background, which is removed. The fit quality is satisfactory and the WS-to-RS signal ratio resulting from the mass fit is negligible and compatible with no signal: $R_{\text{sgn}} = (0.7 \pm 1.7) \times 10^{-7}$, as expected. The D^* mass distributions and the superimposed fit projections, both for RS and WS candidates, are shown in Fig. 7.2. We conclude that the parametric functions used to model the combinatorial background in our central analysis are accurate enough to reproduce the unknown parent distribution of such a fit component, and no systematic uncertainty is assigned to that.

7.1.3 Ghost background pdf

The ghost background component is essentially negligible in the RS fit model, and therefore only the contribution to the WS mass model impacts our final result. Although this is a small addition to the WS model, it cannot be neglected or treated as an additional systematic uncertainty. In fact, not considering such a component in the mass fit, would lead to a $\sim$ 1% increase in WS signal yield, which is comparable to our statistical uncertainty on the R_D parameter ($\sim$ 0.6%). However, being a small correction to the WS-to-RS ratio, any moderate mis-modelling of its mass distribution or inaccuracies in the used constraints would lead to a sub-leading bias in the determination of WS signal yield compared to the scenario where no action is taken and the full bias is assessed as a systematic uncertainty. It is also worth mentioning that the removal of this component already has a statistical uncertainty, on the R_D parameter, associated with its modelling of about 0.37×10^{-5}, about 20% of the total assigned uncertainty. The ghost soft pions component is indeed added to the mass fit with an empirical function, as described in Sec. 6.1.5, where parameters are determined by the fit itself.

Parameters constraints The pdf of the ghost soft pions background, used in the mass fits, is extracted from the CG sub-sample and it is assumed to be the same for WS and RS samples. Any possible differences in the D^* mass distribution between common ghost candidates and the residual ghost candidates (which is the background under our WS and RS signal peaks) are expected to be small (see also next paragraph). This is confirmed by the time-integrated fits in bins of Ghost Probability reported in App. A.2 where the used model is capable of correctly removing the background of residual ghost candidates (using shapes taken from the common ghost candidates data sample). As for the signal peaks we do not expect any perceptible difference between the model of WS and RS residual ghost candidates.

The absolute normalization (number of candidates) of the ghost background component in WS and RS samples is constrained to be the same, as explained in App. A.1. Although we expect this assumption to be accurate, we repeat the mass fits with and without this constraint and no significant changes in the results are observed. This is somewhat expected because the ghost background component is completely negligible in the RS sample. We prefer in any case to keep the constraint to improve the stability and the reproducibility of the fits.

Some parameters of the ghost background pdfs are fixed to the values returned from the decay-time integrated fit. This is done because the shape of the ghost background candidates is poorly dependent on the D^0 decay time. This has been precisely verified by comparing the distribution of CG candidates among different decay-time bins, as reported in App. C.

Test of goodness with data The D^* invariant mass distribution of candidates with ghost soft pions can be reproduced employing a data-driven technique, allowing us to probe for possible differences between the mass distribution of common ghost candidates (from CG sub-sample) and residual ghost candidates (those under our signal peaks).

With this aim, we take a RS D^* candidate having the value of $m(D^0\pi_s)_{\rm DTF}$ around the D^* peak, in order to select candidates where the soft pion is a genuine true soft pion. Then, with a similar procedure, we select a different RS D^* candidate where the soft pion, this time, has an opposite charge but an almost identical direction as the genuine soft pion of the D^* candidate previously selected. This latter will be our ghost soft pion. We can now recompute the numerical value of the $m(D^0\pi_s)_{\rm DTF}$ variable by using the selected genuine D^0 candidates from the first selected sample of RS D^* candidates and the ghost soft pion from the second sample, to artificially create a new sample with the same features of the CG sub-sample. In both cases, the genuine and ghost soft pion enters the T-stations acceptance having the same reconstructed VELO direction. The mass distribution of this new sample is indeed very similar to the one of the common ghost candidates. However, the mass distribution of the residual ghost candidates under our signal peaks could differ from that of the common ghost candidates because the genuine soft pions that originated the ghost cross the VELO and then go out of acceptance, hence it is not reconstructed. Most soft ghost pions present in our signal sample have this feature and populate the high asymmetry region in the vicinity of the borders of our acceptance. In these regions, a soft pion with a given charge is reconstructed (as a ghost), while the true genuine pion with an opposite charge is undetected because of the T-Stations (or fiducial cuts) acceptance. The kinematic distribution of those undetected soft pions can be easily reproduced with our artificial ghost pion candidates described above, by simply inverting the charge of the soft pion detected in the 100% asymmetry regions. This requirement allows selecting a sample of soft pions, where the genuine VELO segment is reconstructed, while the T-Stations segment is not. So we repeat the procedure described above but only with genuine D^* candidates populating the kinematic regions with very high charge asymmetry (the complementary space of our fiducial cuts) by selecting only soft pions with almost the same VELO direction and the same charge of the soft pion previously determined, in order to identify a good 'ghost' T-stations segment to be attached to the genuine VELO segment. Fig. 7.3 shows the distribution of the D^* invariant mass obtained with an artificial sample of ghost pions generated in a similar configuration of the CG candidates (both genuine and ghost pions are within the acceptance) and in a similar configuration of the residual ghost candidates (the ghost pion is in acceptance while the genuine pion is out of acceptance). The two distributions are very similar, as expected, and no additional systematic uncertainty is assigned on the assumption of using the model of CG candidates to describe the shape of residual ghost candidates.

7.1.4 Other backgrounds

In our mass model, three components are considered to describe the D^* mass line shape, *i.e.* signal, combinatorial background, and ghost background. As detailed in Sec. 7.3 the physic background from D^0 multibody mis-reconstructed decays is very small and can be neglected. Moreover, the D^* mass distribution of these backgrounds is not peaking, and, therefore, any residual (very small) contamination is inclusively accounted for in the combinatorial background component. The physics background from singly or doubly

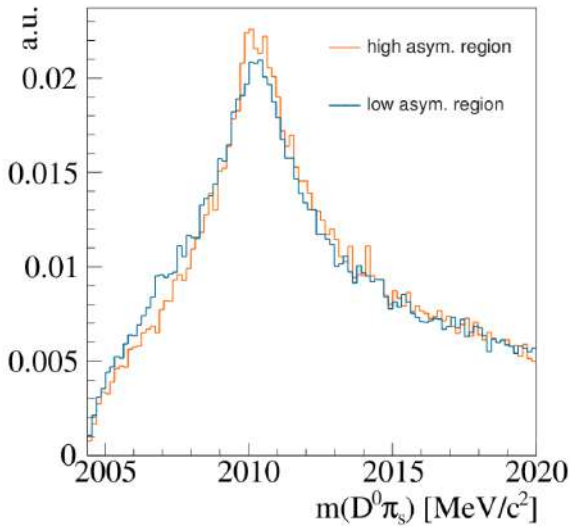

Figure 7.3: The $m(D^0\pi_s)$ distributions of artificial samples of common ghost background (blue) and residual ghost background (orange), generated with a fully data-driven technique (see text).

misidentified $D^0 \to h^+h^-$ decays has, instead, the same D^* mass line shape of our signal. This is because when computing the D^* mass value (as described in eq. 6.3), the D^0 mass is fixed to its PDG value, independently of any K/π mass assignment. As explained in Sec. 7.3, the background from singly misidentified two body decays is negligible, while the one from doubly misidentified $D^0 \to K^-\pi^+$ RS decays, that are reconstructed as $D^0 \to K^+\pi^-$ WS decays, is small, but assessable. The latter is included in the time-dependent mixing fit, as part of the WS signal, and it is treated as a nuisance parameter as explained in Sec. 9.

7.1.5 Validation with simulated experiments

Taken that the chosen empirical pdfs provide a good description of the feature of both signal and background candidates, we verified that the mass fit model is capable of disentangling signal from backgrounds without any significant bias on the parameter of interest: the signal ratio. A set of toy-simulated samples is produced and subsequently analysed following the same procedure that data undergo. For each decay-time bin, a simulated sample of WS, RS and CG is generated for a single D^0 decay mode. A single D^0 decay mode is sufficient because the measurements of R'^+ and R'^- are only slightly correlated by the systematic nuisance parameters, that are neglected in this test. In each decay-time bin the pdfs used for signal, combinatorial background, and ghost background are the ones obtained from the central fit of the corresponding decay-time bins in 2016 data sample. All the normalization values, except for that of the WS signal one, are also taken from ones fitted in each decay-time bin. The normalization of the WS signal is chosen in order to follow the expected parabolic decay-time dependency, where the physical mixing parameters are fixed to the values returned by the global fit [27]. The average of the (squared) decay-time in each decay-time bin is also chosen to be the

one observed in 2016 $K^-\pi^+$ data. Each simulated decay-time bin is fitted with the mass fit model used to fit data, as explained in Sec. 6.1.6. Then the decay-time dependency of the measured ratios is fitted minimizing a simplified version of the χ^2 used to fit data (Eq. 9.1), where all systematic nuisance parameter are removed and only one D^0 decay mode and data-taking period is considered. Only three parameters of interest are fitted: R_D, y' and x'^2. This is the parametrization used in the previously published mesurement [10], however, the parametrization is irrelevant for this test. This procedure is repeated 200 times, each time generating a different set of simulated samples. Each time, knowing the real value of the physical parameters in input, the pulls of the three fitted parameters are computed, populating the histograms reported in Fig. 7.4. The central values are compatible with zero, validating the analysis procedure and showing that the mass fit model is capable of disentangling signal from backgrounds, also accounting for the changing left tail from secondary decays.

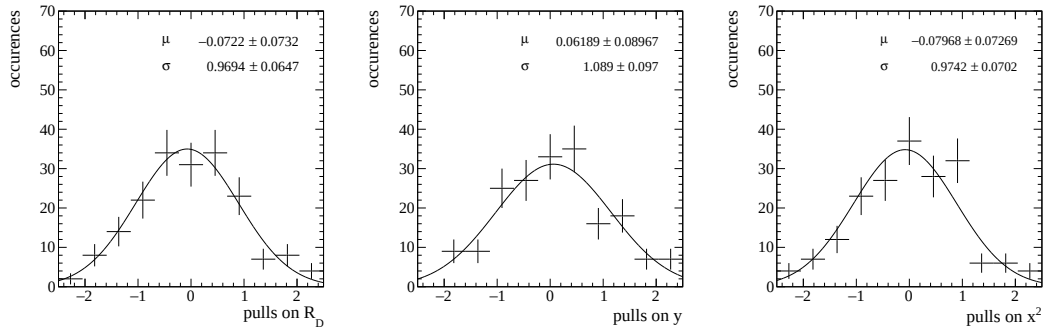

Figure 7.4: Distributions of the pulls of the three fitted parameters (R_D, y' and x'^2) in the measurements to the toy simulated sample. The central values are compatible with zero, validating the analysis procedure.

7.2 Instrumental asymmetries

Instrumental charge asymmetries, such as the production asymmetry between D^{*+} and D^{*-} and the detection asymmetry between positive and negative soft pions, may bias the decay-time ratio and mimic a physical *CP*-violating asymmetry. These asymmetries are mainly due to the following reasons: the initial state (pp collisions) at the LHC is not *CP* symmetric, the LHCb detector is not perfectly left-right symmetric, and pattern recognition, track reconstruction, and selections are intrinsically asymmetric since the detector is made of matter. Appendix B reports the mathematical derivation of the instrumental asymmetries correction for both the standard observable R and the alternative observable R' used in this analysis. As stated in the appendix, the relationship between $\tilde{R'}_i^{\pm}$, the measured value of the WS-to-RS ratio in the decay-time bin i (affected by the instrumental asymmetry), and the theoretical expected value $R_i'^{\pm}$ in the same decay-time bin i is

$$\tilde{R'}_i^{\pm} \simeq R_i'^{\pm} \cdot \left(1 \pm 2A_{D^*\pi_s}^{\int i\pm}\right), \tag{7.9}$$

where $A^{\int i\pm}_{D^*\pi_s}$ is the integrated instrumental asymmetry in the decay-time bin i, coming from the production of the $D^{*\pm}$ and the detection of the $\pi_s^\pm$, for the $K^+\pi^-$ (+ superscript) and $K^-\pi^+$ (− superscript) samples, respectively. For small π_s detection asymmetries in the chosen kinematics domain[1], it can be safely assumed that

$$A^{\int i}_{D^*\pi_s} \equiv A^{\int i+}_{D^*\pi_s} \simeq A^{\int i-}_{D^*\pi_s}. \tag{7.10}$$

These nuisance asymmetries are measured by exploiting the control sample of $D^{*+} \to D^0(\to K^+K^-)\pi_s^+$ decays, collected with identical conditions and requirements as our RS and WS signal decays[2]. As shown in the appendix, if Eq. 7.10 does apply and the direct *CP* asymmetry in the RS sample is assumed to be negligible, a good estimator for $A^{\int i}_{D^*\pi_s}$ is

$$\overline{A}^{\int i}_{D^*\pi_s} \equiv \widetilde{a}_i^{KK,\text{wgt}} - a^{KK}_{CP,i}, \tag{7.11}$$

where $\widetilde{a}_i^{KK,\text{wgt}}$ is the raw asymmetry of the KK sample in the decay-time bin i, measured after a kinematic weighting to the RS sample, and $a^{KK}_{CP,i}$ is the physical *CP* asymmetry of the $D^0 \to K^+K^-$ decay mode in the decay-time bin i. The latter term is derived from external inputs: the direct *CP* asymmetry, $a^d_{K^+K^-}$, and the time-dependent *CP* asymmetry, ΔY. The values of this external input are taken from the world average performed by HFLAV group [27] and dominated by LHCb measurements [2, 46].

The LHCb measurement of $a^d_{K^+K^-}$ makes use of the same RS and KK data samples of this analysis (the offline selection differs from the one used here, but they are largely overlapped). However, this is not a big issue, since correlations between that measurement and this one are very small, and therefore completely negligible. The uncertainties of our measurements are mainly dominated by the size of WS decays sample, while the measurement of $a^d_{K^+K^-}$ is dominated by the size of the calibration data samples ($D^+ \to \bar{K}\pi^+$, $D^+ \to K^-\pi^+\pi^+$, $D_s^+ \to \phi\pi^+$, $D_s^+ \to \bar{K}K^+$) utilized to remove any contribution from detection and production charge asymmetries. The correlation from sharing the $D^0 \to K^-\pi^+$ CF decays can be safely neglected since the contribution of this uncertainty to $a^d_{K^+K^-}$ is almost null. The correlation from sharing the $D^0 \to K^+K^-$ sample is also very small, at a level of a few per cent or less. A correlation of 5% is indeed reported between the D^+ and D_s^+ methods in the $a^d_{K^+K^-}$ measurement, where the $D^0 \to K^+K^-$ decays are shared between the two methods. Here, we expect a much smaller correlation, since the asymmetry correction is just a small correction to some of our physics observables, and therefore can be safely ignored.

However, it is worth reminding that, as a consequence of using the $D^0 \to K^+K^-$ sample to remove detection and production charge asymmetries, and, therefore, using as external input the LHCb measurement of the direct CP asymmetry, $a^d_{K^+K^-}$, the measurement of D^0-$\bar{D}^0$ mixing and *CPV* parameters described in this thesis with WS and RS decays assumes that the direct *CPV* in CF $D^0 \to K^-\pi^+$ decays is equal to zero[3].

[1] The soft pion detection asymmetry is small everywhere due to fiducial cuts and the combination of the magnet polarity.

[2] Requirements on PID variables are different but they do not affect the final results.

[3] This makes the standard and alternative observables, as defined in Eq. 2.65 and 2.67, identical also from a

7.2.1 Measurement of $\tilde{a}^{\text{wgt}}(KK)$

The $D^0 \to K^-K^+$ candidates are selected through the Turbo line `Hlt2CharmHadDstp2D0Pip_D02KmKpTurbo`. At the offline level, candidate decays are further required to satisfy the selection criteria applied to the D^0, π_s^+ and D^{*+} candidates in the $K^-\pi^+$ mode, as described in Table 5.2. A weighting procedure is applied, separately for each data-taking period and D^0 decay-time bins, to precisely equalize the kinematics of already very similar $D^0 \to K^+K^-$ decays to that of $D^0 \to K\pi$ RS decays. Weights are computed by comparing the six-dimensional ($p_T(D^0)$, $\eta(D^0)$, $\phi(D^0)$, $p_T(\pi_s^+)$, $\eta(\pi_s^+)$, $\phi(\pi_s^+)$) background-subtracted[4] D^0,π_s^+ kinematical distribution of the KK sample to match the one of the RS signal. The reweighting is performed with the `GBReweighter` algorithm from the `hep_ml` library [82]. As an example, the comparison of $D^0 \to K^-\pi^+$ and $D^0 \to K^-K^+$ before and after the reweighting for 2018 sample in a given D^0 decay-time bin is shown in Fig. 7.5. The comparison for all D^0 decay-time bins and for each the data-taking period can be found in App. F.

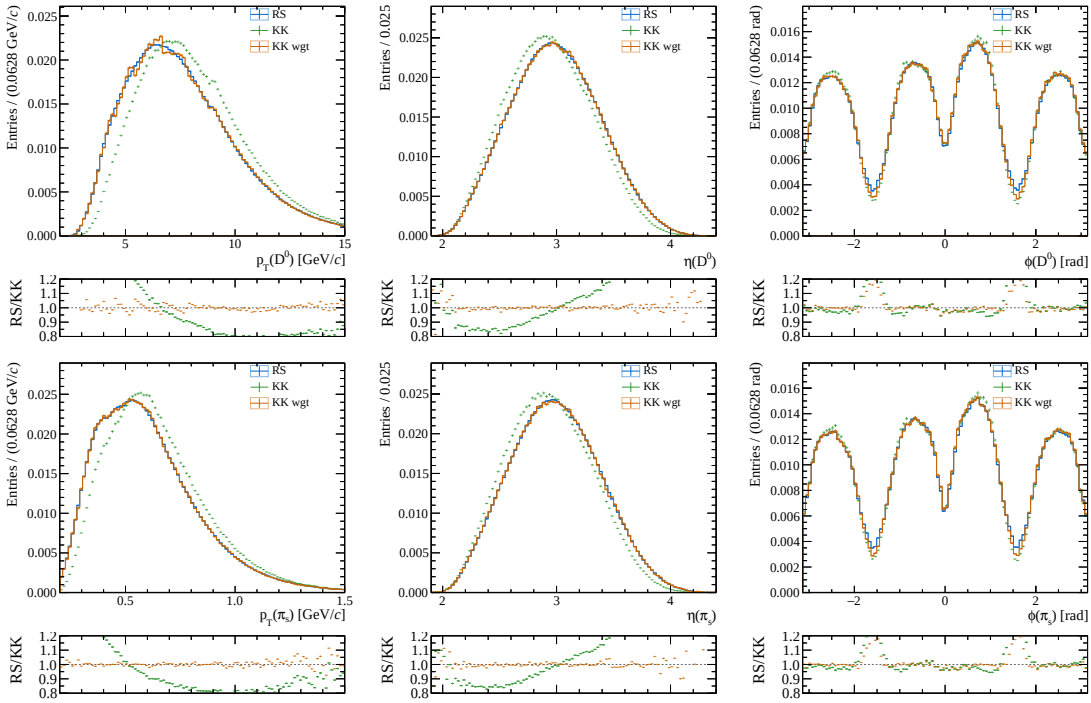

Figure 7.5: Comparison between normalized and background-subtracted kinematic distributions for D^{*+} decay samples, before and after kinematic weighting procedure applied in the first bin of D^0 decay-time for the 2018 data sample. For each plot, the bottom panel shows the ratio between the distributions.

The raw asymmetries, in each sub-sample, are measured by simultaneous binned χ^2 fits to the invariant mass distributions of D^{*+} and D^{*-} decays. The signal and background models are analogous to the ones presented in Sec. 6.1.2. The fit projections

purely theoretical point of view.
[4]A sideband subtraction is performed as explained in Sec. 6.2.

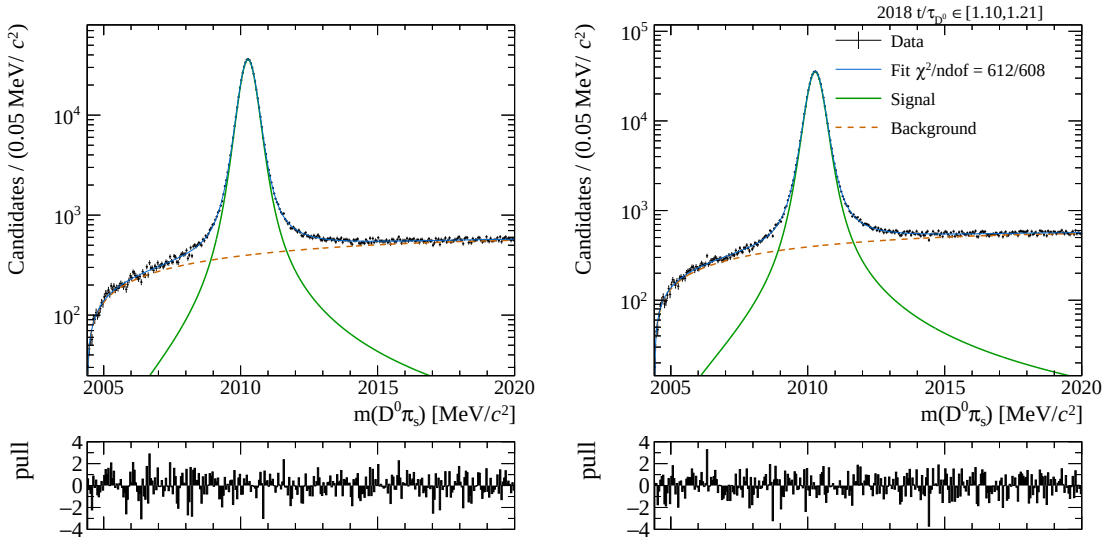

Figure 7.6: Fit projections to the mass distributions of $D^0 \to K^-K^+$ candidates, for a 2018 sample in a representative D^0 decay-time bin.

to the mass distributions of $D^0 \to K^-K^+$ candidates are shown in Fig. 7.6, where the 2018 sample in a typical D^0 decay-time bin is displayed. The fit projections to the mass distributions in each decay-time bin and each data-taking period can be found in App. G. The obtained raw asymmetries are reported in Tab. 7.1 and shown in Fig. 7.7, separately for data-taking periods and D^0 decay-time bins.

decay-time bin	$\widetilde{a}^{KK,\text{wgt}} \times 10^3$		
	16	17	18
0.40 - 0.64	-6.0 ± 1.3	-6.9 ± 1.1	-5.1 ± 1.0
0.64 - 0.77	-3.3 ± 1.1	-4.4 ± 1.1	-7.8 ± 1.0
0.77 - 0.88	-5.1 ± 1.1	-6.9 ± 1.1	-6.7 ± 1.0
0.88 - 0.99	-5.4 ± 1.1	-8.6 ± 1.0	-6.0 ± 1.0
0.99 - 1.10	-2.5 ± 1.1	-8.1 ± 1.0	-6.9 ± 1.0
1.10 - 1.21	-6.0 ± 1.1	-7.0 ± 1.1	-7.1 ± 1.0
1.21 - 1.33	-7.0 ± 1.0	-6.2 ± 1.1	-8.1 ± 1.0
1.33 - 1.46	-1.8 ± 1.0	-6.7 ± 1.1	-7.3 ± 1.0
1.46 - 1.61	-4.5 ± 1.0	-7.5 ± 1.0	-6.8 ± 1.0
1.61 - 1.77	-2.4 ± 1.0	-4.8 ± 1.1	-6.3 ± 1.0
1.77 - 1.97	-4.2 ± 1.0	-7.6 ± 1.0	-8.1 ± 1.0
1.97 - 2.21	-4.9 ± 1.0	-6.5 ± 1.1	-6.8 ± 1.0
2.21 - 2.51	-6.9 ± 1.0	-8.2 ± 1.1	-6.7 ± 1.0
2.51 - 2.93	-6.4 ± 1.0	-5.7 ± 1.1	-6.2 ± 1.0
2.93 - 3.23	-5.7 ± 1.5	-9.9 ± 1.5	-8.6 ± 1.4
3.23 - 3.65	-4.6 ± 1.5	-9.8 ± 1.5	-6.1 ± 1.5
3.65 - 4.36	-8.1 ± 1.5	-8.4 ± 1.6	-8.3 ± 1.5
4.36 - 8.00	-4.6 ± 1.5	-6.8 ± 1.6	-5.6 ± 1.5

Table 7.1: The measured values of $\widetilde{a}^{KK,\text{wgt}}$ in each decay-time bin and for each data-taking period.

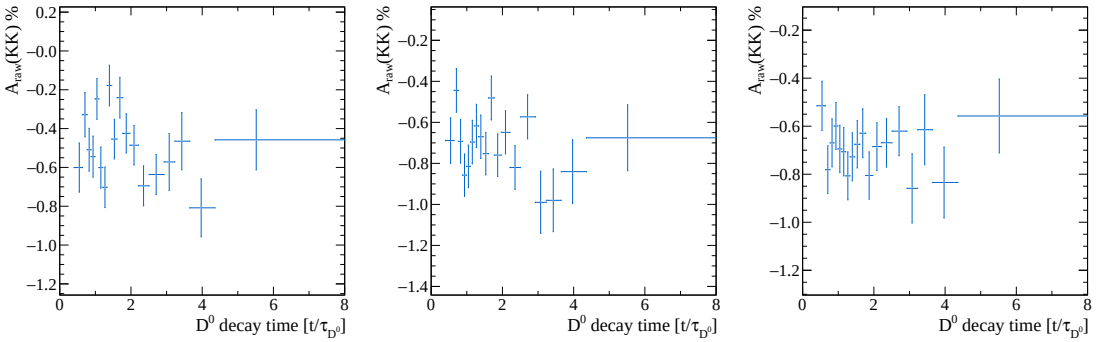

Figure 7.7: Measured raw asymmetry of the KK sample weighted to the RS sample in each decay-time bin for the 2016 (Left), 2017 (Center) and 2018 (Right) data-taking samples.

7.3 Misreconstructed candidates

Multibody and singly mis-ID We know from the previous iteration of this analysis (see [10]) that contaminations from misidentified and/or mis-reconstructed multibody charm decays are extremely small and can be neglected. This is also confirmed by all extensive studies performed in ΔY analysis (see [46]). D^0 mass requirements and PID requirements suppress misidentified and/or mis-reconstructed decays. Since some of the D^0 decay products are not reconstructed, multibody decays are suppressed by other selection requirements, such as momentum thresholds, impact parameter, vertex constraints. Moreover multibody decays produce a broader peak in the D^* mass, hence a significant fraction is fitted as combinatorial background.

In Ref. [46] a detailed study find that the main multibody decay background in the RS sample come from $D^0 \to K^-\ell^+\nu_\ell$ decays and amount to about 0.03% of the RS signal yield. The analysis described in Ref. [46] used the same PID requirement of this analysis but a tighter threshold on $m(K\pi)$ (1847.8 MeV *vs.* 1840.84 MeV), hence the contamination is enhanced by a factor of about 2. However this estimate do not take into account the effects of impact parameter and vertex constraint. Kinematic constraint on the $m(K\pi)$ invariant mass suppress the $D^0 \to K^-\ell^+\nu_\ell$ decays contamination in the WS sample a factor of 5 less than in the RS sample (see Fig. 7.9 left), however this decay is doubly suppressed by PID requirement, making this background negligible.

In Ref. [10], a quantitative upper bound on the contamination from partially reconstructed multibody decays is inferred using a simple phase-space decay generator (to evaluate the efficiency of the mass requirements) and the observed yield of two-body misidentified decays (to estimate the PID requirements efficiency). The PID requirements applied in Ref. [10] are not exactly the same as this analysis. In particular, the PID requirement on the kaon is slightly tighter: PID$K(K) > 8$ with respect to PID$K(K) > 5$ in this analysis. The dominant background to the WS sample is found to be $D^0 \to \pi^+\pi^-\pi^0$ and cannot amount to more than 0.2% of the WS signal yield. This estimate are known to be a quite large overestimation of the real contribution because the efficiency of other selection requirements would greatly further suppress such backgrounds.

Both PID and mass requirement are expected to have the same efficiency in WS and RS for the $D^0 \to \pi^+\pi^-\pi^0$ background, as shown in Fig. 7.9. Taking into account these studies, it can be concluded that multibody and singly-misID backgrounds are negligible.

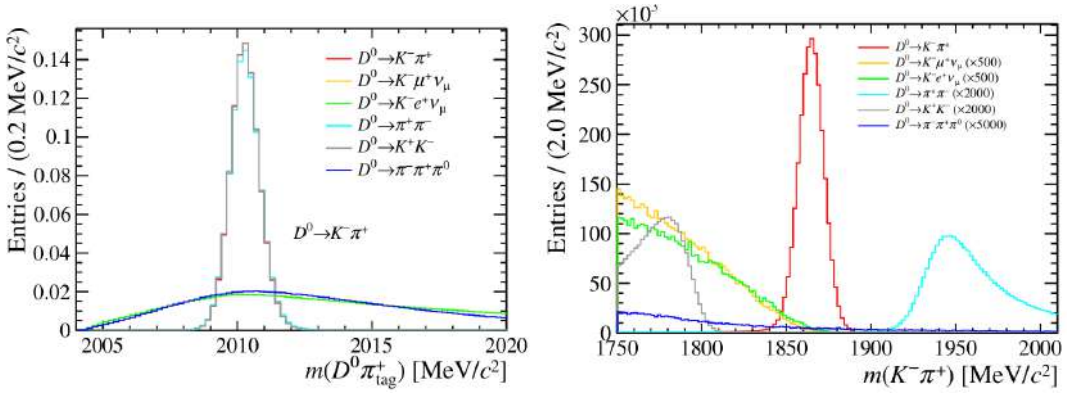

Figure 7.8: `RapidSim` distributions of (left) $m(D^0\pi_s)$ and (right) $m(K\pi)$ of the selected candidates after the sideband subtraction for signal and background components. The distributions are weighted using the PID efficiencies calculated with the PIDCalib package and, when needed, by the D_s^+–to–D^{*+} cross-section ratio. The normalisations relative to the signal component are shown in the legend. Figs. from LHCb internal Ref. [76].

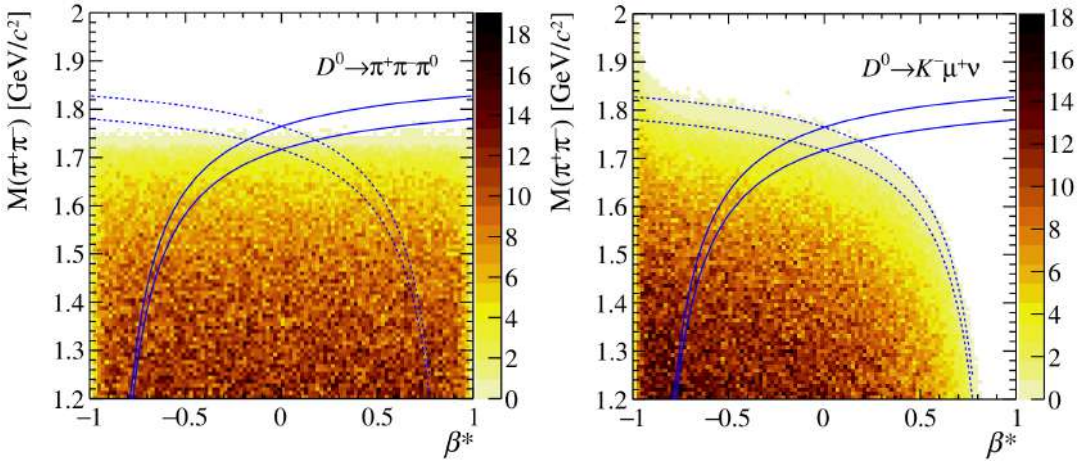

Figure 7.9: Distributions of $m(\pi^+\pi^-)$ versus the D^0 daughter momentum asymmetry, β^*, for simulated (left) $D^0 \to \pi^+\pi^-\pi^0$ and (right) $D^0 \to K^-\mu^\mp\nu_\mu$. Here for $m(\pi^+\pi^-)$ we mean the D^0 mass computed using the pion mass hypothesis for both the two D^0 daughters. The solid (dashed) lines in the plots show the WS (RS) signal region. Figs. from LHCb internal Ref. [83].

Doubly mis-ID backrgound The only physics background affecting this measurement (in addition to the combinatorial background and that of ghost pions) is that from the double misidentified RS decays, which is specifically suppressed as shown in Sec.5.3.3.

A simplified fit to the 2D distribution of the D^0 mass with standard and swapped K/π mass assignment, shown in Fig. 5.7, allows the estimation of the bias to the raw ratio from the double mis-ID background. Without any requirement on $m(K\pi)_{\rm swap}$, the bias

on the WS yield is 2×10^{-3}, in line with the one observed in the previous iteration, which translates in a bias to R_D of 8×10^{-6}, about half of the statistical uncertainty on R_D. After the requirement on $m(K\pi)_{\rm swap}$, the bias is reduced by more than a factor 5. In the fit to the decay-time dependency of the WS-to-RS ratios, performed in Sec. 9, this residual bias is subtracted from the raw ratios, assuming no decay-time dependence. Conservatively the uncertainty on this correction is taken as half the value of the correction itself.

7.4 Common candidates removal

The removal of common candidates, as described in Sec. 5.4, is the only asymmetric requirement applied to our $D \to K\pi$ signal. The fraction of discarded genuine WS events must be bounded and negligible to avoid the introduction of any bias on the measurement of R_D observable. A D^0 candidate can be associated with two distinct soft pions forming both a RS and a WS D^* candidate in three different ways:

1. the D^0 comes from a genuine RS decay, and the WS candidate is generated by associating a random slow pion to the D^0;
2. the D^0 comes from a genuine WS decay, and the RS candidate is generated by associating a random slow pion to the D^0;
3. the D^0 is genuine, but it does not come from any D^* and the two RS and WS candidates are generated by associating two random pions with different charges.

Let us consider only D^0 candidates of these types and require that both D^* associated candidates, either RS or WS, have a reconstructed mass $m(D^0\pi_s^+)$ within 3σ from the nominal D^* mass[5]. If a D^* candidate is genuine, its mass will almost always be in a 3σ range around the nominal D^* mass. If a D^* candidate is generated with the association of a random slow pion, it will satisfy this mass requirement with a given probability p. Therefore, the numbers of D^0 candidates of each type are:

1. $N_{RS} \cdot p$,
2. $N_{WS} \cdot p = R_D \cdot N_{RS} \cdot p$,
3. $N_{D^0} \cdot p'^2$,

where R_D is the time integrated WS-to-RS ratio. Here p' is the probability that the association of a random slow pion to a true D^0, not coming from a D^* decay, would produce a fake D^* with a mass in the selected window[6]. Hence in this sample[7] the fraction of type 2 events is:

$$f = \frac{n(2.)}{n(1.)+n(2.)+n(3.)} = \frac{R_D \cdot N_{RS} \cdot p}{N_{RS} \cdot p + R_D \cdot N_{RS} \cdot p + N_{D^0} \cdot p'^2} \lesssim \frac{R_D \cdot N_{RS} \cdot p}{N_{RS} \cdot p + N_{D^0} \cdot p'^2} \lesssim R_D.$$

[5]The WS-RS common candidates that we vetoed do not have a mass constraint on WS candidates, however here we are trying to estimate the number of discarded true WS decays and almost all of these satisfy this requisite.

[6]In principle this probability could be different from p.

[7]D^0 candidates associated with a RS and a WS D^* candidates with $m(D^0\pi_s^+)$ within 3σ from the nominal D^{*+} mass.

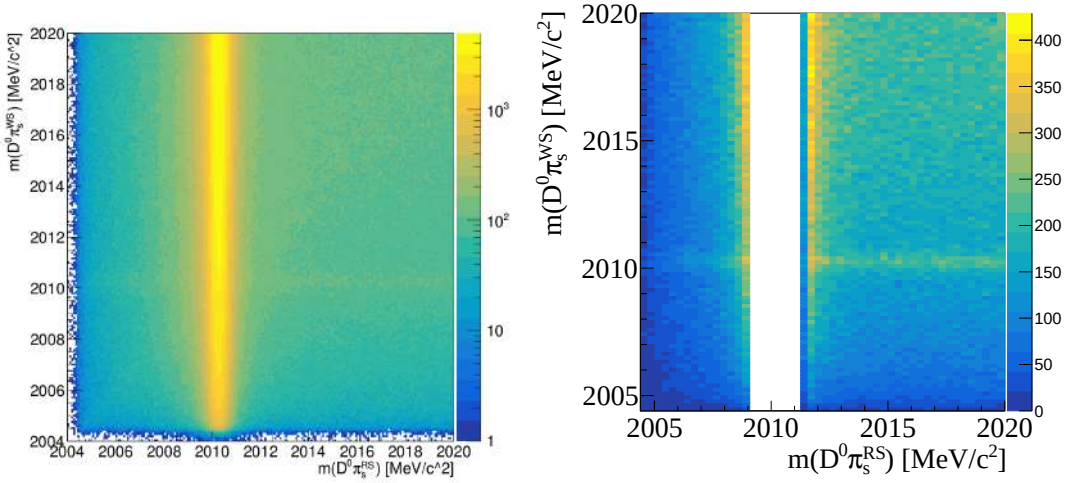

Figure 7.10: D^* mass distribution of common candidates, where the requirement on the D^* mass of the RS candidates has been relaxed, computed using the WS soft pion versus the one that uses the RS soft pion. Here ghost are removed requiring $\theta(\pi_s^{\rm RS}, \pi_s^{\rm WS}) > 1 \times 10^{-3}$ rad. On the left the full sample is shown, while on the left the RS signal region is removed in order to increase the colour dinamic and make the true WS signal more visible.

(7.12)

This same quantity is estimated by a simplified fit to the 2D distribution of D^* mass of common candidates computed using WS versus RS soft pion. The estimated ratio between true RS and true WS is about 0.3%, as expected. We are interested in the absolute bias (*i.e.* number of true WS removed with respect to the WS signal yield). Considering that the WS signal yield is about three times the statistic of the common sample ($n(1.) + n(2.) + n(3.)$) and that $R \sim 4 \times 10^{-3}$, we conclude that the bias on WS yield is about 0.1%. It follows that the bias on the measurement of the R_D parameter is $\sim 4 \times 10^{-6}$: at least five times smaller than the statistical uncertainties. In the fit to the decay-time dependency of the WS-to-RS ratios, performed in Sec. 9, this residual bias is subtracted from the raw ratios, assuming that the fraction of removed WS is constant, thus this is a multiplicative correction. Conservatively the uncertainty on this correction is taken as half the value of the correction itself.

Chapter 8

Decay-time biases

This chapter presents and asses the known biases to the previously determined raw average values of the D^0 meson decay time, in each decay-time bin, focusing on the main background source and on the secondary D^* decays. A new technique developed to remove all time biases, making use of the LHCb simulation after an in-depth tuning process, is also detailed.

8.1 Decay-time bias sources

The raw average decay time measured in Sect. 6.2 is computed as

$$t = \frac{\mathrm{FD}(D^0) \cdot \overline{m}_{D^0}}{p(D^0)}, \tag{8.1}$$

where $\mathrm{FD}(D^0)$ is the D^0 flight distance computed from the PV to which the D^* is associated, $p(D^0)$ is the D^0 momentum and $\overline{m}_{D^0}$ is the value of the D^0 mass as averaged from the PDG. This measurement of the proper decay time can be affected by different types of bias:

- background from secondary D^* not produced in the primary vertex, but originating from a B meson decay;
- the D^0 flight distance measurement can be biased, *e.g.* due to trigger selection;
- the D^0 can be associated with the wrong PV due to pileup;
- the D^0 momentum can be biased;
- other unsubtracted backgrounds.

Next sections are fully devoted to the methodologies and techniques developed in this thesis to remove all the biases mentioned above with the desired level of precision. Some of these methods are new and are implemented here for the first time.

8.1.1 Secondary D^{*+} decays

Along with primary D^{*+} produced in the PV, a fraction of the data sample consists of secondary D^{*+} produced from $\overline{B}^0$ or $B^\pm$ decays. Secondary decays are a background

source that can bias the determination of mixing parameters if not adequately treated. In particular, the bias produced by this background was the largest source of systematic uncertainty in the previous iteration of this analysis [10] and the decay-time bias from this source is the most relevant one. The reconstructed decay time of these D^0 candidates is systematically larger than the true decay time because it is calculated from the primary vertex,[1] which does not coincide with the D^0 production vertex, as shown in Fig. 8.1. The average lifetime of $\overset{(-)}{B^0}$ ($B^\pm$) is 1.52 ps (1.64 ps), which is nearly a factor 4 larger than the lifetime of the D^0 meson ($\sim$ 0.41 ps). We are interested in the determination of the

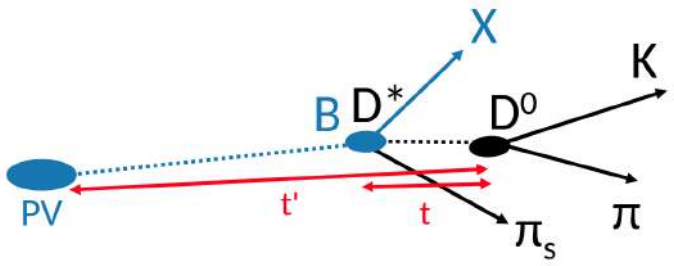

Figure 8.1: Simple sketch of a secondary D^{*+} decay.

WS-to-RS ratio of promptly-produced decays in the i^{th} decay-time bin:

$$R_i^P \equiv \frac{N_i^P(WS)}{N_i^P(RS)}, \tag{8.2}$$

where N_i^P is the number of primary decays. However, secondary decays contaminate the WS and RS samples. So the observed WS-to-RS yield ratio, $\widetilde{R}_i$, is actually equal to:

$$\widetilde{R}_i \equiv \frac{N_i^P(WS) + N_i^S(WS)}{N_i^P(RS) + N_i^S(RS)}, \tag{8.3}$$

where N_i^S is the number of secondary candidates. $\widetilde{R}_i$ can also be written as follows,

$$\begin{aligned}
\widetilde{R}_i &= \frac{N_i^P(WS) + N_i^S(WS)}{N_i^P(RS) + N_i^S(RS)} = \\
&= \frac{N_i^P(WS)}{N_i^P(RS)} \frac{N_i^P(RS)}{N_i^P(RS) + N_i^S(RS)} + \frac{N_i^S(WS)}{N_i^S(RS)} \frac{N_i^S(RS)}{N_i^P(RS) + N_i^S(RS)} = \\
&= \frac{N_i^P(WS)}{N_i^P(RS)} \left(1 - \frac{N_i^S(RS)}{N_i^P(RS) + N_i^S(RS)}\right) + \frac{N_i^S(WS)}{N_i^S(RS)} \frac{N_i^S(RS)}{N_i^P(RS) + N_i^S(RS)} = \\
&= R_i^P \cdot \left(1 - f_i^S\right) + R_i^S \cdot f_i^S,
\end{aligned} \tag{8.4}$$

[1] This is done because the D^{*+} vertex resolution is very poor and computing the D^0 flight distance from this point would degrade the D^0 decay time resolution, producing a relevant bias to the measurement.

where f_i^S is the fraction of RS secondary decays in the i^{th} decay-time bin

$$f_i^S \equiv \frac{N_i^S(RS)}{N_i^P(RS) + N_i^S(RS)}, \tag{8.5}$$

and R_i^S is the WS-to-RS ratio of secondary decays

$$R_i^S \equiv \frac{N_i^S(WS)}{N_i^S(RS)}. \tag{8.6}$$

8.1.2 Trigger induced flight distance bias

The requirement at the HLT2 level, such as $\chi^2_{\rm FD}/{\rm ndof} > 25$, introduces a bias in the D^0 flight distance, as shown in Fig. 8.2. This requirement selects by construction candidates where the decay vertex is reconstructed far from the PV (the candidates we want to select), favouring statistical fluctuations towards high positive values of the z coordinate of the decay vertex[2]. Looking at the simulated sample we see that the bias to the average D^0 decay time measurement from this source is relatively constant at different values of D^0 decay time and amounts to $\sim 0.15\,\tau(D^0)$, as we will see at the end of this section, for example in Fig. 8.23. Except for the first decay-time bins, this bias is always much smaller than the one from secondary D^* decays.

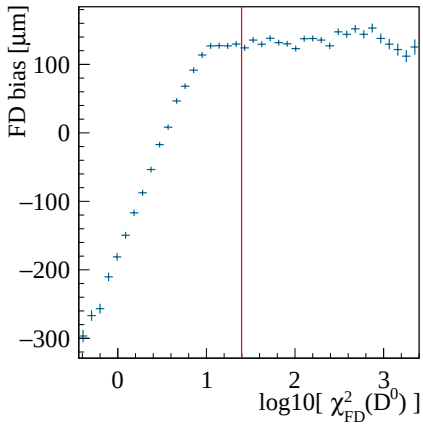

Figure 8.2: Observed bias on the D^0 flight distance as a function of $\log_{10}(\chi^2_{\rm FD})$, as observed in an unfiltered Particle Gun signal sample, after the truth-matching process. The red line indicates the HLT2 threshold.

8.1.3 Other minor sources

PV mis-association In principle, another source of bias is PV mis-association. We use the fully simulated sample, which include the full underlying event, to estimate the fraction of D^* candidates associated with the wrong PV, and a mis-association probability

[2]The behaviour of this bias, *e.g.* reason why it saturates, is not fully understood.

smaller than 0.2% is found. The distribution of the decay-time bias of those candidates to whom the wrong PV has been assigned is shown in Fig. 8.3, from which we verify that the average decay-time bias of those few candidates is also small $\sim -0.06\,\tau(D^0)$, making the final bias from this source negligible: $0.2\% \times -0.06\,\tau(D^0) = -1.4 \times 10^{-4}\tau(D^0)$.

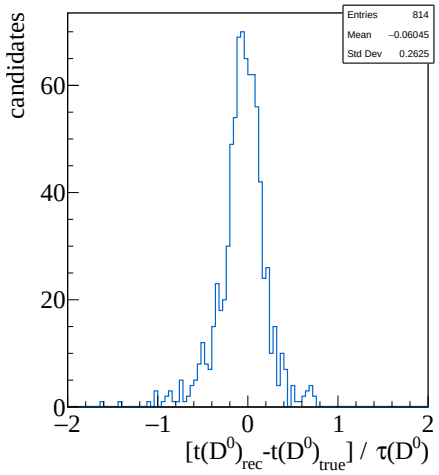

Figure 8.3: Distribution of the decay-time bias of fully simulated signal candidates to whom the wrong PV has been assigned.

D^0 momentum bias No significative bias due to trigger selection is observed in simulated candidates, and no issues are known on momentum calibration.

Other unsubtracted backgrounds The sideband subtraction method used in Sect. 6.2 allows removing the combinatorial background. The size of the unsubtracted backgrounds (doubly-misID, multibody decays and ghost soft pions) is very small in the RS sample and entirely negligible for the measurement of the average D^0 decay time.

8.2 Bias subtraction model

The expected value of the WS-to-RS ratio in a given sub-sample is the average of $R'^{+}(t)$ (as shown in Eq. 2.68) over all the candidates in that sub-sample. Therefore, given a reconstructed decay-time bin i and a signal sub-sample X[3], we can write:

$$R_i^X \equiv \langle R(t)\rangle_i^X \simeq \left\langle a + b\,t + c\,t^2\right\rangle_i^X = a + b\langle t\rangle_i^X + c\langle t^2\rangle_i^X, \tag{8.7}$$

[3]This expression is fully general, and it stands for any subsample X, selected with any requirement, because terms a, b and c are physical constant, as shown in Eq. 2.68. Here we are interested in the subsample of prompt decays, P, and or secondary decays, S.

where $\langle\,\rangle_i^X$ is the average over the candidates in the given sub-sample, and t is the true D^0 decay time. Hence, combining Eqs. 8.4 and 8.7, the observed ratio is:

$$\begin{aligned}\tilde{R}_i &= R_i^P \cdot \left(1 - f_i^S\right) + R_i^S \cdot f_i^S \\ &\simeq \left[a + b\langle t\rangle_i^P + c\langle t^2\rangle_i^P\right] \cdot \left(1 - f_i^S\right) + \left[a + b\langle t\rangle_i^S + c\langle t^2\rangle_i^S\right] \cdot f_i^S \\ &= a + b\left[\langle t\rangle_i^P(1 - f_i^S) + \langle t\rangle_i^S f_i^S\right] + c\left[\langle t^2\rangle_i^P(1 - f_i^S) + \langle t^2\rangle_i^S f_i^S\right].\end{aligned} \tag{8.8}$$

In Sec. 6.2 we measure the average values of the D^0 reconstructed decay time computed from the PV, $\tilde{t}$, that can be different from the true D^0 decay time t displayed in Eq. 8.8:

$$\langle t\rangle_i^X = \langle t + \tilde{t} - \tilde{t}\rangle_i^X = \langle\tilde{t}\rangle_i^X - \langle\tilde{t} - t\rangle_i^X = \langle\tilde{t}\rangle_i^X - \langle\delta t\rangle_i^X, \tag{8.9}$$

$$\langle t^2\rangle_i^X = \langle t^2 + \tilde{t}^2 - \tilde{t}^2\rangle_i^X = \langle\tilde{t}^2\rangle_i^X - \langle\tilde{t}^2 - t^2\rangle_i^X = \langle\tilde{t}^2\rangle_i^X - \langle\delta t^2\rangle_i^X \tag{8.10}$$

where $\delta t \equiv (\tilde{t} - t)$ and $\delta t^2 \equiv (\tilde{t}^2 - t^2)$ are the biases on the D^0 reconstructed decay time and on its square, respectively. For promptly-produced decays, $\tilde{t}$ should be an unbiased estimator of true time t. Still, the observed bias induced by the trigger selection leads to a small bias on the decay time $\langle\delta t\rangle_i^P \approx 1.5 \times 10^{-2}\tau_{D^0}$. For secondary decays, instead, the true decay time t is always smaller than the reconstructed one.
Equation 8.8, displaying the observed WS-to-RS ratio, can be rewritten as

$$\begin{aligned}\tilde{R}_i &= a + b\left[(\langle\tilde{t}\rangle_i^P - \langle\delta t\rangle_i^P)(1 - f_i^S) + (\langle\tilde{t}\rangle_i^S - \langle\delta t\rangle_i^S)f_i^S\right] \\ &\quad + c\left[(\langle\tilde{t}^2\rangle_i^P - \langle\delta t^2\rangle_i^P)(1 - f_i^S) + (\langle t^2\rangle_i^S - \langle\delta t^2\rangle_i^S)f_i^S\right] \\ &= a + b\left[\langle\tilde{t}\rangle_i - \langle\delta t\rangle_i^P(1 - f_i^S) - \langle\delta t\rangle_i^S f_i^S\right] + c\left[\langle\tilde{t}^2\rangle_i - \langle\delta t^2\rangle_i^P(1 - f_i^S) - \langle\delta t^2\rangle_i^S f_i^S\right] \\ &= a + b\left(\tilde{t}_i - \delta t_i\right) + c\left(\tilde{t}_i^2 - \delta t_i^2\right),\end{aligned} \tag{8.11}$$

where the final values of biases to the measured average decay times, $\tilde{t}_i$ and $\tilde{t}_i^2$, can be written as

$$\delta t_i \equiv \langle\delta t\rangle_i^P(1 - f_i^S) + \langle\delta t\rangle_i^S f_i^S, \tag{8.12}$$

$$\delta t_i^2 \equiv \langle\delta t^2\rangle_i^P(1 - f_i^S) + \langle\delta t^2\rangle_i^S f_i^S, \tag{8.13}$$

and their determination will be described in Sec. 8.6.3. As it will be shown in the next sections (see, for instance, Fig. 8.22), the measured value of $\langle\delta t\rangle_i^P$ is approximately constant in time. In contrast, both values of $\langle\delta t\rangle_i^S$ and f^S have an approximately linear trend as a function of decay time. Neglecting the bias due to the contamination of secondary decays would lead to an underestimation of the linear and quadratic terms and, consequently, an underestimation of the $c_{K\pi}$ and $c'_{K\pi}$ parameters. In contrast, the bias on the reconstructed decay time of prompt candidates (being constant) mainly impacts the estimate of a.

8.3 Signal discriminating variables

To determine the relative fraction of secondary D^* decays, it is necessary to identify observables with a high separation power between prompt and secondary components. The main feature that differentiates prompt from secondary decays is that the prompt D^{*+} meson is produced in the PV and its decay products (D^0 and π_s), neglecting the measurement uncertainty, should point back almost exactly to the PV[4], while for the secondary decays, this does not necessarily happen. A very direct and intuitive discrimination variable would be the distance between the PV and the D^{*+} decay vertex. However, the D^{*+} decay vertex has a very poor resolution because, due to the low Q-value of the decay, the decay products are almost collinear. Hence the uncertainties in the direction of the D^{*+} momentum is large ($\sim 10\,\text{mm}$). That is why all the quantities that should be calculated starting from the D^{*+} decay vertex are instead calculated starting from the PV, which coincides with the D^{*+} decay vertex for prompt decays.

In the following, we indicate a 3-dimensional vector with the symbol $\vec{a}$, its modulus with $|\vec{a}|$, and the associated unit vector with $\hat{a} \equiv \vec{a}/|\vec{a}|$.

8.3.1 Flight distance

The D^0 meson has a too short lifetime to be directly detected, so only its decay products ($K^\pm$ and $\pi^\pm$) can be reconstructed. From the fit to the trajectories of these decay products, it is possible to reconstruct the spatial position of the D^0 decay vertex, $\overrightarrow{\text{DV}}$. Hence, the flight distance vector is computed as

$$\overrightarrow{\text{FD}} \equiv \overrightarrow{\text{DV}} - \overrightarrow{\text{PV}}. \tag{8.14}$$

The modulus of the vector flight distance, FD, for the promptly-produced D^0, coincides with the travelled distance of the D^0 meson from the PV, where it has been produced, to the decay vertex $\overrightarrow{\text{DV}}$. On the other hand, for secondary D^0 decays, FD is the spatial distance between the PV, where the b-hadron has been produced, and the D^0 decay vertex. Since both b-hadrons and D^{*+} mesons are produced with a large boost at the LHC[5], the FD for secondary D^{*+} decays is higher than that one of promptly-produced decays, resulting in a distribution with a very long tail.

8.3.2 Direction angle

The direction angle of the D^0, θ_{DIRA}, is the angle between the unit vector of the flight distance $\widehat{\text{FD}}$ and the unit vector of the D^0 momentum $\hat{p}(D^0)$

$$\sin\theta_{\text{DIRA}} = |\widehat{\text{FD}} \times \hat{p}(D^0)|. \tag{8.15}$$

For promptly-produced $D^{*+} \to D^0\pi^+$ decays, this angle is identically zero up to resolution effects. The primary vertex, in fact, belongs to the trajectory of the D^0 meson, and,

[4]The D^* average flight distance is effectively null for our purposes.
[5]This is particularly true in LHCb where only the forward region enters the detector acceptance.

therefore, the unit vector $\widehat{FD}$ coincides with the unit vector $\hat{p}(D)$. For secondary decays, the true distribution of θ_{DIRA} is broad and different from that of prompt D^{*+} decays. Each secondary decay process contributing to the cocktail generically indicated with $B^{0,+} \to D^{*+}X$, has a different θ_{DIRA} distribution that strongly depends on the distribution of the invariant mass of the X object of the single decay. If, on average, the X mass is small, like in $B^0 \to D^{*-}e^+\nu_e$[6], the Q-value of the decay will be large. It follows that the typical angle between the D^{*+} direction and that of the total momentum of the X object will be significant, and therefore also the direction angle will be large. While if the mass of the X object is big, like in $B^0 \to D^{*-}D^*(2007)K^+$, then the Q-value will be small and, therefore, the direction angle will also be small. When the X mass is near to saturate the B^0/B^+ mass, then the θ_{DIRA} distribution for that decay becomes indistinguishable from that of prompt D^{*+} decays. An accurate knowledge of the composition of the cocktail secondaries is needed to correctly reproduce the θ_{DIRA} distribution (and that of the impact parameter) of the D^0 mesons from b-hadron secondary D^* decays.

8.3.3 Impact parameter

The impact parameter, $\overrightarrow{\mathrm{IP}}_{\vec{X}}(x)$, is the vector distance between the point of interest $\vec{X}$ and the trajectory of the particle x. The distance between the point $\vec{X}$ and a track is defined as the distance from $\vec{X}$ to the point of closest approach of the track. In our case, the point of interest is $\overrightarrow{\mathrm{PV}}$, the primary vertex associated to the D^{*+}, which for prompt candidates coincides with the D^{*+} decay vertex. The particles x of interest are the D^{*+} decay products: the D^0 meson and the soft pion π_{s}. In the following, the impact parameters will always be calculated with respect to the D^{*+} primary vertex. Therefore for brevity, we will omit the subscript $\overrightarrow{\mathrm{PV}}$.
In the LHCb experiment, trajectories of particles in the VELO, near the point of interaction, are straight lines, considering the magnetic field is nearly zero. Therefore, the trajectory of the D^{*+} meson and its decay products can be approximated with good accuracy as a straight line that passes through the $\overrightarrow{\mathrm{DV}}$. In the following, we will consider only $\mathrm{IP}(D^0)$ because $\mathrm{IP}(\pi_{\mathrm{s}})$ is highly correlated and has a much worse resolution: due to its low momentum, the soft pion is particularly susceptible to multiple scattering. The vector impact parameter of the D^0 meson, $\overrightarrow{\mathrm{IP}}(D^0)$[7], can be expressed as a function of the $\overrightarrow{\mathrm{FD}}$ and $\vec{p}(D^0)$,

$$\overrightarrow{\mathrm{IP}}(D^0) = \overrightarrow{\mathrm{FD}} - \left(\overrightarrow{\mathrm{FD}} \cdot \hat{p}(D^0)\right) \hat{p}(D^0), \tag{8.16}$$

and its modulus is just the product of the flight distance and direction angle:

$$\mathrm{IP}(D^0) \equiv |\overrightarrow{\mathrm{IP}}(D^0)| = \mathrm{FD} \cdot \sin(\theta_{\mathrm{DIRA}}). \tag{8.17}$$

The $\overrightarrow{\mathrm{IP}}$ is the projection of $\overrightarrow{\mathrm{FD}}$ on the plane perpendicular to the D^0 momentum. It may be useful to choose an axis system to be able to write the two components of the $\overrightarrow{\mathrm{IP}}$

[6]The X mass here depends on the angle between e^+ and ν_e. However, we can verify that in the secondaries' cocktail, this is one of the decay channels with the smallest average X mass.
[7]The modulus of the impact parameter $\overrightarrow{\mathrm{IP}}$ is often referred as $\mathrm{IP} \equiv |\overrightarrow{\mathrm{IP}}|$.

explicitly. A possible choice is: $\hat{\phi}(D^0)$ and $\hat{\eta}(D^0)$, *i.e.* the unit vector that point in the direction where $\phi(D^0)$ and $\eta(D^0)$ increase, that form a right-handed triad with $\hat{p}(D^0)$

$$\hat{\phi}(D^0) \equiv \frac{\hat{z} \times \hat{p}(D^0)}{|\hat{z} \times \hat{p}(D^0)|}, \qquad \hat{\eta}(D^0) \equiv \hat{p}(D^0) \times \hat{\phi}(D^0), \tag{8.18}$$

therefore we can write

$$\overrightarrow{\mathrm{IP}}(D^0) = \mathrm{IP}_\phi\, \hat{\phi}(D^0) + \mathrm{IP}_\eta\, \hat{\eta}(D^0) = \left(\mathrm{DV}_\phi - \mathrm{PV}_\phi\right) \hat{\phi}(D^0) + \left(\mathrm{DV}_\eta - \mathrm{PV}_\eta\right) \hat{\eta}(D^0). \tag{8.19}$$

The IP_ϕ component lies in the $x-y$ plane, and it is often referred to as the transverse impact parameter (TIP).

Not accounting for resolution effects, the impact parameter of promptly-produced candidates must be identically zero because θ_{DIRA} is zero. Hence, the reconstructed distribution for the $\overrightarrow{\mathrm{IP}}$ and the θ_{DIRA} observables coincides with the detector resolution. The IP_ϕ and IP_η resolutions are approximately independent and similar. IP_η resolution ($\sim 16\,\mu\mathrm{m}$) is slightly worse than the IP_ϕ one ($\sim 15\,\mu\mathrm{m}$), because the PV resolution is much worse along z and $\hat{\eta}(D^0)$ has a component along the z axis. If, for simplicity, we take $\sigma(\mathrm{IP}_\phi) = \sigma(\mathrm{IP}_\eta)$, the 2D-Gaussian distribution can be easily rewritten in polar coordinates and integrated along the angle: $\frac{1}{\sigma} \exp\left(\frac{-r^2}{2\sigma^2}\right) rdr$. This is the approximate distribution of the IP of prompt candidates. Being the modulus of $\overrightarrow{\mathrm{IP}}$, it is always positive and the distribution peaks at $\sigma \sim \sigma(\mathrm{IP}_\phi) \sim \sigma(\mathrm{IP}_\eta) \sim 15\,\mu\mathrm{m}$.

On the other side, the distribution of the $\overrightarrow{\mathrm{IP}}$ for secondary decays is broader, with a long tail, especially at high decay time values. In this case, the value of θ_{DIRA} is not zero, so candidates with high reconstructed decay time will likely also have high flight distances and, consequently, significant impact parameters. The IP_ϕ distribution of secondary decays is symmetrical with respect to zero, while the IP_η distribution shows some asymmetry because of the z axis component. This feature increases the discrimination power of the 2D $\overrightarrow{\mathrm{IP}}$ observable only marginally. Therefore, the simpler IP observable is preferred. This variable has a very good separation power and has the advantage that its distribution for prompt candidates depends little on kinematics and experimental acceptance. Figure 8.4 shows the D^0 impact parameter distribution in a sub-sample of RS candidates. We can clearly identify the prompt component at low IP values and the long tail due to the contamination of secondary decays. The separation power of this observable depends on the experimental resolution: a better resolution would reduce the width of the prompt component peak, making it possible to cut at lower IP values and increase background rejection without sacrificing signal efficiency.

As shown in Eq. 8.19, the ingredients of the IP resolution and its decay-time dependency are the PV resolution, the DV resolution and the D^0 momentum direction resolution.[8]

PV resolution The average values of the PV resolution are $\sigma_z^{\mathrm{PV}} \simeq 60\,\mu\mathrm{m}$, $\sigma_x^{\mathrm{PV}} \simeq \sigma_y^{\mathrm{PV}} \simeq 8\,\mu\mathrm{m}$. The uncertainties are approximately uncorrelated in the x, y, and z directions.

[8]The uncertainty on the D^0 momentum direction has a negligible effect on the IP resolution.

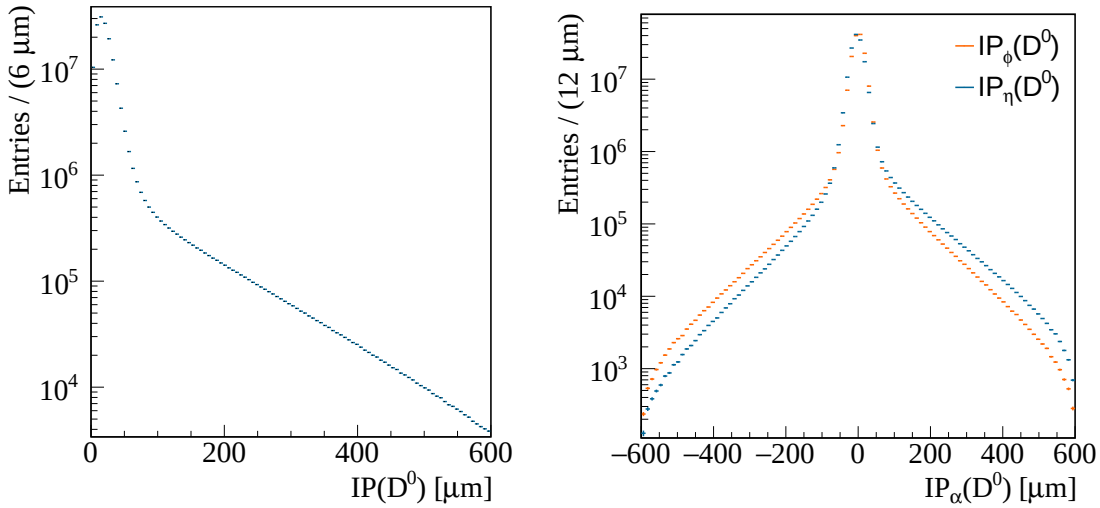

Figure 8.4: Distribution of the reconstructed D^0 impact parameter $\mathrm{IP}(D^0)$ for a subset RS candidates (Left). Distribution of the reconstructed D^0 impact parameter projection along $\vec{\phi}$ direction, $\mathrm{IP}_\phi(D^0)$ (orange), and along $\vec{\eta}$ direction, $\mathrm{IP}_\eta(D^0)$ (blue), for a subset of RS candidates (Right).

The uncertainty is worse in the z direction because of the LHCb forward geometry. The uncertainty mainly depends on the number of tracks that are involved in the vertex fit, and it shows a hyperbolic behaviour, as shown in Fig. 8.5. The trigger requirements, such as cuts on χ^2_{IP} (K), χ^2_{IP} (π) and $\chi^2_{\mathrm{FD}}(D^0)$, introduce a correlation between the PV resolution and the D^0 candidates direction and decay time[9], as shown in Fig. 8.5.

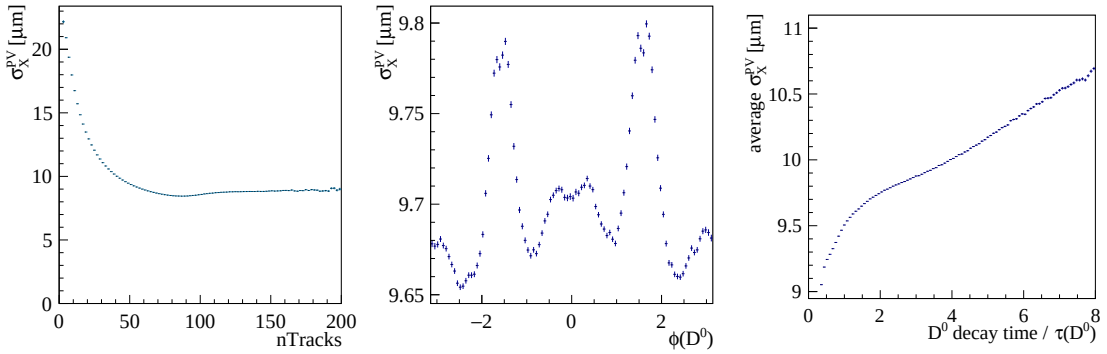

Figure 8.5: Average estimated uncertainties of the x coordinate of the D^0 PV, as observed in 2018 data, as a function of the number of tracks in the PV fit (Left), the D^0 azimuthal direction (Center) and the D^0 decay time (Right). The range of uncertainty variation in the latter two cases is much smaller than in the former; to accentuate this, the uncertainty axis scale has been zoomed in.

[9]We have verified that this correlation does not come from using the D^0 candidates in PV fit. This correlation is only trigger-induced due to the requirement on quantities that are computed using information from D^0 and the PV simultaneously.

DV resolution The decay vertex uncertainties along x, y and z are strongly correlated with each other, with the correlation depending on the D^0 direction. The best coordinates system to study these uncertainties, in which the uncertainties are almost uncorrelated with each other, is the one shown in Fig. 8.6 right. In the lab frame, the typical angle between the D^0 decay products is quite small. Hence the vertex resolution is worse approximately in the direction of the D^0 momentum, $\sigma_p^{\mathrm{DV}} \simeq 100\,\mu\mathrm{m}$. However, the uncertainty in this direction is irrelevant to the IP resolution. The resolution along the $\hat{\phi}(D^0)$ and $\hat{\eta}(D^0)$ directions is almost uncorrelated and on average is $\sigma_\phi^{\mathrm{DV}} \simeq \sigma_\eta^{DV} \simeq 13\,\mu\mathrm{m}$. The DV uncertainty shows a strong dependence on $\eta(D^0)$, as shown in Fig. 8.7. This is because the DV resolution improves when the DV is closer to the first hits on the VELO detector because the positions of the tracks are determined with a smaller lever arm. Due to the VELO geometry, this happens at low $\eta(D^0)$ values. This is one of the driving effects which correlate the DV resolution to the D^0 decay time, which we observe in Fig. 8.7.

In addition to the tracking uncertainties described above, the $\overrightarrow{\mathrm{DV}}$ estimator is also biased due to some inaccuracy in the VELO alignment. The main consequence of these misalignments is that particles crossing the VELO C-side are shifted towards the positive x direction by about 5 µm, while the ones crossing the A-side side are shifted in the opposite direction by about the same amount. The net effect of this bias is a degradation of the DV resolution, as the bias averages out at zero between left and right.

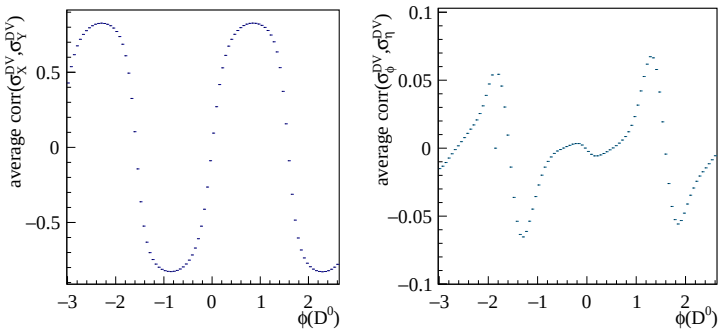

Figure 8.6: Average correlation between the estimated uncertainties of the D^0 decay vertex along x and y (Left) and along $\hat{\phi}$ and $\hat{\eta}$ (Right), as observed in 2018 data, as a function of the D^0 azimuthal direction ϕ.

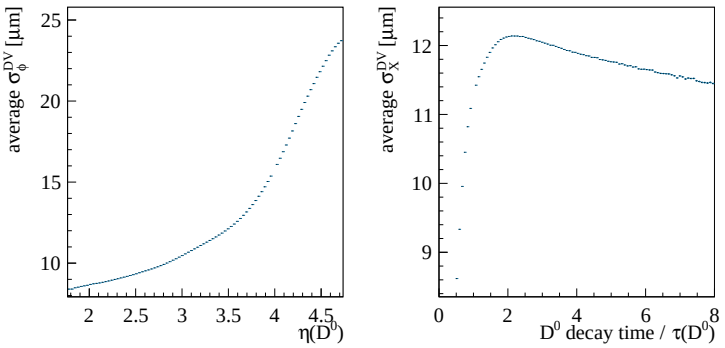

Figure 8.7: Average estimated uncertainties of the x coordinate of the D^0 decay vertex, as observed in 2018 data, as a function of the D^0 pseudorapidity (Left) and the D^0 decay time (Right).

8.4 Bias subtraction strategy

In order to reduce the fraction of secondary decays, we ask for $\mathrm{IP}(D^0) < 60\,\mu\mathrm{m}$ in the offline selection. To determine the residual secondary D^* fraction, f_i^S, in each decay time bin i, we perform a 2D template fit to sideband-subtracted data in the D^0 decay time and $\mathrm{IP}(D^0)$ variables. The templates for both the prompt and secondary components are generated by exploiting the `ParticleGun` simulation samples. However, before proceeding to the fit, some tuning is applied to the simulated samples to improve the agreement with data. The tuned `ParticleGun` simulation samples are also used to determine for each reconstructed decay-time bin, and separately for prompt (P) and secondary (S) D^* decays, the average biases: $\langle \delta t \rangle_i^P$, $\langle \delta t \rangle_i^S$, $\langle \delta t^2 \rangle_i^P$ and $\langle \delta t^2 \rangle_i^S$.

8.5 Tuning of simulation

Henceforth, it becomes important the distinction between *true uncertainties*, indicated with σ, and *estimated uncertainties*, indicated with $\overline{\sigma}$. Assuming we can repeat the measurement of an observable infinite times, the *true uncertainty* about that observable will be the standard deviation of the distribution of measurements. We call *estimated uncertainty* of an observable the uncertainty returned by the LHCb reconstruction software, which is an estimator of the true uncertainty.

During the reconstruction of an event, the estimated uncertainties on track parameters and vertices positions are used in order to compute χ^2-like variables, which are used in turn for trigger purposes (due to their high separation power). Those complex objects, *e.g.* tracks and vertices, are the results of fits to the hits positions and their estimated uncertainties. The estimated uncertainty on the position of the hit comes from a parametric model. Two parametric models were used in data reconstruction during the data taking. The first one, used from 2011 to 2016 was tuned on LHCb simulation, while the one used from 2017 to 2018 was tuned on data residuals. Only one parametric model is used in the LHCb simulation (for the simulation of any data-taking period), the first

one. Since this parametric model was tuned on the LHCb simulation, in the simulation estimated uncertainties and true uncertainties coincide.

8.5.1 PV resolution tuning

In the `ParticleGun` simulation, which lacks the underlying event, the uncertainty on the PV position must be simulated alternatively. The `ParticleGun` was produced with the standard PV smearing model: a single 3D Gaussian with $\sigma_x = \sigma_y = 8.3\,\mu\text{m}$, $\sigma_z = 45\,\mu\text{m}$, no correlation among x, y and z, equal for all the events. However, this model of the true uncertainty of the PV position is not accurate enough for our aims. Actually, the true uncertainty of the PV position has a large variability, depending on the number of fitted tracks, with σ_ϕ^{PV} and σ_η^{PV} that go from 5 µm to about 20 µm with a long right tail. This directly affects the uncertainty on the IP, determining the shape of the IP distribution of promptly-produced D^0 candidates. In particular, using a single uncertainty value for all the events does not allow for reproducing the tail of the IP distribution of promptly produced D^0 candidates and the decay-time correlation induced by the trigger selection.

Intending to also reproduce these features, we adopt a more realistic PV resolution model by using estimated uncertainties from data, superseding the PV smearing of the already simulated `ParticleGun` events. We should use the true uncertainties here. However, reproducing even approximately the distribution of the uncertainties is more important than setting the absolute scale of the uncertainties[10]. Therefore, the estimated uncertainties are assumed to be a better model than the default configuration of the `ParticleGun`.

We run over all the simulated events, and for each one, we randomly extract a candidate from the RS data sample around the D^{*+} peak. From MC truth, for each simulated event, we know the true PV position, and we smear it accordingly to the covariance matrix of the PV position[11] of the extracted data candidate. Hence, the new ones superseded the previously simulated PV smeared position and estimated covariance matrix. Then, all the variables correlated with the PV position or with its estimated uncertainty, used at the trigger or offline level, are recomputed: $\chi^2_{\text{IP}}(h^\pm)$, $\chi^2_{\text{IP}}(D^0)$, $\chi^2_{\text{FD}}(D^0)$, $\text{IP}(D^0)$ and so on. We assume that the small change in the PV reconstructed position has a negligible impact on the already reconstructed kinematics observable, *e.g.* particles' momenta. All trigger and offline requirements are applied to the recomputed variables.

This procedure has two sources of systematic uncertainty. We use estimated uncertainty on the PV position from data as a proxy for the true uncertainty, but data are inevitably already filtered with trigger requirements. Therefore, the distribution of these uncertainties could be biased. Moreover, estimated uncertainties can be a biased estimator for the true uncertainties. To account for these systematic effects in the template fit, three scenarios are considered, *i.e.* the tuning is repeated in three different configurations. The central scenario uses the estimated uncertainty on the PV position from data (`PVres_Cn`),

[10] This is because the absolute scale of the uncertainties will be fitted as a nuisance parameter later in the template fit.

[11] Those are the covariance matrix that comes from the HLT2 fit, hence DTF quantities are not used here.

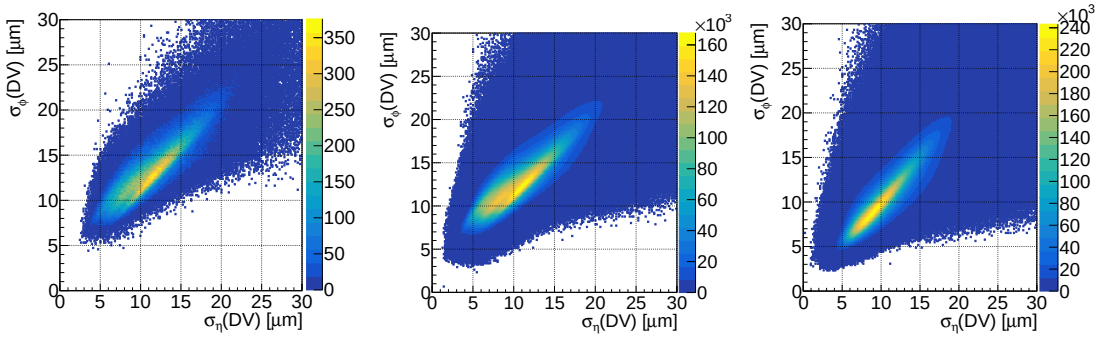

Figure 8.8: Distributions of the estimated uncertainties of the DV position, projected along the $\hat{\phi}(D^0)$ and $\hat{\eta}(D^0)$ directions, for the simulation (left), 2016 (center) and 2017 (right) data candidates.

as previously described, while the other two use the same resolutions but scaled by +10% (`PVres_Up`) and -10% (`PVres_Dw`). In the template fit, this PV uncertainty scale factor is fitted, and intermediate values are obtained through a linear interpolation of the histograms of the three scenarios.

8.5.2 DV resolution tuning

Originally in 2011, the parametrization of the estimated uncertainties of the VELO hits position was tuned on simulation. This parametrization was used in the reconstruction of real data until the end of 2016 and is still used in the simulation (also for 2017-18 simulation). For real data, estimated uncertainties matched true uncertainties in 2011, but as the VELO aged, hit resolution and average cluster sizes significantly changed. From 2012 onward, the original estimated uncertainty parametrization overestimated the true uncertainty in real data. In 2017–2018, the parametrization of the estimated uncertainty of VELO hits position used in the data-taking was updated with a tuning on real data residuals [84], hence in this period, the estimated uncertainties approximately match the true uncertainties in real data.

Since in the LHCb simulation by default, the true uncertainty of the VELO hits position coincides with the estimated uncertainty, this means that in the entire Run 2, the true uncertainty of the VELO hits position is worse in simulation than in data. This means that neglecting misalignment effects, the IP distribution of promptly-produced candidates from the LHCb simulation is wider than in real data. Figure 8.8 shows the 2D distribution of the estimated uncertainties of the DV position, along the $\hat{\phi}(D^0)$ and $\hat{\eta}(D^0)$ directions, in simulation, 2016 and 2017 data candidates. The estimated uncertainty of the DV position is directly linked to the estimated uncertainty of the VELO hits positions, hence looking at Fig. 8.8 we can see that the estimated uncertainty parametrization changed from 2016 to 2017 and that the one used in 2016 coincides with the one used in the LHCb simulation.

Two types of variables use estimated uncertainties of VELO hits positions:

- *residual* type, which is defined in terms of residuals and their errors (*e.g.* vertex χ^2, χ^2_{IP} of prompt particles); data-simulation agreement requires that the estimated

uncertainty correctly models the true uncertainty;
- *displacement* type, which measures a displacement significance given the errors (*e.g.* χ^2_{IP} of displaced tracks, χ^2_{FD}); the data-simulation agreement is good if the estimated uncertainty is the same between data and simulation.

Requirements on displacement variables ($\chi^2_{\text{IP}}(K)$, $\chi^2_{\text{IP}}(\pi)$ and $\chi^2_{\text{FD}}(D^0)$) are the most stringent and have a significant impact in determining the efficiency and its decay-time dependence. Hence in 2016, the data-simulation agreement of the decay-time distribution was good, while it worsened in 2017–2018. Table 8.1 summarises the average true and estimated uncertainty of the DV position, both in data and simulation, in 2016 and 2017–18 periods. Not being able to modify the parametrization of the estimated uncertainties

2016				2017-18			
$\sigma_{\phi,\eta}(\text{DV})$ [μm]		$\overline{\sigma}_{\phi,\eta}(\text{DV})$ [μm]		$\sigma_{\phi,\eta}(\text{DV})$ [μm]		$\overline{\sigma}_{\phi,\eta}(\text{DV})$ [μm]	
data	sim	data	sim	data	sim	data	sim
8	12	12	12	8	12	8	12

Table 8.1: Approximate average of the true and estimated uncertainty of the DV position, both in data and simulation, in 2016 and 2017–18 periods.

of the positions of the hits, what has been decided is a tuning of the distributions of the true and estimated uncertainties of the DV positions. This tuning is effective because the DV uncertainties derive directly from the VELO hit uncertainties. In particular, due to the strong dependence of the DV resolution on $\eta(D^0)$, the tuning will take place in 20 $\eta(D^0)$ bins in the $[1.7, 5.1]$ domain. The position of the DV is a 3D quantity so the covariance matrix will be a 3 by 3 matrix. For the calculation of the IP, only the $\hat{\phi}(D^0)$ and $\hat{\eta}(D^0)$ directions are relevant, and the projection along those directions has the advantage that uncertainties are almost uncorrelated.

In the following, we will indicate with the subscript x the direction of projection, which can be $\hat{\phi}(D^0)$ or $\hat{\eta}(D^0)$. Summarizing, to improve the data-simulation agreement of the IP(D^0) distribution, we need the distribution of the true uncertainties of the DV position of simulated candidates, $\sigma^{\text{sim}}_{i,x}(\text{DV})$, to match that of data candidates, $\sigma^{\text{data}}_{i,x}(\text{DV})$. On the other hand, to improve the data-simulation agreement of the decay-time distribution, we also need the distribution of the estimated uncertainties of the DV position of simulated candidates, $\overline{\sigma}^{\text{sim}}_{i,x}(\text{DV})$, to match that of data candidates, $\overline{\sigma}^{\text{data}}_{i,x}(\text{DV})$.

Tuning of DV true uncertainty Let's call the quantities in the simulated ntuples with the superscript *old* and the quantities that supersede them with the superscript *new*. The superscript *sim* will be used to indicate quantities in the simulation, while the superscript *data* for those in real data. In the absence of the data/sim superscript, we always refer to simulation.

From MC truth, for each simulated event, we know the true DV position, $\text{DV}^{\text{true}}_x$, the reconstructed DV position, DV^{old}_x, and the estimated uncertainty, $\overline{\sigma}^{\text{old}}_x$, that coincides by default with the true covariance matrix: $\sigma^{\text{old}}_x = \overline{\sigma}^{\text{old}}_x$. Thus for each candidate, we know

both the true uncertainty, *i.e.* the size σ_x^{old} of the Gaussian smearing originally applied to the true DV position, and the residual, $\text{DV}_x^{\text{old}} - \text{DV}_x^{\text{true}}$, *i.e.* the value of the random smearing originally applied to the true DV position. If a residual is scaled by a quantity k, *i.e.* the smeared DV position is updated with the new value

$$\text{DV}_x^{\text{new}} = \text{DV}_x^{\text{true}} + (\text{DV}_x^{\text{old}} - \text{DV}_x^{\text{true}}) \cdot k, \tag{8.20}$$

then the net effect is that the same quantity also scales the true uncertainty of the DV position:

$$\sigma_x^{\text{new}} = \sigma_x^{\text{old}} \cdot k. \tag{8.21}$$

In order to tune the true uncertainties in our simulation, we need a good proxy for them. Since 2017, the estimated uncertainties (used in data reconstruction) have been directly obtained from the residuals observed in data. Therefore, we can safely assume that estimated and true uncertainties coincide with a good level of approximation in 2017–2018 data samples. For the 2016 sample, instead, we decided to use the 2017 estimated uncertainties and verified a *posteriori* they are a good proxy, as expected.

Let us now consider the distributions of the true uncertainties in the sample c, where c can denote either real data or the old simulation (*i.e.* before any correction). These distributions can be computed for each bin i of $\eta(D^0)$ and for each direction x ($\hat{\phi}(D^0)$ or $\hat{\eta}(D^0)$). For each distribution, it is possible to compute the average, $\mu_{i,x}^c$, and standard deviation, $s_{i,x}^c$. It is possible to compute a scale factor so that the average and standard deviation of the distribution of the new rescaled true uncertainties match the ones of real data in each bin i of $\eta(D^0)$ and each direction x:

$$\sigma_x^{\text{new}} = \alpha_{i,x} \cdot \sigma_x^{\text{old}} + \beta_{i,x}, \tag{8.22}$$

where $\alpha_{i,x}$ and $\beta_{i,x}$ terms are defined as follows:

$$\alpha_{i,x} = s_{i,x}^{\text{data}} / s_{i,x}^{\text{sim}}, \tag{8.23}$$

$$\beta_{i,x} = \mu_{i,x}^{\text{data}} - \alpha_{i,x} \cdot \mu_{i,x}^{\text{sim}}. \tag{8.24}$$

Finally, to tune the true uncertainties of the DV position, we run over all the simulated candidates and supersede the previously reconstructed DV position with a new one computed as follows:

$$\text{DV}_x^{\text{new}} = \text{DV}_x^{\text{true}} + (\text{DV}_x^{\text{old}} - \text{DV}_x^{\text{true}}) \cdot \frac{\sigma_x^{\text{new}}}{\sigma_x^{\text{old}}}, \tag{8.25}$$

where the ratio $\frac{\sigma_x^{\text{new}}}{\sigma_x^{\text{old}}}$ depends on the $\eta(D^0)$ bin.

Tuning of DV estimated uncertainty We run over the simulated candidates and supersede the estimated uncertainties of the DV position with a new computed one:

$$\overline{\sigma}_x^{\text{new}} = \alpha_{i,x} \cdot \overline{\sigma}_x^{\text{old}} + \beta_{i,x}. \tag{8.26}$$

This is done for all three data-taking periods (2016, 2017, 2018), but the correction is notable only in 2017–18 simulated samples. The new estimated uncertainties and the new DV position are used to recompute the displacement variables (χ^2_{IP} (K), χ^2_{IP} (π) and $\chi^2_{\text{FD}}(D^0)$) and the IP. We assume this changes to the DV reconstructed position and its estimated uncertainty has a negligible impact on other kinematic variables, such as particles' momenta. All the trigger and offline requirements are applied only after the DV tuning. As for tuning the PV uncertainty, to account for the inaccuracy of this process, three scenarios are considered in the template fit. The central scenario (`PVres_Cn`) is the one described above, while the other two differ for a pre-scale of the new true resolutions, $\overline{\sigma}_x^{new}$, by +10%[12] (`PVres_Up`) and -10% (`PVres_Dw`). This DV resolution scale factor is fitted in the template fit, and intermediate values are obtained through a linear interpolation of the histograms of the three scenarios.

8.5.3 DV bias injection

A significant bias is observed in the $\overrightarrow{\text{IP}}$ distribution in data, both for D^0 and π_{s}^+. Most reconstructed D^0 mesons (or soft pions) come from the PV. Hence they should have a zero $\overrightarrow{\text{IP}}$, neglecting resolution effects. However, we observe that the peak of the resolution distribution is not centred at zero. This bias is, with high probability, due to VELO misalignments[13] and mainly affects the DV position. The PV position results from a fit to many tracks with hits around the VELO. Hence the bias is mainly averaged out[14].

In general, a misalignment of a VELO station can be modelled as a 3D translation (T_x, T_y and T_z) and a rotation around z (R_z) of each VELO station[15]. The parameters of these transformations, for a given VELO layer, can be determined by looking at the statistical mode of the IP_x (π_{s}), IP_y (π_{s}), IP_z (π_{s}) and IP_ϕ (π_{s}) distributions of soft pions with the first associated hit belonging to the VELO station under consideration. They show that the most relevant effect, clearly appreciable in the offline analysis, is that all the VELO stations placed in the right(left) half of the detector are shifted in the right(left) direction with a difference of about 10 µm between the two halves. To better visualize these shifts, it is helpful to integrate the measured bias over all the stations in each half of the VELO detector. Figure 8.9 shows the 2D distribution of the D^0 $\overrightarrow{\text{IP}}$ projections *vs.* the D^0 ϕ angle, while Fig. 8.10 displays the mean value[16] of the distribution in each ϕ bin. The observed bias depends on the data-taking year, as shown in Fig. 8.11, and run-by-run variations can also be observed.

A bias with similar behaviour but a smaller size is also observed in the `ParticleGun` simulation, as shown in Fig. 8.12. The translation in the x direction is much smaller than that observed in data (about 1 µm), while the effect in the y direction has a comparable size

[12] This value is chosen a posteriori after the template fit.

[13] A VELO misalignment compatible with the effects seen in this analysis as been observed also in other analysis [85].

[14] The assumption that the bias on the PV position from the VELO misalignment is on average small is reasonable but is not in the critical path. This is an effective correction to increase the data-MC agreement.

[15] Misalignment due to rotation around x and y are observed to be small in other LHCb analysis. However, this assumption is not used, and we will not account for the misalignment of each module independently.

[16] The mean value is obtained by fitting the distribution of the bias in x (y or z) direction, in the given ϕ bin, with a Gaussian function.

(about 0.5 µm). This is because the LHCb simulation accounts for possible misalignment, but still, now, the size of the misalignment does not match real data.

In conclusion, the size of the observed bias in data is comparable to the value of the IP resolution ($\sim$ 14 µm). Therefore, it leads to a visible deterioration of the IP uncertainty. Unfortunately, this effect is not reproduced in simulation. Hence to get good data–simulation agreement, we injected the effect into the simulation by hand. For simplicity, we use the average measured bias in each $\phi(D^0)$ bin along the three axes, as computed for each data-taking year. The bias graph is interpolated with a spline to make a smooth correction, as shown in Fig 8.13. Then we simulated each candidate depending on its ϕ we sum to DV_x, DV_y and DV_z, the corresponding bias along the x, y and z axis, respectively, as measured for that specific value of $\phi(D^0)$. The correlations between the bias along different directions can be safely neglected because the bias along the x is much more significant than the ones along y and z, making it the only relevant correction.

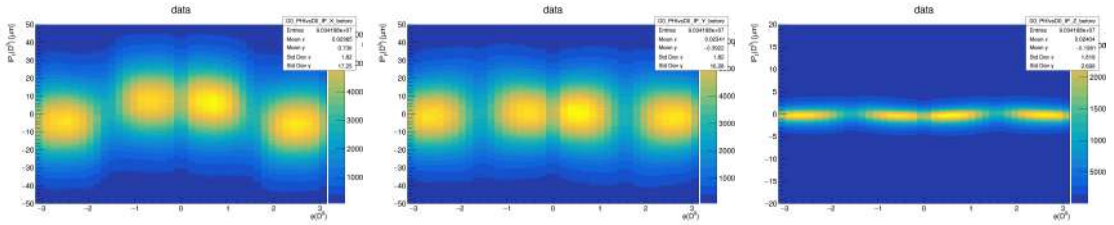

Figure 8.9: The 2D distributions of the D^0 azimuthal angle ϕ versus the D^0 impact parameter vector projection along x (Left), y (Center) and z (Right), in the 2018 data sample.

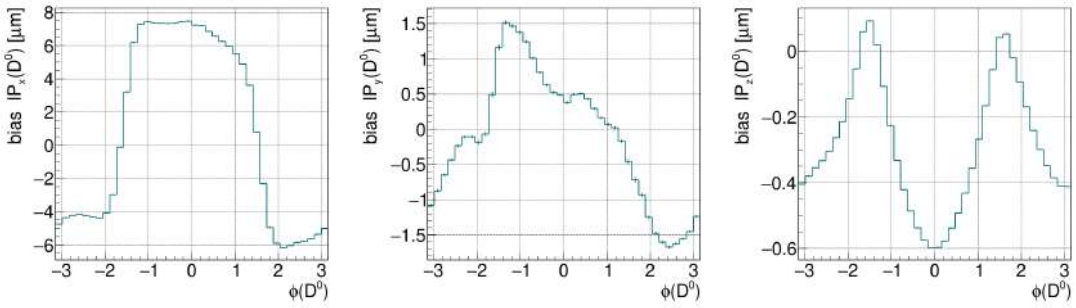

Figure 8.10: The fitted bias on the D^0 impact parameter along x (Left), y (Center) and z (Right) as a function of the D^0 azimuthal angle ϕ, in the 2018 data sample.

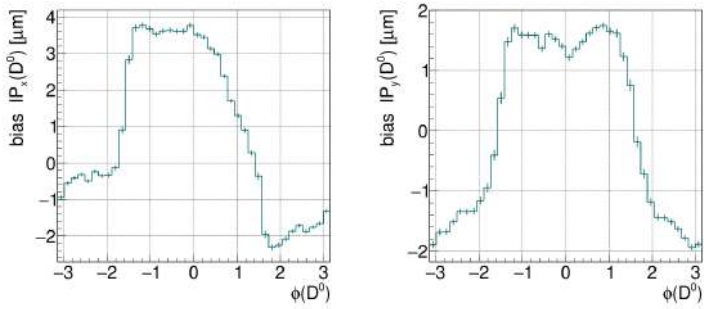

Figure 8.11: The fitted bias on the D^0 impact parameter along x (Left), y (Right) as a function of the D^0 azimuthal angle ϕ, in the 2015 data sample.

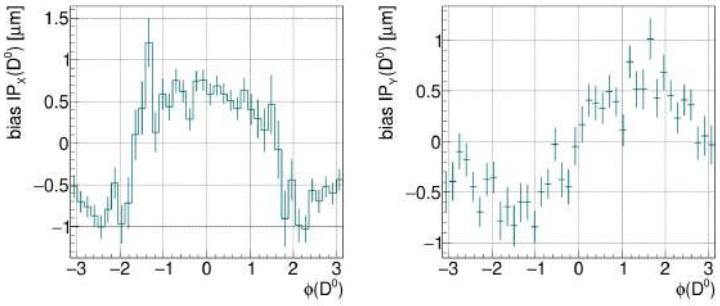

Figure 8.12: The fitted bias on the D^0 impact parameter along x (Left) and y (Right) as a function of the D^0 azimuthal angle ϕ, in the prompt simulated sample.

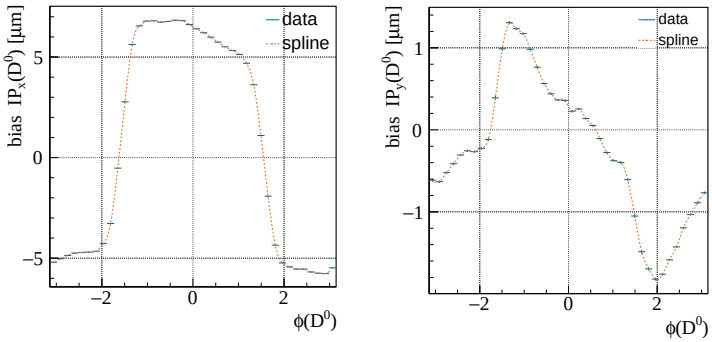

Figure 8.13: The fitted bias on the D^0 impact parameter along x (Left), y (Right) as a function of the D^0 azimuthal angle ϕ, in the 2018 data sample. The spline used in order to obtain a smooth correction is superimposed.

8.5.4 Kinematic weighting

The 6D distribution $[p_{\mathrm{T}}(D^0), \eta(D^0), \phi(D^0), p_{\mathrm{T}}(\pi_{\mathrm{s}}), \eta(\pi_{\mathrm{s}}), \phi(\pi_{\mathrm{s}})]$ of simulated candidates is weighted to that of data to account for the limited knowledge of the input momentum spectrum of the D^* mesons, and the sculpting due to trigger variables difficult to accurately reproduce in simulation (*e.g.* PID). The weighting is performed separately for the samples of prompt decays, inclusive secondary decays, and secondary decays reconstructed as $D^{*+}\mu^-$ pairs. Since the size of the available data samples is huge, much higher than simulated samples, the weighting target samples are just sub-samples of the total:

- 4% of randomly sampled data with $\mathrm{IP}(D^0) < 60\,\mu\mathrm{m}$ for each data-taking period, to weight the promptly produced simulated candidates;
- 30% of randomly sampled data with $\mathrm{IP}(D^0) \in [120, 600]\,\mu\mathrm{m}$ for each data-taking period, to weight the inclusive secondary simulated candidates;
- the full $D^{*+}\mu^-$ data sample with $\mathrm{IP}(D^0) < 600\,\mu\mathrm{m}$ for each data-taking period, to weight the $D^{*+}\mu^-$ simulated candidates.

All the data samples are sideband subtracted (the same procedure described in Sect. 6.2) to remove the combinatorial background. The weighting is performed with the `GBReweighter` class of the `hep_ml` package [82] and it is performed independently for all the data-taking periods and all the scenarios considered. The distributions of the kinematic variables of simulation and the target data samples are compared in Figs. 8.14, 8.15 and 8.16 for prompt, inclusive secondary and $D^{*+}\mu^-$ of the 2018 samples, all in the central scenario. The comparison for all the data-taking periods can be found in App. D. The agreement between weighted simulated samples and data samples is sometimes not perfect. This is likely due to a non-optimal choice of meta-parameters in training the `GBReweighter` tool. However, this is not a problem here, as the weighting aims to remove the large discrepancies observed comparing data and simulation due to macroscopic and known issues, such as the input momentum spectrum of mother particles in `ParticleGun`. All small residual discrepancies produce second-order effects on the IP and proper decay time, which are fully covered by the large systematic uncertainties assigned in the template fit (on PV and DV tracking uncertainties and on the limited knowledge of secondary decays cocktail), as will be shown in Sect. 8.6.

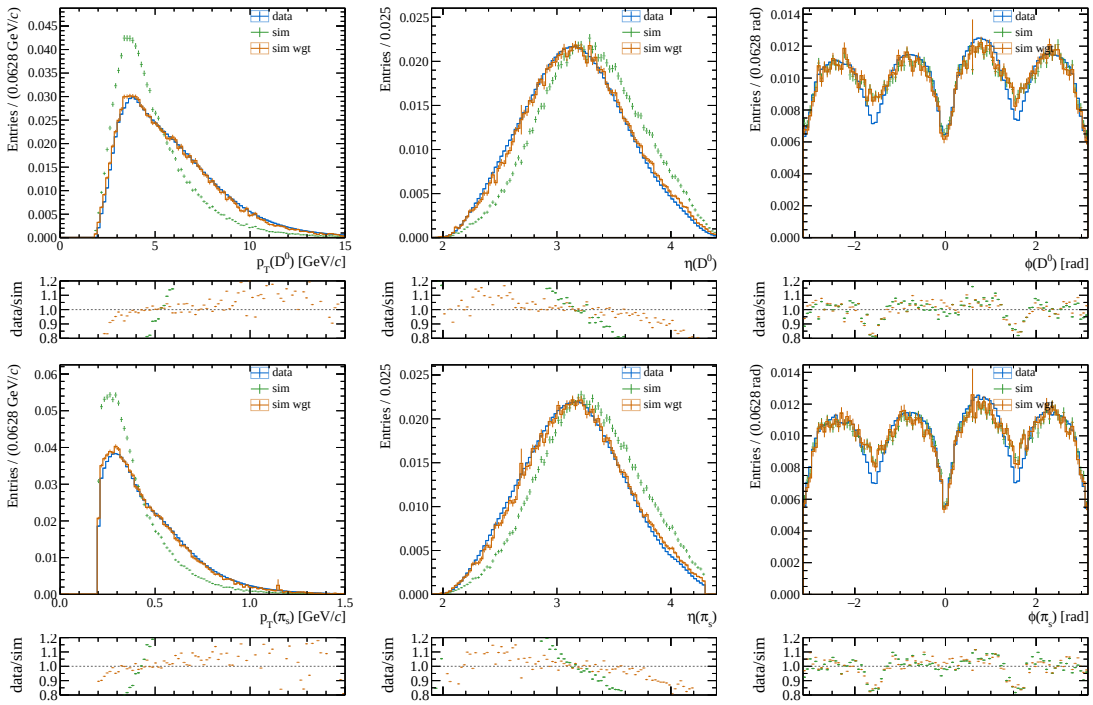

Figure 8.14: Comparison between the kinematic distributions of RS primary decays of 2018 sample in data and simulation (central scenario), both before and after the six-dimensional weighting. The data sample is selected using 4% of candidates satisfying the requirement $\mathrm{IP}(D^0) < 60\,\mu\mathrm{m}$.

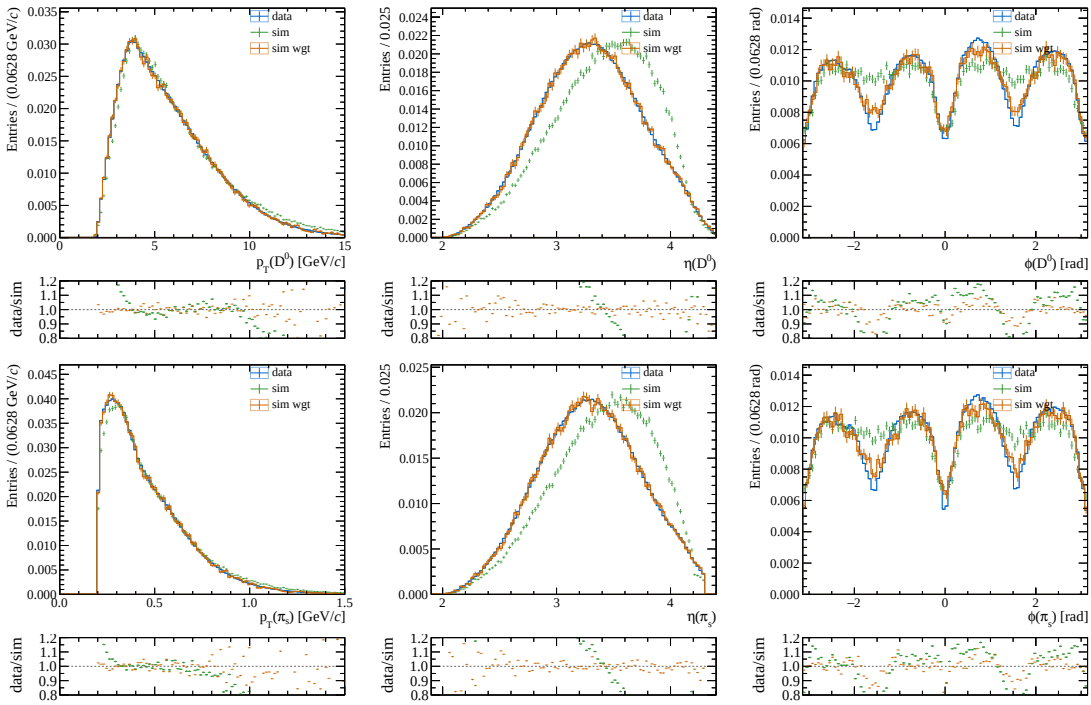

Figure 8.15: Comparison between the kinematic distributions of RS secondary decays of 2018 sample in data and simulation (central scenario), both before and after the six-dimensional weighting. The data sample is selected using 30% of the candidates satisfying the requirement $120\,\mu\text{m} < \text{IP}(D^0) < 600\,\mu\text{m}$.

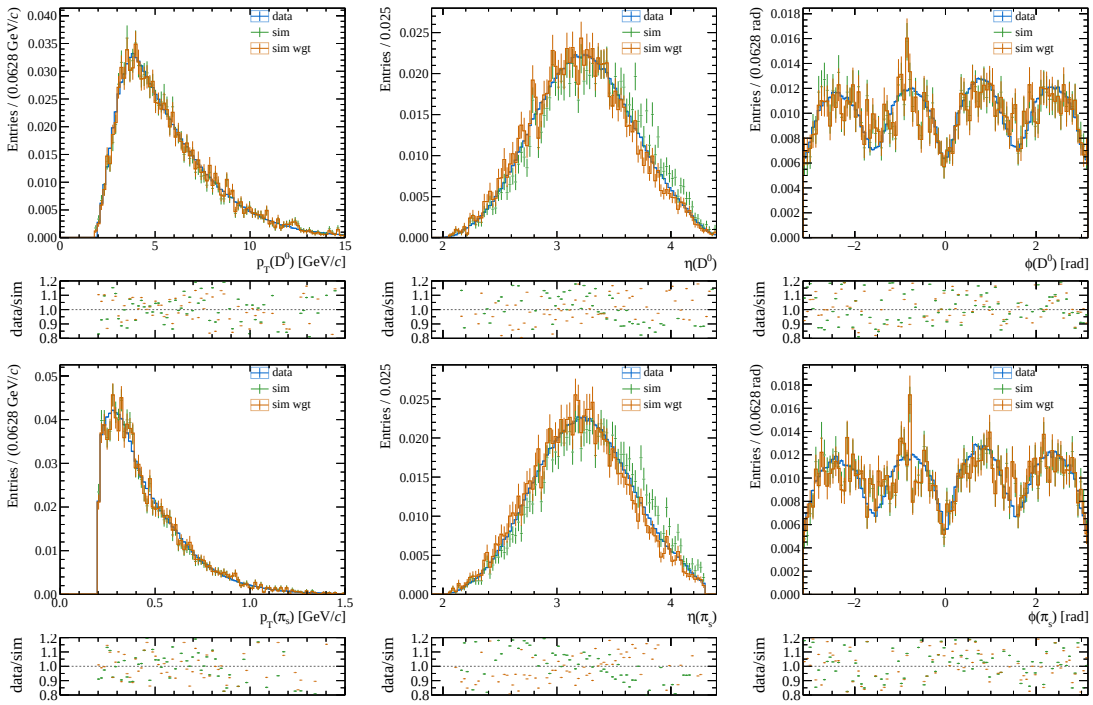

Figure 8.16: Comparison between the kinematic distributions of $D^{*+}\mu^-$ decays of 2018 sample in data and simulation (central scenario), both before and after the six-dimensional weighting. The data sample is selected using the candidates satisfying the requirement $\mathrm{IP}(D^0) < 600\,\mu\mathrm{m}$.

8.5.5 Cocktail composition

Figure 8.17 shows two comparisons between simulated samples of secondary D^* decays and data in the D^0 decay time *vs.* IP (D^0) 2D distribution. The left panel shows the differences between data with IP (D^0) > 120 μm, so that only secondary D^* are selected, and the inclusive secondaries simulation with the same IP requirements. On the other hand, the right panel shows the discrepancies between the $D^*\mu$ control data sample (see Sec. 5.5) and the $B^0 \to D^{*+}\mu^-\nu_\mu$ simulated sample. The data-simulation agreement is good for the $B^0 \to D^{*+}\mu^-\nu_\mu$ sample, while relevant discrepancies are observed in the inclusive secondaries sample. In particular, the observed discrepancy indicates a lack of simulated candidates with low values of the θ_{DIRA} (D^0) angle, which can hardly be explained due to a non-perfect simulation of the trigger requirements. This region has, in fact, such a high impact parameter value that any trigger's effect should be completely negligible. Furthermore, the good data-simulation agreement obtained by comparing the distributions of the $D^{*+}\mu^-$ secondaries sample (see Fig. 8.17) strongly suggests that the observed discrepancy is due to a limited knowledge of the composition of the secondaries cocktail mixture. The list of decay processes, reported in Tabs.5.4 and 5.5, is taken from PDG, and it is our best knowledge, at the moment, about the composition of the secondary processes in our sample. While it collects almost all decays contributing to the background of secondary D^{*+} decay modes, it is not complete, and we expect a small fraction to be missing (mainly composed of multi-body decay processes not yet observed). In addition to the uncertainty related to the knowledge of simulated decays, it is also worth mentioning that the relative fractions of some simulated decays, listed in Tabs.5.4 and 5.5, have very large uncertainties, which can potentially influence in a non-negligible way the kinematic distributions of the variables of interest of the cocktail.

In order to account for these uncertainties, a small fraction of $B^0 \to D^{*+}X_P$ decays is added to the secondary cocktail, where both the relative fraction of the decay mode and the mass of the X_P particle are unknown and will be fitted through the template fit. We assume that the relative fraction of missing decays is small[17] and that they do not cover a large range in the X_P mass spectrum. This is intended to be an effective correction, supported by the small size of observed discrepancies. Three X_P mass values (1.5, 2 and 2.5 GeV/c^2) are simulated using a toy[18] and added with 3 different relative fractions (0%, 5%, 10%) to the nominal cocktail before the kinematic reweighing. The best value of the mass of the X_P particle and its relative fraction are free parameters of the fit template and are, therefore, determined using data.

8.6 Template fit

The relative fraction of secondary decays is measured as a function of decay time employing a χ^2 template fit to the 2D $\left[\text{IP}(D^0), t(D^0)\right]$ distribution, integrated over the D^0 flavour and separately performed for each data-taking period. The binning scheme is

[17] A posteriori the fitted fraction of unknown decay is about 5%.

[18] The toy is generated using the TGenPhaseSpace [86] library, applying the LHCb angular acceptance, realistic smearing of PV and DV, and a realistic trigger selection.

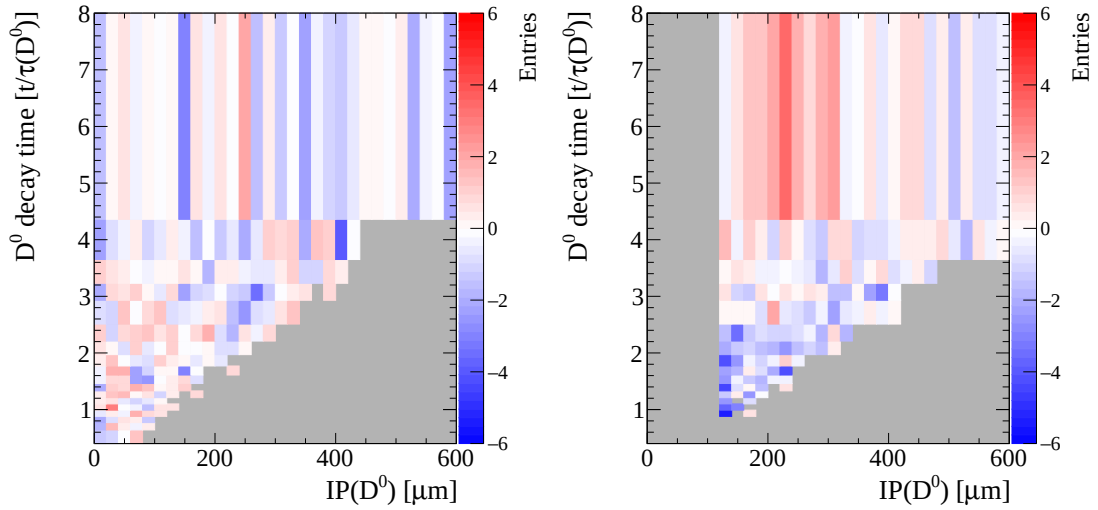

Figure 8.17: Pulls of the comparison between data and simulation, in the 2D distributions, IP(D^0) *vs.* D^0 decay time, of $D^{*+}\mu^-$ (Left) and inclusive secondary (Right) decays of the 2018 sample. The inclusive secondary decays' data sample is selected using candidates satisfying the requirement IP(D^0) $> 120\,\mu$m. Unpopulated bins are shown in grey.

30 equal bins for the IP(D^0), from 0 μm to 600 μm, and the already used (see Sect. 6.1.2) 18 bins for the D^0 decay time.

8.6.1 Multi-linear interpolation

The 2D templates of prompt and secondary decays are the result of piece-wise multi-linear interpolation of the histograms generated from the combinations of different scenarios described in the previous sections[19]. For simplicity, we describe here the methodology for a 1D template and only for one nuisance parameter, α. Thus to each bin of the 1D template, a 1D piece-wise linear interpolation is performed. We have histogram templates for distributions at nominal, $s_i(0)$, $+1\sigma$, $s_i(1)$, and -1σ, $s_i(-1)$, values of the systematic effect associated to the α parameter. At this point, it is necessary to identify a 'morphing' algorithm to determine the distribution, $s_i(\alpha)$, for each value of α. The simplest solution is the piece-wise linear interpolation for each bin, as shown in Fig. 8.18, while Fig. 8.19 displays a visualization of bin-by-bin linear interpolation of the whole distribution, $s_i(\alpha)$.

The piece-wise multi-linear interpolation for 2D templates and multiple (two or four in our case) nuisance parameters is just an extension of the method explained above in the 1D case. We have 9 template histograms for promptly-produced decays, one for each combination (3^2) of the three PV resolution scale factors, α, and the three DV resolution scale factors, β. For secondary decays, instead, we have 81 template histograms (3^4) because in addition to the 9 configurations covering PV and DV resolution uncertainties, we also have all the combinations of the three values of the X_P mass, γ, and the three values of the relative fraction of the added $B^0 \to D^{*+}X_P$ decay mode, δ. We indicate $\vec{N}_{P,i}$, the vector of the 9 prompt templates, where i is an index that runs over all the bins of

[19]For instance, our procedure follows closely what is done in the RooFit package HistFactory.

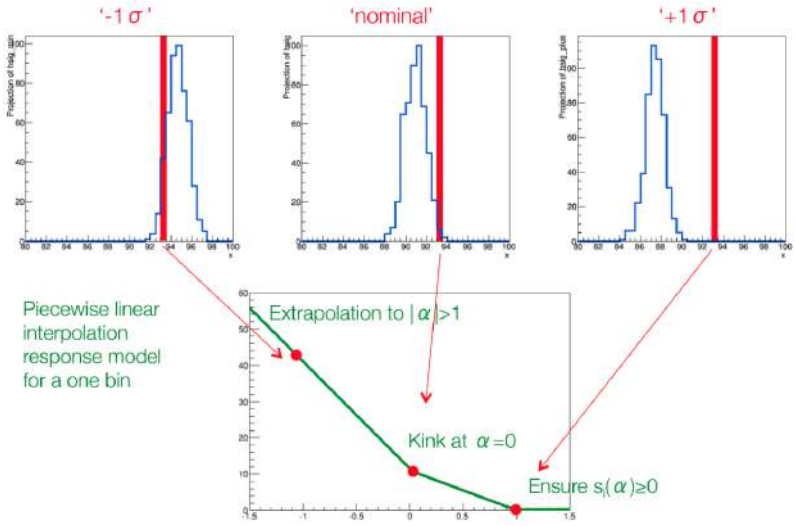

Figure 8.18: Example of piece-wise linear interpolation for a single bin of a 1D template. Fig. adapted from W. Verkerke, 2016.

each 2D histogram, while $\vec{N}_{S,i}$ is the vector of the 81 secondary templates. Hence, the 2D histograms, $N_{P,i}(\alpha,\beta)$ and $N_{S,i}(\alpha,\beta,\gamma,\delta)$ are defined as

$$N_{P,i}(\alpha,\beta) = I_{2D}(\vec{N}_{P,i}\,;\,\alpha,\beta) \qquad N_{S,i}(\alpha,\beta,\gamma,\delta) = I_{4D}(\vec{N}_{S,i}\,;\,\alpha,\beta,\gamma,\delta), \tag{8.27}$$

where I_{2D} and I_{4D} are piece-wise bilinear and quadrilinear interpolation function, respectively.

8.6.2 Beeston-Barlow method

If the number of simulated events (for prompt and secondary decays) were much higher than the number of reconstructed candidates in data, statistical uncertainties associated with each bins of Monte Carlo templates could be neglected, and the χ^2 to be minimized would have been:

$$\chi^2 = \sum_i \frac{(N_i - c_P \cdot N_{P,i}(\alpha,\beta) - c_S \cdot N_{S,i}(\alpha,\beta,\gamma,\delta))^2}{\sigma_i^2}, \tag{8.28}$$

Here c_P and c_S are the normalizations of prompt and secondary templates, respectively. Instead, N_i and σ_i^2 are the content and the variance of the bin i of the 2D data histogram, respectively. Data histogram has very high statistics and producing a large sample of simulated decays is not doable because of the computational workload. Therefore, we account for the limited statistics of the simulated samples by implementing the Beeston-Barlow method [87]. The interpolated histogram bin values, $N_{P,i}(\alpha,\beta)$ and $N_{S,i}(\alpha,\beta,\gamma,\delta)$, are estimators, affected by statistical uncertainty, for the true values, $n_{P,i}(\alpha,\beta)$ and $n_{S,i}(\alpha,\beta,\gamma,\delta)$, that we would have if disposing of infinite statistics. Those new nuisance

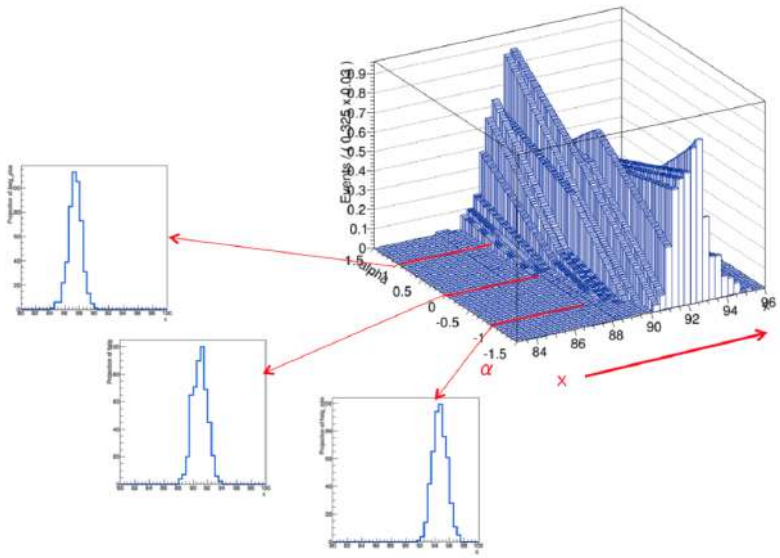

Figure 8.19: Visualization of bin-by-bin linear interpolation of the distribution, $s_i(\alpha)$. Fig. adapted from W. Verkerke, 2016.

parameters need to be fitted, so χ^2 summation becomes:

$$\chi^2 = \sum_i \frac{(N_i - c_P \cdot n_{P,i}(\alpha,\beta) - c_S \cdot n_{S,i}(\alpha,\beta,\gamma,\delta))^2}{\sigma_i^2} \tag{8.29}$$

$$+ \sum_i \frac{(N_{P,i}(\alpha,\beta) - n_{P,i}(\alpha,\beta))^2}{\sigma_{P,i}^2(\alpha,\beta)} \tag{8.30}$$

$$+ \sum_i \frac{(N_{S,i}(\alpha,\beta,\gamma,\delta) - n_{S,i}(\alpha,\beta,\gamma,\delta))^2}{\sigma_{S,i}^2(\alpha,\beta,\gamma,\delta)}. \tag{8.31}$$

We use here a Gaussian distribution instead of a Poisson distribution because the number of entries is not an integer (entries are weighted). In order to avoid any bias, we restrict our fit domain to bins with enough statistics[20], by requiring $\sigma^2(N_i) > 5$. For this reason, the variance of the bin values, $\sigma_{P,i}^2(\alpha,\beta)$ and $\sigma_{S,i}^2(\alpha,\beta,\gamma,\delta)$, is also multi-linearly interpolated. If a bin is empty, no new nuisance parameters are introduced for that bin. With this approach, we introduce about 120 new nuisance parameters for the primary template, $n_{P,i}$, and about 240 new nuisance parameters for the secondary template, $n_{S,i}$.

8.6.3 Determination of δt and δt^2

The free fitted parameters are the time-integrated normalizations of prompt and secondary templates (c_P and c_S), the four nuisance interpolation parameters (α,β, γ and δ, corresponding to PV and DV resolution scale factor, mass and relative fraction of the $B^0 \to D^{*+}X_P$ added decay) and the value of each populated bin of the templates ($n_{P,i}$ and $n_{S,i}$). The results for the fitted nuisance parameters are reported in Tab. E.2 in App. E.1. The projections of the fit results to the IP(D^0) distribution for some representative decay-

[20]We verified that the result of the fit is stable for a change of this threshold.

time bin of the 2018 data-taking period are shown in Fig. 8.20. The projections for every decay-time bin and data-taking period are reported in App. E. The agreement with data is satisfactory, as shown in Figs. 8.21. Minor discrepancies (always below 10% level) are observed mainly in the first decay time bin, likely due to inaccuracies in the reproduction of the trigger requirements in the signal simulated samples and consequently to a wrong time distribution in the first bins of decay time, which are the most sensitive to this effect.

For each scenario (combination of nuisance parameters values) and for each bin in the [D^0 decay-time,IP (D^0)] space we produce the 2D distribution of δt *vs.* δt^2, separately for simulated candidates of prompt and secondaries. Then we interpolate the [δt, δt^2] distributions of all scenarios with the same linear interpolation coefficient found as a results of the template fit to the [D^0 decay-time,IP (D^0)] distribution. Subsequently each [δt, δt^2] distribution is weighted, depending of the [D^0 decay-time,IP (D^0)] bin where it was obtained, with the same weight of that bin as resulted from the Beeston-Barlow method. We than integrate over IP bins, to obtain a unique [δt, δt] distribution for each time bin and separately for prompt and secondaries. For each of these distribution we compute the average of δt and the average of δt^2, obtaining the desired $\langle \delta t \rangle_i^X$ and $\langle \delta t^2 \rangle_i^X$, where i is the decay-time bin index and X is P or S for prompt or secondaries, respectively. The $\langle \delta t \rangle_i^X$ values are obviously correlated to $\langle \delta t^2 \rangle_i^X$. Moreover, the nuisance parameters used in the linear interpolation correlate all the values in each decay-time bin among them. The covariance matrix is found by propagating the uncertainties numerically.

For each decay-time bin, we determine the nuisance parameters δt and δt^2 that are correlated between each other and among all the decay-time bins. Figure 8.22 shows the measured values of $\langle \delta t \rangle^P$, $\langle \delta t \rangle^S$ and f^B for every reconstructed decay-time bin and every data-taking period. Those are the intermediate results used to compute the final decay-time biases, which are shown in Fig. 8.23, while the numerical values are reported in Tab. 8.2 (correlation between δt and δt^2 and among all the decay-time bins are not reported). In order to account for inaccuracy and systematic errors in the estimation of the f^B, the error is inflated by $\sqrt{\chi^2/\text{ndof}}$ from the template fit, separately for each decay-time bin. The values of inflation factors are reported in Tab. E.1 in App. E.1. Moreover, this statistical (inflated) error is summed in quadrature with the difference between the fitted central value with and without the correction to resolution and cocktail composition tunings.

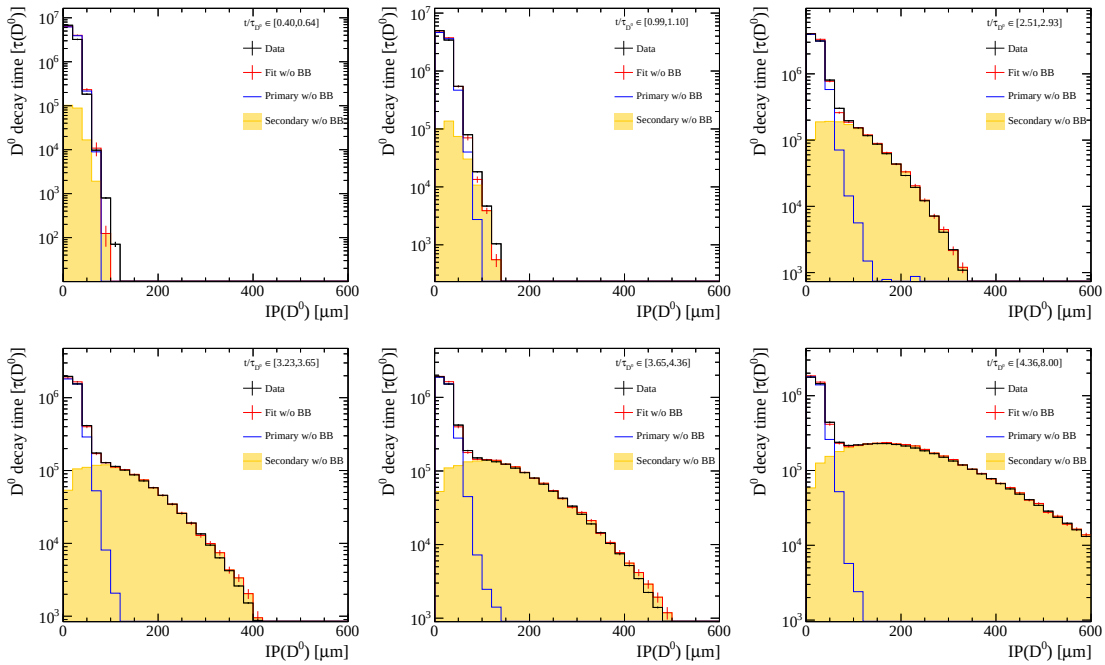

Figure 8.20: Distributions of the D^0 impact parameter for some example of the 2018 sample decay-time bins. The template fit projection is superimposed. Here, instead of the fitted values $n_{P,i}(\alpha,\beta)$ and $n_{S,i}(\alpha,\beta,\gamma,\delta)$, for the value of each bin of the interpolated template, as from the Beeston-Barlow approach, we use the interpolated template, $N_{P,i}(\alpha,\beta)$ and $N_{S,i}(\alpha,\beta,\gamma,\delta)$, instead. This allows us to directly visualize the discrepancies between data and templates that would otherwise be observed only by looking at the pulls between fitted bin values and interpolated ones.

decay-time bin	$\delta t \,/\, \tau(D^0) \times 10^3$			$\delta t^2 \,/\, \tau^2(D^0) \times 10^3$		
	16	17	18	16	17	18
0.40 - 0.64	18.3 ± 7.8	16.1 ± 7.3	15.4 ± 6.2	10.5 ± 1.3	10.6 ± 1.2	10.2 ± 1.0
0.64 - 0.77	20.3 ± 6.3	20.3 ± 7.5	21.4 ± 3.7	15.1 ± 1.3	15.5 ± 1.4	14.1 ± 0.7
0.77 - 0.88	26.2 ± 6.0	25.8 ± 3.0	24.6 ± 4.9	19.0 ± 1.4	18.6 ± 0.8	17.6 ± 1.0
0.88 - 0.99	29.2 ± 5.2	28.6 ± 4.8	31.4 ± 3.6	22.4 ± 1.2	21.5 ± 1.2	21.0 ± 0.9
0.99 - 1.10	33.4 ± 4.9	33.5 ± 4.7	31.2 ± 3.8	25.3 ± 1.3	25.4 ± 1.5	23.9 ± 1.0
1.10 - 1.21	36.7 ± 4.2	35.2 ± 4.3	33.9 ± 2.7	29.0 ± 1.2	28.9 ± 1.3	27.5 ± 0.7
1.21 - 1.33	37.1 ± 2.4	40.9 ± 3.4	37.4 ± 3.7	32.5 ± 0.7	33.9 ± 1.2	31.9 ± 1.1
1.33 - 1.46	41.8 ± 1.8	39.9 ± 3.0	40.0 ± 1.9	36.9 ± 0.6	37.9 ± 1.2	36.4 ± 0.6
1.46 - 1.61	47.8 ± 2.0	46.0 ± 3.0	45.8 ± 3.0	42.9 ± 0.8	42.9 ± 1.1	41.5 ± 1.1
1.61 - 1.77	47.7 ± 2.0	50.8 ± 4.5	49.5 ± 2.7	48.9 ± 0.9	50.5 ± 2.0	48.0 ± 1.0
1.77 - 1.97	52.3 ± 2.9	55.7 ± 2.6	52.6 ± 4.0	58.6 ± 1.4	58.9 ± 1.2	58.6 ± 1.8
1.97 - 2.21	57.3 ± 3.2	60.4 ± 3.1	56.9 ± 3.1	69.4 ± 1.7	70.0 ± 1.7	66.4 ± 1.7
2.21 - 2.51	66.8 ± 2.8	64.7 ± 2.8	66.6 ± 2.6	85.9 ± 2.2	86.4 ± 1.7	85.5 ± 1.6
2.51 - 2.93	72.6 ± 3.2	76.5 ± 2.8	77.0 ± 2.5	110.4 ± 3.1	113.1 ± 2.0	112.1 ± 2.0
2.93 - 3.23	87.3 ± 3.5	86.4 ± 3.4	89.8 ± 3.2	145.0 ± 3.9	145.6 ± 3.0	150.1 ± 3.3
3.23 - 3.65	96.3 ± 3.7	98.5 ± 3.9	100.0 ± 2.5	181.4 ± 5.4	186.3 ± 4.2	191.5 ± 3.1
3.65 - 4.36	117.5 ± 3.5	126.3 ± 4.2	117.9 ± 3.3	260.4 ± 7.4	283.5 ± 6.5	267.2 ± 5.0
4.36 - 8.00	218.8 ± 7.6	216.6 ± 6.8	220.4 ± 5.1	790.7 ± 27.7	768.8 ± 20.5	791.1 ± 16.2

Table 8.2: Measured values of the bias on the decay time, δt, and on its square, δt^2, in each decay-time bin and for each data-taking period.

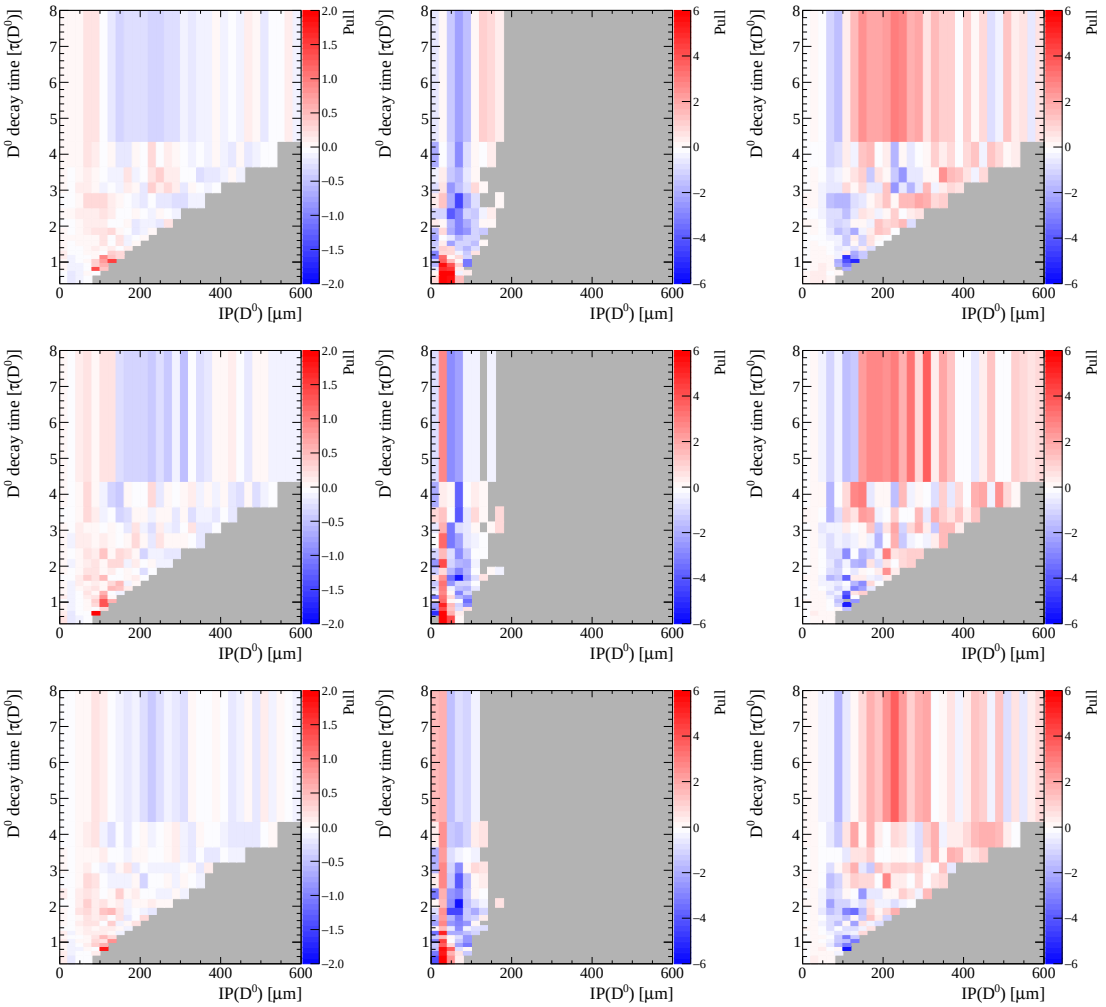

Figure 8.21: Pull distributions of (Left) data, $\frac{N_i - c_P \cdot n_{P,i}(\alpha,\beta) - c_S \cdot n_{S,i}(\alpha,\beta,\gamma,\delta)}{\sigma_i}$ (corresponding to first row of Eq.8.29), (Center) prompt template, $\frac{N_{P,i}(\alpha,\beta) - n_{P,i}(\alpha,\beta)}{\sigma_{P,i}(\alpha,\beta)}$ (corresponding to second row of Eq.8.29), and (Right) secondary template, $\frac{N_{S,i}(\alpha,\beta,\gamma,\delta) - n_{S,i}(\alpha,\beta,\gamma,\delta)}{\sigma_{S,i}(\alpha,\beta,\gamma,\delta)}$ (corresponding to third row of Eq.8.29), of the 2016 (Top), 2017 (Center) and 2018 (Bottom) samples. Bins removed from the fit due to low statistics are shown in grey.

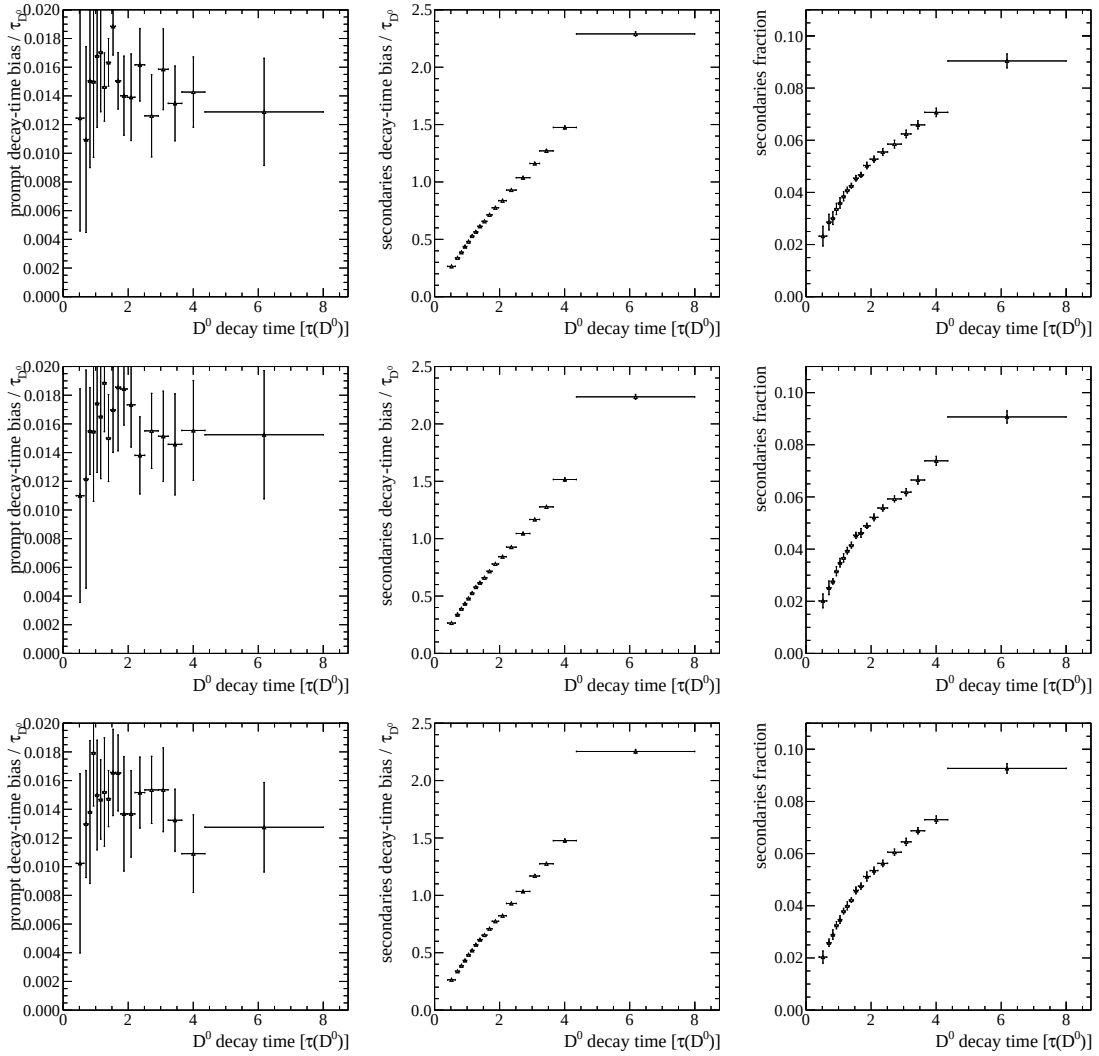

Figure 8.22: Fitted values of the primary (Left) and secondary (Center) bias on the decay time, $\langle \delta t \rangle^P$ and $\langle \delta t \rangle^S$, and the secondary fraction, f^S, as a function of the D^0 decay-time bin for the 2016 (Top), 2017 (Center) and 2018 (Bottom) samples.

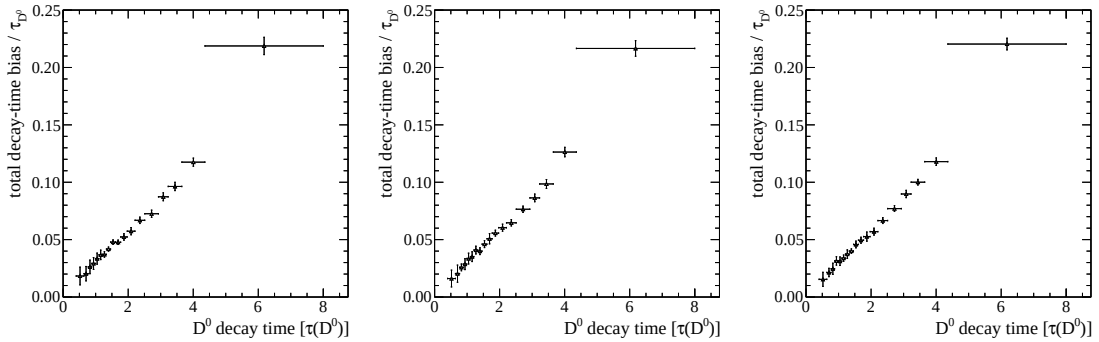

Figure 8.23: Measured values of the total decay-time bias, δt, as a function of the reconstructed D^0 decay-time bin for the 2016 (Left), 2017 (Center) and 2018 (Right) samples.

Chapter 9

Time-dependent fit

This chapter outlines the fit model used to determine the physics parameter of interest while accounting for all the systematic sources of bias examined throughout the thesis. It follows a comprehensive set of cross-checks performed to validate the analysis methodology.

9.1 Fit model

The dependence of the yield ratios (reported in Tab. 6.1) on the decay time is fitted simultaneously for D^{*+} and D^{*-} samples to determine the mixing and *CP*-violation parameters. In the following, we use uppercase for the nuisance parameters and lowercase for their input measured values[1]. The mixing and *CP* violation parameters and the WS-to-RS ratio at zero decay time, which this analysis aims to measure, are shown in bold. The minimized χ^2 is

$$\chi^2 = \sum_{t,y} \left[\left(\frac{\widetilde{r}'^{+}_{ty} - R'^{+}_{ty}}{\epsilon \cdot \sigma(\widetilde{r}'^{+}_{ty})} \right)^2 + \left(\frac{\widetilde{r}'^{-}_{ty} - R'^{-}_{ty}}{\epsilon \cdot \sigma(\widetilde{r}'^{-}_{ty})} \right)^2 \right] + \chi^2_{\text{nuis}}, \tag{9.1}$$

the sum spans over all the decay-time bins t and data-taking periods y. The $\widetilde{r}'^{+}_{ty}$ and $\widetilde{r}'^{-}_{ty}$ are the measured raw WS-to-RS yield ratios for D^{*+} and D^{*-} candidates, respectively, while $\sigma(\widetilde{r}^{+}_{ty})$ and $\sigma(\widetilde{r}^{-}_{ty})$ are their associated uncertainties. Here ϵ is an inflation factor to the uncertainties of the raw ratios, which account for possible mismodeling in the D^{*+} mass fit, chosen in order to correct the average χ^2/ndf of the fits to D^* mass (see Sec. **??**). The expected value of the WS-to-RS yield ratio $R'^{\pm}_{ty}$, accounting for the known correction is

$$\begin{aligned} R'^{\pm}_{ty} \equiv & \left(\boldsymbol{R}_D(1 \pm \boldsymbol{A}_D) + \sqrt{\boldsymbol{R}_D(1 \pm \boldsymbol{A}_D)}\,(\boldsymbol{c}_{K\pi} \pm \boldsymbol{\Delta c}_{K\pi}) T_{ty} + (\boldsymbol{c}'_{K\pi} \pm \boldsymbol{\Delta c}'_{K\pi}) T^2_{ty} \right) \times \\ & \times \left(1 \pm 2A_{ty} - C\right) + D, \end{aligned} \tag{9.2}$$

[1] Except for the external measured value of the decay-time slope of the $D^0 \to K^+K^-$ *CP* asymmetry, that is already known in the literature as ΔY. The corresponding nuisance parameters will be written as δy.

where $\boldsymbol{R_D}$, $\boldsymbol{c_{K\pi}}$, $\boldsymbol{c'_{K\pi}}$, $\boldsymbol{A_D}$, $\boldsymbol{\Delta c_{K\pi}}$ and $\boldsymbol{\Delta c'_{K\pi}}$ are the six parameters of interest. The fit is also repeated using the parametrization used in the previously published measurement [10]:

$$R'^{\pm}_{ty} \equiv \left(\boldsymbol{R_D^{\pm}} + \sqrt{\boldsymbol{R_D^{\pm}}} \, (\boldsymbol{y'^{\pm}} T_{ty} + \frac{1}{4} (\boldsymbol{y'^{2\pm}} + \boldsymbol{x'^{2\pm}}) T^2_{ty} \right) \cdot \left(1 \pm 2 A_{ty} - C\right) + D, \tag{9.3}$$

where the parameters of interest are $\boldsymbol{R_D^{\pm}}$, $\boldsymbol{y'^{\pm}}$ and $\boldsymbol{x'^{2\pm}}$. The terms T_{ty} and T^2_{ty} are the corrected average decay time and squared decay time in the bin ty, defined as

$$T_{ty} \equiv \left(\tilde{t}_{ty} - \delta T_{ty}\right) \cdot S \tag{9.4}$$

$$T^2_{ty} \equiv \left(\tilde{t}^2_{ty} - \delta T^2_{ty}\right) \cdot S^2. \tag{9.5}$$

Here $\tilde{t}_{ty}$ and $\tilde{t}^2_{ty}$ are the measured averages of the decay time and squared decay time in the bin ty (see Sect. 6.2). δT_{ty} and δT^2_{ty} are the nuisance parameters that account for the decay-time bias due to the secondary decays contamination and D^0 decay vertex reconstruction bias. Finally, since the D^0 decay times are computed as shown in Eq. 8.1 using the current average of the measurements of D^0 mass and decay time (performed by PDG [26]), in order to take into account the uncertainty on the knowledge of m_{D^0}/τ_{D^0} we multiply the measured decay-times by the scale factor S. This nuisance parameters is constrained in the χ^2_{nuis} term, with the uncertainties of m_{D^0}/τ_{D^0}.
The A_{ty} term is the nuisance asymmetry in the bin ty, defined as

$$A_{ty} \equiv A^{KK,\text{wgt}}_{ty} - (A^d_{KK} + \delta y \cdot T_{ty}), \tag{9.6}$$

where $A^{KK,\text{wgt}}_{ty}$, A^d_{KK} and δy are the nuisance parameters that account for the raw asymmetry of the KK sample (reweighted to the RS sample) in the bin ty, the integrated CP asymmetry in the KK sample and its decay-time slope, respectively.
The nuisance parameter C is the fraction of signal WS removed with the common sample, while D is the nuisance parameter accounting for the correction of the bias from to doubly misidentified RS candidates.
All the nuisance parameters associated with the corrections are free to float in the fit, and to account for the statistical and systematic error of their measurements, the associated χ^2_{nuis} term is added:

$$\chi^2_{\text{nuis}} = \chi^2_{\delta t} + \chi^2_a + \chi^2_c + \chi^2_d + \chi_{\text{ext}}, \tag{9.7}$$

where

$$\chi^2_{\delta t} = \sum_y \sum_{i,j} (\delta\theta^i_y - \delta\Theta^i_y)[\mathrm{Cov}^{-1}_y(\delta\theta)]^{ij}(\delta\theta^j_y - \delta\Theta^j_y) \tag{9.8}$$

$$\chi^2_a = \sum_{t,y} \left(\frac{\widetilde{a}^{KK,\mathrm{wgt}}_{ty} - A^{KK,\mathrm{wgt}}_{ty}}{\sigma(\widetilde{a}^{KK,\mathrm{wgt}}_{ty})} \right)^2, \tag{9.9}$$

$$\chi^2_c = \left(\frac{c - C}{\sigma(c)} \right)^2, \tag{9.10}$$

$$\chi^2_d = \left(\frac{d - D}{\sigma(d)} \right)^2, \tag{9.11}$$

$$\chi^2_{\mathrm{ext}} = \left(\frac{a^d_{KK} - A^d_{KK}}{\sigma(a^d_{KK})} \right)^2 + \left(\frac{\delta y - \Delta Y}{\sigma(\Delta Y)} \right)^2 + \left(\frac{s - S}{\sigma(s)} \right)^2. \tag{9.12}$$

The θ_y term is the vector of the measured decay-time bias in the data-taking period y, defined as

$$\theta_y = [\delta t_{1y}, \delta t^2_{1y}, \delta t_{2y}, \delta t^2_{2y}, \cdots, \delta t_{18y}, \delta t^2_{18y}] \tag{9.13}$$

The Θ_y term is the vector of the nuisance parameter associated with the decay-time bias in the data-taking period y, defined as

$$\Theta_y = [\delta T_{1y}, \delta T^2_{1y}, \delta T_{2y}, \delta T^2_{2y}, \cdots, \delta T_{18y}, \delta T^2_{18y}]. \tag{9.14}$$

The $[\mathrm{Cov}(\delta\theta)]_y$ term is the covariance matrix of the measured decay-time bias in the data-taking period y, defined as

$$\mathrm{Cov}^{ij}_y = \mathrm{Cov}(\theta^i_y, \theta^j_y). \tag{9.15}$$

The $\tilde{a}^{KK,\mathrm{wgt}}_{ty}$ and $\sigma(\tilde{a}^{KK,\mathrm{wgt}}_{ty})$ terms are the measured raw KK asymmetry in the bin ty and its uncertainty. The c and $\sigma(c)$ terms are the estimated fractions of WS signal candidates removed by the common WS-RS veto (see Sec. 7.4) and its uncertainty, conservatively fixed to half of the central value. The d and $\sigma(d)$ terms are the estimated bias from doubly-misID RS (see Sec 7.3) and its uncertainty, conservatively fixed to half of the central value. The parameters $a^d_{K^+K^-}$, ΔY, $m(D^0)$ and $\tau(D^0)$ are the external inputs in this analysis and their values and uncertainties are taken from the world average performed by HFLAV and PDG group [26,27]:

$$a^d_{K^+K^-} = (4.5 \pm 5.3) \times 10^{-4}, \qquad \Delta Y = (0.89 \pm 1.13) \times 10^{-4},$$
$$m_{D^0} = (1864.84 \pm 0.05)\,\mathrm{MeV}/c^2, \qquad \tau_{D^0} = (410.3 \pm 1.0)\,\mathrm{fs}.$$

Finally, $s = 1$ and $\sigma(s) = \sqrt{\frac{\sigma^2(m_{D^0})}{m^2_{D^0}} + \frac{\sigma^2(\tau_{D^0})}{\tau^2_{D^0}}}$.

9.2 Cross checks

The analysis and all the methodologies developed and described in this thesis allow performing the time-dependent fit by minimizing the χ^2 quantity described in Eq. 9.1 to determine both mixing and *CP*-violating physics observables. Various consistency checks are performed looking for possible unexpected variations of the measured parameters as a function of different observables related to the kinematic and topology of the decay/event or different conditions of the detector, suitably chosen to be sensitive to the main sources of systematic uncertainties. The returned physics observables must be stable, within the assigned uncertainties, when measured as a function of any variable related to the experimental environment. This approach is very computationally expensive since it requires performing the full analysis, described in the previous chapters in all its aspects and stages, multiple times in different bins of the chosen variable to be studied.

When the analysis is repeated in two or more subsamples, each returns a 6D observable, ω^i with an associated 6×6 covariance matrix, $\mathrm{Cov}^{i,j}(\omega)$ The compatibility between the different results, which are independent, can't be done directly comparing the individual parameters, since they are highly correlated. The different sets of 6D results are fitted to a 6D constant term Ω^i, by minimizing the standard χ^2:

$$\chi^2 = \sum_{i,j} (\omega^i - \Omega^i)[\mathrm{Cov}^{-1}(\omega)]^{ij}(\omega^j - \Omega^j) \tag{9.16}$$

In each table is reported the minimum χ^2 value, its number of degrees of freedom and the associated p-value. This procedure neglects the small correlation between the subsamples from shared external input. All the studies show consistent results, as reported in Tab. 9.1-9.8, with p-values always inside the [0.05,0.95] range. Results are shown in the parametrization used in the previously published measurement [10] and central values are blinded, adding a random shift different for each parameter of interest.

Data taking period The final results must return to be stable as a function of different data-taking periods. Here, we use the same period split used throughout the analysis. The results of this test are reported in Tab. 9.1.

2016							
Parameters		Correlations					
	$[10^{-5}]$	R^+	y'^+	x'^{2+}	R^-	y'^-	x'^{2-}
R^+	555.5 ± 4.7	1	-93.3%	84.9%	-1.9%	1.1%	-1.1%
y'^+	879.8 ± 84.8		1	-96.5%	1.1%	-1.2%	1.2%
x'^{2+}	225.8 ± 4.5			1	-1.0%	1.2%	-1.2%
R^-	671.5 ± 4.8				1	-93.0%	83.8%
y'^-	819.8 ± 82.5					1	-96.2%
x'^{2-}	311.5 ± 4.2						1
2017							
Parameters		Correlations					
	$[10^{-5}]$	R^+	y'^+	x'^{2+}	R^-	y'^-	x'^{2-}
R^+	559.4 ± 4.8	1	-92.7%	83.5%	-1.8%	1.1%	-1.0%
y'^+	829.1 ± 85.7		1	-96.2%	1.1%	-1.1%	1.1%
x'^{2+}	228.5 ± 4.5			1	-1.0%	1.1%	-1.2%
R^-	663.0 ± 4.7				1	-92.9%	84.1%
y'^-	986.9 ± 85.9					1	-96.5%
x'^{2-}	302.7 ± 4.6						1
2018							
Parameters		Correlations					
	$[10^{-5}]$	R^+	y'^+	x'^{2+}	R^-	y'^-	x'^{2-}
R^+	558.4 ± 4.5	1	-92.7%	83.4%	-1.8%	1.0%	-0.9%
y'^+	847.8 ± 80.2		1	-96.2%	1.0%	-1.1%	1.1%
x'^{2+}	228.4 ± 4.3			1	-0.9%	1.0%	-1.1%
R^-	678.5 ± 4.6				1	-92.5%	82.6%
y'^-	707.9 ± 79.7					1	-95.7%
x'^{2-}	316.5 ± 4.0						1
χ^2/ndof	7.8/12	p-value	81%				

Table 9.1: Results of independent fit in different disjointed subsets, divided by data-taking period.

Magnet polarity: `MagUp` vs `MagDown` One critical check for the whole analysis strategy is the stability of the measurement results in the two sub-samples obtained by splitting the dataset by magnet polarity. It is worth mentioning that, without the application of the charge asymmetry corrections, this test would significantly fail, as these corrections are very different when switching from one polarity to another. The results of this test are reported in Tab. 9.2. In addition, the final measurement also benefits from additional charge asymmetry cancellations, due to the averaging of these two data samples, making

the final results even more robust against any detection charge asymmetry effects.

MagUp							
Parameters		Correlations					
	$[10^{-5}]$	R^+	y'^+	x'^{2+}	R^-	y'^-	x'^{2-}
R^+	557.7 ± 3.7	1	-92.5%	83.6%	-2.2%	1.0%	-1.0%
y'^+	838.4 ± 65.8		1	-96.3%	1.0%	-1.1%	1.2%
x'^{2+}	228.5 ± 3.4			1	-1.0%	1.2%	-1.3%
R^-	669.0 ± 3.7				1	-92.4%	83.1%
y'^-	817.3 ± 64.6					1	-96.1%
x'^{2-}	312.1 ± 3.3						1
MagDw							
Parameters		Correlations					
	$[10^{-5}]$	R^+	y'^+	x'^{2+}	R^-	y'^-	x'^{2-}
R^+	557.2 ± 3.6	1	-92.4%	83.2%	-2.3%	1.1%	-1.0%
y'^+	838.6 ± 64.8		1	-96.2%	1.0%	-1.1%	1.2%
x'^{2+}	227.9 ± 3.4			1	-1.0%	1.2%	-1.2%
R^-	670.3 ± 3.7				1	-92.8%	83.4%
y'^-	851.7 ± 64.7					1	-96.1%
x'^{2-}	308.8 ± 3.4						1
χ^2/ndof	2.5/6	p-value	86%				

Table 9.2: Results of independent fit in different disjointed subsets, divided by magnet polarity.

L0 requirements The L0Hadron trigger decision depends on transverse energy. The transverse energy of D^0 crossing the electromagnetic calorimeter near the $y-z$ plane is always low, hence it is unlikely that these D^0 will trigger this L0 line. On the other hand, the transverse energy of D^0 crossing the electromagnetic calorimeter far from this plane is enhanced, making it much more likely to trigger this line. Since D^0 and π_s direction are strongly correlated, most of the π_s associated to D^0 candidates triggered by L0Hadron line are in the region closest to the edges of the geometrical acceptance, the one with the greatest soft pion detection asymmetry. The final results must be stable as a function of the L0 requirements, hence the analysis is repeated in the subsample where the D^0 is triggered by L0Hadron and the complementary one. The results of this test are reported in Tab. 9.3.

L0Hadron TOS on D^0							
Parameters		Correlations					
	$[10^{-5}]$	R^+	y'^+	x'^{2+}	R^-	y'^-	x'^{2-}
R^+	562.1 ± 3.4	1	-92.1%	82.6%	-2.6%	1.2%	-1.1%
y'^+	763.4 ± 61.6		1	-95.9%	1.2%	-1.3%	1.4%
x'^{2+}	232.3 ± 3.2			1	-1.2%	1.4%	-1.5%
R^-	673.1 ± 3.4				1	-92.1%	82.3%
y'^-	804.8 ± 61.4					1	-95.8%
x'^{2-}	312.5 ± 3.3						1
L0Hadron not TOS on D^0							
Parameters		Correlations					
	$[10^{-5}]$	R^+	y'^+	x'^{2+}	R^-	y'^-	x'^{2-}
R^+	552.3 ± 4.2	1	-93.4%	85.2%	-1.7%	0.8%	-0.8%
y'^+	928.2 ± 72.1		1	-96.7%	0.8%	-0.8%	0.9%
x'^{2+}	223.1 ± 3.8			1	-0.8%	0.9%	-1.0%
R^-	667.3 ± 4.1				1	-93.2%	84.4%
y'^-	849.9 ± 70.0					1	-96.4%
x'^{2-}	309.5 ± 3.5						1
χ^2/ndof	11/6	p-value	9%				

Table 9.3: Results of independent fit in different disjointed subsets, divided by L0 requirements.

Soft pion momentum The soft pion momentum is an observable very sensitive to both the instrumental asymmetry correction and the doubly-misID correction. Low momentum pions bend more in the magnetic field and exhibit higher detection asymmetry. Moreover, pions momentum is strongly correlated to the momentum of the D^0 decay product, which directly affects the misidentification probability, hence higher momentum is correlated with a higher misidentification of the D^0. The dataset is divided into four bins of the soft pion and the full analysis is independently repeated in each bin. Test results are reported in Tab. 9.4, showing compatibility. For instance, removing the requirement on $m(K\pi)_{\text{swap}}$ described in Sec. 5.3.3, this test would significantly fail.

$p(\pi_s) < 3.2\,\text{GeV}/c$							
Parameters		Correlations					
	$[10^{-5}]$	R_D^+	y'^+	x'^{2+}	R_D^-	y'^-	x'^{2-}
R_D^+	565.5 ± 9.4	1	-94.4%	86.4%	-2.4%	2.2%	-2.1%
y'^+	945.8 ± 158.6		1	-96.9%	2.2%	-2.3%	2.3%
x'^{2+}	340.1 ± 8.2			1	-2.1%	2.3%	-2.5%
R_D^-	641.7 ± 9.4				1	-94.2%	86.4%
y'^-	960.2 ± 162.4					1	-97.1%
x'^{2-}	328.2 ± 8.7						1
$p(\pi_s) \in [3.2, 4.7]\,\text{GeV}/c$							
Parameters		Correlations					
	$[10^{-5}]$	R_D^+	y'^+	x'^{2+}	R_D^-	y'^-	x'^{2-}
R_D^+	557.7 ± 4.7	1	-93.1%	84.9%	-3.0%	2.5%	-2.3%
y'^+	1044.0 ± 85.3		1	-96.8%	2.5%	-2.7%	2.8%
x'^{2+}	335.8 ± 4.6			1	-2.4%	2.8%	-3.0%
R_D^-	654.9 ± 4.7				1	-92.7%	83.1%
y'^-	662.3 ± 80.2					1	-96.0%
x'^{2-}	340.5 ± 4.1						1
$p(\pi_s) \in [4.7, 6.4]\,\text{GeV}/c$							
Parameters		Correlations					
	$[10^{-5}]$	R_D^+	y'^+	x'^{2+}	R_D^-	y'^-	x'^{2-}
R_D^+	574.2 ± 4.8	1	-92.3%	82.3%	-3.0%	2.5%	-2.3%
y'^+	745.9 ± 85.9		1	-95.7%	2.5%	-2.6%	2.6%
x'^{2+}	351.4 ± 4.4			1	-2.3%	2.6%	-2.7%
R_D^-	646.8 ± 4.8				1	-92.6%	83.4%
y'^-	803.0 ± 87.9					1	-96.2%
x'^{2-}	334.9 ± 4.7						1
$p(\pi_s) > 6.4\,\text{GeV}/c$							
Parameters		Correlations					
	$[10^{-5}]$	R_D^+	y'^+	x'^{2+}	R_D^-	y'^-	x'^{2-}
R_D^+	576.7 ± 4.7	1	-92.1%	82.0%	-3.4%	2.7%	-2.5%
y'^+	744.1 ± 83.2		1	-95.6%	2.7%	-2.8%	2.8%
x'^{2+}	350.6 ± 4.3			1	-2.4%	2.8%	-3.0%
R_D^-	658.6 ± 4.6				1	-92.0%	82.0%
y'^-	643.0 ± 81.2					1	-95.6%
x'^{2-}	343.4 ± 4.2						1
χ^2/ndof	26.3/18	p-value	9.3%				

Table 9.4: Results of independent fit in different disjointed subsets, divided in bins of soft pion momentum.

Soft pion acceptance In this test the dataset is divided into two region of the geometrical acceptance of the soft pion. The division is inspired by the fiducial requirement defined in Sec. 5.3.6 and in Ref. [1]. The inside of the π_s geometrical acceptance is defined as

$$[|p_x| < 0.317 \cdot (|p| - 1100)] \wedge \\ \wedge \left[\left|\frac{p_y}{p_z}\right| > 0.030 \vee |p_x| < 350 - 0.01397 \cdot p_z \vee |p_x| > 550 + 0.01605 \cdot p_z\right], \tag{9.17}$$

where units are in MeV/c. The border region is the complementary one. The fit is repeated independently in the two subsets showing perfect compatibility. Results are shown in Tab. 9.5.

border of π_s geo. acceptance							
Parameters		Correlations					
	$[10^{-5}]$	R^+	y'^+	x'^{2+}	R^-	y'^-	x'^{2-}
R^+	561.0 ± 3.5	1	-92.1%	82.6%	-2.4%	1.0%	-1.0%
y'^+	785.6 ± 61.7		1	-96.0%	1.0%	-1.1%	1.1%
x'^{2+}	230.8 ± 3.2			1	-0.9%	1.1%	-1.1%
R^-	672.8 ± 3.5				1	-92.2%	82.4%
y'^-	766.0 ± 60.7					1	-95.8%
x'^{2-}	312.9 ± 3.1						1
inside of π_s geo. acceptance							
Parameters		Correlations					
	$[10^{-5}]$	R^+	y'^+	x'^{2+}	R^-	y'^-	x'^{2-}
R^+	555.7 ± 4.3	1	-93.0%	84.0%	-1.8%	0.9%	-0.9%
y'^+	857.5 ± 74.7		1	-96.3%	0.9%	-1.0%	1.0%
x'^{2+}	226.8 ± 3.9			1	-0.9%	1.0%	-1.1%
R^-	666.7 ± 4.3				1	-93.0%	84.1%
y'^-	886.6 ± 74.7					1	-96.4%
x'^{2-}	309.1 ± 3.9						1
χ^2/ndof	7.0/6	p-value	32%				

Table 9.5: Results of independent fit in different disjointed subsets, divided into two regions of the soft pion geometrical acceptance..

Track-based Ghost Probability The track-based ghost probability of the soft pion is the output of a neural network trained to distinguish genuine tracks from ghost ones. This observable has a good discriminating power for the ghost background. The analysis is repeated independently in two bins of this variable, returning consistent results, showed in Tab. 9.6.

GhostProb(π_s) < 0.005							
Parameters		Correlations					
	$[10^{-5}]$	R^+	y'^+	x'^{2+}	R^-	y'^-	x'^{2-}
R^+	563.3 ± 3.7	1	-93.0%	83.9%	-2.4%	1.1%	-1.1%
y'^+	752.0 ± 65.5		1	-96.0%	1.1%	-1.2%	1.3%
x'^{2+}	232.4 ± 3.4			1	-1.1%	1.3%	-1.3%
R^-	666.1 ± 3.7				1	-92.5%	83.4%
y'^-	894.4 ± 66.0					1	-96.2%
x'^{2-}	307.6 ± 3.5						1
GhostProb(π_s) > 0.005							
Parameters		Correlations					
	$[10^{-5}]$	R^+	y'^+	x'^{2+}	R^-	y'^-	x'^{2-}
R^+	550.4 ± 3.9	1	-92.8%	84.3%	-1.9%	0.8%	-0.8%
y'^+	943.9 ± 70.0		1	-96.6%	0.8%	-0.9%	0.9%
x'^{2+}	222.9 ± 3.8			1	-0.8%	0.9%	-1.0%
R^-	672.1 ± 3.9				1	-92.6%	83.2%
y'^-	791.0 ± 67.1					1	-96.0%
x'^{2-}	312.7 ± 3.4						1
χ^2/ndof	7.7/6	p-value	26%				

Table 9.6: Results of independent fit in different disjointed subsets, divided into two bins of the track-based ghost probability of the soft pion.

Number of Primary Vertices The dataset is divided among events with only one primary pp vertex and events with multiple primary vertex and the analysis is repeated independently. This test is sensitive to bias in the flight distance determination, related to PV misassociation. The test results return good consistency and are reported in Tab. 9.7.

number of PV per event $= 1$							
Parameters		Correlations					
	$[10^{-5}]$	R^+	y'^+	x'^{2+}	R^-	y'^-	x'^{2-}
R^+	557.8 ± 3.8	1	-92.4%	82.9%	-2.6%	1.4%	-1.3%
y'^+	833.5 ± 68.4		1	-96.0%	1.3%	-1.4%	1.5%
x'^{2+}	228.6 ± 3.6			1	-1.3%	1.4%	-1.5%
R^-	677.2 ± 3.8				1	-92.2%	81.8%
y'^-	724.3 ± 65.5					1	-95.5%
x'^{2-}	317.0 ± 3.4						1
number of PV per event > 1							
Parameters		Correlations					
	$[10^{-5}]$	R^+	y'^+	x'^{2+}	R^-	y'^-	x'^{2-}
R^+	564.4 ± 3.8	1	-92.4%	82.3%	-2.4%	1.2%	-1.2%
y'^+	716.2 ± 66.7		1	-95.7%	1.2%	-1.3%	1.4%
x'^{2+}	235.4 ± 3.5			1	-1.2%	1.4%	-1.4%
R^-	667.0 ± 3.8				1	-92.4%	83.0%
y'^-	874.5 ± 67.4					1	-96.1%
x'^{2-}	308.9 ± 3.5						1
χ^2/ndof	7.2/6	p-value	30%				

Table 9.7: Results of independent fit in different disjointed subsets, divided among events with only one PV and events with multiple PVs.

Split of the last decay-time bin In the simultaneous fit of the D^* invariant mass of WS and RS candidates, we use the same signal pdf for WS and RS. This is a good assumption if the kinematics distributions of WS and RS are similar enough, which translates into having decay-time bins that are small enough. The last decay-time bin, the one with the higher decay-time values, is also the biggest one. In order to test the stability of the fit method depending on the decay-time bin dimension, the dataset is randomly divided into two equipopulated subsets and the analysis is performed on the first subset with the standard decay-time binning already described and on the second one, splitting the last bin into two smaller bins. The test results returned good consistency and are reported in Tab. 9.8.

standard time binning							
Parameters		Correlations					
	$[10^{-5}]$	R^+	y'^+	x'^{2+}	R^-	y'^-	x'^{2-}
R^+	560.1 ± 3.9	1	-92.6%	83.5%	-3.2%	2.4%	-2.1%
y'^+	808.4 ± 68.7		1	-96.2%	2.4%	-2.8%	2.5%
x'^{2+}	229.7 ± 3.6			1	-2.1%	2.6%	-2.4%
R^-	670.0 ± 3.8				1	-92.6%	83.5%
y'^-	876.0 ± 67.6					1	-96.2%
x'^{2-}	308.8 ± 3.5						1
last time bin splitted							
Parameters		Correlations					
	$[10^{-5}]$	R^+	y'^+	x'^{2+}	R^-	y'^-	x'^{2-}
R^+	559.5 ± 3.9	1	-92.5%	82.9%	-2.1%	1.0%	-0.9%
y'^+	785.2 ± 68.2		1	-96.0%	1.0%	-1.1%	1.1%
x'^{2+}	231.5 ± 3.6			1	-1.0%	1.1%	-1.1%
R^-	670.0 ± 3.8				1	-92.4%	82.4%
y'^-	791.7 ± 66.4					1	-95.8%
x'^{2-}	313.9 ± 3.5						1
χ^2/ndof	7.2/6	p-value	29%				

Table 9.8: Results of independent fit in different disjointed subsets. The division is random, but the analysis method differs, with the higher decay-time bin that is divided in half.

Chapter 10

Final results and conclusions

This chapter exhibits the final results of the analysis. An average with Run 1 data sample is performed using raw results from the previous iteration of this analysis and the impact of this legacy Run 1 + 2 measurement is evaluated using the global fit of all charm observables.

10.1 Decay-time fit results

Four different fits are performed under each of the following hypotheses.

- **No CP violation** The fit parameters are R_D, $c_{K\pi}$ and $c'_{K\pi}$ with the following conditions,

$$A_D = 0, \qquad \Delta c_{K\pi} = 0 \quad \text{and} \quad \Delta c'_{K\pi} = 0. \tag{10.1}$$

- **No CP violation in decay and in the mixing** The fit parameters are R_D, $c_{K\pi}$, $c'_{K\pi}$ and $\Delta c_{K\pi}$ with the following conditions,

$$A_D = 0, \quad \text{and} \quad \Delta c'_{K\pi} = 0. \tag{10.2}$$

- **No CP violation in decay** The fit parameters are R_D, $c_{K\pi}$, $c'_{K\pi}$, $\Delta c_{K\pi}$ and $\Delta c'_{K\pi}$ with the following condition,

$$A_D = 0. \tag{10.3}$$

- **CP violation in the decay, mixing and interference** All parameters R_D, $c_{K\pi}$, $c'_{K\pi}$, A_D, $\Delta c_{K\pi}$ and $\Delta c'_{K\pi}$ are free to float.

These approximations are justifiable by the current measured limits, shown in Sec. 2.6 and theoretical prediction for *CPV* parameters, reported in Sec. 2.5. The *CP* violation in DCS decays is expected to be negligible in the SM. Given the world average measured values for x, y, $\delta_{K\pi}$ and the SM prediction for ϕ^M and ϕ^Γ, the predicted SM value for $\Delta c_{K\pi}$ and $\Delta c'_{K\pi}$ are $\mathcal{O}(10^{-5})$ and $\mathcal{O}(10^{-8})$, at least one order of magnitude smaller than the current precision level. Accounting for possible enhancement from BSM particle to the

CP parameters and using the current experimental limit on ϕ^M and ϕ^Γ, we find the limit for the $\Delta c'_{K\pi}$ to be about 5×10^{-7}, five times smaller than the current precision on $\Delta c'_{K\pi}$. The results obtained from these fits, performed on the full Run 2 data sample, corresponding to an integrated luminosity of about 5.9 fb^{-1}, are listed in Tabs. 10.1-10.4. Only the values of the parameters of interest and their correlations are shown. The results of all the nuisance parameters are reported for completeness in App. H.2, for the *CPV* allowed scenario. Figure 10.1 shows the measured ratio (separately for the $K^+\pi^-$ and $K^-\pi^+$ samples and the three data-taking periods) with the relative fit projection. There are no evidence of *CPV* violation, both in decay, mixing and interference.

No *CP* violation				
Parameters		Correlations		
		R_D	$c_{K\pi}$	$c'_{K\pi}$
R_D	$(343.1 \pm 2.0) \times 10^{-5}$	1	-92.4%	80.0%
$c_{K\pi}$	$(51.4 \pm 3.5) \times 10^{-4}$		1	-94.1%
$c'_{K\pi}$	$(13.1 \pm 3.7) \times 10^{-6}$			1
χ^2/ndof	85.3 / 105	p-value	0.92	

Table 10.1: Fit results for mixing parameters not allowing for *CPV*.

No *CP* violation in the decay and in the mixing					
Parameters		Correlations			
		R_D	$c_{K\pi}$	$c'_{K\pi}$	$\Delta c_{K\pi}$
R_D	$(343.1 \pm 2.0) \times 10^{-5}$	1	-92.4%	80.0%	0.0%
$c_{K\pi}$	$(51.4 \pm 3.5) \times 10^{-4}$		1	-94.1%	0.2%
$c'_{K\pi}$	$(13.1 \pm 3.7) \times 10^{-6}$			1	-0.0%
$\Delta c_{K\pi}$	$(-0.2 \pm 7.0) \times 10^{-5}$				1
χ^2/ndof	85.3 / 104	p-value	0.91		

Table 10.2: Fit results for mixing parameters allowing only *CPV* in the interference between mixing and decay.

No CP violation in the decay						
Parameters		Correlations				
		R_D	$c_{K\pi}$	$c'_{K\pi}$	$\Delta c_{K\pi}$	$\Delta c'_{K\pi}$
R_D	$(343.1 \pm 2.0)\times10^{-5}$	1	-92.4%	80.0%	0.3%	-0.2%
$c_{K\pi}$	$(51.4 \pm 3.5)\times10^{-4}$		1	-94.1%	-0.2%	0.1%
$c'_{K\pi}$	$(13.1 \pm 3.7)\times10^{-6}$			1	0.2%	0.0%
$\Delta c_{K\pi}$	$(-0.9 \pm 1.4)\times10^{-4}$				1	-87.4%
$\Delta c'_{K\pi}$	$(1.7 \pm 2.3)\times10^{-6}$					1
χ^2/ndof	84.7 / 103	p-value	0.90			

Table 10.3: Fit results for mixing parameters allowing only CPV in the mixing and the interference between mixing and decay.

CP violation in the decay, mixing and interference							
Parameters		Correlations					
		R_D	$c_{K\pi}$	$c'_{K\pi}$	A_D	$\Delta c_{K\pi}$	$\Delta c'_{K\pi}$
R_D	$(343.1 \pm 2.0)\times10^{-5}$	1	-92.4%	80.0%	0.9%	-0.8%	0.1%
$c_{K\pi}$	$(51.4 \pm 3.5)\times10^{-4}$		1	-94.1%	-1.4%	1.4%	-0.7%
$c'_{K\pi}$	$(13.1 \pm 3.7)\times10^{-6}$			1	0.7%	-0.7%	0.1%
A_D	$(-7.1 \pm 6.0)\times10^{-3}$				1	-91.5%	79.4%
$\Delta c_{K\pi}$	$(3.0 \pm 3.6)\times10^{-4}$					1	-94.1%
$\Delta c'_{K\pi}$	$(-1.9 \pm 3.8)\times10^{-6}$						1
χ^2/ndof	83.3 / 102	p-value	0.91				

Table 10.4: Fit results for mixing parameters allowing for CPV in the decay, mixing, and interference.

It is also worth reminding that the new experimental parametrization adopted in this thesis (R_D, $c_{K\pi}$, $c'_{K\pi}$, A_D, $\Delta c_{K\pi}$, $\Delta c'_{K\pi}$) has the advantage of fully decorrelate uncertainties, both statistical and systematic. This is evident by looking at Tabs. 10.1-10.4, and at Tabs. 10.5-10.8 reported in the next section. This is very useful since it allows immediate visualization of how uncertainties, in the various scenarios, combine to contribute to the final total uncertainty on each physics parameter.

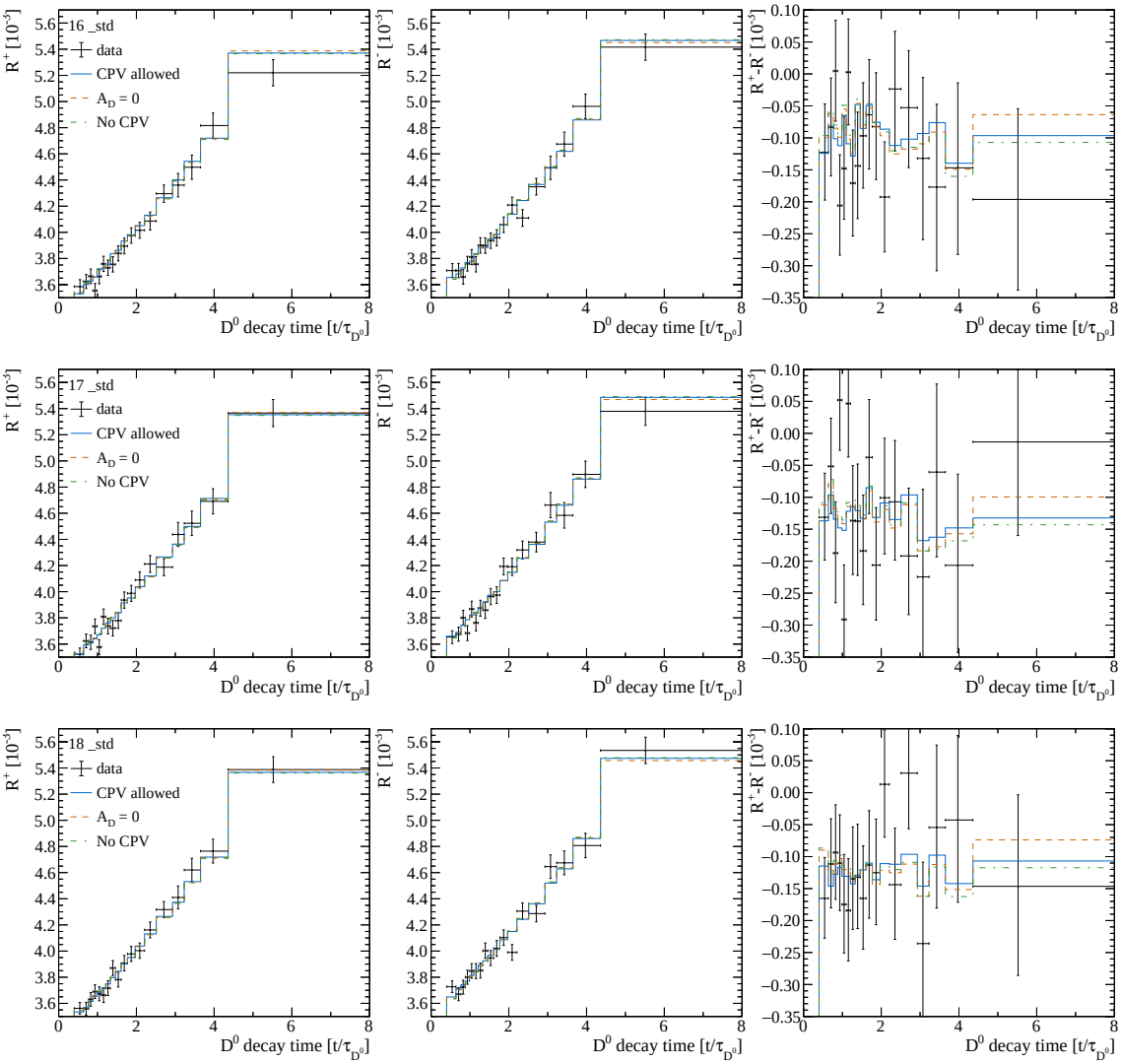

Figure 10.1: Raw WS-to-RS ratio for the $K^-\pi^+$ (Left) and $K^+\pi^-$ (Center) D^0 final state and their difference (Right) in the 2016 (Up), 2017 (Center) and 2018 (Bottom) data-taking period. Projections of the fits are superimposed. The abscissa of the data points corresponds to the raw average decay time measured in that bin.

10.2 Systematic uncertainties

All the systematic uncertainties are already included in the time-dependent fit results through Gaussian constraints on the nuisance parameters. The returned fit uncertainties, therefore, incorporate both the statistical and systematic contribution of all known sources. For illustrative purposes, to determine the statistical uncertainty and to separate its contribution from the systematic one, the fits are repeated with the values of nuisance parameters fixed to their input central values. We then calculate the systematic uncertainty by performing a subtraction in quadrature between the two returned uncertainties (with and without fixing all nuisance parameters to the input). A similar procedure can be

repeated to distinguish the contribution of each systematic uncertainty. The precision of the measurements is driven by statistical uncertainties, as shown in Tabs. 10.5-10.8. In the tables, the "instrumental asymm." source refers to the uncertainties coming from the nuisance parameters $A_{ty}^{KK,\text{wgt}}$, and accounts for the statistical uncertainties from the fit of the raw asymmetry in the KK sample; the "decay-time bias" source account for all the uncertainties in the determination of the decay-time biases. The systematic uncertainty linked to the ghost background subtraction is included in the statistical uncertainties through the nuisance parameters that describe the ghost pdf in the $m(D^0\pi_s)$ fit. No further systematics are evaluated for mass modelling, as justified in Sec. 7.1. Using this new experimental parametrization it is evident that the sources of systematic uncertainties linked to the instrumental asymmetry correction (instrumental asymm., $a^d_{K^+K^-}$ and ΔY external input), affect almost only CP violating parameters, in particular the $a^d_{K^+K^-}$ external input mainly influences the A_D parameters, when fitted, while the ΔY input affects the linear term $\Delta c_{K\pi}$. Ratio biases with little or no time dependency, such as the doubly mis-iD background and the common removal, only impact R_D. Decay-time biases, that have a substantial decay-time trend, impact all parameters, but CP-even ones are the most affected. Finally, the knowledge of m_{D^0} and τ_{D^0} determine the decay-time scale, thus this source mainly impacts $c_{K\pi}$ and $c'_{K\pi}$. The systematic uncertainty related to ghost background removal can not be disentangled from the statist uncertainty, as done for all the other systematics sources, which are inserted in the final fit in the form of nuisance parameters. To get an estimate of the significance of this correction, one can repeat all the D^* mass fits fixing the ghost component shape. With this test, it is possible to determine that ghosts have a predominant effect on R_D and that on this observable they are the main systematic source (about 1/5 of the statistical uncertainty).

No CP violation			
Source	R_D $[10^{-5}]$	$c_{K\pi}$ $[10^{-4}]$	$c'_{K\pi}$ $[10^{-6}]$
Mass mismodeling	0.46	0.83	0.88
Ghost soft pions	0.39	0.76	0.80
Instrumental asymm.	0.02	0.03	0.03
$a^d_{K^+K^-}$ ext. input	< 0.01	0.02	0.02
ΔY ext. input	0.02	0.03	0.03
Doubly Mis-ID bkg.	0.10	0.03	0.03
Common removal	0.22	0.03	0.02
Decay-time bias	0.09	0.15	0.14
m_{D^0}, τ_{D^0} ext. inputs	0.01	0.13	0.07
Total syst. uncertainty	0.65	1.13	1.18
Statistical uncertainty	1.88	3.32	3.52
Total uncertainty	1.99	3.51	3.72

Table 10.5: Summary of statistical and systematic uncertainties in the mixing parameter fit not allowing for CPV.

No *CP* violation in the decay and in the mixing				
Source	R_D $[10^{-5}]$	$c_{K\pi}$ $[10^{-4}]$	$c'_{K\pi}$ $[10^{-6}]$	$\Delta c_{K\pi}$ $[10^{-5}]$
Mass mismodeling	0.46	0.83	0.88	1.38
Ghost soft pions	0.39	0.76	0.80	1.41
Instrumental asymm.	< 0.01	< 0.01	< 0.01	1.19
$a^d_{K^+K^-}$ ext. input	< 0.01	< 0.01	< 0.01	3.39
ΔY ext. input	< 0.01	< 0.01	< 0.01	1.73
Doubly Mis-ID bkg.	0.10	< 0.01	< 0.01	< 0.01
Common removal	0.22	< 0.01	< 0.01	< 0.01
Decay-time bias	0.09	0.14	0.14	0.02
m_{D^0}, τ_{D^0} ext. inputs	< 0.01	0.12	0.06	< 0.01
Total syst. uncertainty	0.65	1.13	1.18	4.40
Statistical uncertainty	1.88	3.32	3.52	5.46
Total uncertainty	1.99	3.51	3.72	7.02

Table 10.6: Summary of statistical and systematic uncertainties in the mixing parameter fit allowing for *CPV* only in the interference between mixing and decay.

No *CP* violation in the decay					
Source	R_D $[10^{-5}]$	$c_{K\pi}$ $[10^{-4}]$	$c'_{K\pi}$ $[10^{-6}]$	$\Delta c_{K\pi}$ $[10^{-4}]$	$\Delta c'_{K\pi}$ $[10^{-6}]$
Mass mismodeling	0.46	0.83	0.88	0.30	0.52
Ghost soft pions	0.39	0.76	0.80	0.28	0.45
Instrumental asymm.	0.02	0.04	0.04	0.26	0.47
$a^d_{K^+K^-}$ ext. input	0.01	0.02	0.02	0.62	0.53
ΔY ext. input	0.01	0.02	0.03	0.13	0.08
Doubly Mis-ID bkg.	0.10	0.03	0.03	< 0.01	< 0.01
Common removal	0.22	0.03	0.03	< 0.01	< 0.01
Decay-time bias	0.09	0.15	0.15	< 0.01	0.01
m_{D^0}, τ_{D^0} ext. inputs	0.01	0.13	0.07	< 0.01	< 0.01
Total syst. uncertainty	0.65	1.13	1.18	0.79	0.99
Statistical uncertainty	1.88	3.32	3.52	1.21	2.09
Total uncertainty	1.99	3.51	3.72	1.44	2.31

Table 10.7: Summary of statistical and systematic uncertainties in the mixing parameter fit allowing for *CPV* only in the mixing and the interference between mixing and decay.

CP violation in the decay, in the mixing and the interference						
Source	R_D $[10^{-5}]$	$c_{K\pi}$ $[10^{-4}]$	$c'_{K\pi}$ $[10^{-6}]$	A_D $[10^{-3}]$	$\Delta c_{K\pi}$ $[10^{-4}]$	$\Delta c'_{K\pi}$ $[10^{-6}]$
Mass mismodeling	0.46	0.83	0.87	1.35	0.83	0.88
Ghost soft pions	0.39	0.76	0.80	1.13	0.76	0.80
Instrumental asymm.	0.01	0.03	0.02	1.20	0.73	0.80
$a^d_{K^+K^-}$ ext. input	0.01	0.02	0.02	1.06	0.03	0.01
ΔY ext. input	0.01	0.02	0.02	0.02	0.12	0.09
Doubly Mis-ID bkg.	0.10	< 0.01	< 0.01	< 0.01	< 0.01	< 0.01
Common removal	0.22	0.01	< 0.01	0.03	0.02	0.02
Decay-time bias	0.09	0.15	0.14	0.07	0.04	0.04
m_{D^0}, τ_{D^0} ext. inputs	< 0.01	0.13	0.07	0.02	0.01	0.01
Total syst. uncertainty	0.65	1.13	1.18	2.37	1.34	1.42
Statistical uncertainty	1.88	3.32	3.52	5.47	3.32	3.52
Total uncertainty	1.99	3.51	3.72	5.96	3.58	3.80

Table 10.8: Summary of statistical and systematic uncertainties in the mixing parameter fit allowing for *CPV* in the decay, in the mixing, and interference.

10.3 Legacy results Run 1 + Run 2

The obtained results must be averaged with Run 1 results to provide the final legacy Run 1 + 2 LHCb measurement with D^*-tagged $D^0 \to K\pi$ decays. The published Run 1 measurement [31] cannot be directly used for the average because the soft ghost pions were not accounted for in the analysis then. Consequently, the mixing parameters (in particular R_D) might be significantly biased in that sub-sample. The most recent published measurement that adds data from 2015-2016 [10] considers the background from ghost soft pions. Still, unfortunately, the result of the fit is not reported for the two datasets (Run 1 and 2015-16) separately, neither in the paper nor in the internal analysis note, so it is impossible to make a naive average with the mixing parameter measured in Run 1. However, the LHCb internal analysis note [83], associated to the article of Ref. [10], encloses all the raw information to recompute the χ^2 term of the Run 1 data, so it is possible to sum the Run 1 χ^2 term (Eq. 17 from [10]) and the Run 2 χ^2 term (Eq 9.1) and perform a simultaneous fit. In order to verify that the χ^2 term and all raw information are correctly collected and implemented we compare the results of the mixing fit from Ref. [10], reported for convenience in Tab. 10.9, with the ones obtained using the raw information, reported this time in Tab. 10.10. We find that any difference is much smaller than the associated uncertainties, and is probably due to numerical approximations.

Parameters		Correlations					
	$[10^{-5}]$	R^+	y'^+	x'^{2+}	R^-	y'^-	x'^{2-}
R^+	345.4 ± 4.4	1	-93.5%	84.3%	-1.2%	-0.3%	0.2%
y'^+	501 ± 74		1	-96.3%	-0.3%	0.4%	-0.3%
x'^{2+}	6.1 ± 3.8			1	0.2%	-0.4%	0.3%
R^-	345.5 ± 4.3				1	-93.5%	84.6%
y'^-	554 ± 74					1	-96.5%
x'^{2-}	1.6 ± 3.8						1

Table 10.9: Fit results for mixing parameters as reported in Ref. [10].

Parameters		Correlations					
	$[10^{-5}]$	R^+	y'^+	x'^{2+}	R^-	y'^-	x'^{2-}
R^+	344.9 ± 4.3	1	-93.5%	84.4%	-1.2%	-0.3%	0.2%
y'^+	513 ± 72		1	-96.3%	-0.3%	0.4%	-0.4%
x'^{2+}	5.5 ± 3.6			1	0.2%	-0.4%	0.4%
R^-	345.5 ± 4.3				1	-93.5%	84.6%
y'^-	552 ± 72					1	-96.5%
x'^{2-}	1.5 ± 3.7						1

Table 10.10: Fit results for mixing parameters obtained recomputing χ^2 minimization using raw information from Ref. [83].

This test confirms that we can safely combine our Run 2 results from this thesis to those obtained with Run 1 data using exactly the raw information utilized to publish the results reported in Ref. [10]. Anyway, small numerical differences are completely irrelevant, since the relative size of Run 1 data, with respect to that of Run 2, is very small.

As described in Sec. 10.1, this Run 1+Run 2 combined fit is performed four times using the same constraints on CPV observables, and repeated with the new experimental parametrization (R_D, $c_{K\pi}$, $c'_{K\pi}$, A_D, $\Delta c_{K\pi}$, $\Delta c'_{K\pi}$) and with the one used in the previously published measurement [10], for easier comparison of results. The obtained results and the systematic errors decomposition are shown in Tabs. 10.11-10.18. The results expressed with the old parametrization, used in the previously published measurement [10], are reported in App. H.1. The gain in precision when adding Run 1 data is, on average, about 7% on the physics parameters of interest. In the previous iteration of this analysis, instead of subtracting the bias, in order to account for the ghost background the uncertainties of the raw ratios were inflated. For the Run 1 ratios this inflation factor is about $\sqrt{1.5}$. It follows that the minimum of the Run 1 χ^2 is expected to be smaller than its number of degree of freedom, and consequently this will apply in the simultaneous with Run 2 χ^2 term.

No *CP* violation					
Parameters		Correlations			
		R_D	$c_{K\pi}$	$c'_{K\pi}$	
R_D	$(342.7 \pm 1.9)\times10^{-5}$	1	-92.7%	80.3%	
$c_{K\pi}$	$(52.8 \pm 3.3)\times10^{-4}$		1	-94.2%	
$c'_{K\pi}$	$(12.0 \pm 3.5)\times10^{-6}$			1	
χ^2/ndof	150.3 / 209	p-value	1.00		

Table 10.11: Fit results not allowing for CPV, simultaneously fitting Run 1 and Run 2.

No *CP* violation			
Source	R_D $[10^{-5}]$	$c_{K\pi}$ $[10^{-4}]$	$c'_{K\pi}$ $[10^{-6}]$
Mass mismodeling	0.43	0.74	0.77
Ghost soft pions	0.48	0.95	1.03
Instrumental asymm.	< 0.01	0.02	0.01
$a^d_{K^+K^-}$ ext. input	< 0.01	< 0.01	< 0.01
ΔY ext. input	< 0.01	< 0.01	< 0.01
Doubly Mis-ID bkg.	0.10	0.07	0.07
Common removal	0.23	0.04	0.04
Decay-time bias	0.09	0.14	0.13
m_{D^0}, τ_{D^0} ext. inputs	< 0.01	0.10	0.06
Total syst. uncertainty	0.69	1.19	1.27
Statistical uncertainty	1.79	3.10	3.24
Total uncertainty	1.92	3.33	3.48

Table 10.12: Summary of statistical and systematic uncertainties in the mixing fit not allowing for CPV, for the legacy Run 1 + Run 2 results.

No *CP* violation in the decay and in the mixing						
Parameters		Correlations				
		R_D	$c_{K\pi}$	$c'_{K\pi}$	$\Delta c_{K\pi}$	
R_D	$(342.7 \pm 1.9)\times10^{-5}$	1	-92.7%	80.3%	0.1%	
$c_{K\pi}$	$(52.8 \pm 3.3)\times10^{-4}$		1	-94.2%	-0.0%	
$c'_{K\pi}$	$(12.0 \pm 3.5)\times10^{-6}$			1	0.1%	
$\Delta c_{K\pi}$	$(-2.3 \pm 6.4)\times10^{-5}$				1	
χ^2/ndof	150.1 / 208	p-value	1.00			

Table 10.13: Fit results allowing only CPV in the interference between mixing and decay, simultaneously fitting Run 1 and Run 2.

No *CP* violation in the decay and in the mixing				
Source	R_D $[10^{-5}]$	$c_{K\pi}$ $[10^{-4}]$	$c'_{K\pi}$ $[10^{-6}]$	$\Delta c_{K\pi}$ $[10^{-5}]$
Mass mismodeling	0.43	0.74	0.77	1.15
Ghost soft pions	0.48	0.95	1.03	1.88
Instrumental asymm.	< 0.01	0.02	0.02	1.48
$a^d_{K^+K^-}$ ext. input	< 0.01	< 0.01	< 0.01	2.89
ΔY ext. input	< 0.01	< 0.01	< 0.01	1.46
Doubly Mis-ID bkg.	0.10	0.07	0.07	< 0.01
Common removal	0.23	0.04	0.05	< 0.01
Decay-time bias	0.09	0.14	0.13	0.01
m_{D^0}, τ_{D^0} ext. inputs	< 0.01	0.10	0.06	< 0.01
Total syst. uncertainty	0.69	1.19	1.27	4.05
Statistical uncertainty	1.79	3.10	3.24	4.97
Total uncertainty	1.92	3.33	3.48	6.41

Table 10.14: Summary of statistical and systematic uncertainties in the mixing fit allowing for *CPV* only in the interference between mixing and decay, for the legacy Run 1 + Run 2 results.

No *CP* violation in the decay						
Parameters		Correlations				
		R_D	$c_{K\pi}$	$c'_{K\pi}$	$\Delta c_{K\pi}$	$\Delta c'_{K\pi}$
R_D	$(342.7 \pm 1.9)\times10^{-5}$	1	-92.7%	80.3%	0.4%	-0.0%
$c_{K\pi}$	$(52.8 \pm 3.3)\times10^{-4}$		1	-94.2%	-0.3%	-0.0%
$c'_{K\pi}$	$(12.0 \pm 3.5)\times10^{-6}$			1	0.2%	0.1%
$\Delta c_{K\pi}$	$(-1.6 \pm 1.3)\times10^{-4}$				1	-87.8%
$\Delta c'_{K\pi}$	$(2.6 \pm 2.1)\times10^{-6}$					1
χ^2/ndof	148.7 / 207	p-value	1.00			

Table 10.15: Fit results allowing only *CPV* in the mixing and in the interference between mixing and decay, simultaneously fitting Run 1 and Run 2.

No *CP* violation in the decay					
Source	R_D [10^{-5}]	$c_{K\pi}$ [10^{-4}]	$c'_{K\pi}$ [10^{-6}]	$\Delta c_{K\pi}$ [10^{-4}]	$\Delta c'_{K\pi}$ [10^{-6}]
Mass mismodeling	0.43	0.74	0.77	0.26	0.45
Ghost soft pions	0.48	0.95	1.03	0.38	0.63
Instrumental asymm.	0.01	0.02	0.02	0.28	0.43
$a^d_{K^+K^-}$ ext. input	< 0.01	0.02	0.02	0.54	0.47
ΔY ext. input	< 0.01	< 0.01	< 0.01	0.11	0.07
Doubly Mis-ID bkg.	0.10	0.07	0.07	< 0.01	< 0.01
Common removal	0.23	0.04	0.04	< 0.01	< 0.01
Decay-time bias	0.09	0.14	0.13	< 0.01	< 0.01
m_{D^0}, τ_{D^0} ext. inputs	0.02	0.10	0.07	< 0.01	0.01
Total syst. uncertainty	0.69	1.19	1.27	0.75	0.98
Statistical uncertainty	1.79	3.10	3.24	1.11	1.91
Total uncertainty	1.92	3.33	3.48	1.34	2.15

Table 10.16: Summary of statistical and systematic uncertainties in the mixing fit allowing for *CPV* only in the mixing and the interference between mixing and decay, for the legacy Run 1 + Run 2 results.

CP violation in the decay, mixing and interference							
Parameters		Correlations					
		R_D	$c_{K\pi}$	$c'_{K\pi}$	A_D	$\Delta c_{K\pi}$	$\Delta c'_{K\pi}$
R_D	$(342.7 \pm 1.9)\times10^{-5}$	1	-92.7%	80.3%	0.9%	-0.7%	0.2%
$c_{K\pi}$	$(52.8 \pm 3.3)\times10^{-4}$		1	-94.2%	-1.3%	1.2%	-0.7%
$c'_{K\pi}$	$(12.0 \pm 3.5)\times10^{-6}$			1	0.7%	-0.7%	0.2%
A_D	$(-6.6 \pm 5.7)\times10^{-3}$				1	-91.9%	79.7%
$\Delta c_{K\pi}$	$(2.0 \pm 3.4)\times10^{-4}$					1	-94.1%
$\Delta c'_{K\pi}$	$(-0.7 \pm 3.6)\times10^{-6}$						1
χ^2/ndof	147.4 / 206	p-value	1.00				

Table 10.17: Fit results allowing for *CPV* in the decay, in the mixing and the interference, simultaneously fitting Run 1 and Run 2.

CP violation in the decay, in the mixing and the interference						
Source	R_D $[10^{-5}]$	$c_{K\pi}$ $[10^{-4}]$	$c'_{K\pi}$ $[10^{-6}]$	A_D $[10^{-3}]$	$\Delta c_{K\pi}$ $[10^{-4}]$	$\Delta c'_{K\pi}$ $[10^{-6}]$
Mass mismodeling	0.43	0.74	0.77	1.26	0.74	0.77
Ghost soft pions	0.48	0.95	1.03	1.43	0.96	1.05
Instrumental asymm.	0.01	0.03	0.02	1.11	0.68	0.71
$a^d_{K^+K^-}$ ext. input	< 0.01	< 0.01	< 0.01	1.07	0.05	0.06
ΔY ext. input	< 0.01	< 0.01	< 0.01	0.01	0.10	0.07
Doubly Mis-ID bkg.	0.10	0.07	0.07	0.02	0.01	0.01
Common removal	0.23	0.03	0.04	< 0.01	< 0.01	< 0.01
Decay-time bias	0.09	0.14	0.13	0.06	0.04	0.04
m_{D^0}, τ_{D^0} ext. inputs	< 0.01	0.10	0.06	0.02	< 0.01	< 0.01
Total syst. uncertainty	0.69	1.19	1.27	2.41	1.36	1.45
Statistical uncertainty	1.79	3.10	3.24	5.22	3.10	3.24
Total uncertainty	1.92	3.33	3.48	5.75	3.39	3.55

Table 10.18: Summary of statistical and systematic uncertainties in the mixing fit allowing for *CPV* in the decay, in the mixing, and interference, for the legacy Run 1 + Run 2 results.

10.4 Improvement over previous measurements

Table. 10.19 shows the comparison between the results of the legacy measurement performed in this thesis exploiting the full LHCb dataset (Run 1 plus Run 2) and the one of the previously published measurement [10] which made use of the data collected till the end of 2016. The improvement in the statistical uncertainty is a factor 1.4 for time-dependent parameters and a factor 1.6 for the others, in line with the increase in data sample statistics, while the reduction of systematic uncertainties is more substantial, ranging from a factor 1.8 to a factor 2.1 reduction.

Parameters	This result	LHCb 2011-16 [10]	stat. ratio	syst. ratio
R_D^+ $[10^{-5}]$	$340.4 \pm 2.5 \pm 1.1$	$345.4 \pm 4.0 \pm 2.0$	1.6	1.8
R_D^- $[10^{-5}]$	$345.0 \pm 2.5 \pm 1.1$	$345.4 \pm 4.0 \pm 2.0$	1.6	1.8
y'^+ $[10^{-4}]$	$54.8 \pm 4.6 \pm 1.8$	$50.1 \pm 6.4 \pm 3.8$	1.4	2.1
y'^- $[10^{-4}]$	$50.8 \pm 4.6 \pm 1.8$	$55.4 \pm 6.4 \pm 3.8$	1.4	2.1
x'^{2+} $[10^{-5}]$	$1.5 \pm 2.4 \pm 1.0$	$6.1 \pm 3.2 \pm 1.9$	1.3	1.9
x'^{2-} $[10^{-5}]$	$2.5 \pm 2.4 \pm 1.0$	$1.6 \pm 3.3 \pm 1.9$	1.4	1.9
A_D $[10^{-3}]$	$-6.6 \pm 5.2 \pm 2.4$	$-0.1 \pm 8.1 \pm 4.2$	1.6	1.8

Table 10.19: Comparison between the results of this thesis and the one of the previously published measurement [10].

The GammaCombo software [7] is used to combine the WS-to-RS prompt measure-

ment with the external measurements of the $\delta_{K\pi}$ strong phase from CLEO [8], BESIII [40] and the beauty observables sensitive to this parameter from LHCb measurement, as done in the LHCb average of beauty and charm observables [7]. This is done with the results of the previously published measurement [10] and repeated with the measurement results reported in this thesis. The combination is performed in the most general case, allowing for *CP* violation in the decay, mixing and interference between decay and mixing. A comparison of the 2D confidence intervals between the previous measurements and these new results are shown in Fig. 10.2 for the mixing parameters, x and y; and for the *CPV* parameters, $\left|\frac{q}{p}\right|$ and ϕ.

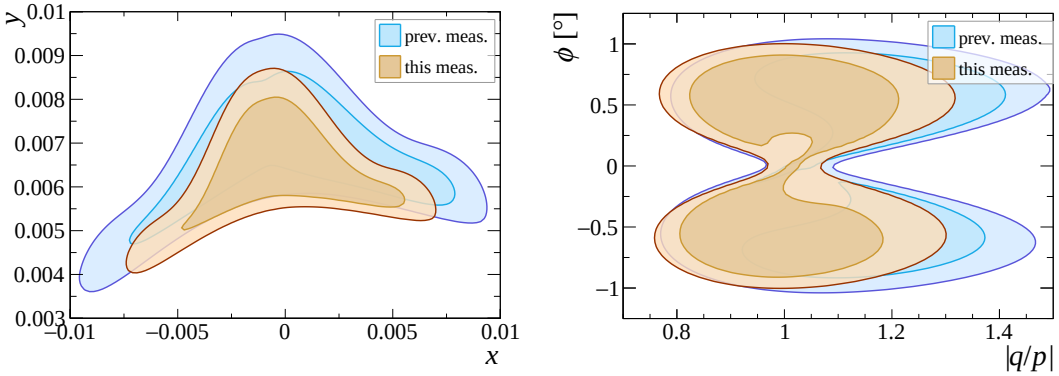

Figure 10.2: Comparison of the profile likelihood contours for the x *vs.* y (left) and $\left|\frac{q}{p}\right|$ *vs.* ϕ (right), between the previously published measurement [10] and the results of this thesis (central values are fixed to those of Ref. [10]). The $\delta_{K\pi}$ strong phase is constrained by external measurements from CLEO [8], BESIII [40] and LHCb [7]. The contours indicate the 68.3% and 95.4% confidence regions.

A LHCb average of all charm and beauty observable, using all currently available experimental information, is performed using the same approach of Ref. [7]. The same average is repeated by adding the results of the measurement performed in this thesis to show the impact of this measurement on the world average (largely dominated by LHCb results). The combination is performed in the most general case, allowing for *CP* violation in the decay, mixing and interference between decay and mixing. The resulting confidence intervals are shown in Fig. 10.3 for the for the mixing parameters, x and y (left panel) and for the *CPV* parameters, $\left|\frac{q}{p}\right|$ and ϕ (right panel) and in Fig. 10.4 for the strong phase, $\delta_{K\pi}$ and the DCS-to-CF ratio R_D.

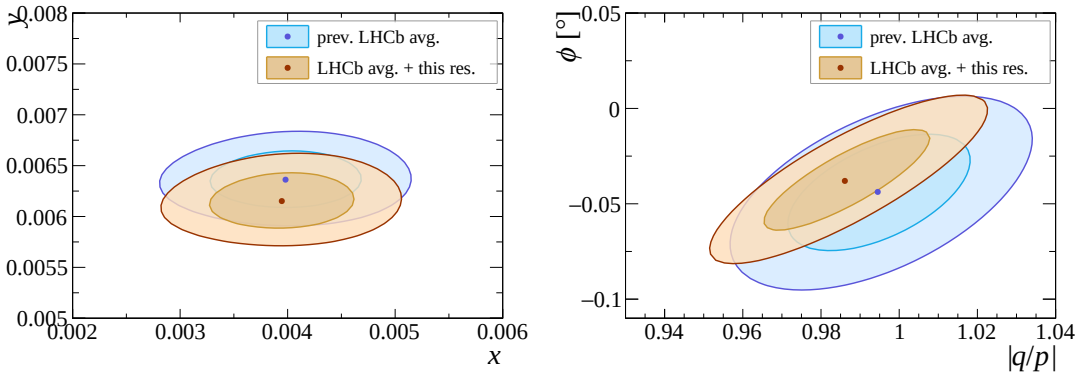

Figure 10.3: Comparison of the profile likelihood contours for the x *vs.* y (left) and $\left|\frac{q}{p}\right|$ *vs.* ϕ (right), between an LHCb global average of charm and beauty observables (like the one performed in Ref. [7]), with and without the results of this thesis. The contours indicate the 68.3% and 95.4% confidence regions.

As seen in Eq. 2.79, the $c_{K\pi}$ parameter is a rotation of angle $\delta_{K\pi}$ of the CPV parameters Δy and Δx: $c_{K\pi} \simeq \Delta y \cos\delta_{K\pi} - \Delta x \sin\delta_{K\pi}$. Since $\delta_{K\pi}$ is small (about 0.18 rad), $c_{K\pi}$ is mostly sensitive to Δy, with a correction from Δx. As explained in Sec. 10.1, constraints to the CP violation in the decay are theoretically motivated and, as shown in Tab. 10.13, can boost the precision of the $c_{K\pi}$ and $c'_{K\pi}$ parameters. The impact of this measurement on the world average of CPV parameters is comparable to the one of the last measurement of ΔY [46], and increases further if we include the additional constraint, such as the one on $\Delta c_{K\pi}$ or the superweak approximation.

The combination of the y_{CP} measurement with this measurement lead to an improvement of our knowledge of the $\delta_{K\pi}$ strong phases, resulting in the evidence of the $SU(3)_F$ symmetry breaking, as shown in Fig. 10.4 (right panel).

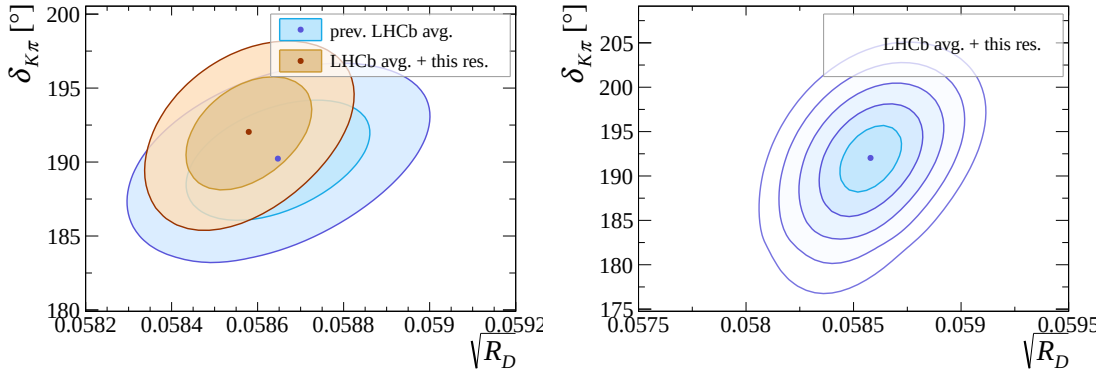

Figure 10.4: (Left) Comparison of the profile likelihood contours for R_D *vs.* $\delta_{K\pi}$ between an LHCb global average of charm and beauty observables (like the one performed in Ref. [7]), with and without the results of this thesis The contours indicate the 68.3% and 95.4% confidence regions. (Right) The same profile likelihood contour performed with the results of this thesis with contours which are drawn out to 5σ and contain 68.3%, 95.4%, 99.7%, etc. of the distribution.

10.5 Conclusions and future prospects

The thesis presents a measurement of D^0 mixing parameters and *CP*-violating asymmetries in $D^0 \to K^+\pi^-$ decays using the full Run 2 data sample collected with the LHCb experiment from 2015 to 2018, corresponding to an integrated luminosity of about 5.9 fb^{-1} at a centre-of-mass energy of 13 TeV. During the LHC Run 2 the LHCb experiment collected an unprecedented sample of extremely clean $D^0 \to K^-\pi^+$ RS decays, about 430 million, and a huge sample of suppressed $D^0 \to K^+\pi^-$ WS decays, about 1.7 million. The thesis, therefore, extends the previous world's most precise LHCb measurement of these parameters [10] to the whole available data sample, achieving an unprecedented level of precision and rapidly bringing us towards the LHCb Upgrade era, where a still much higher precision regime is foreseen. The global strategy of the analysis is already well established owing to the work performed during the last years by the LHCb collaborators, however, in preparation for future measurements, it has required a revisitation, and, consequently, a substantial improvement of almost all its aspects, to reduce as much as possible the size of systematic uncertainties. Results from Run 1 data, published in Ref [10], are averaged with those of this thesis increasing the final precision of about 7%, to provide the legacy Run 1+Run 2 LHCb measurement of D^0 mixing parameters and *CP*-violating asymmetries in $D^0 \to K^+\pi^-$ decays. An article summarising the analysis method and the results presented in this thesis will be soon submitted to the journal Physical Review D.

The selection of the data sample has been re-optimized to reduce the impact of the requirements that could make difficult a reduction of the systematic uncertainties. Trigger and offline requirements have been equalized, to make the sample much more uniform over the data-taking periods, and in order to partially restore the loss in purity due to the removal of a multivariate selection on the soft pion observables. Although such techniques are very powerful in discriminating signals from backgrounds, they sculpt the multi-dimensional space of input observables in a non-trivial way, making very difficult their modelling, and introducing subtle effects difficult to keep under control at the desired level of precision. In the end, no significant loss of statistical power has resulted. The principle of simplifying strategies and analysis approaches, even at the cost of losing part of the statistical power of available data, is increasingly becoming crucial in high-precision measurements such as those carried out in the charm sector. This aspect is even more relevant in view of future Runs where LHCb plans to collect much more abundant data samples than the current ones.

The fitting methodology to the invariant D^* mass, used to determine the signal yields, has been improved to properly account for the statistical correlations between WS and RS mass shapes. Contrary to the previous measurement, a simultaneous fit of the D^* invariant mass is now performed to the RS and WS samples, and to the soft pion ghost background. The addition of the latter component is of particular relevance because, for the first time, this subtle component has been studied and successfully isolated using a fully data-driven technique. In all previous similar analyses, also including measurement involving $D^{*+} \to D^0\pi_s^+$ decays where the D^0 meson goes to $K^0_S\pi^+\pi^-$ or $K^+\pi^+\pi^-\pi^+$, this subtle background was ignored or treated by assigning a considerable systematic

uncertainty on the R_D parameter. The mass modelling was studied in detail for the first time, and all the used empirical functions were justified and checked, from a quantitative point of view, to accurately reproduce the parent distributions of the various components of the fit. This might seem like a mere technicality, but it isn't. At the current level of precision, and in particular, for future analyses with even higher statistics, an unbiased separation of the different components of the fit becomes of paramount importance.

Particular attention has been dedicated to the reduction of the size of the systematic uncertainty, resulting in being the dominant one in the previous measurement, due to a few per cent residual contamination of D^0 mesons originating from weak decays of b-hadrons, and not in the pp primary vertex. Since the reconstructed decay time of secondary D^0 mesons is biased towards higher values, the measurement of the time-dependent ratio $R(t)$ can be significantly affected, and consequently the determination of physics observables, such as x' and y', can be falsified. This is in general a very difficult problem to overcome in a hadronic environment, such as LHCb. The effect of the presence of this residual contamination has been deeply studied, and a new methodology has been developed in order to remove all the approximations adopted in the past, that are not accurate for the current level of precision, and precisely include such effect in the time-dependent fit to the signal yields. The work of this thesis addresses for the first time, systematically, the difficult problem of tuning accurately the simulation using control data samples of secondary decays, as well as the problem of the limited knowledge of the multiple processes contributing to the b-hadrons cocktail. It results in a drastic reduction of the associated systematic uncertainty, about a factor of thirty less than the previous one assessed in the published measurement.

The methodology for correcting for the detection and production charge asymmetries, which are essential for probing *CP*-violating effects, has been completely superseded with a more robust and precise approach, by exploiting a more natural calibration data sample, $D^{*+} \to D^0(\to K^+K^-)\pi_s^+$. This sample has an almost identical topology of our signal RS and WS data samples, and, therefore, it is very suitable for this task, being selected in exactly the same manner as our RS and WS signal samples. The systematic uncertainty on A_D is reduced by a factor of about 2.6 with respect to the previous measurement, and it is fully dominated by the uncertainty on the measurement of the direct *CP*-violation parameter $a_{CP}(D^0 \to K^+K^-)$. The origin of this uncertainty is well determined, and it is expected to decrease with the increase in statistics foreseen for future data samples. The implementation of this new method was eased by the introduction of a new experimental observable, $R'(t)$, used for the first time in this thesis. The new observable probes the time-dependent WS/RS ratio at a given final state of decay of the neutral D meson, instead of a given initial state of the D meson (its flavour at production).

As a result, the systematic uncertainty improves by an average factor of 1.9. The total uncertainties, including both statistical and systematic components, improve by a factor of 1.6 with respect to those of the published LHCb measurement with 2011-2016 data sample, for both *CP*-averaged and *CP*-violating mixing parameters.

Last but not least, it is worth mentioning that the number of collected (signal) events approximately doubled compared to the previously published measurement [10], with a final number of about 500M of RS decays and about 2M of WS decays; therefore,

significant effort was put into the parallelization of the reading and processing of this large data sample.

This legacy Run 1 + 2 results will remain the most precise measurement of mixing and CPV parameters in $D^0 \to K^+\pi^-$ decay at least until 2025, at the end of LHC Run 3, when the LHCb experiment foreseen to collect additional $17\,\text{fb}^{-1}$ of integrated luminosity. In a similar time scale, the Belle II experiment foreseen to collect $50\,\text{ab}^{-1}$ of integrated luminosity of electron-positron collisions and predict to measure these parameters with an uncertainty similar to that reported in the results of this thesis [88]. If Upgrade II of the LHCb experiment will reach the foreseen instantaneous luminosity, tenfold greater than the one scheduled during Upgrade I, this would lead to a total recorded integrated luminosity of approximately $300\,\text{fb}^{-1}$ by approximately 2037. The recorded number of WS decays would consequently increase to over 100 million and could lead to a reduction in the statistical precision on $\Delta c_{K\pi}$ below 0.2×10^{-5}, comparable to or even less than the predictions within the Standard Model.

Appendices

Appendix $\mathcal{A}$

Ghost soft pions studies

A.1 Ghosts classification

The background of WS (RS) ghost candidates is produced by genuine soft pions from both WS and RS candidates. After going through the VELO, these genuine soft pions could be reconstructed or undetected (*e.g.*, they go out of acceptance due to the magnetic field or do not pass some trigger requirement). Suppose a ghost soft pion has the same charge as the associated reconstructed genuine soft pion. In that case, both pass the same HLT2 trigger line, resulting in multiple candidates excluded by the offline selection. If a WS ghost candidate is produced from a reconstructed genuine RS decay, this results in a common candidate, also removed by the offline selection.
The residual ghost background after the offline selection is mainly associated with genuine unreconstructed soft pions that cross the VELO. Some considerations can be made on the number and type of these ghost candidates. Let's define:

- N, the number of genuine RS decays that generate ghost candidates, for which the tagging pion is not correctly reconstructed;
- p_r, (p_u), the probability of a ghost track to have the same charge of the associated genuine reconstructed (unreconstructed) track (expected to be around 50%);
- k, the reconstructed-to-unreconstructed ratio of genuine decays that cross the VELO (estimated to be $\mathcal{O}(1)$ in the simulated samples);
- R_{sgn}, the time-integrated WS-to-RS signal ratio ($\approx 4 \times 10^{-3}$).

Each of these quantities is decay-time dependent.
The WS ghost candidates can be classified according to the type of associated genuine decays, and the corresponding yield can be estimated:

1. unreconstructed RS decays, $N(1 - p_u)$;
2. reconstructed RS decays, $Nk(1 - p_r)$ (removed common candidates);
3. unreconstructed WS decays, $NR_{\text{sgn}}p_u$;
4. reconstructed WS decays, $NR_{\text{sgn}}kp_r$ (removed multiple candidates).

Similarly, RS ghost candidates are produced from:

5. unreconstructed RS decays, Np_u;
6. reconstructed RS decays, Nkp_r (removed multiple candidates);
7. unreconstructed WS decays, $NR_{\text{sgn}}(1-p_u)$;
8. reconstructed WS decays, $NR_{\text{sgn}}k(1-p_r)$.

After the offline selection, the main source of both WS and RS ghost candidates is the genuine unreconstructed RS decays. They correspond to the ghost types 1 and 5 in the classification above, which we define *residual ghost candidates*. The expected WS-to-RS ratio of ghost candidates is

$$R_{\text{gst}} = \frac{N(1-p_u) + NR_{\text{sgn}}p_u}{Np_u + NR_{\text{sgn}}k(1-p_u) + NR_{\text{sgn}}(1-p_r)} \simeq \frac{1-p_u}{p_u} = \mathcal{O}(1), \tag{A.1}$$

since p_u is about 50%.

A.2 Test of fit sensitivity to ghost component

In this section, a test of our ability to discern ghost background from signal and combinatorial background is performed. The study is performed in 6 bins of track-based ghost probability, $\mathcal{P}_{\text{ghost}}(\pi_s)$, according to the following binning scheme:

$$\mathcal{P}_{\text{ghost}}(\pi_s) \in [0, 0.003, 0.005, 0.01, 0.05, 0.1, 0.25]. \tag{A.2}$$

For each $\mathcal{P}_{\text{ghost}}(\pi_s)$ bin, the time-integrated WS-to-RS ratios $R'^{\pm}$ are measured fitting the $m(D^0\pi_{\text{s}})_{\text{DTF}}$ distribution, both with and without taking into account a component associated with the ghost background contribution. The fit is performed independently for each bin of $\mathcal{P}_{\text{ghost}}(\pi_s)$, data-taking period and $K^+\pi^-/K^-\pi^+$ samples, using a χ^2 fit simultaneously to the $m(D^0\pi_{\text{s}})_{\text{DTF}}$ distributions of WS, RS (and CG, when the ghost background component is considered), with empirical modelling of signal, combinatorial background and ghost background. The $m(D^0\pi_{\text{s}})_{\text{DTF}}$ binning scheme is 312 bins for both WS and RS and 26 bins for CG, from 2004.4 MeV/c^2 to 2020.0 MeV/c^2. The signal, combinatorial background and ghost background pdfs are the same used in the yield fit described in Sect. 6 and are better detailed there. The fits projection to the 2016 $K^+\pi^-$ data sample are shown in Fig. A.1.

The detection asymmetry, mainly due to the soft pion charge asymmetry, shows a trend with respect to the soft pion ghost probability. If this effect is unaccounted for, a trend (with opposite direction for the $K^+\pi^-$ and $K^-\pi^+$ samples) appears in the WS-to-RS signal ratio that is not linked to the ghost background. To subtract this effect, the detection asymmetry is measured in each bin of $\mathcal{P}_{\text{ghost}}(\pi_s)$ and for each data-taking period. This measurement is performed as in Sect. 7.2, reweighting the KK sample weighted to the RS sample, and subsequently fitting the $m(D^0\pi_{\text{s}})_{\text{DTF}}$ distribution of the $D^* \to D^0\,(\to K^+K^-)\,\pi^+$ and $D^* \to D^0\,(\to K^+K^-)\,\pi^-$ samples simultaneously. Figure A.2

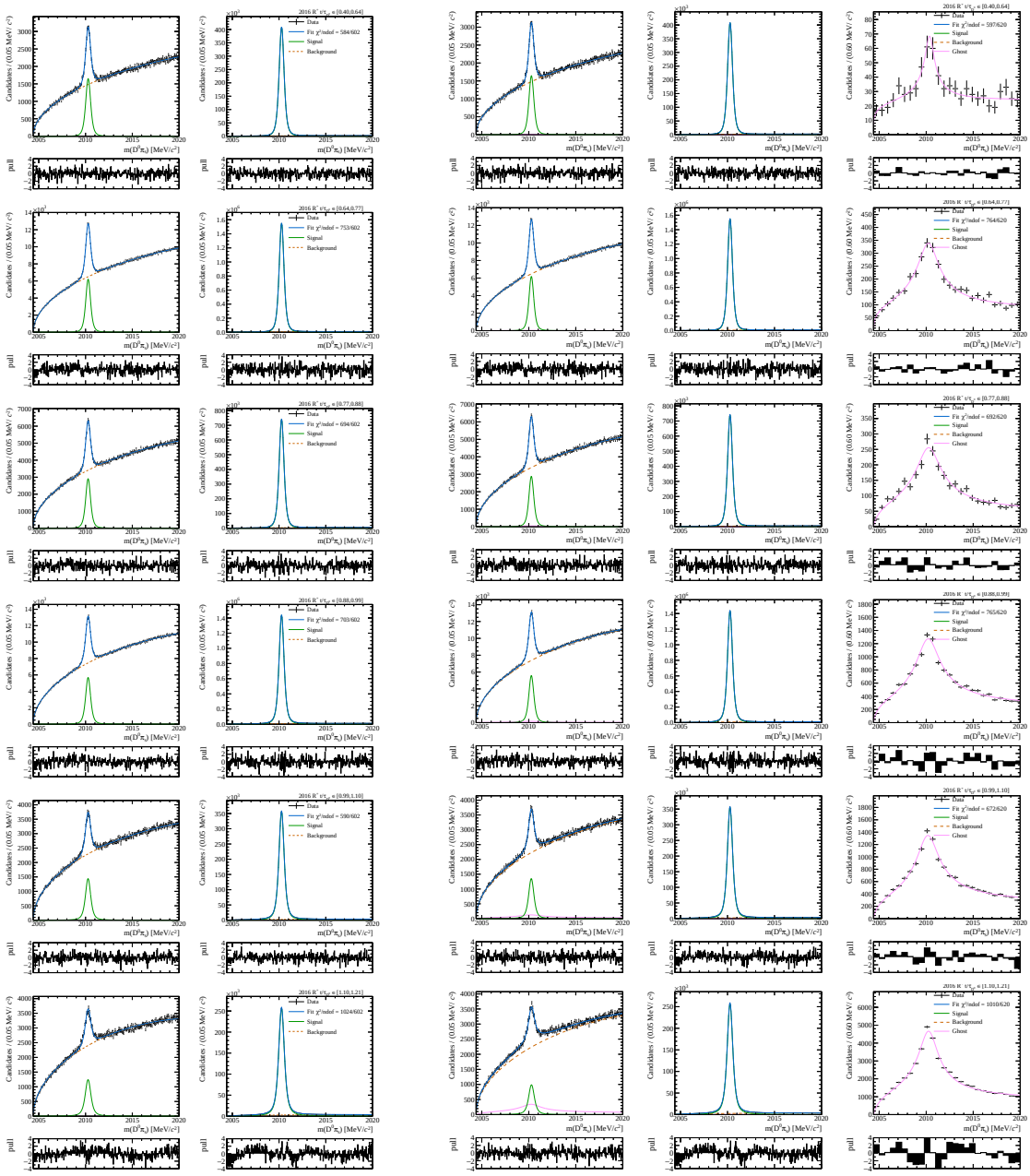

Figure A.1: Results of the mass fits to 2016 $K^+\pi^-$ data in bins of $\mathcal{P}_{\text{ghost}}(\pi_s)$, each line refers to a bin, from (top) bin 1 to (bottom) bin 6. The two plots on the left refer to the fits performed without the ghost component, and the three plots on the right refer to the fit that includes the ghost component.

shows the measured raw asymmetry in each bin of $\mathcal{P}_{\text{ghost}}(\pi_s)$ and for each data-taking period.

Finally, the detection asymmetry correction is applied to the WS-to-RS signal ratio, as shown in Fig. A.3. The $\mathcal{P}_{\text{ghost}}(\pi_s)$ has a great discrimination power between signal and ghost background. In high $\mathcal{P}_{\text{ghost}}(\pi_s)$ bins, the ghost background becomes relevant, and if we neglect it in the fit, R_{sgn} is visibly biased. However, including the ghost component, the fit correctly separates the combinatorial background and the ghost background, and the ratio no longer shows dependence on the $\mathcal{P}_{\text{ghost}}(\pi_s)$.

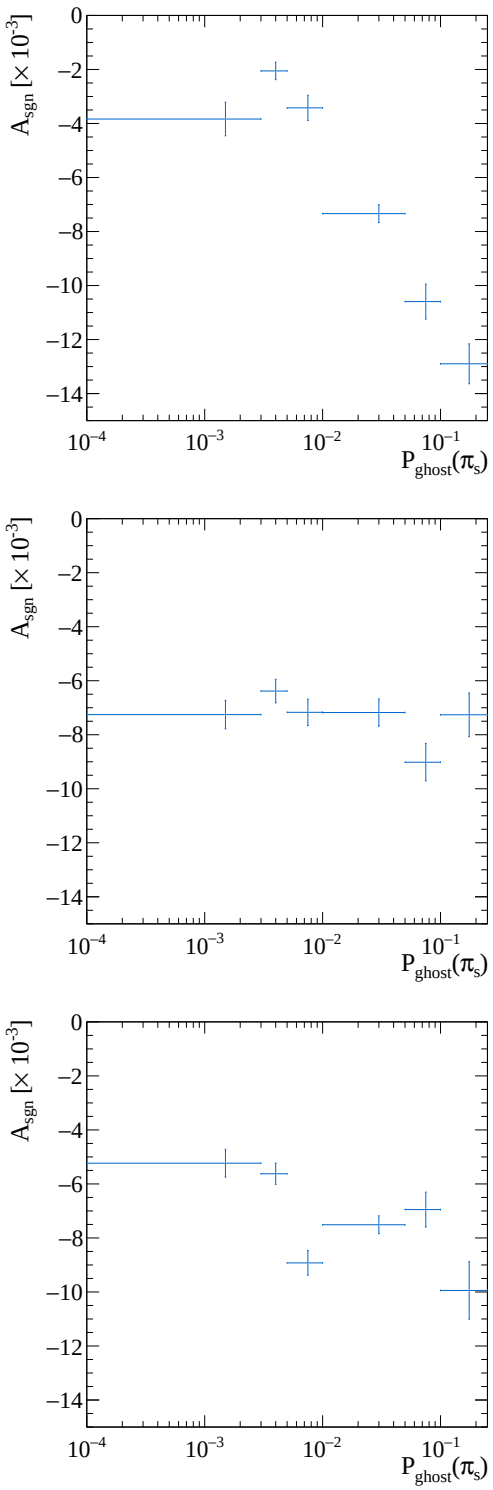

Figure A.2: Measured raw asymmetry of the *KK* sample weighted to the RS sample in each $\mathcal{P}_{\text{ghost}}(\pi_s)$ bin for the 2016 (Top), 2017 (Center) and 2018 (Bottom) data-taking samples.

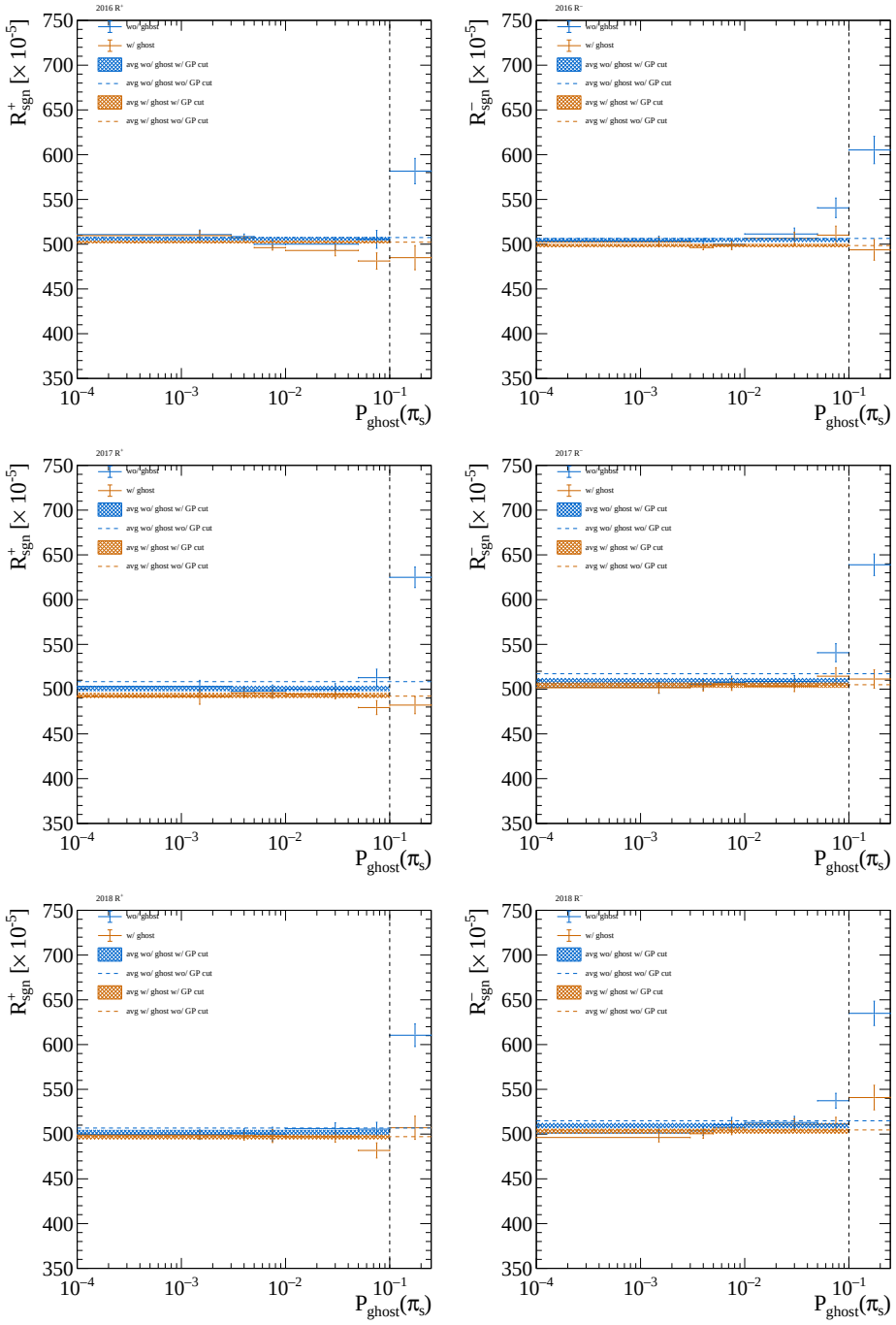

Figure A.3: Corrected WS-to-RS signal ratio as a function of the soft pion ghost probability, $\mathcal{P}_{\text{ghost}}(\pi_s)$, as a result of the fit to the $K^+\pi^-$ (Left) and $K^-\pi^+$ (Right) samples, in the 2016 (Top), 2017 (Centre) and 2018 (Bottom) samples, with (orange) and without (blue) the ghost background component. The black vertical dashed line shows the threshold of the $\mathcal{P}_{\text{ghost}}(\pi_s)$ offline requirement. The orange (blue) horizontal dashed line shows the average WS-to-RS signal ratio (not) accounting for the ghost background without any offline requirement on $\mathcal{P}_{\text{ghost}}(\pi_s)$. The orange (blue) horizontal box shows the $\pm1\sigma$ range around the average WS-to-RS signal ratio (not) accounting for the ghost background when the $\mathcal{P}_{\text{ghost}}(\pi_s)$ requirement is applied. The R_{sgn} absolute value is kept blind, adding a random shift.

Appendix $\mathcal{B}$

Instrumental asymmetry bias

The purpose of this appendix is to explain the assumptions and approximations underlying the detection asymmetry correction process. As we will illustrate, the presence of regions of the phase space where the detection asymmetry of the soft pion is very large can lead to bias in the measurement of the R_D and A_D parameters. Calculations are reported for both the standard and the alternative observables used in this analysis.

B.1 Standard observable

The theoretical standard observable to measure the WS-to-RS ratio is

$$R^+(t) = \frac{\Gamma(D^0(t) \to K^+\pi^-; t)}{\Gamma(D^0(t) \to K^-\pi^+; t)} \simeq a^+ + b^+ t + c^+ t^2 \tag{B.1}$$

$$R^-(t) = \frac{\Gamma(\bar{D}^0(t) \to K^-\pi^+; t)}{\Gamma(\bar{D}^0(t) \to K^+\pi^-; t)} \simeq a^- + b^- t + c^- t^2, \tag{B.2}$$

where $\Gamma(\overset{(-)}{D^0}(t) \to K\pi; t)$ is the branching fraction of a $\overset{(-)}{D^0}$ meson to decay in a $K\pi$ final state after a time t.

What we actually measure is

$$\tilde{R}_i^+ = \frac{N_i[D^{*+} \to D^0(\to K^+\pi^-)\pi_s^+]}{N_i[D^{*+} \to D^0(\to K^-\pi^+)\pi_s^+]} \quad \text{and} \quad \tilde{R}_i^- = \frac{N_i[D^{*-} \to \bar{D}^0(\to K^-\pi^+)\pi_s^-]}{N_i[D^{*-} \to \bar{D}^0(\to K^+\pi^-)\pi_s^-]}, \tag{B.3}$$

the subscript i indicates the decay-time bin in which the ratio is computed. If we focus our attention on the numerator, for instance, the WS^+ observed yield in each decay bin i

can be written as

$$N_i[D^{*+} \to D^0(\to K^+\pi^-)\pi_s^+] = \tag{B.4}$$
$$= \int^{t_i} \big[\mathcal{L}\,\sigma(pp \to D^{*+};\,\vec{p}_{D^*})\,|\mathcal{A}(D^{*+} \to D^0\pi_s^+;\,\vec{p}_{D^0},\vec{p}_{\pi_s})|^2$$
$$\Gamma(D^0 \to K^+\pi^-;\,t,\vec{p}_K,\vec{p}_\pi)\epsilon(K^+\pi^-\pi_s^+;\,t,\vec{p}_K,\vec{p}_\pi,\vec{p}_{\pi_s})\big]\,dt\,d\vec{p}_K\,d\vec{p}_\pi\,d\vec{p}_{\pi_s}$$

where

- $\mathcal{L}$ is the integrated luminosity;
- $\sigma(pp \to D^{*+};\,\vec{p}_{D^*})$ is the D^{*+} production cross section. It depends on the D^* momentum, and it is slightly different from $\sigma(pp \to D^{*-};\,\vec{p}_{D^*})$ as the pp initial state is not *CP* symmetric. The charge independent term can be factorized:[1] $\epsilon(D^{*+};\,\vec{p}_{D^0})\sigma(pp \to D^*;\,\vec{p}_{D^*})$, where $\sigma(pp \to D^*;\,\vec{p}_{D^*}) \equiv \max(\sigma(pp \to D^{*+};\,\vec{p}_{D^*}),\sigma(pp \to D^{*-};\,\vec{p}_{D^*}))$ and consequently $\epsilon(D^{*+};\,\vec{p}_{D^*}) \equiv \frac{\sigma(pp\to D^{*+};\,\vec{p}_{D^*})}{\sigma(pp\to D^{*};\,\vec{p}_{D^*})}$
- $\mathcal{A}(D^{*+} \to D^0\pi^+;\,\vec{p}_{D^0},\vec{p}_{\pi_s})$ is the differential amplitude of the strong decay $D^{*+} \to D^0\pi^+$. It depends on the D^0 and π_s momenta and it is equal to $\mathcal{A}(D^{*-} \to \overline{D}^0\pi^-;\,\vec{p}_{D^0},\vec{p}_{\pi_s})$, as strong decays are *CP* symmetric;
- $\Gamma(D^0 \to K^+\pi^-;\,t,\vec{p}_K,\vec{p}_\pi)$ is the differential decay rate of the weak decay $D^0 \to K^+\pi^-$. It depends on the D^0 decay time, K and π momentum. From the theoretical observable definition we can write $\Gamma(D^0 \to K^+\pi^-;\,t,\vec{p}_K,\vec{p}_\pi) = R^+(t)\Gamma^{RS+}(t,\vec{p}_K,\vec{p}_\pi)$; its analogue with the substitution $(+ \to -)$ holds for the charge-conjugate decay. Dependence on phase space and decay time can be factorized as $\Gamma^{RS+}(t)\cdot\Omega(\vec{p}_K,\vec{p}_\pi)$, where the phase space term $\Omega(\vec{p}_K,\vec{p}_\pi)$ is normalized and equal for the four $\overleftrightarrow{D^0} \to K^\pm\pi^\mp$ decays;
- $\epsilon(K^+\pi^-\pi_s^+;\,t,\vec{p}_K,\vec{p}_\pi,\vec{p}_{\pi_s})$ is the detection efficiency of the final states. It depends on the momenta of the three particles. It can be factorized with high accuracy: $\epsilon(K^-\pi^+;\,\vec{p}_K,\vec{p}_\pi)\epsilon(\pi_s^+,\,\vec{p}_{\pi_s})$. The $K^\pm\pi^\mp$ efficiency always appears together, hence one can integrate out $\Omega(D^0 \to K^+\pi^-;\,\vec{p}_K,\vec{p}_\pi)\epsilon(K^+\pi^-;\,t,\vec{p}_K,\vec{p}_\pi)$, obtaining $\epsilon(K^+\pi^-;\,t,\vec{p}_{D^0})$.

Therefore, the WS^+ yield can be rewritten as:

$$N_i[D^{*+} \to D^0(\to K^+\pi^-)\pi_s^+] = \tag{B.5}$$
$$= \int^{t_i} \mathcal{L}\,R^+(t)\Gamma^{RS+}(t)\epsilon(D^{*+}\pi_s^+,\,\vec{p}_{D^*};\,\vec{p}_{\pi_s})\epsilon(K^+\pi^-;\,t,\vec{p}_{D^0})\rho(\vec{p}_{D^*};\,\vec{p}_{\pi_s})\,dt\,d\vec{p},$$

where to streamline the notation we defined

$$\epsilon(D^{*+}\pi_s^+,\,\vec{p}_{D^0};\,\vec{p}_{\pi_s}) \equiv \epsilon(D^{*+};\,\vec{p}_{D^*})\epsilon(\pi_s^+,\,\vec{p}_{\pi_s}), \tag{B.6}$$
$$\rho(\vec{p}_{D^*};\,\vec{p}_{\pi_s}) \equiv \sigma(pp \to D^*;\,\vec{p}_{D^0})\,|\mathcal{A}(D^{*+} \to D^0\pi_s^+;\,\vec{p}_{D^0},\vec{p}_{\pi_s})|^2, \tag{B.7}$$
$$d\vec{p}_{D^0}d\vec{p}_{\pi_s} \equiv d\vec{p}. \tag{B.8}$$

[1] To treat the production asymmetry just like the other detector asymmetries, we define the charge-dependent term as an "efficiency" that multiplies the maximum of the production cross sections, which is charge independent by definition.

It is convenient to rewrite all the previous equations (and the new ones) by using averaged quantities and asymmetries, defined as

$$\Gamma^{\rm RS}(t) \equiv \frac{\Gamma^{\rm RS+}(t) + \Gamma^{\rm RS-}(t)}{2}, \tag{B.9}$$

$$A_{CP}^{\rm RS}(t) \equiv \frac{\Gamma^{\rm RS+}(t) - \Gamma^{\rm RS-}(t)}{\Gamma^{\rm RS+}(t) + \Gamma^{\rm RS-}(t)}, \tag{B.10}$$

$$\epsilon(K\pi;\, t, \vec{p}_{D^0}) \equiv \frac{\epsilon(K^+\pi^-;\, t, \vec{p}_{D^0}) + \epsilon(K^-\pi^+;\, t, \vec{p}_{D^0})}{2}, \tag{B.11}$$

$$A(K\pi;\, t, \vec{p}_{D^0}) \equiv \frac{\epsilon(K^+\pi^-;\, t, \vec{p}_{D^0}) - \epsilon(K^-\pi^+;\, t, \vec{p}_{D^0})}{\epsilon(K^+\pi^-;\, t, \vec{p}_{D^0}) + \epsilon(K^-\pi^+;\, t, \vec{p}_{D^0})}, \tag{B.12}$$

$$\epsilon(D^*\pi_{\rm s};\, \vec{p}_{D^0}, \vec{p}_{\pi_{\rm s}}) \equiv \frac{\epsilon(D^{*+}\pi_{\rm s}^+;\, \vec{p}_{D^0}, \vec{p}_{\pi_{\rm s}}) + \epsilon(D^{*-}\pi_{\rm s}^-;\, \vec{p}_{D^0}, \vec{p}_{\pi_{\rm s}})}{2}, \tag{B.13}$$

$$A(D^*\pi_{\rm s};\, \vec{p}_{D^0}, \vec{p}_{\pi_{\rm s}}) \equiv \frac{\epsilon(D^{*+}\pi_{\rm s}^+;\, \vec{p}_{D^0}, \vec{p}_{\pi_{\rm s}}) - \epsilon(D^{*-}\pi_{\rm s}^-;\, \vec{p}_{D^0}, \vec{p}_{\pi_{\rm s}})}{\epsilon(D^{*+}\pi_{\rm s}^+;\, \vec{p}_{D^0}, \vec{p}_{\pi_{\rm s}}) + \epsilon(D^{*-}\pi_{\rm s}^-;\, \vec{p}_{D^0}, \vec{p}_{\pi_{\rm s}})}, \tag{B.14}$$

obtaining

$$\begin{aligned} N_i[D^{*+} \to & D^0(\to K^+\pi^-)\pi_{\rm s}^+] = \\ &= \mathcal{L}\int^{t_i} R^+(t)[1 + A_{CP}^{\rm RS}(t)][1 + A(D^*\pi_{\rm s};\, \vec{p}_{D^0}, \vec{p}_{\pi_{\rm s}})][1 + A(K\pi;\, t, \vec{p}_{D^0})] \\ &\qquad \Gamma^{\rm RS}(t)\epsilon(D^*\pi_{\rm s},\, \vec{p}_{D^0};\, \vec{p}_{\pi_{\rm s}})\epsilon(K\pi;\, t, \vec{p}_{D^0})\rho(\vec{p}_{D^0};\, \vec{p}_{\pi_{\rm s}})\, dtd\vec{p} \\ &\simeq \mathcal{L}\int^{t_i} R^+(t)\omega(t, \vec{p}_{D^*}, \vec{p}_{\pi_{\rm s}})[1 + A_{CP}^{\rm RS}(t) + A(D^*\pi_{\rm s};\, \vec{p}_{D^0}, \vec{p}_{\pi_{\rm s}}) + A(K\pi;\, t, \vec{p}_{D^0}) \\ &\qquad + A_{CP}^{\rm RS}(t)A(D^*\pi_{\rm s};\, \vec{p}_{D^0}, \vec{p}_{\pi_{\rm s}}) + A(K\pi;\, t, \vec{p}_{D^0})A(D^*\pi_{\rm s};\, \vec{p}_{D^0}, \vec{p}_{\pi_{\rm s}})]dtd\vec{p} \end{aligned} \tag{B.15}$$

where we kept only terms up to the first order in $A_{CP}^{\rm RS}(t)$ and $A(K\pi;\, t, \vec{p}_{D^0})$, which are expected to be small ($\leq 1\%$) everywhere and we defined

$$\omega(t, \vec{p}_{D^0}, \vec{p}_{\pi_{\rm s}}) \equiv \Gamma^{\rm RS}(t)\epsilon(D^*\pi_{\rm s},\, \vec{p}_{D^0};\, \vec{p}_{\pi_{\rm s}})\epsilon(K\pi;\, t, \vec{p}_{D^0})\rho(\vec{p}_{D^0};\, \vec{p}_{\pi_{\rm s}}). \tag{B.16}$$

We can similarly compute the denominator

$$\begin{aligned} N_i[D^{*+} \to & D^0(\to K^-\pi^+)\pi_{\rm s}^+] = \\ &= \mathcal{L}\int^{t_i} \omega(t, \vec{p}_{D^0}, \vec{p}_{\pi_{\rm s}})[1 + A_{CP}^{\rm RS}(t)][1 + A(D^*\pi_{\rm s};\, \vec{p}_{D^0}, \vec{p}_{\pi_{\rm s}})][1 - A(K\pi;\, t, \vec{p}_{D^0})]dtd\vec{p} \\ &\simeq \mathcal{L}\int^{t_i} \omega(t, \vec{p}_{D^*}, \vec{p}_{\pi_{\rm s}})[1 + A_{CP}^{\rm RS}(t) + A(D^*\pi_{\rm s};\, \vec{p}_{D^0}, \vec{p}_{\pi_{\rm s}}) - A(K\pi;\, t, \vec{p}_{D^0}) \\ &\qquad - A_{CP}^{\rm RS}(t)A(D^*\pi_{\rm s};\, \vec{p}_{D^0}, \vec{p}_{\pi_{\rm s}}) - A(K\pi;\, t, \vec{p}_{D^0})A(D^*\pi_{\rm s};\, \vec{p}_{D^0}, \vec{p}_{\pi_{\rm s}})]dtd\vec{p} \end{aligned} \tag{B.17}$$

Hence, the observed ratio becomes (time and momentum dependencies are implicit inside the integral):

$$\tilde{R}_i^+ = \frac{\int^{t_i} R^+\omega[1 + A_{CP}^{\rm RS} + A(D^*\pi_{\rm s}) + A(K\pi) + A_{CP}^{\rm RS}A(D^*\pi_{\rm s}) + A(K\pi)A(D^*\pi_{\rm s})]dtd\vec{p}}{\int^{t_i} \omega[1 + A_{CP}^{\rm RS} + A(D^*\pi_{\rm s}) - A(K\pi) + A_{CP}^{\rm RS}A(D^*\pi_{\rm s}) - A(K\pi)A(D^*\pi_{\rm s})]dtd\vec{p}}. \tag{B.18}$$

Now we define the following quantity

$$\omega'(t,\vec{p}_{D^0},\vec{p}_{\pi_s}) \equiv \frac{\omega(t,\vec{p}_{D^0},\vec{p}_{\pi_s})}{\int^{t_i}\omega(t,\vec{p}_{D^0},\vec{p}_{\pi_s})dtd\vec{p}}, \tag{B.19}$$

and we expand the denominator, taking advantage of the fact that the integral of the three asymmetries (or of their product) is always much smaller than the unit, so we keep the first order:

$$\tilde{R}_i^+ = \frac{\int^{t_i} R^+\omega'[1+A_{CP}^{RS}+A(D^*\pi_s)+A(K\pi)+A_{CP}^{RS}A(D^*\pi_s)+A(K\pi)A(D^*\pi_s)]dtd\vec{p}}{1+\int^{t_i}\omega'[A_{CP}^{RS}+A(D^*\pi_s)-A(K\pi)+A_{CP}^{RS}A(D^*\pi_s)-A(K\pi)A(D^*\pi_s)]dtd\vec{p}} \tag{B.20}$$

$$\begin{aligned}
&\simeq \left\{\int^{t_i} R^+\omega'[1+A_{CP}^{RS}+A(D^*\pi_s)+A(K\pi)+A_{CP}^{RS}A(D^*\pi_s)+A(K\pi)A(D^*\pi_s)]dtd\vec{p}\right\} \\
&\quad\cdot\left\{1-\int^{t_i}\omega'[A_{CP}^{RS}+A(D^*\pi_s)-A(K\pi)+A_{CP}^{RS}A(D^*\pi_s)-A(K\pi)A(D^*\pi_s)]dtd\vec{p}\right\} \\
&\simeq \int^{t_i} R^+\omega' dtd\vec{p} \\
&\quad+\int^{t_i} R^+\omega'[A_{CP}^{RS}+A(D^*\pi_s)+A_{CP}^{RS}A(D^*\pi_s)]\,dtd\vec{p} \\
&\quad-\int^{t_i} R^+\omega' dtd\vec{p}\cdot\int^{t_i}\omega'[A_{CP}^{RS}+A(D^*\pi_s)+A_{CP}^{RS}A(D^*\pi_s)]\,dtd\vec{p} \\
&\quad+\int^{t_i} R^+\omega'[A(K\pi)+A(K\pi)A(D^*\pi_s)]\,dtd\vec{p} \\
&\quad+\int^{t_i} R^+\omega' dtd\vec{p}\cdot\int^{t_i}\omega'[A(K\pi)+A(K\pi)A(D^*\pi_s)]\,dtd\vec{p} \\
&\simeq \int^{t_i} R^+\omega' dtd\vec{p}\cdot\left\{1+2\int^{t_i}\omega'[A(K\pi)+A(K\pi)A(D^*\pi_s)]\,dtd\vec{p}\right\}.
\end{aligned}$$

In the last step, we are assuming that the correlation between $R(t)$ and the asymmetries is negligible, which is equivalent to assuming that the decay-time dependency of $A_{CP}^{RS}(t)$ and $\int A(K\pi;t,\vec{p}_{D^0})d\vec{p}_{D^0}$ is small, at least inside a decay-time bin. This assumption is supported by the experimental limits on $A_\Gamma(RS)$ and the measurement of $A(K\pi)$ from the previous iteration of this analysis.
Now we can do the same to compute the correction to $R^-(t)$. The numerator is

$$\begin{aligned}
&N_i[D^{*-}\to\overline{D}^0(\to K^-\pi^+)\pi_s^-] = \\
&= \mathcal{L}\int^{t_i} R^-(t)\omega(t,\vec{p}_{D^*},\vec{p}_{\pi_s})[1-A_{CP}^{RS}(t)][1-A(D^*\pi_s;\vec{p}_{D^0},\vec{p}_{\pi_s})][1-A(K\pi;t,\vec{p}_{D^0})] \\
&\simeq \mathcal{L}\int^{t_i} R^-(t)\omega(t,\vec{p}_{D^*},\vec{p}_{\pi_s})[1-A_{CP}^{RS}(t)-A(D^*\pi_s;\vec{p}_{D^0},\vec{p}_{\pi_s})-A(K\pi;t,\vec{p}_{D^0}) \\
&\qquad+A_{CP}^{RS}(t)A(D^*\pi_s;\vec{p}_{D^0},\vec{p}_{\pi_s})+A(K\pi;t,\vec{p}_{D^0})A(D^*\pi_s;\vec{p}_{D^0},\vec{p}_{\pi_s})]dtd\vec{p},
\end{aligned} \tag{B.21}$$

while the denominator is

$$
\begin{aligned}
N_i[D^{*-} \to \overline{D}^0(\to K^+\pi^-)\pi_s^-] = & \qquad \text{(B.22)}\\
= \mathcal{L}\int^{t_i} & \omega(t,\vec{p}_{D^0},\vec{p}_{\pi_s})[1-A_{CP}^{RS}(t)][1-A(D^*\pi_s;\,\vec{p}_{D^0},\vec{p}_{\pi_s})][1+A(K\pi;\,t,\vec{p}_{D^0})]dtd\vec{p}\\
\simeq \mathcal{L}\int^{t_i} & \omega(t,\vec{p}_{D^*},\vec{p}_{\pi_s})[1-A_{CP}^{RS}(t)-A(D^*\pi_s;\,\vec{p}_{D^0},\vec{p}_{\pi_s})+A(K\pi;\,t,\vec{p}_{D^0})\\
& -A_{CP}^{RS}(t)A(D^*\pi_s;\,\vec{p}_{D^0},\vec{p}_{\pi_s})-A(K\pi;\,t,\vec{p}_{D^0})A(D^*\pi_s;\,\vec{p}_{D^0},\vec{p}_{\pi_s})]dtd\vec{p}.
\end{aligned}
$$

Hence the ratio is

$$
\tilde{R}_i^- \simeq \frac{\int^{t_i} R^-\omega'[1-A_{CP}^{RS}-A(D^*\pi_s)-A(K\pi)+A_{CP}^{RS}A(D^*\pi_s)+A(K\pi)A(D^*\pi_s)]dtd\vec{p}}{1+\int^{t_i}\omega'[-A_{CP}^{RS}-A(D^*\pi_s)+A(K\pi)-A_{CP}^{RS}A(K\pi)-A(D^*\pi_s)A(K\pi)]dtd\vec{p}} \qquad \text{(B.23)}
$$

$$
\simeq \int^{t_i} R^-\omega' dtd\vec{p}\cdot\left\{1-2\int^{t_i}\omega'[A(K\pi)-A_{CP}^{RS}A(D^*\pi_s)-A(K\pi)A(D^*\pi_s)]\,dtd\vec{p}\right\}.
$$

Finally, the correction due to nuisance asymmetries is:

$$
\begin{aligned}
\tilde{R}_i^{\pm} &= \int^{t_i} R^{\pm}(t)\omega'(t,\vec{p}_{D^0},\vec{p}_{\pi_s})\,dt\,d\vec{p}_{D^0}\,d\vec{p}_{\pi_s}\cdot\left(1\pm 2A_{K\pi}^{\int i\pm}\right) \qquad \text{(B.24)}\\
&\simeq \int^{t_i}\left(a^{\pm}+b^{\pm}t+c^{\pm}t^2\right)\omega'(t,\vec{p}_{D^0},\vec{p}_{\pi_s})\,dt\,d\vec{p}_{D^0}\,d\vec{p}_{\pi_s}\cdot\left(1\pm 2A_{K\pi}^{\int i\pm}\right)\\
&= \left(a^{\pm}+b^{\pm}\langle t\rangle+c^{\pm}\langle t^2\rangle\right)\cdot\left(1\pm 2A_{K\pi}^{\int i\pm}\right)
\end{aligned}
$$

where

$$
A_{K\pi}^{\int i\pm} \equiv \int^{t_i} A(K\pi)\,\omega'\,dt\,d\vec{p} \pm \int^{t_i}\left[A_{CP}^{RS}A(D^*\pi_s)+A(K\pi)A(D^*\pi_s)\right]\omega'\,dt\,d\vec{p}. \qquad \text{(B.25)}
$$

In conclusion, R^+ and R^- need a different correction for detection asymmetry. Even if the main source comes from the detection asymmetry of the $K\pi$ pair, that must be weighted with the π_s^+ acceptance, which is different for positively and negatively charged soft pions and therefore different for R^+ and R^- observables.

B.2 Detection asymmetry correction of the standard observable

To correct for the detection asymmetry, we use a single estimator $\overline{A}^{\int i}_{K\pi}$, for both $A^{\int i+}_{K\pi}$ and $A^{\int i-}_{K\pi}$, hence we neglect the $\pm \int^{t_i} A(K\pi)A(D^*\pi)\omega'$ term[2],

$$\overline{A}^{\int i}_{K\pi} \equiv A^{i,\mathrm{rwgt}}_{\mathrm{raw}}(KK) - A^{i}_{\mathrm{raw}}(RS) - A^{\mathrm{KK},i}_{CP}, \tag{B.26}$$

where

$$A^{i}_{\mathrm{raw}}(RS) \equiv \frac{N_i[D^{*+} \to D^0(\to K^-\pi^+)\pi^+_{\mathrm{s}}] - N_i[D^{*-} \to \overline{D}^0(\to K^+\pi^-)\pi^-_{\mathrm{s}}]}{N_i[D^{*+} \to D^0(\to K^-\pi^+)\pi^+_{\mathrm{s}}] + N_i[D^{*-} \to \overline{D}^0(\to K^+\pi^-)\pi^-_{\mathrm{s}}]}, \tag{B.27}$$

$$A^{i,\mathrm{rwgt}}_{\mathrm{raw}}(KK) \equiv \frac{\sum_j \left(N_{ij}[D^{*+} \to D^0(\to K^-K^+)\pi^+_{\mathrm{s}}] - N_{ij}[D^{*-} \to \overline{D}^0(\to K^-K^+)\pi^-_{\mathrm{s}}]\right) \mathrm{w}_j}{\sum_k \left(N_{ik}[D^{*+} \to D^0(\to K^-K^+)\pi^+_{\mathrm{s}}] + N_{ik}[D^{*-} \to \overline{D}^0(\to K^-K^+)\pi^-_{\mathrm{s}}]\right) \mathrm{w}_k}, \tag{B.28}$$

$$A^{\mathrm{KK},i}_{CP} \equiv A_{CP}(KK) - A_{\Gamma}(KK) \cdot \langle t \rangle_i \tag{B.29}$$

with $A_{CP}(KK)$ and $A_{\Gamma}(KK)$ external inputs and w_j (or w_k) the weights needed to reweight the kinematic distribution of the KK sample to that of the RS one in phase space bins. For instance, in a given bin j of kinematics, we can write:

$$\mathrm{w}_{ij} \equiv \frac{N_{ij}[D^{*+} \to D^0(\to K^-\pi^+)\pi^+_{\mathrm{s}}] + N_{ij}[D^{*-} \to \overline{D}^0(\to K^+\pi^-)\pi^-_{\mathrm{s}}]}{N_{ij}[D^{*+} \to D^0(\to K^-K^+)\pi^+_{\mathrm{s}}] + N_{ij}[D^{*-} \to \overline{D}^0(\to K^-K^+)\pi^-_{\mathrm{s}}]}. \tag{B.30}$$

Then, we can rewrite $A^{i}_{\mathrm{raw}}(RS)$ as

$$A^{i}_{\mathrm{raw}}(RS) = \frac{\int^{t_i} \Gamma^{\mathrm{RS}+}\epsilon(D^{*+}\pi^+_{\mathrm{s}})\epsilon(K^-\pi^+)\rho\, dt\, d\vec{p} - \int^{t_i} \Gamma^{\mathrm{RS}-}\epsilon(D^{*-}\pi^-_{\mathrm{s}})\epsilon(K^+\pi^-_{\mathrm{s}})\rho\, dt\, d\vec{p}}{\int^{t_i} \Gamma^{\mathrm{RS}+}\epsilon(D^{*+}\pi^+_{\mathrm{s}})\epsilon(K^-\pi^+)\rho\, dt\, d\vec{p} + \int^{t_i} \Gamma^{\mathrm{RS}-}\epsilon(D^{*-}\pi^-_{\mathrm{s}})\epsilon(K^-\pi^+)\rho\, dt\, d\vec{p}}. \tag{B.31}$$

The numerator can be rewritten as

$$\begin{aligned}
&\int^{t_i} \Gamma^{\mathrm{RS}+}\epsilon(D^{*+}\pi^+_{\mathrm{s}})\epsilon(K^-\pi^+)\rho\, dt\, d\vec{p} - \int^{t_i} \Gamma^{\mathrm{RS}-}\epsilon(D^{*-}\pi^-_{\mathrm{s}})\epsilon(K^+\pi^-_{\mathrm{s}})\rho\, dt\, d\vec{p} = \qquad \text{(B.32)}\\
&= \int^{t_i} [1 + A^{\mathrm{RS}}_{CP}][1 + A(D^*\pi_{\mathrm{s}})][1 - A(K\pi)]\Gamma^{\mathrm{RS}}\epsilon(K\pi)\epsilon(D^*\pi_{\mathrm{s}})\rho\, dt\, d\vec{p}\\
&- \int^{t_i} [1 - A^{\mathrm{RS}}_{CP}][1 - A(D^*\pi_{\mathrm{s}})][1 + A(K\pi)]\Gamma^{\mathrm{RS}}\epsilon(K\pi)\epsilon(D^*\pi_{\mathrm{s}})\rho\, dt\, d\vec{p}\\
&= \int^{t_i} 2\left[A^{\mathrm{RS}}_{CP} + A(D^*\pi_{\mathrm{s}}) - A(K\pi) - A^{\mathrm{RS}}_{CP}A(D^*\pi_{\mathrm{s}})A(K\pi)\right]\omega dt\, d\vec{p},
\end{aligned}$$

[2]The $\int^{t_i} A^{\mathrm{RS}}_{CP}A(D^*\pi_{\mathrm{s}})$ term is also neglected because the direct CPV in CF decays is assumed zero throughout all the analysis.

while the denominator

$$\int^{t_i} \Gamma^{\mathrm{RS}+}\epsilon(D^{*+}\pi_{\mathrm{s}}^{+})\epsilon(K^{-}\pi^{+})\rho\,dt\,d\vec{p} + \int^{t_i} \Gamma^{\mathrm{RS}-}\epsilon(D^{*-}\pi_{\mathrm{s}}^{-})\epsilon(K^{+}\pi_{\mathrm{s}}^{-})\rho\,dt\,d\vec{p} = \quad \text{(B.33)}$$
$$= \int^{t_i} [1 + A_{CP}^{\mathrm{RS}}][1 + A(D^{*}\pi_{\mathrm{s}})][1 - A(K\pi)]\Gamma^{\mathrm{RS}}\epsilon(D^{*}\pi_{\mathrm{s}})\epsilon(K\pi)\rho\,dt\,d\vec{p}$$
$$+ \int^{t_i} [1 - A_{CP}^{\mathrm{RS}}][1 - A(D^{*}\pi_{\mathrm{s}})][1 + A(K\pi)]\Gamma^{\mathrm{RS}}\epsilon(D^{*}\pi_{\mathrm{s}})\epsilon(K\pi)\rho\,dt\,d\vec{p}$$
$$= \int^{t_i} 2\left[1 - A_{CP}^{\mathrm{RS}}A(K\pi) + A_{CP}^{\mathrm{RS}}A(D^{*}\pi_{\mathrm{s}}) - A(K\pi)A(D^{*}\pi_{\mathrm{s}})\right]\omega\,dt\,d\vec{p},$$

then the ratio becomes

$$A_{\mathrm{raw}}^{i}(RS) = \frac{\int^{t_i}\left[A_{CP}^{RS}(t) - A(K\pi;t) + A(D^{*}\pi_{\mathrm{s}}) - A_{CP}^{RS}(t)A(K\pi;t)A(D^{*}\pi_{\mathrm{s}})\right]\omega'(t)\,dt\,d\vec{p}}{1 + \int^{t_i}\left[-A_{CP}^{RS}(t)A(K\pi;t) + A_{CP}^{RS}(t)A(D^{*}\pi_{\mathrm{s}}) - A(K\pi;t)A(D^{*}\pi_{\mathrm{s}})\right]\omega'(t)\,dt\,d\vec{p}} \quad \text{(B.34)}$$
$$\simeq \int^{t_i}\left[A_{CP}^{RS}(t) - A(K\pi;t) + A(D^{*}\pi_{\mathrm{s}})\right]\omega'(t)\,dt\,d\vec{p}.$$

As for $A_{\mathrm{raw}}^{i}(RS)$, the asymmetry $A_{\mathrm{raw}}^{i,\mathrm{rwgt}}(KK)$ can be rewritten as

$$A_{\mathrm{raw}}^{i,\mathrm{rwgt}}(KK) = \frac{\int^{t_i}\Gamma^{\mathrm{KK}+}\epsilon(D^{*+}\pi_{\mathrm{s}}^{+})\epsilon(K^{-}K^{+})\rho\mathrm{w}\,dt\,d\vec{p} - \int^{t_i}\Gamma^{\mathrm{KK}-}\epsilon(D^{*-}\pi_{\mathrm{s}}^{-})\epsilon(K^{-}K^{+})\rho\mathrm{w}\,dt\,d\vec{p}}{\int^{t_i}\Gamma^{\mathrm{KK}+}\epsilon(D^{*+}\pi_{\mathrm{s}}^{+})\epsilon(K^{-}K^{+})\rho\,dt\,d\vec{p} + \int^{t_i}\Gamma^{\mathrm{KK}-}\epsilon(D^{*-}\pi_{\mathrm{s}}^{-})\epsilon(K^{-}K^{+})\rho\,dt\,d\vec{p}}. \quad \text{(B.35)}$$

Then the numerator can be rewritten as

$$\int^{t_i}\Gamma^{\mathrm{KK}+}\epsilon(D^{*+}\pi_{\mathrm{s}}^{+})\epsilon(K^{-}K^{+})\rho\mathrm{w}\,dt\,d\vec{p} - \int^{t_i}\Gamma^{\mathrm{KK}-}\epsilon(D^{*-}\pi_{\mathrm{s}}^{-})\epsilon(K^{-}K^{+})\rho\mathrm{w}\,dt\,d\vec{p} = \quad \text{(B.36)}$$
$$= \int^{t_i}[1 + A_{CP}^{\mathrm{KK}}][1 + A(D^{*}\pi_{\mathrm{s}})]\Gamma^{\mathrm{KK}}\epsilon(D^{*}\pi_{\mathrm{s}})\epsilon(KK)\rho\mathrm{w}\,dt\,d\vec{p}$$
$$- \int^{t_i}[1 - A_{CP}^{\mathrm{KK}}][1 - A(D^{*}\pi_{\mathrm{s}})]\Gamma^{\mathrm{KK}}\epsilon(D^{*}\pi_{\mathrm{s}})\epsilon(KK)\rho\mathrm{w}\,dt\,d\vec{p}$$
$$= \int^{t_i} 2\left[A_{CP}^{\mathrm{KK}} + A(D^{*}\pi_{\mathrm{s}})\right]\Gamma^{\mathrm{KK}}\epsilon(D^{*}\pi_{\mathrm{s}})\epsilon(KK)\rho\mathrm{w}\,dt\,d\vec{p},$$

while the denominator

$$\int^{t_i}\Gamma^{\mathrm{KK}+}\epsilon(D^{*+}\pi_{\mathrm{s}}^{+})\epsilon(K^{-}K^{+})\rho\mathrm{w}\,dt\,d\vec{p} + \int^{t_i}\Gamma^{\mathrm{KK}-}\epsilon(D^{*-}\pi_{\mathrm{s}}^{-})\epsilon(K^{-}K^{+})\rho\mathrm{w}\,dt\,d\vec{p} = \quad \text{(B.37)}$$
$$= \int^{t_i}[1 + A_{CP}^{\mathrm{KK}}][1 + A(D^{*}\pi_{\mathrm{s}})]\Gamma^{\mathrm{KK}}\epsilon(D^{*}\pi_{\mathrm{s}})\epsilon(KK)\rho\mathrm{w}\,dt\,d\vec{p}$$
$$+ \int^{t_i}[1 - A_{CP}^{\mathrm{KK}}][1 - A(D^{*}\pi_{\mathrm{s}})]\Gamma^{\mathrm{KK}}\epsilon(D^{*}\pi_{\mathrm{s}})\epsilon(KK)\rho\mathrm{w}\,dt\,d\vec{p}$$
$$= \int^{t_i} 2\left[1 + A_{CP}^{\mathrm{KK}}A(D^{*}\pi_{\mathrm{s}})\right]\Gamma^{\mathrm{KK}}\epsilon(D^{*}\pi_{\mathrm{s}})\epsilon(KK)\rho\mathrm{w}\,dt\,d\vec{p}.$$

Now the weights are

$$\mathrm{w}_{i,j} = \frac{\int^{t_i,\phi_j} \Gamma^{\mathrm{RS}+}\epsilon(D^{*+}\pi_{\mathrm{s}}^{+})\epsilon(K^{-}\pi^{+})\rho dt d\vec{p} + \int^{t_i} \Gamma^{\mathrm{RS}-}\epsilon(D^{*-}\pi_{\mathrm{s}}^{-})\epsilon(K^{+}\pi^{-})\rho dt d\vec{p}}{\int^{t_i} \Gamma^{\mathrm{KK}+}\epsilon(D^{*+}\pi_{\mathrm{s}}^{+})\epsilon(K^{-}K^{+})\rho dt d\vec{p} + \int^{t_i,\phi_j} \Gamma^{\mathrm{KK}-}\epsilon(D^{*-}\pi_{\mathrm{s}}^{-})\epsilon(K^{-}K^{+})\rho dt d\vec{p}}, \tag{B.38}$$

where $\int^{t_i,\phi_j}$ is the integral in the decay-time bin t_i and the phase-space bin ϕ_j. If the binning is sufficiently fine than $\mathrm{w}_{i,j}$ is a good approximation of the continuous function $\mathrm{w}(t, \vec{p}_{D^0}, \vec{p}_{\pi_{\mathrm{s}}})$ and the ratio of Eq. B.38 becomes

$$\mathrm{w}(t, \vec{p}_{D^0}, \vec{p}_{spi}) = \frac{\left[1 - A_{CP}^{\mathrm{RS}}A(K\pi) + A_{CP}^{\mathrm{RS}}A(D^*\pi_{\mathrm{s}}) - A(K\pi)A(D^*\pi_{\mathrm{s}})\right]\Gamma^{\mathrm{RS}}\epsilon(K\pi)}{\left[1 + A_{CP}^{\mathrm{KK}}A(D^*\pi_{\mathrm{s}})\right]\Gamma^{\mathrm{KK}}\epsilon(KK)} \tag{B.39}$$

From this, it follows that

$$\begin{aligned} A_{\mathrm{raw}}^{i,\mathrm{rwgt}}(KK) &= \frac{\int^{t_i}\left[A_{CP}^{\mathrm{KK}} + A(D^*\pi_{\mathrm{s}})\right]\Gamma^{\mathrm{KK}}\epsilon(D^*\pi_{\mathrm{s}})\epsilon(KK)\rho\mathrm{w}\, dt\, d\vec{p},}{\int^{t_i}\left[1 + A_{CP}^{\mathrm{KK}}A(D^*\pi_{\mathrm{s}})\right]\Gamma^{\mathrm{KK}}\epsilon(D^*\pi_{\mathrm{s}})\epsilon(KK)\rho\mathrm{w}\, dt\, d\vec{p}} \qquad \text{(B.40)} \\ &= \int^{t_i} \frac{[A_{CP}^{\mathrm{KK}} + A(D^*\pi_{\mathrm{s}})][1 - A_{CP}^{\mathrm{RS}}A(K\pi) + A_{CP}^{\mathrm{RS}}A(D^*\pi_{\mathrm{s}}) - A(K\pi)A(D^*\pi_{\mathrm{s}})]}{1 + A_{CP}^{\mathrm{KK}}A(D^*\pi_{\mathrm{s}})}\omega\, dt\, d\vec{p}\cdot \\ &\quad \cdot \frac{1}{\int^{t_i}\left[1 - A_{CP}^{\mathrm{RS}}A(K\pi) - A_{CP}^{\mathrm{RS}}A(D^*\pi_{\mathrm{s}}) + A(K\pi)A(D^*\pi_{\mathrm{s}})\right]\omega\, dt\, d\vec{p}} \\ &\simeq \int^{t_i}[A_{CP}^{\mathrm{KK}} + A(D^*\pi_{\mathrm{s}}) + A_{CP}^{\mathrm{RS}}A^2(D^*\pi_{\mathrm{s}}) - A(K\pi)A^2(D^*\pi_{\mathrm{s}}) - A_{CP}^{\mathrm{KK}}A^2(D^*\pi_{\mathrm{s}})]\omega'\, dt\, d\vec{p} \end{aligned}$$

Finally, we can rewrite $\overline{A}_{K\pi}^{\int i}$:

$$\begin{aligned} \overline{A}_{K\pi}^{\int i} &= A_{\mathrm{raw}}^{i,\mathrm{rwgt}}(KK) - A_{\mathrm{raw}}^{i}(RS) - A_{CP}^{\mathrm{KK},i} = \qquad \text{(B.41)} \\ &\simeq \int^{t_i} A(K\pi)\omega'(t)\, dt\, d\vec{p} - \int^{t_i}\left\{A_{CP}^{\mathrm{RS}} + A^2(D^*\pi_{\mathrm{s}})\left[A(K\pi) - A_{CP}^{\mathrm{RS}} + A_{CP}^{\mathrm{KK}}\right]\right\}\omega'(t)\, dt\, d\vec{p} \end{aligned}$$

Neglecting A_{CP}^{RS} and A_{CP}^{KK}, the $K\pi$ asymmetry is weighted with a term $(1 - A^2(D^*\pi_{\mathrm{s}}))$. This term is 0 in the region where the asymmetry is ± 1. This is because it is impossible to measure $A(K\pi)$ in the phase-space regions where the efficiency in reconstructing one of the two soft pions is 0 due to the soft pion acceptance.

Estimation of bias on R_D and A_D Let's now compute the bias on the physics parameters caused by the use of $\overline{A}_{K\pi}^{\int i}$ instead of $A_{K\pi}^{\int i\pm}$. First of all, it is useful to define the following quantities:

$$\alpha \equiv \int^{t_i}\left[A_{CP}^{\mathrm{RS}}A(D^*\pi_{\mathrm{s}}) + A(K\pi)A(D^*\pi_{\mathrm{s}})\right]\omega'\, dt\, d\vec{p} \tag{B.42}$$

$$\beta \equiv \int^{t_i}\left\{A_{CP}^{\mathrm{RS}} + A^2(D^*\pi_{\mathrm{s}})\left[A(K\pi) - A_{CP}^{\mathrm{RS}} + A_{CP}^{\mathrm{KK}}\right]\right\}\omega'(t)\, dt\, d\vec{p} \tag{B.43}$$

The measured observable, $\tilde{R}_i^{\pm}$, is biased by the detection asymmetry and is linked to the unbiased ratio that we want to measure, $R_i^{\pm}$, as

$$R_i^{\pm} \equiv \frac{\tilde{R}_i^{\pm}}{\left(1 \pm 2A_{K\pi}^{\int i\pm}\right)}. \tag{B.44}$$

However, the correction is not exact, so instead of computing the unbiased ratio $R_i^{\pm}$, we obtain

$$\overline{R}_i^{\pm} \equiv \frac{\tilde{R}_i^{\pm}}{\left(1 \pm 2\overline{A}_{K\pi}^{\int i}\right)}, \tag{B.45}$$

implying that

$$\overline{R}_i^{\pm}\left(1 \pm 2\overline{A}_{K\pi}^{\int i}\right) = R_i^{\pm}\left(1 \pm 2A_{K\pi}^{\int i\pm}\right), \tag{B.46}$$

hence

$$\overline{R}_i^{\pm} \simeq R_i^{\pm}\left(1 \pm 2A_{K\pi}^{\int i\pm} \mp 2\overline{A}_{K\pi}^{\int i}\right) = R_i^{\pm}\left(1 + 2\alpha \pm 2\beta\right). \tag{B.47}$$

Hence our estimator $\overline{R}_{CP} \equiv \frac{\overline{R}_D^+ + \overline{R}_D^-}{2}$ and $\overline{A}_D \equiv \frac{\overline{R}_D^+ - \overline{R}_D^-}{\overline{R}_D^+ + \overline{R}_D^-}$ for the physical parameters $R_{CP} \equiv \frac{R_D^+ + R_D^-}{2}$ and $A_D \equiv \frac{R_D^+ - R_D^-}{R_D^+ + R_D^-}$, is:

$$\overline{R}_{CP} \equiv \frac{\overline{R}_D^+ + \overline{R}_D^-}{2} \simeq \frac{R_D^+}{2}\left(1 + 2a + 2b\right) + \frac{R_D^-}{2}\left(1 + 2a - 2b\right) = R_{CP}\left(1 + 2a + 2A_D b\right), \tag{B.48}$$

and

$$\overline{A}_D \equiv \frac{\overline{R}^+ - \overline{R}^-}{\overline{R}^+ + \overline{R}^-} \simeq \frac{R_D^+}{2R_{CP}}\left(1 + 2\alpha + 2\beta\right) - \frac{R_D^-}{2R_{CP}}\left(1 + 2\alpha - 2\beta\right) = A_D\left(1 + 2\alpha\right) + 2\beta. \tag{B.49}$$

Let's make a first rough estimate of these contributions, assuming no fiducial cuts. Both $A(K\pi)$ and $A(D^*\pi_s)$ can be written as the sum of an even part and an odd part (by inversion of the x component of $\vec{p}_{D^*}$). Considering the two samples with different magnet polarity separately, $A(D^*\pi_s)$ is mostly odd, as this asymmetry depends mainly on the acceptance of the soft pion. The even part of $A(K\pi)$ is primarily due to K interaction with matter. At the same time, the odd one is due to acceptance effects (because the K is more massive, generating an imbalance of momenta of the pair). Detection asymmetry due to acceptance effects can be large in the regions at the edge of the acceptance. Still, usually, this is not an issue since the asymmetry is integrated over an even region, and this contribution cancels out almost completely. However, in the term $\int^{t_0} A(K\pi)A(D^*\pi)\omega'$, the product of the two odd parts produces an even function which does not cancel out when integrated over the even domain, making this term difficult to estimate.

The $A(D^*\pi)$ asymmetry is not a smooth function and can be approximated as 0 in the low asymmetry regions and ± 1 in the high asymmetry regions. The latter contains about 20% of the signal. Hence $A^2(D^*\pi)$ is equal to 1 in these regions, and the term $\int^{t_0} A(K\pi)A^2(D^*\pi)\omega'$ can be approximated as $0.2 \times \int^{t_0,H} A(K\pi)\omega'$, where the integral is performed only in the high asymmetry regions. Since these regions are even, only K interaction with matter is relevant. From the previous iteration of this analysis, we know that the integrated $A(K\pi)$ is $\mathcal{O}(1\%)$; since it is integrated on even phase space, this is an estimate of the even part of $A(K\pi)$, the one due to K interaction with the detector matter. Hence we expect this term to be around 0.2%.
Finally, the relevant biases are:

$$\overline{R}_i^{\pm} \simeq R_D\,(1+2\alpha) = R_D\left(1+2\int^{t_i}\left[A_{CP}^{\mathrm{RS}}A(D^*\pi_\mathrm{s}) + A(K\pi)A(D^*\pi_\mathrm{s})\right]\omega'\,dt\,d\vec{p}\right), \tag{B.50}$$

$$\simeq R_D\left(1+2\int\left[A(K\pi)A(D^*\pi_\mathrm{s})\right]\omega\,dt\,d\vec{p}\right), \tag{B.51}$$

$$\overline{A}_D \simeq A_D + 2\beta = A_D + 2\int^{t_i}\left\{A_{CP}^{\mathrm{RS}} + A^2(D^*\pi_\mathrm{s})\left[A(K\pi) - A_{CP}^{\mathrm{RS}} + A_{CP}^{\mathrm{KK}}\right]\right\}\omega'(t)\,dt\,d\vec{p} \tag{B.52}$$

$$\simeq A_D + 2\int A^2(D^*\pi_\mathrm{s})\left[A(K\pi) + A_{CP}^{\mathrm{KK}}\right]\omega\,dt\,d\vec{p}. \tag{B.53}$$

The final relative precision on R_{CP} is about 0.6%, while the final absolute precision on A_D is about 0.6% (see Tab. 10.11). The estimated value of the bias on A_D ($\sim 0.4\%$) is in the same ballpark of the final statistical uncertainty, while we do not have reliable strategies to measure the bias on R_D precisely. The application of loose fiducial cuts strongly reduces the sizes of these biases, making them negligible. As a collateral benefit, they also reduce the background from ghost soft pions (see Sec. 5.4). For these reasons, we decided to introduce fiducial requirements in the offline selection of this analysis that remove kinematic regions of the soft pions with very high ($\approx \pm 100\%$) charge asymmetry. All previously published versions of this analysis never considered these effects and did not set fiducial requirements.

B.3 Alternative observable

It is possible to define an alternative experimental observable substantially equivalent to the standard one:

$$\tilde{R}'^{+}_i = \frac{N_i[D^{*+}\to D^0(\to K^+\pi^-)\pi_\mathrm{s}^+]}{N_i[D^{*-}\to \overline{D}^0(\to K^+\pi^-)\pi_\mathrm{s}^-]} \quad \text{and} \quad \tilde{R}'^{-}_i = \frac{N_i[D^{*-}\to \overline{D}^0(\to K^-\pi^+)\pi_\mathrm{s}^-]}{N_i[D^{*+}\to D^0(\to K^-\pi^+)\pi_\mathrm{s}^+]}, \tag{B.54}$$

The new observable, is indistinguishable from that in Eq. B.1, up to a multiplicative factor of $(1 \pm 2a_f^d)$ [89]. Let's compute the correction for the nuisance asymmetries for this new

variable as we did in the previous sections of this appendix,

$$\tilde{R'}_i^{\pm} \simeq \frac{\int^{t_i} R^{\pm}\omega'[1 \pm A_{CP}^{\mathrm{RS}} \pm A(D^*\pi_\mathrm{s}) \pm A(K\pi) + A_{CP}^{\mathrm{RS}}A(D^*\pi_\mathrm{s}) + A(K\pi)A(D^*\pi_\mathrm{s})]dtd\vec{p}}{1 + \int^{t_i} \omega'[\mp A_{CP}^{\mathrm{RS}} \mp A(D^*\pi_\mathrm{s}) \pm A(K\pi) + A_{CP}^{\mathrm{RS}}A(D^*\pi_\mathrm{s}) - A(K\pi)A(D^*\pi_\mathrm{s})]dtd\vec{p}} \tag{B.55}$$

$$\begin{aligned}
&\simeq \left\{\int^{t_i} R^{\pm}\omega'[1 \pm A_{CP}^{\mathrm{RS}} \pm A(D^*\pi_\mathrm{s}) \pm A(K\pi) + A_{CP}^{\mathrm{RS}}A(D^*\pi_\mathrm{s}) + A(K\pi)A(D^*\pi_\mathrm{s})]dtd\vec{p}\right\} \\
&\quad \cdot \left\{1 - \int^{t_i} \omega'[\mp A_{CP}^{\mathrm{RS}} \mp A(D^*\pi_\mathrm{s}) \pm A(K\pi) + A_{CP}^{\mathrm{RS}}A(D^*\pi_\mathrm{s}) - A(K\pi)A(D^*\pi_\mathrm{s})]dtd\vec{p}\right\} \\
&\simeq \int^{t_i} R^{\pm}\omega' dtd\vec{p} \\
&\quad + \int^{t_i} R^{\pm}\omega'[\pm A(K\pi) + A_{CP}^{\mathrm{RS}}A(D^*\pi_\mathrm{s})]\, dtd\vec{p} \\
&\quad - \int^{t_i} R^{\pm}\omega' dtd\vec{p} \cdot \int^{t_i} \omega'[A(K\pi) + A_{CP}^{\mathrm{RS}}A(D^*\pi_\mathrm{s})]\, dtd\vec{p} \\
&\quad + \int^{t_i} R^{\pm}\omega'[\pm A_{CP}^{\mathrm{RS}} \pm A(D^*\pi_\mathrm{s}) + A(K\pi)A(D^*\pi_\mathrm{s})]\, dtd\vec{p} \\
&\quad + \int^{t_i} R^{\pm}\omega' dtd\vec{p} \cdot \int^{t_i} \omega'[\pm A_{CP}^{\mathrm{RS}} \pm A(D^*\pi_\mathrm{s}) + A(K\pi)A(D^*\pi_\mathrm{s})]\, dtd\vec{p} \\
&\simeq \int^{t_i} R^{\pm}\omega' dtd\vec{p} \cdot \left\{1 \pm 2\int^{t_i} \omega'[A_{CP}^{\mathrm{RS}} + A(D^*\pi_\mathrm{s}) \pm A(K\pi)A(D^*\pi_\mathrm{s})]\, dtd\vec{p}\right\}.
\end{aligned}$$

Hence, the correction due to nuisance asymmetries is:

$$\tilde{R'}_i^{\pm} \simeq \left(a^{\pm} + b^{\pm}\langle t\rangle + c^{\pm}\langle t^2\rangle\right) \cdot \left(1 \pm 2A_{D^*\pi_\mathrm{s}}^{\int i\pm}\right) \tag{B.56}$$

where

$$A_{D^*\pi_\mathrm{s}}^{\int i\pm} \equiv \int^{t_i} A(D^*\pi_\mathrm{s})\omega'\, dtd\vec{p} + \int^{t_i} A_{CP}^{\mathrm{RS}}\, dtd\vec{p} \pm \int^{t_i} A(K\pi)A(D^*\pi_\mathrm{s})\, dtd\vec{p}. \tag{B.57}$$

B.4 Detection asymmetry correction of the alternative observable

As for the standard observable, to correct for the detection asymmetry, we use a single estimator $\overline{A}_{D^*\pi_\mathrm{s}}^{\int i}$, for both $A_{D^*\pi_\mathrm{s}}^{\int i+}$ and $A_{D^*\pi_\mathrm{s}}^{\int i-}$, hence, we neglect the $\pm\int^{t_i} A(K\pi)A(D^*\pi)\omega'$ term. The $\overline{A}_{D^*\pi_\mathrm{s}}^{\int i}$ asymmetry is defined as

$$\begin{aligned}
\overline{A}_{D^*\pi_\mathrm{s}}^{\int i} &\equiv A_{\mathrm{raw}}^{i,\mathrm{rwgt}}(KK) - A_{CP}^{\mathrm{KK},i} \\
&\simeq \int^{t_i} A(D^*\pi_\mathrm{s})\omega'(t)\, dt\, d\vec{p} - \int^{t_i} A^2(D^*\pi_\mathrm{s})\left[A(K\pi) - A_{CP}^{\mathrm{RS}} + A_{CP}^{\mathrm{KK}}\right]\omega'(t)\, dt\, d\vec{p}.
\end{aligned} \tag{B.58}$$

Estimation of bias on R_D and A_D As for the standard observable, we can now compute the bias on the new physics parameters caused by the use of $\overline{A}_{D^*\pi_\mathrm{s}}^{\int i}$ instead of $A_{D^*\pi_\mathrm{s}}^{\int i\pm}$,

finding that the final bias is exactly the same as of the standard variable.

Appendix C

Ratio fits' projections

This appendix collects the D^* invariant mass distributions of WS, RS and CG (common ghost) candidates in each deacy-time bin and data-taking period. The results of the corresponding fits are superimposed.

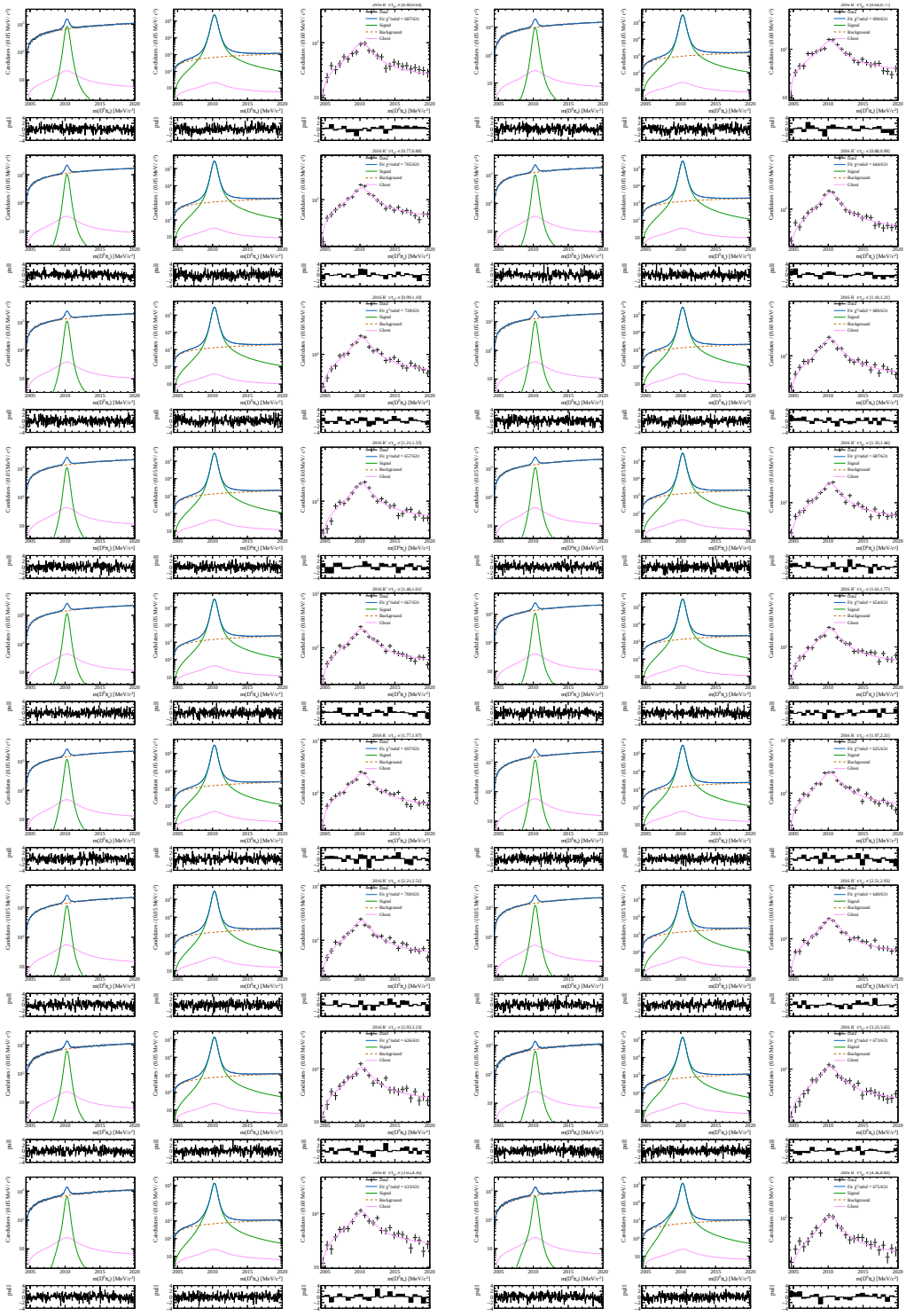

Figure C.1: Distributions of the $m(D^0\pi_s)_{\mathrm{DTF}}$ of WS (Left), RS (Center) and CG (Right) in each D^0 decay-time bins of the $K^+\pi^-$ 2016 sample. Fit projection are superimposed.

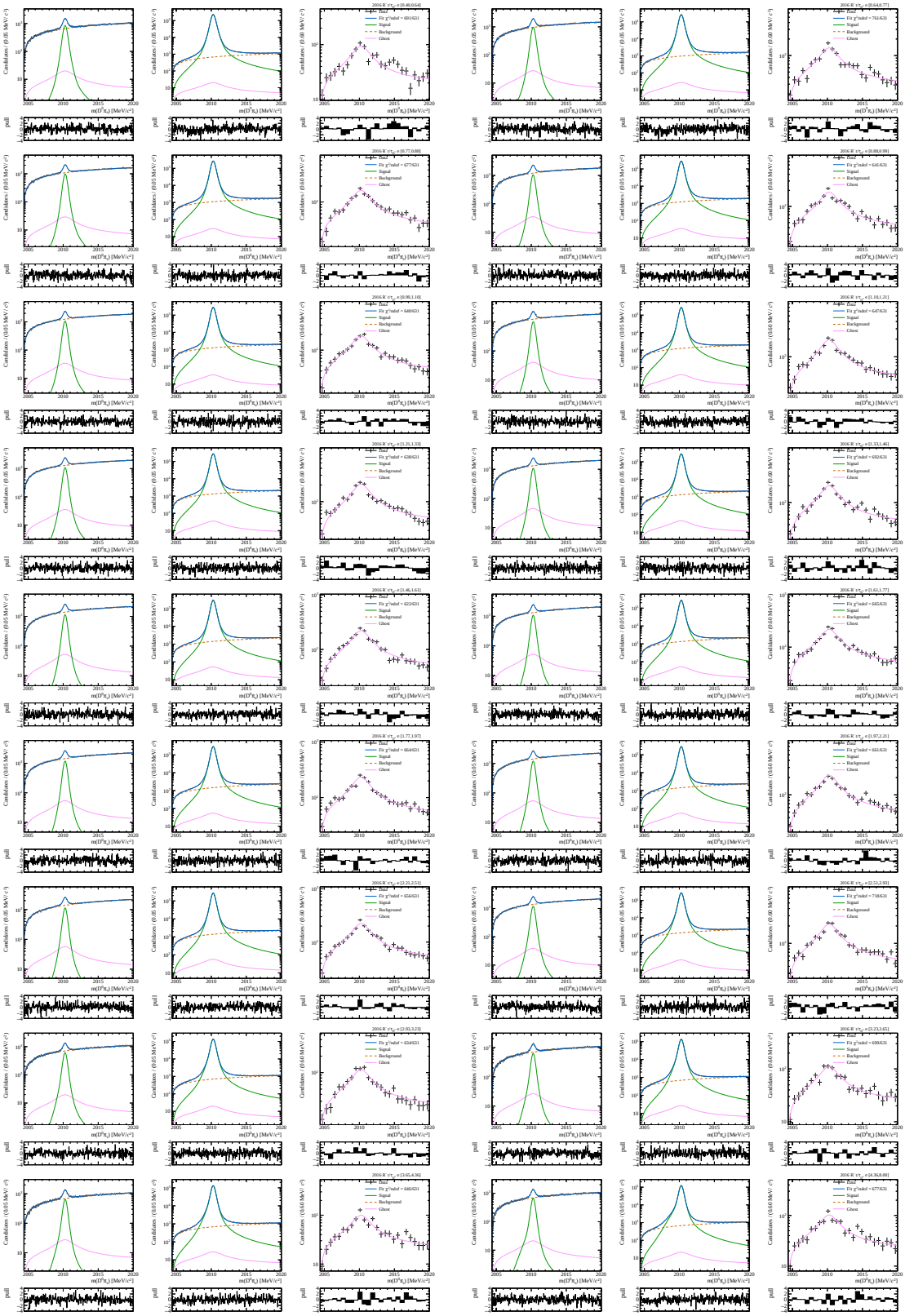

Figure C.2: Distributions of the $m(D^0\pi_s)_{\mathrm{DTF}}$ of WS (Left), RS (Center) and CG (Right) in each D^0 decay-time bins of the $K^-\pi^+$ 2016 sample. Fit projection are superimposed.

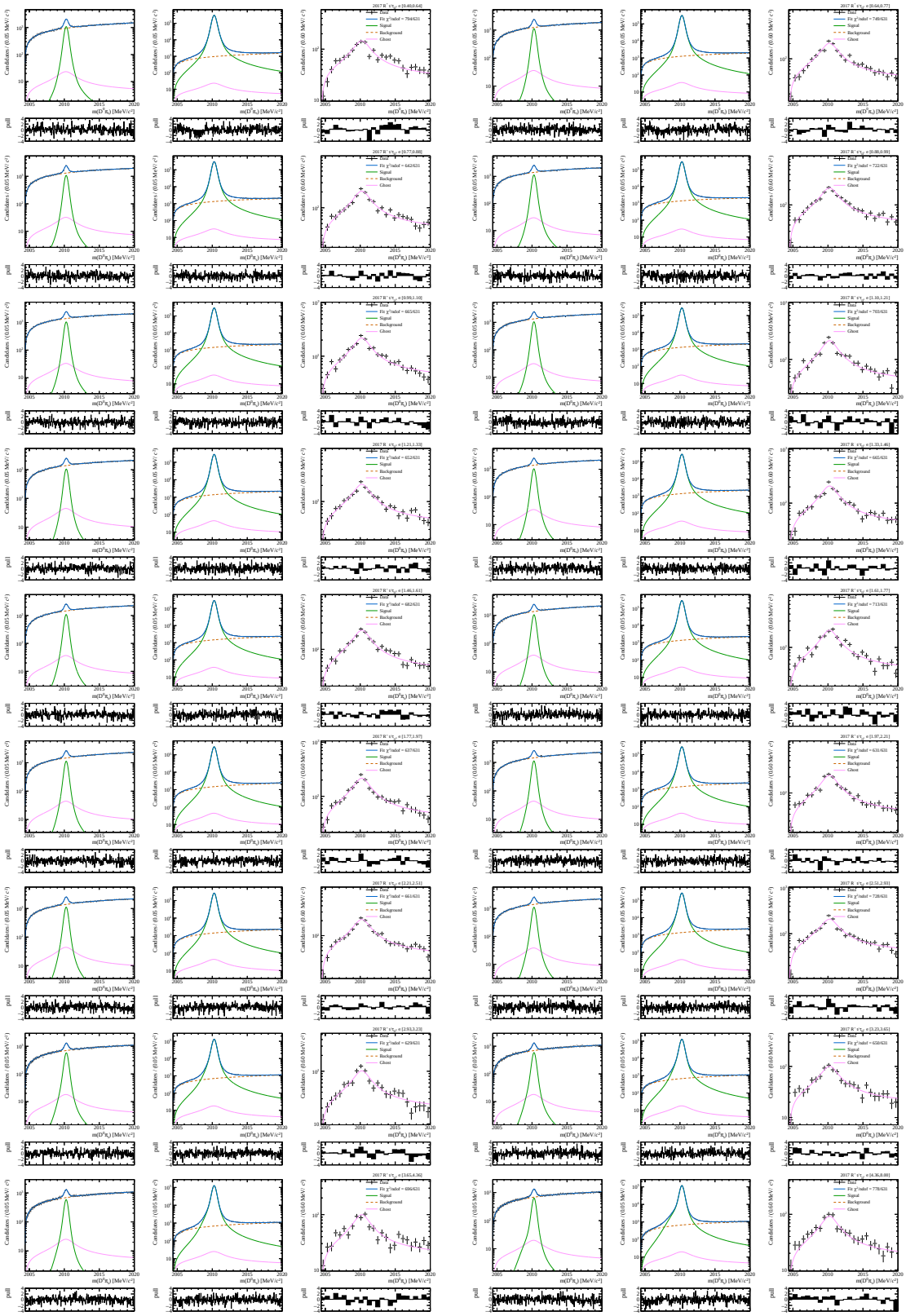

Figure C.3: Distributions of the $m(D^0\pi_s)_{\mathrm{DTF}}$ of WS (Left), RS (Center) and CG (Right) in each D^0 decay-time bins of the $K^+\pi^-$ 2017 sample. Fit projection are superimposed.

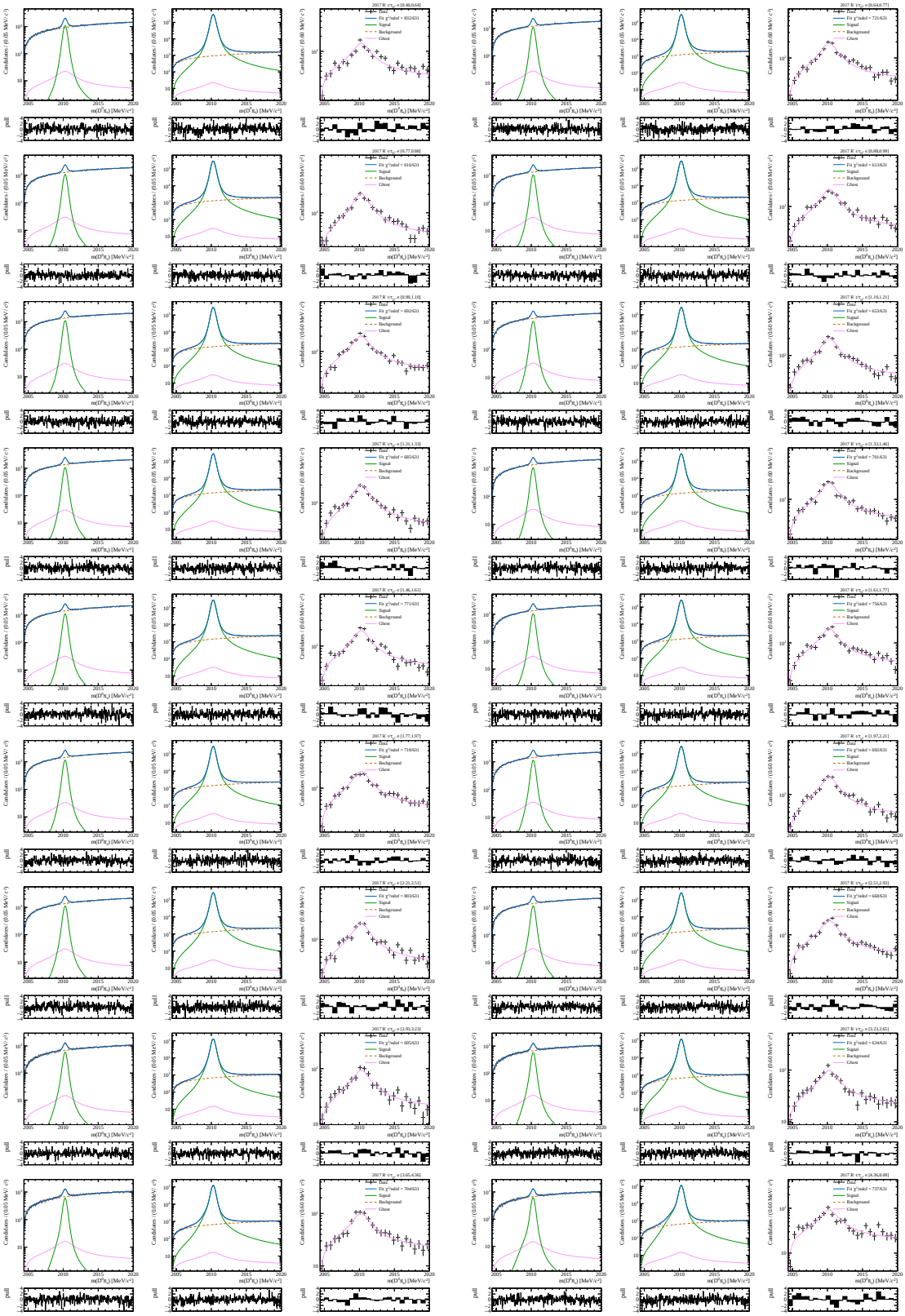

Figure C.4: Distributions of the $m(D^0\pi_s)_{\mathrm{DTF}}$ of WS (Left), RS (Center) and CG (Right) in each D^0 decay-time bins of the $K^-\pi^+$ 2017 sample. Fit projection are superimposed.

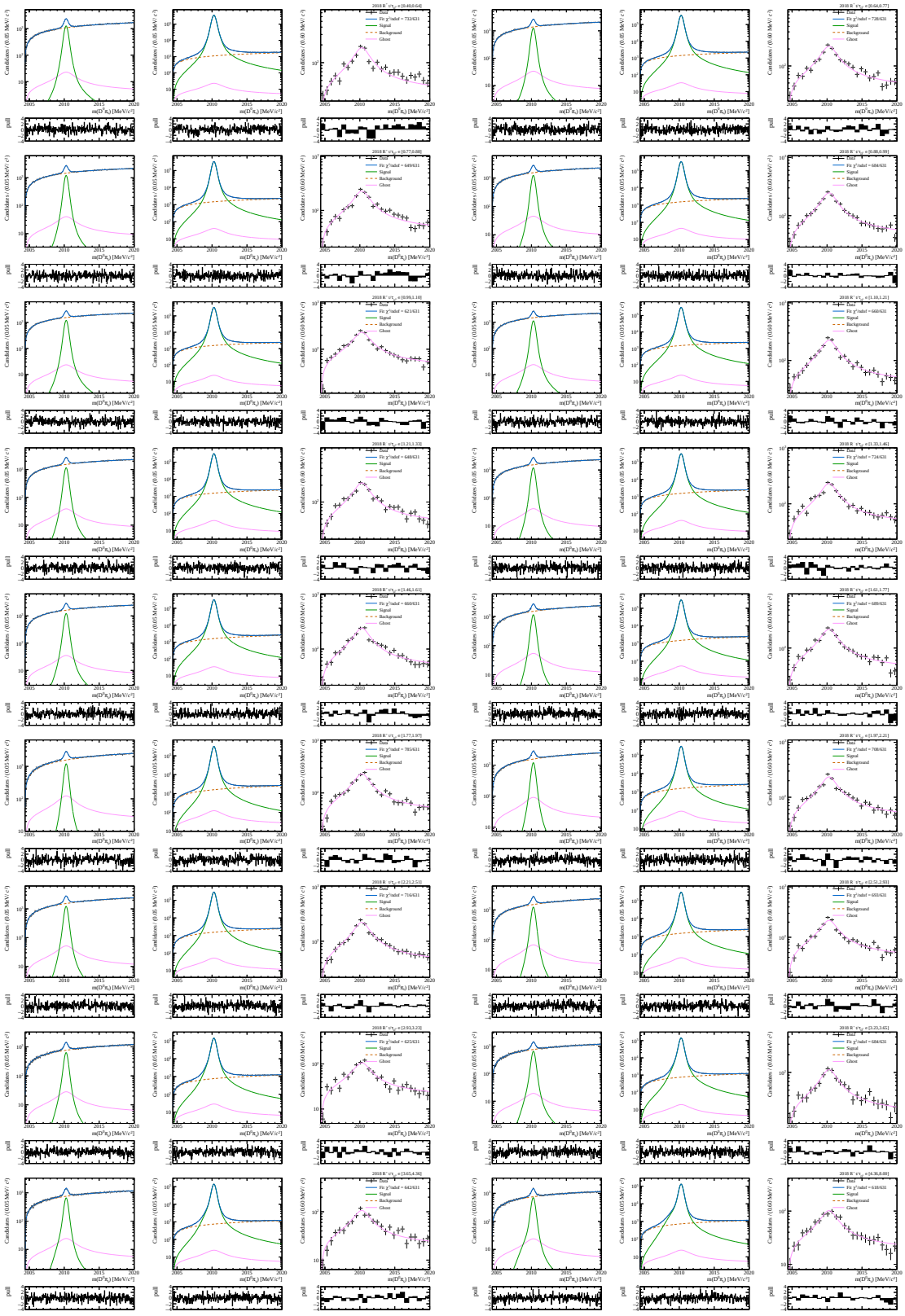

Figure C.5: Distributions of the $m(D^0\pi_s)_{\mathrm{DTF}}$ of WS (Left), RS (Center) and CG (Right) in each D^0 decay-time bins of the $K^+\pi^-$ 2018 sample. Fit projection are superimposed.

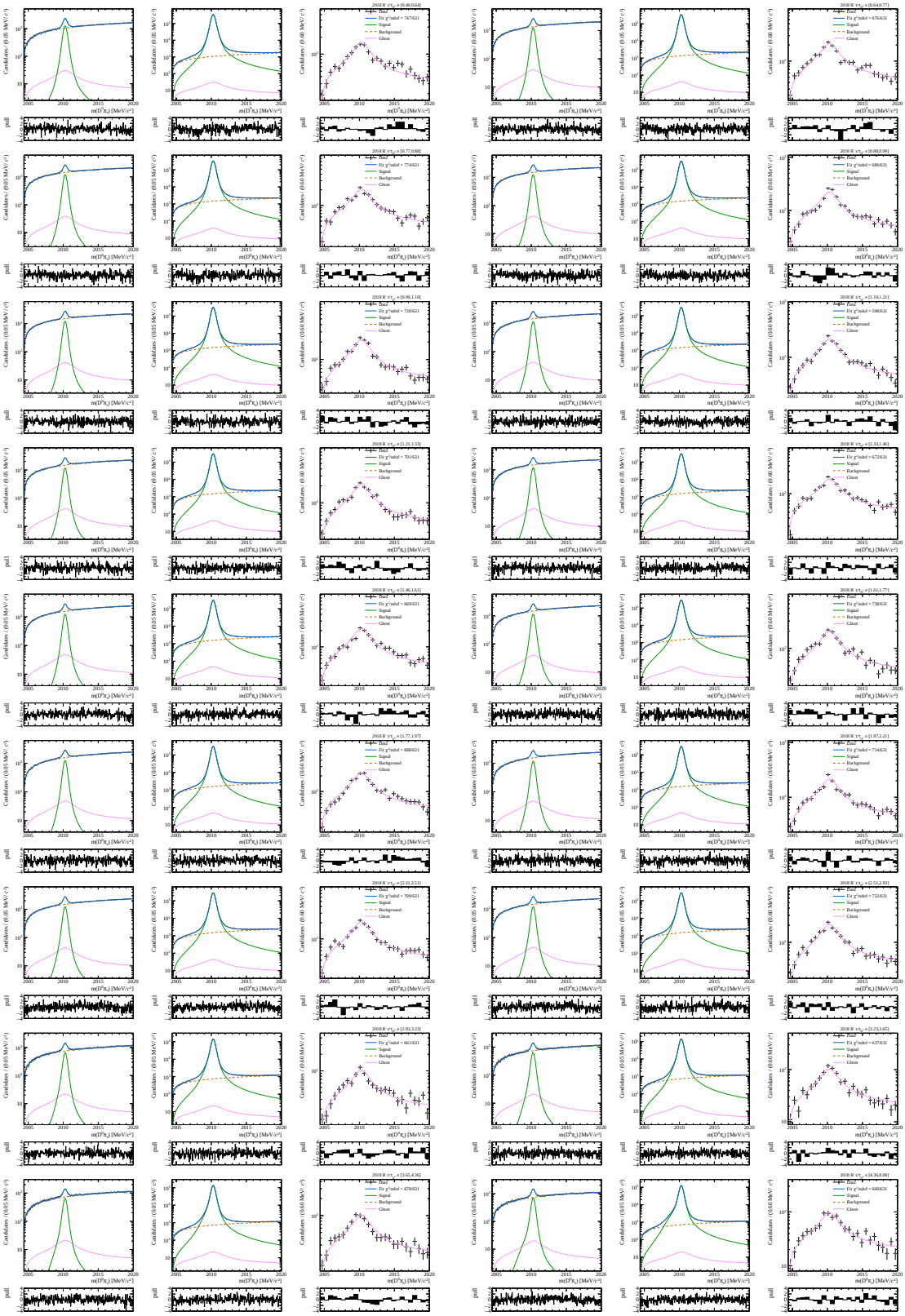

Figure C.6: Distributions of the $m(D^0\pi_s)_{\mathrm{DTF}}$ of WS (Left), RS (Center) and CG (Right) in each D^0 decay-time bins of the $K^-\pi^+$ 2018 sample. Fit projection are superimposed.

Appendix $\mathcal{D}$

Simulated samples weighting

This appendix collects the kinematic distributions of simulated samples and data-taking period, before and after the weighting procedure.

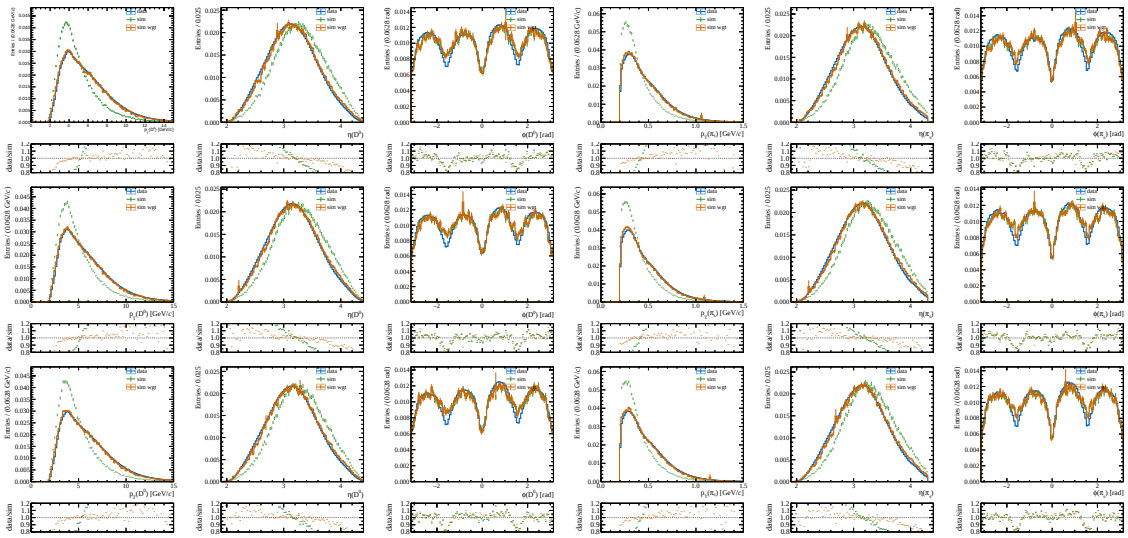

Figure D.1: Comparison between the kinematic distributions of RS primary decays of 2016 (Top), 2017 (Center) and 2018 (Bottom) sample in data and simulation (central scenario), both before and after the six-dimensional weighting. The data sample of primary decays is selected using 4% of the candidates satisfying the requirement IP$(D^0) < 60\,\mu$m.

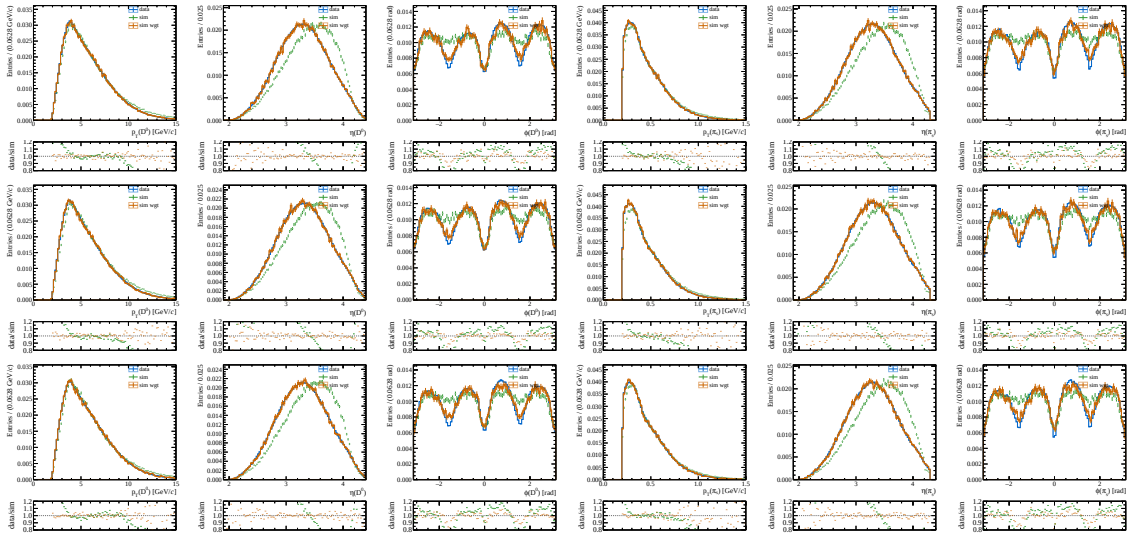

Figure D.2: Comparison between the kinematic distributions of RS secondary decays of 2016 (Top), 2017 (Center) and 2018 (Bottom) sample in data and simulation (central scenario), both before and after the six-dimensional weighting. The data sample of secondary decays is selected using 30% of the candidates satisfying the requirement 120 µm $<$ IP(D^0) $<$ 600 µm.

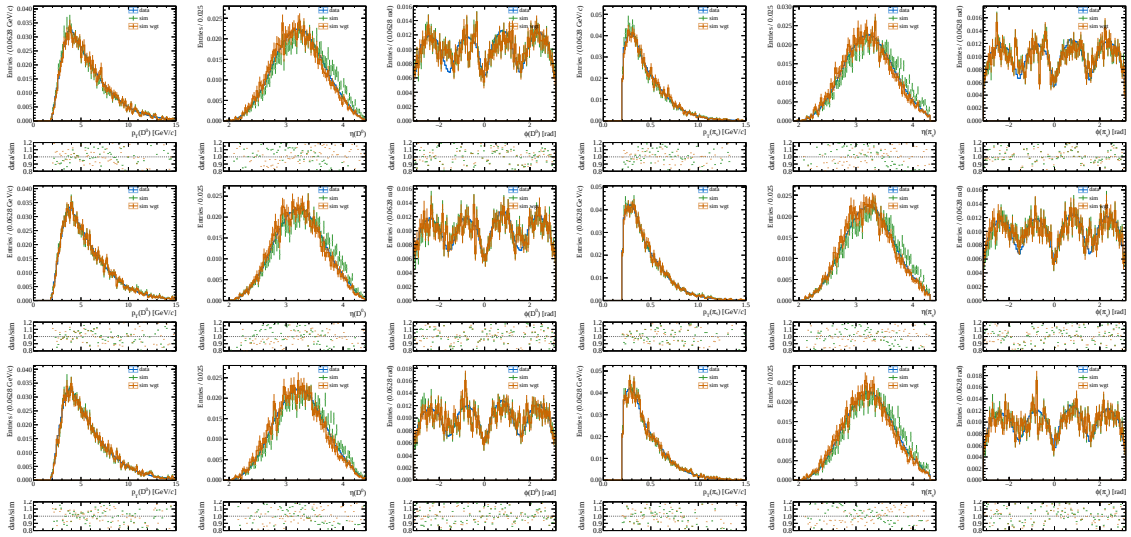

Figure D.3: Comparison between the kinematic distributions of D^{*+} µm decays of of 2016 (Top), 2017 (Center) and 2018 (Bottom) sample in data and simulation (central scenario), both before and after the six-dimensional weighting. The data sample of decays is selected using the candidates satisfying the requirement IP(D^0) $<$ 600 µm.

Appendix $\mathcal{E}$

Impact parameter fits

This appendix reports the results for the nuisance parameters of the template fits and the inflation factor applied to the returned statistical errors. It also illustrates the D^0 impact parameter distributions of RS candidates in each decay-time bin and data-taking period. The results of the template fits to data are superimposed.

E.1 Nuisance parameters and uncertainties inflation

The inflation factors to the statistical uncertainties of the measured δt_i is reported in Tab. E.1.

	1	2	3	4	5	6	7	8	9	10	11	12	13	14	15	16	17	18
16	5.8	4.7	3.9	3.3	2.7	2.7	1.5	1.1	1.6	1.4	1.6	1.4	1.6	1.8	1.6	1.0	1.1	1.7
17	6.4	6.6	2.6	3.4	3.6	2.5	2.0	2.1	1.9	2.7	1.5	1.9	1.5	1.7	1.2	1.4	1.4	2.0
18	5.3	2.9	3.0	2.5	2.5	2.2	2.5	1.4	2.2	1.9	2.7	2.4	1.8	1.6	1.3	1.0	1.1	1.8

Table E.1: Inflation factors to the statistical uncertainties of the measured δt_i, as reported in Sec. 8.6.3. Columns indexes are the decay-time bin index, while rows indexes refer to the data-taking period.

Table E.2 report the results for the nuisance parameters in the template fit to the three data-taking period. The fitted scale factors to the PV and DV resolution are $1 + \alpha$ and $1 + \beta$, respectively, while γ is the mass of X in the $B \to D^{*+}X$ and δ the relative fraction of this additional decay with respect to the total inclusive secondary sample.

Table E.2: Nuisance parameters results from the template fit to 2016, 2017 and 2018 (top to bottom) data sample.

E.2 Data and fit projections

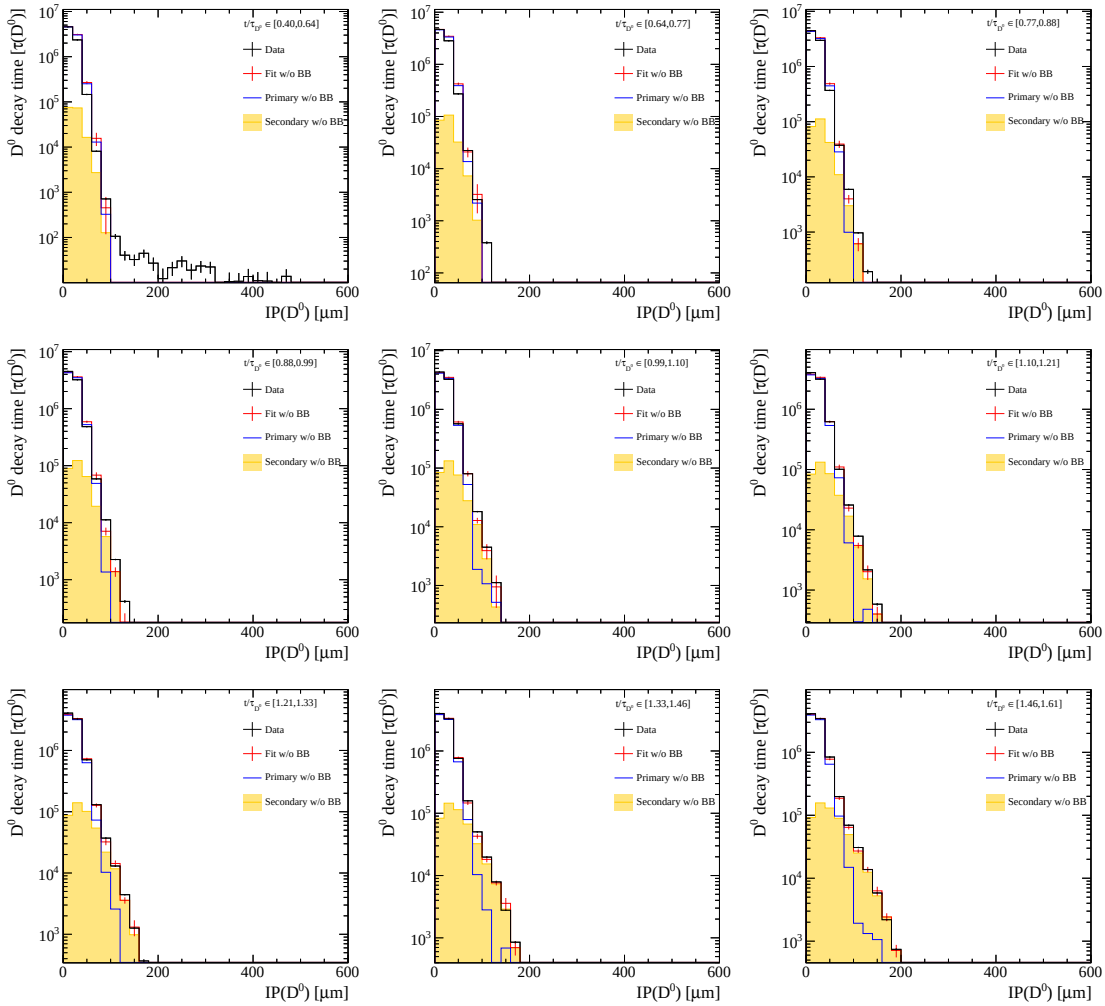

Figure E.1: Distributions of the D^0 impact parameter for some example decay-time bin of the 2016 sample. The template fit projection is superimposed. Here the new fitted values n_i of each bin of the interpolated template, as from the Beeston-Barlow approach, are not shown. The prior interpolated template bin values, N_i, are shown instead. This is done in order to make visible any discrepancies that would otherwise be observed only from the n_i pulls.

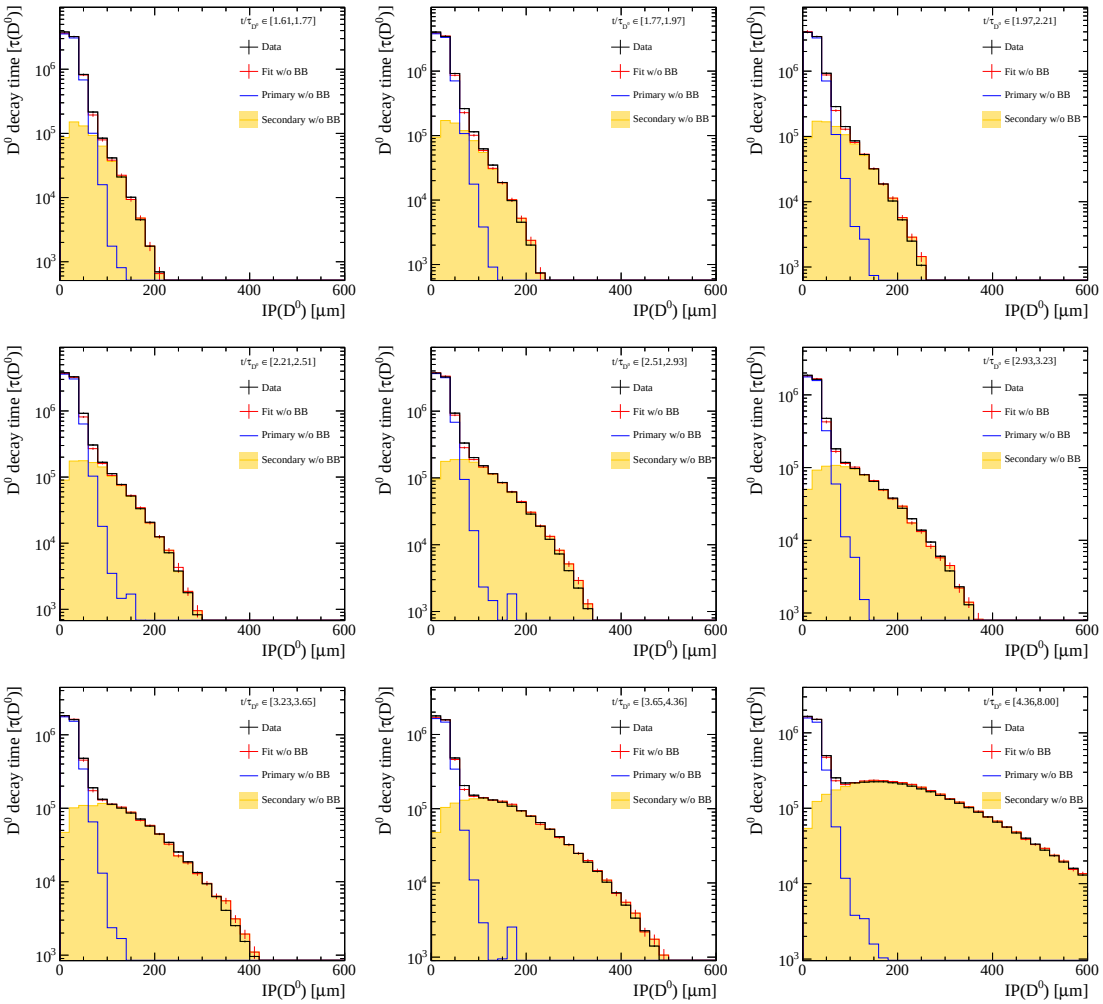

Figure E.2: Distributions of the D^0 impact parameter for some example decay-time bin of the 2016 sample. The template fit projection is superimposed. Here the new fitted values n_i of each bin of the interpolated template, as from the Beeston-Barlow approach, are not shown. The prior interpolated template bin values, N_i, are shown instead. This is done in order to make visible any discrepancies that would otherwise be observed only from the n_i pulls.

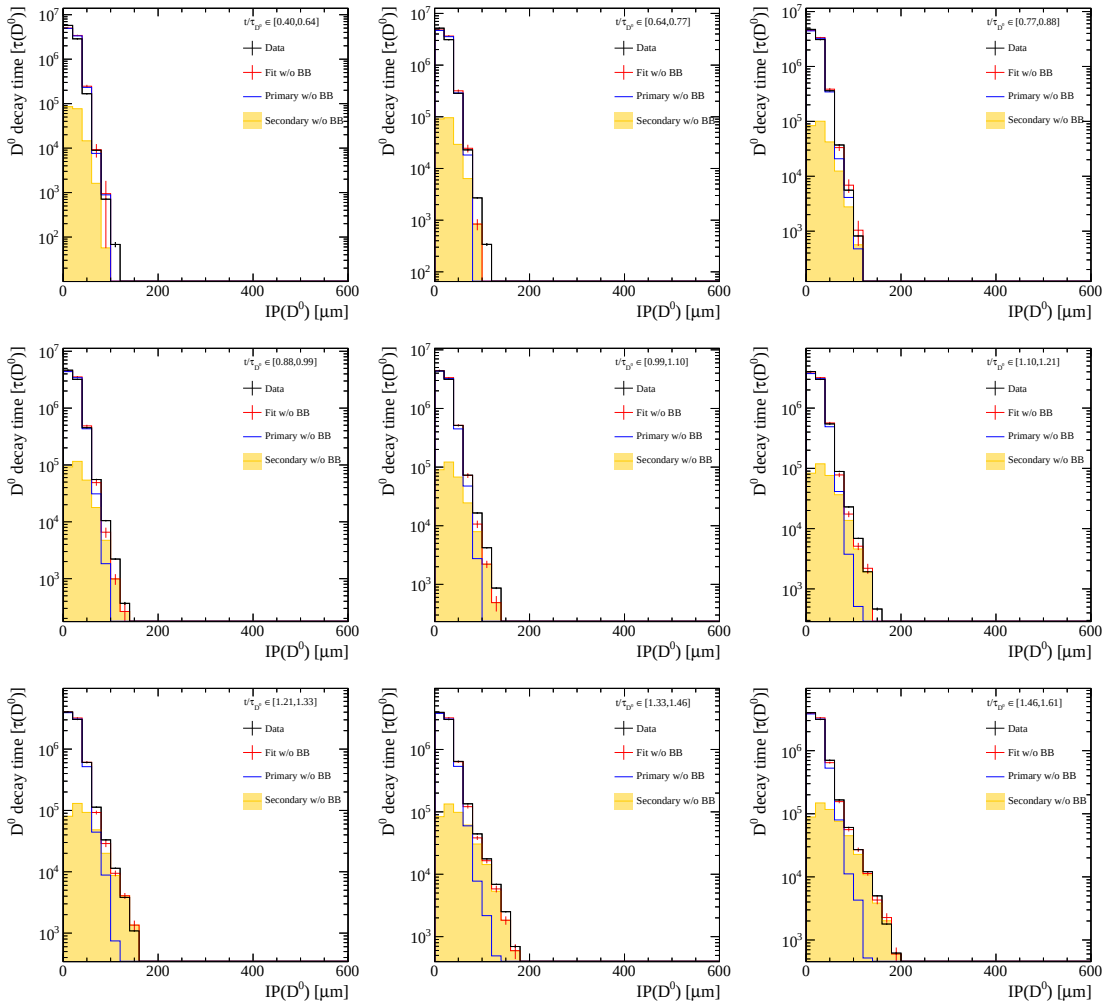

Figure E.3: Distributions of the D^0 impact parameter for some example decay-time bin of the 2017 sample. The template fit projection is superimposed. Here the new fitted values n_i of each bin of the interpolated template, as from the Beeston-Barlow approach, are not shown. The prior interpolated template bin values, N_i, are shown instead. This is done in order to make visible any discrepancies that would otherwise be observed only from the n_i pulls.

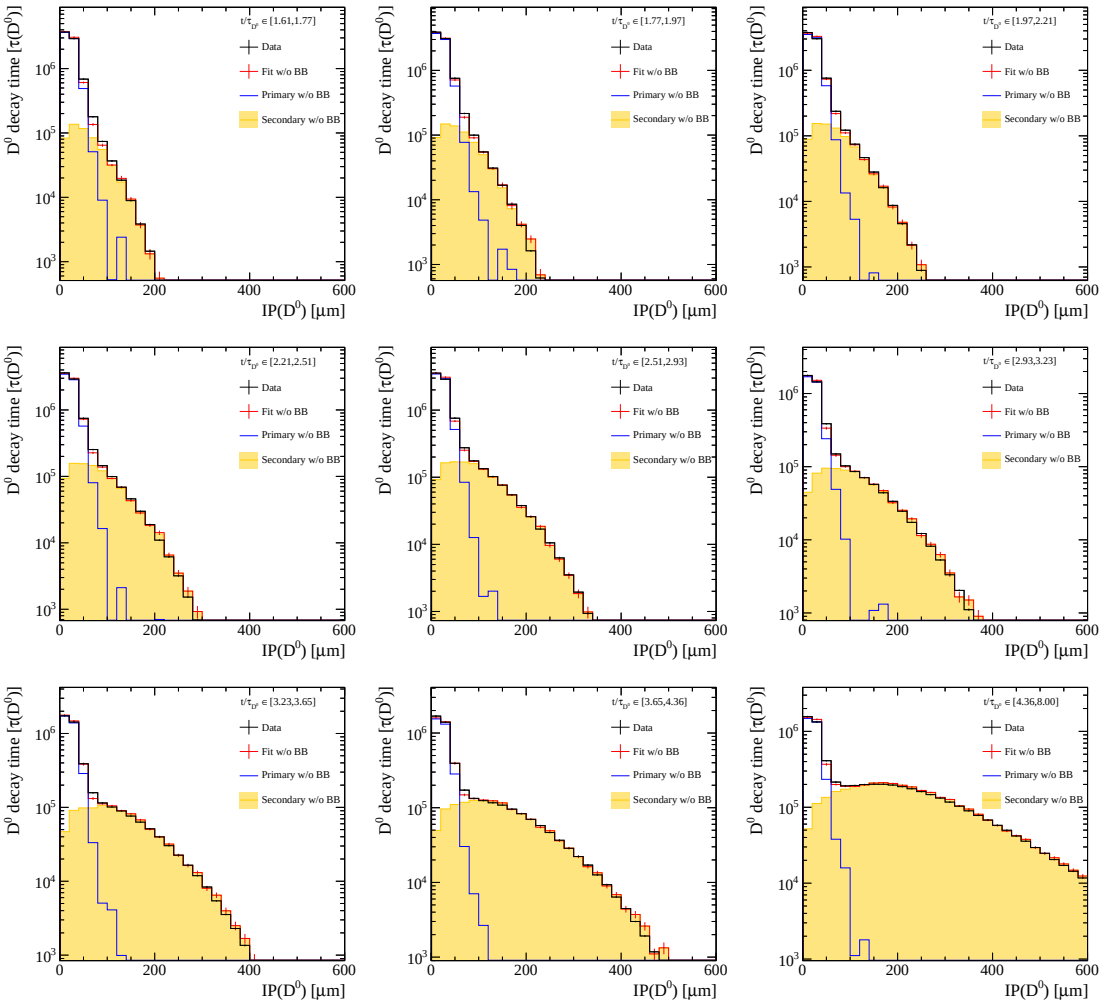

Figure E.4: Distributions of the D^0 impact parameter for some example decay-time bin of the 2017 sample. The template fit projection is superimposed. Here the new fitted values n_i of each bin of the interpolated template, as from the Beeston-Barlow approach, are not shown. The prior interpolated template bin values, N_i, are shown instead. This is done in order to make visible any discrepancies that would otherwise be observed only from the n_i pulls.

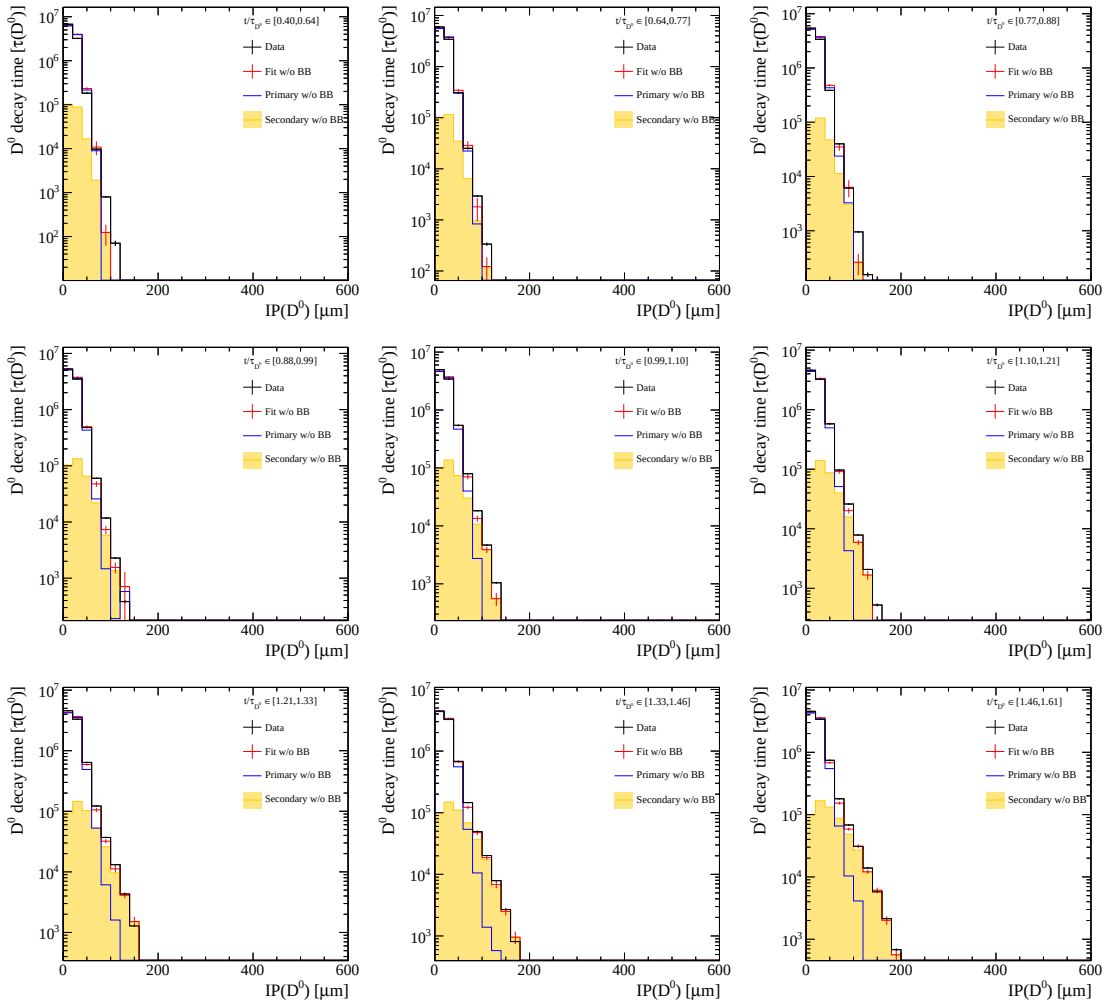

Figure E.5: Distributions of the D^0 impact parameter for some example decay-time bin of the 2018 sample. The template fit projection is superimposed. Here the new fitted values n_i of each bin of the interpolated template, as from the Beeston-Barlow approach, are not shown. The prior interpolated template bin values, N_i, are shown instead. This is done in order to make visible any discrepancies that would otherwise be observed only from the n_i pulls.

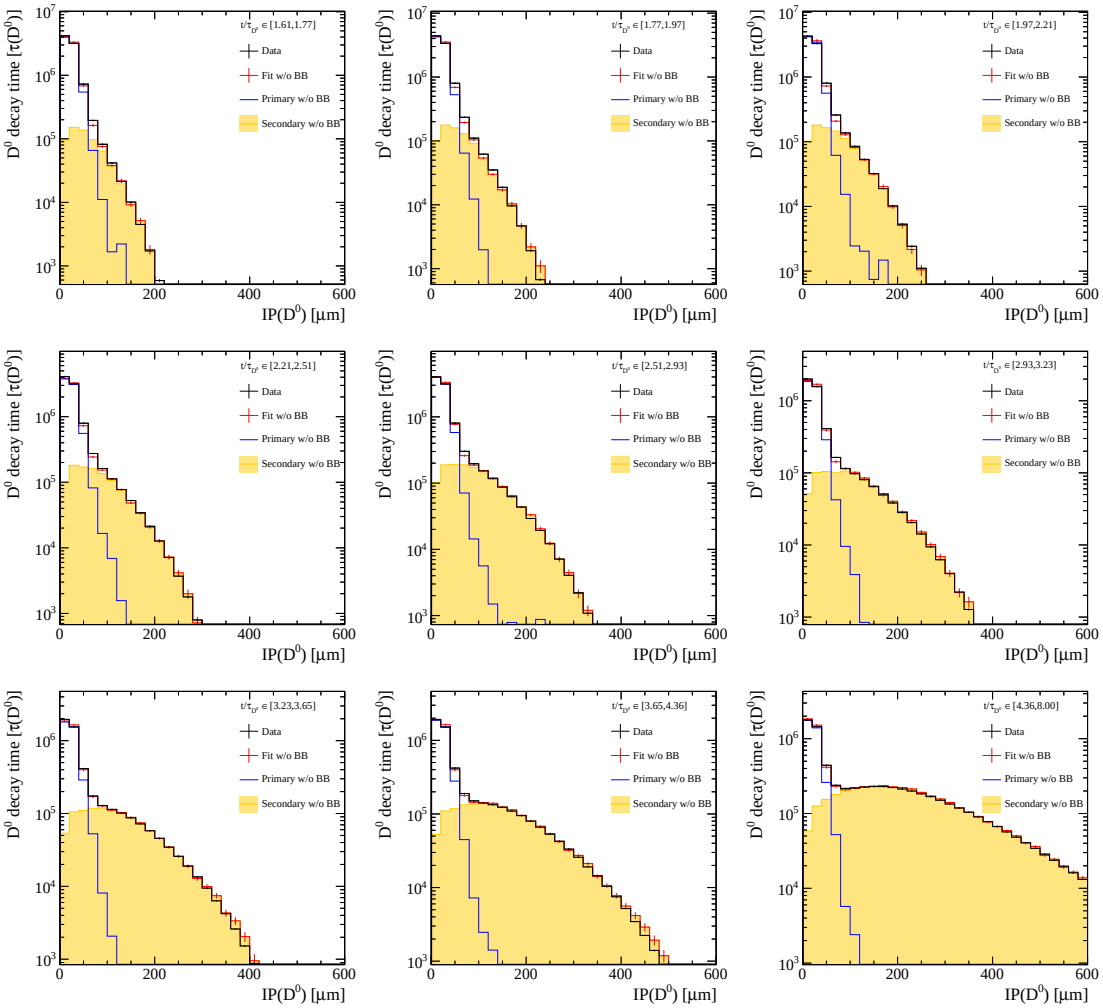

Figure E.6: Distributions of the D^0 impact parameter for some example decay-time bin of the 2018 sample. The template fit projection is superimposed. Here the new fitted values n_i of each bin of the interpolated template, as from the Beeston-Barlow approach, are not shown. The prior interpolated template bin values, N_i, are shown instead. This is done in order to make visible any discrepancies that would otherwise be observed only from the n_i pulls.

Appendix $\mathcal{F}$

KK sample weighting

This appendix collects the kinematic distributions of RS and KK samples for each decay-time bin and data-taking period, before and after the weighting procedure.

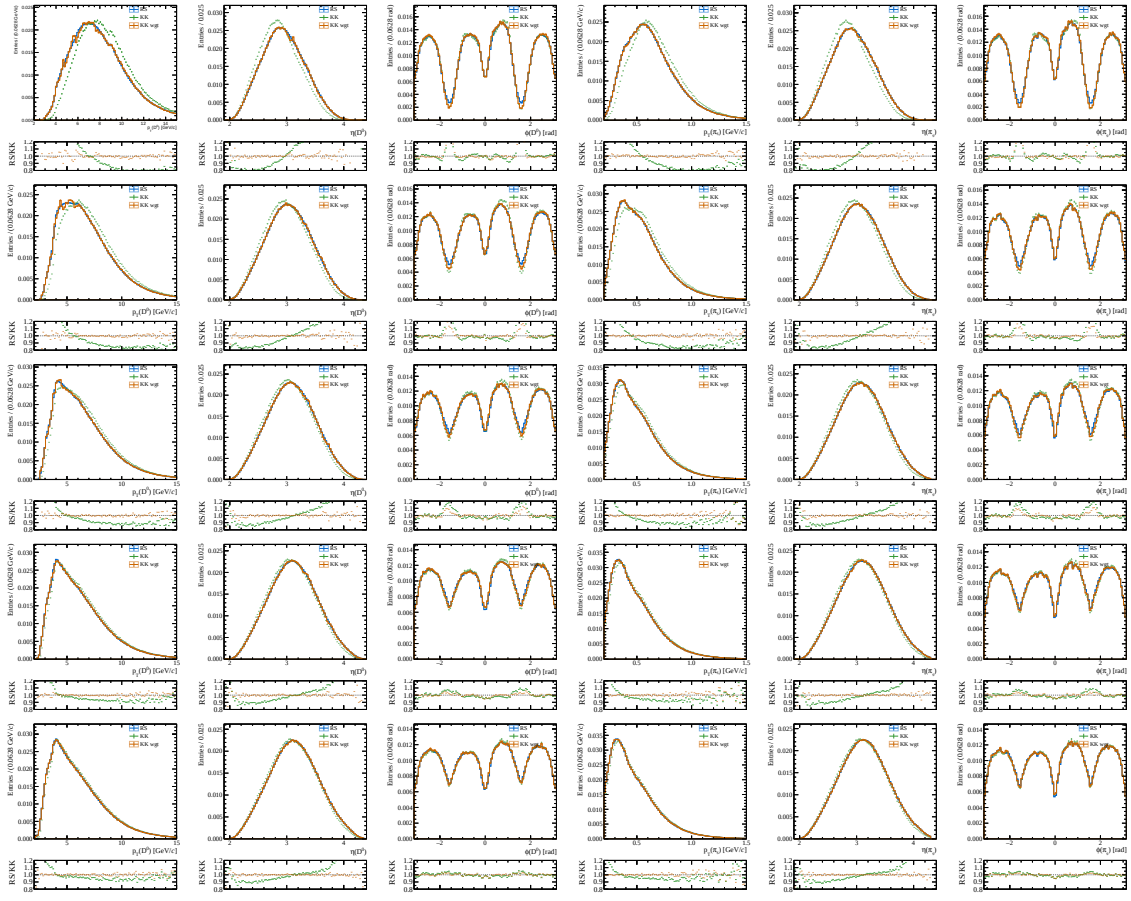

Figure F.1: Comparison between the kinematic distributions of RS and *KK* for the first five D^0 decay-time bin (each row is a different decay-time bin) of 2016 sample in both before and after the six-dimensional weighting.

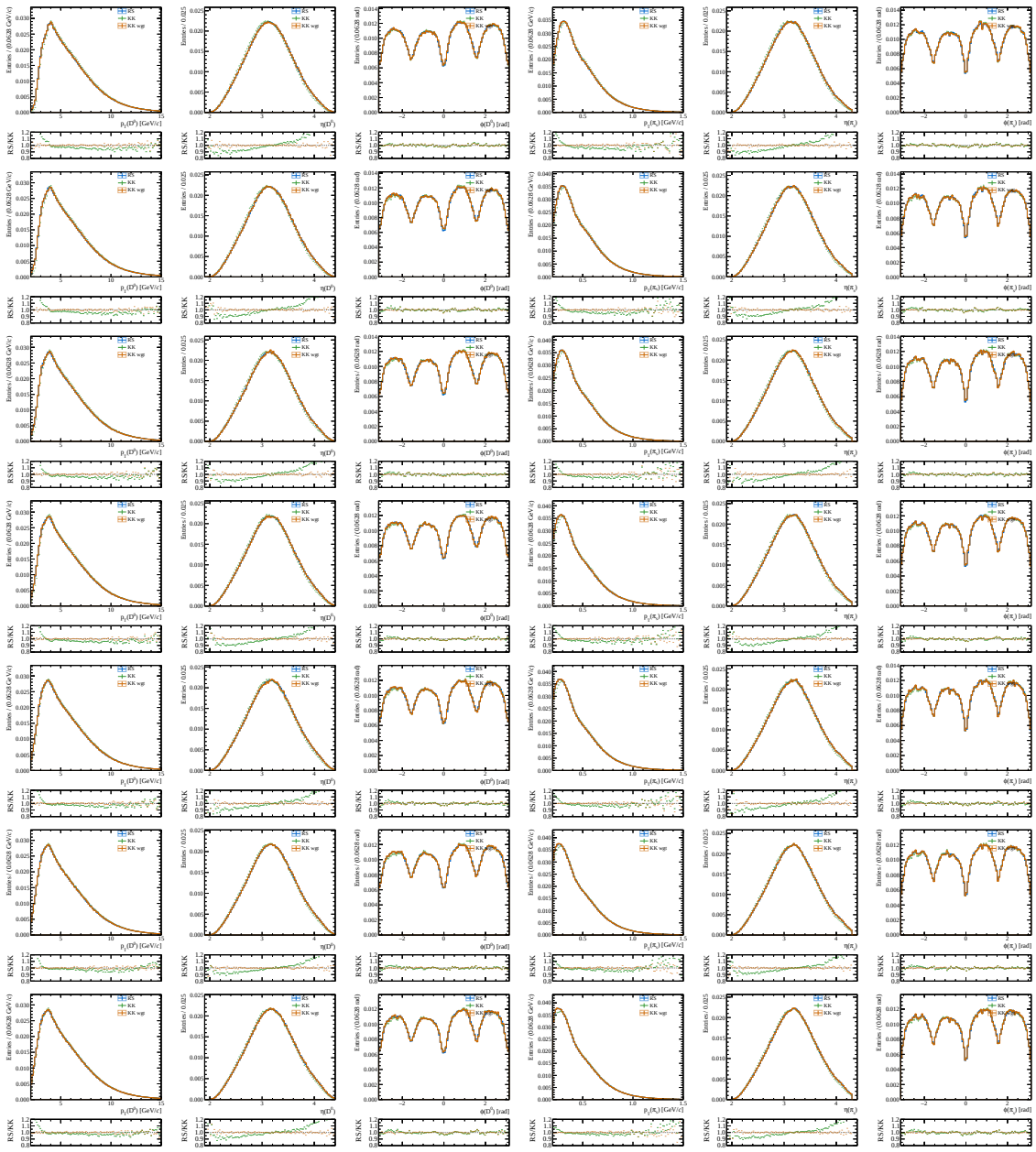

Figure F.2: Comparison between the kinematic distributions of RS and *KK* for the central seven D^0 decay-time bin (each row is a different decay-time bin) of 2016 sample in both before and after the six-dimensional weighting.

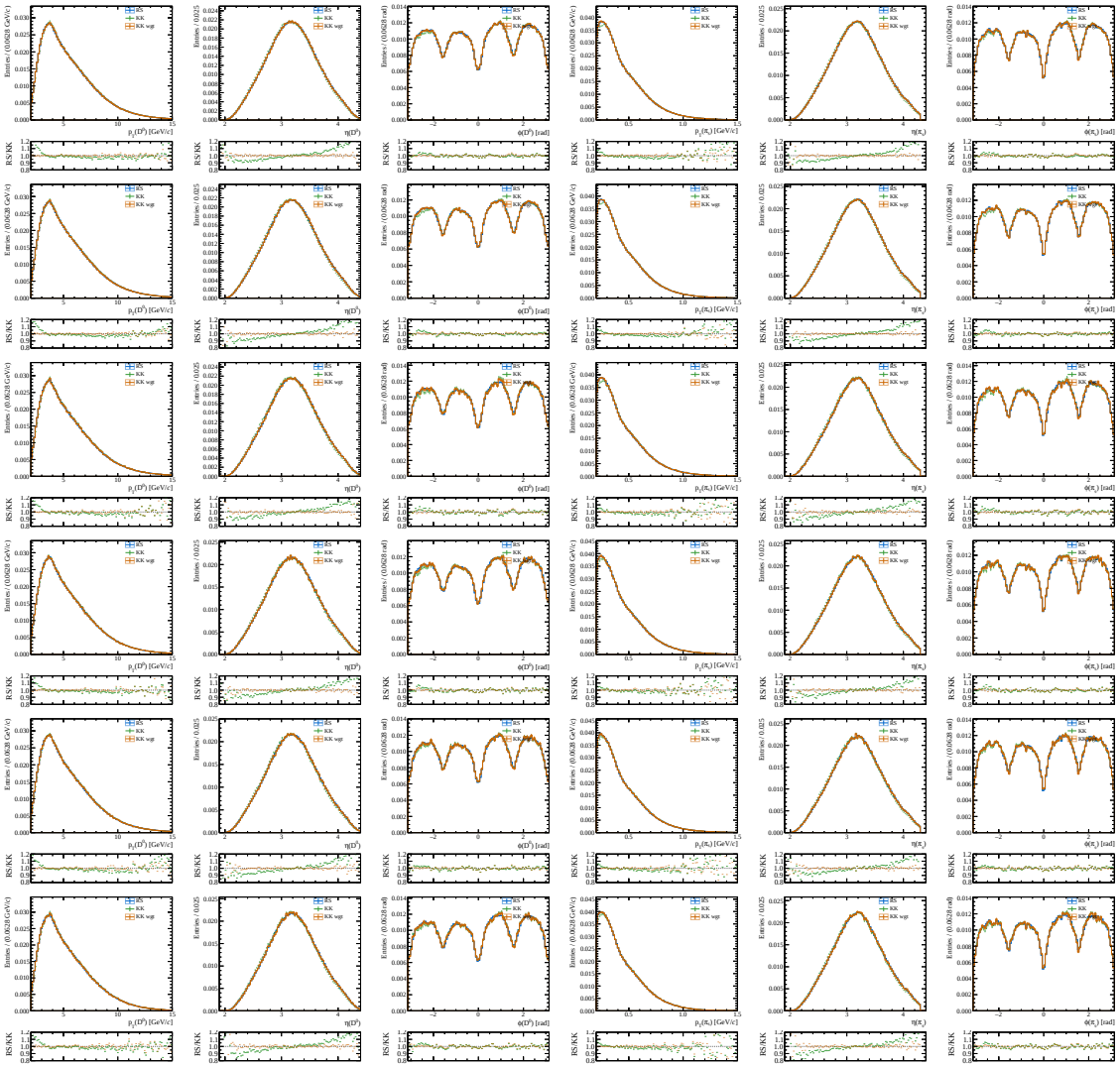

Figure F.3: Comparison between the kinematic distributions of RS and *KK* for the last six D^0 decay-time bin (each row is a different decay-time bin) of 2016 sample in both before and after the six-dimensional weighting.

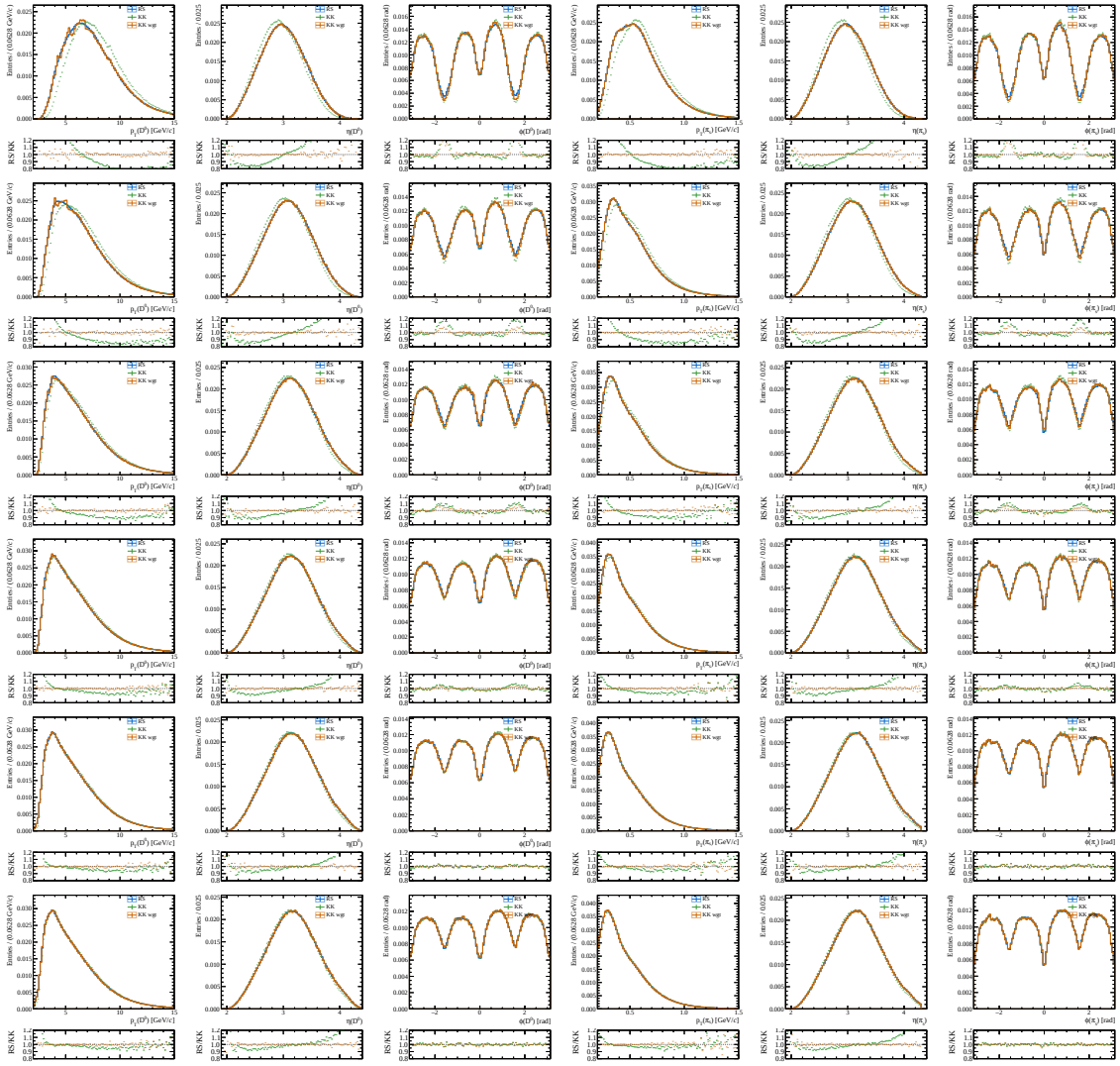

Figure F.4: Comparison between the kinematic distributions of RS and *KK* for the first six D^0 decay-time bin (each row is a different decay-time bin) of 2017 sample in both before and after the six-dimensional weighting.

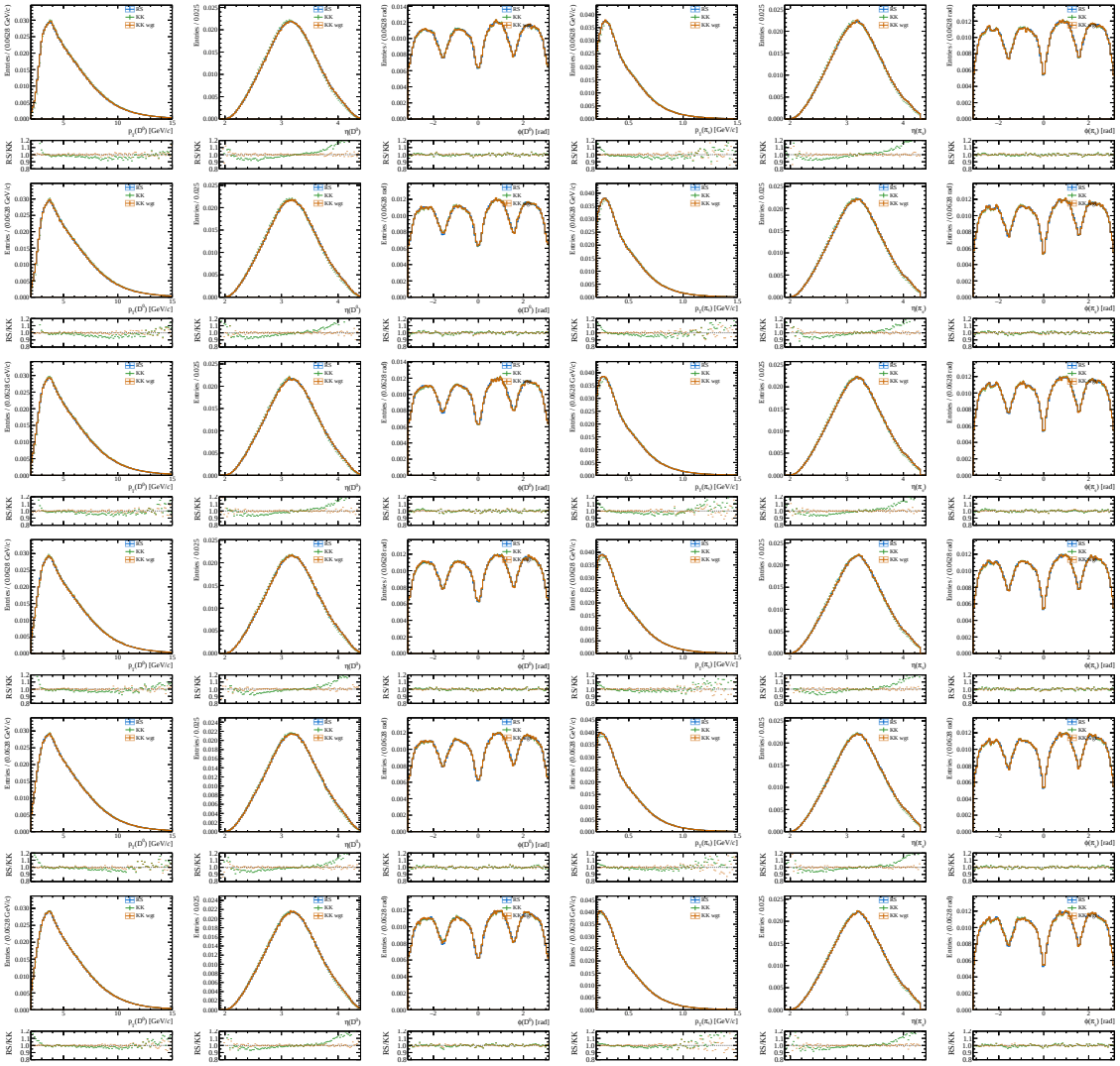

Figure F.5: Comparison between the kinematic distributions of RS and *KK* for the central six D^0 decay-time bin (each row is a different decay-time bin) of 2017 sample in both before and after the six-dimensional weighting.

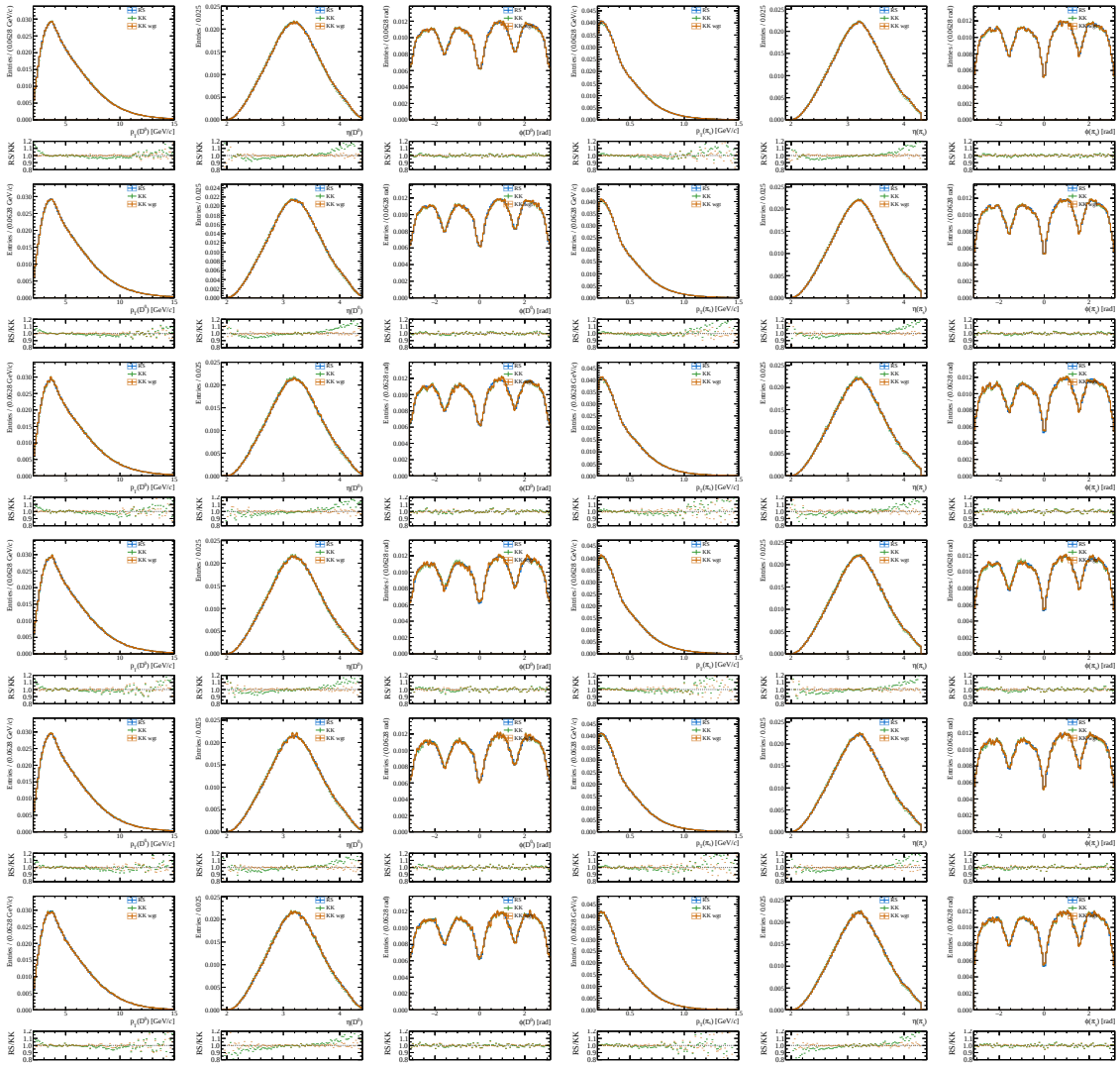

Figure F.6: Comparison between the kinematic distributions of RS and *KK* for the last six D^0 decay-time bin (each row is a different decay-time bin) of 2017 sample in both before and after the six-dimensional weighting.

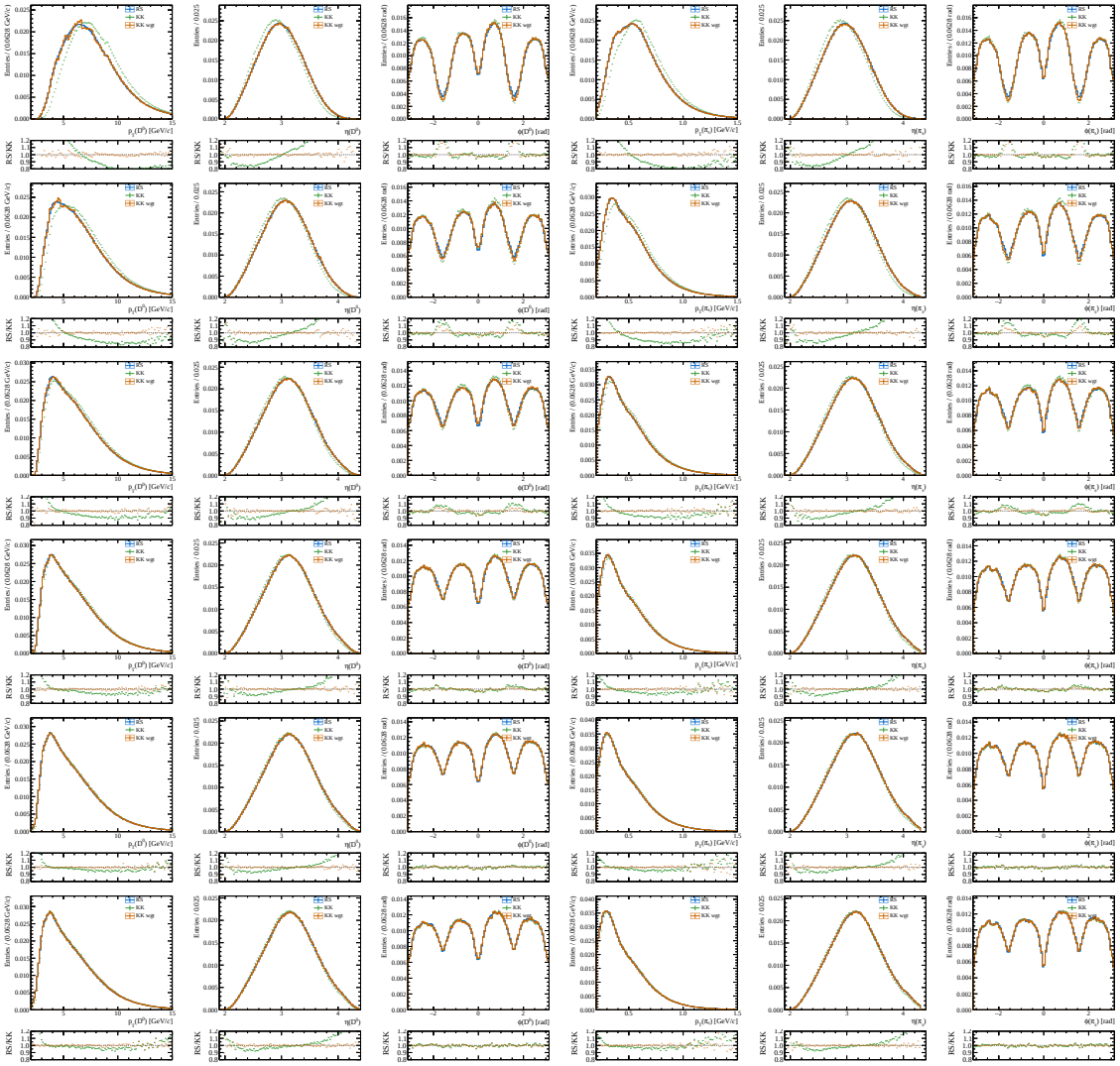

Figure F.7: Comparison between the kinematic distributions of RS and *KK* for the first six D^0 decay-time bin (each row is a different decay-time bin) of 2018 sample in both before and after the six-dimensional weighting.

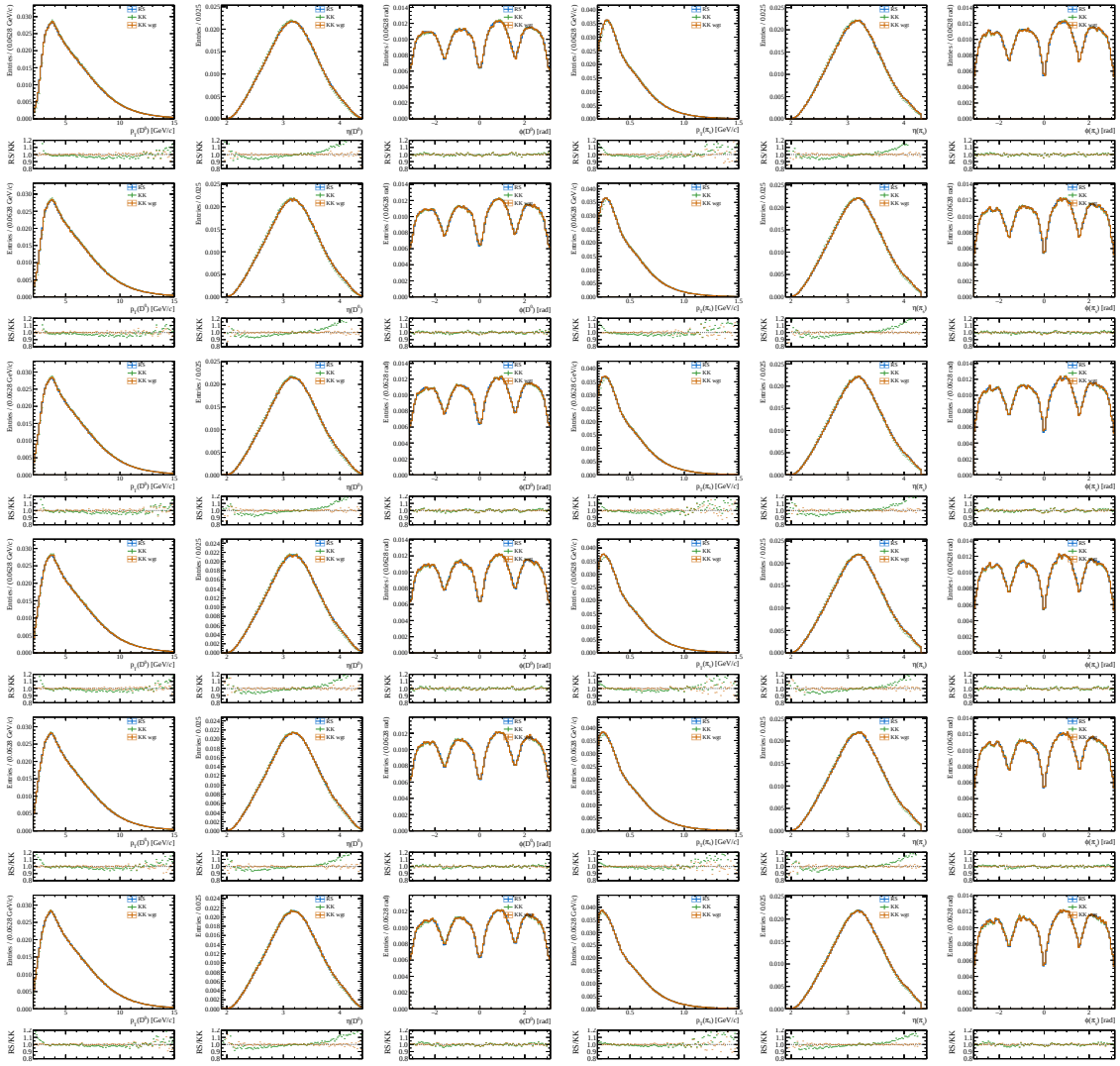

Figure F.8: Comparison between the kinematic distributions of RS and *KK* for the central six D^0 decay-time bin (each row is a different decay-time bin) of 2017 sample in both before and after the six-dimensional weighting.

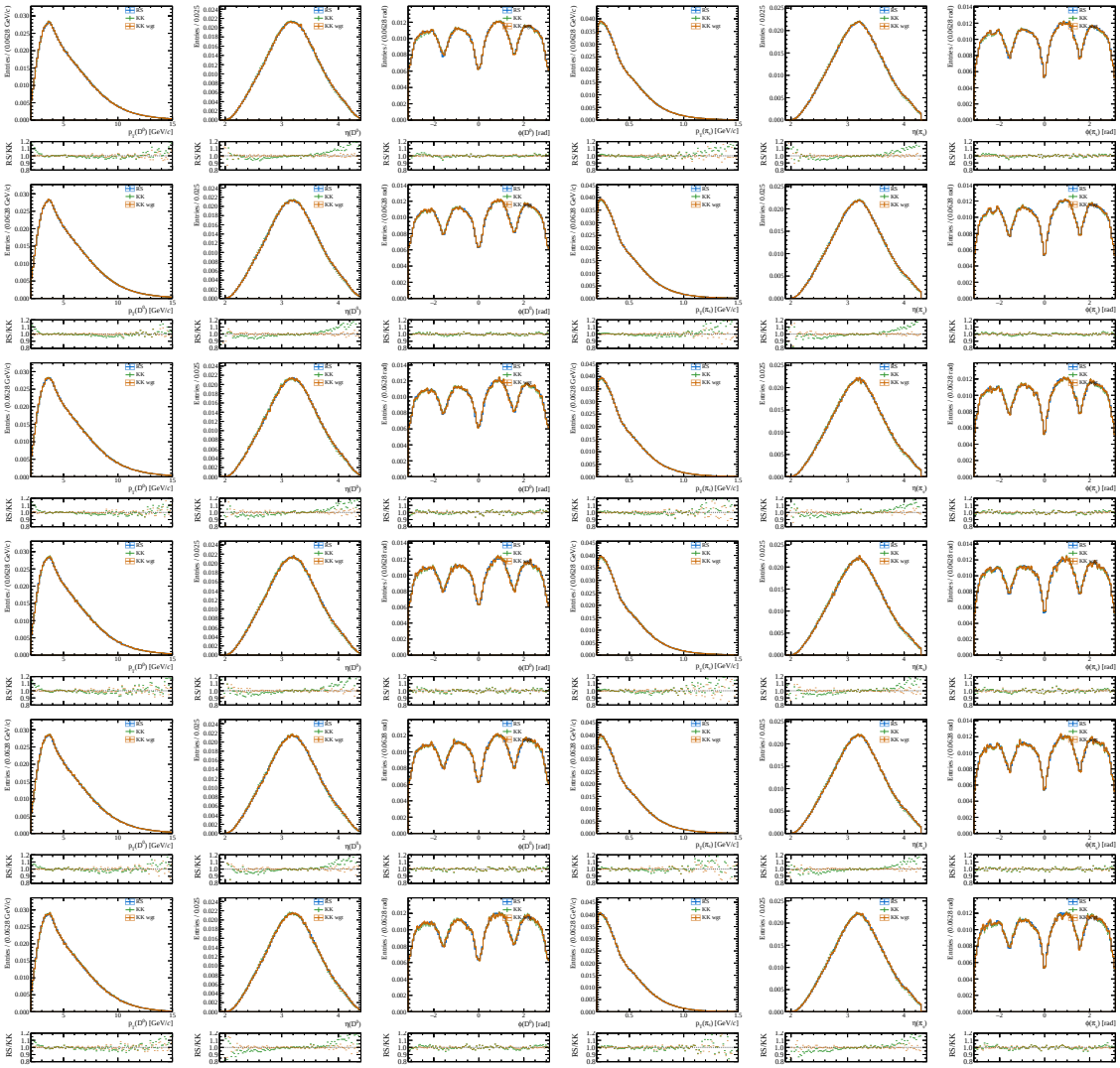

Figure F.9: Comparison between the kinematic distributions of RS and *KK* for the last six D^0 decay-time bin (each row is a different decay-time bin) of 2017 sample in both before and after the six-dimensional weighting.

Appendix G

KK asymmetry fits

This appendix reports the D^* invariant mass of the $D^0 \to K^+K^-$ sample in each decay-time bin and data-taking period. The results of the fits are superimposed.

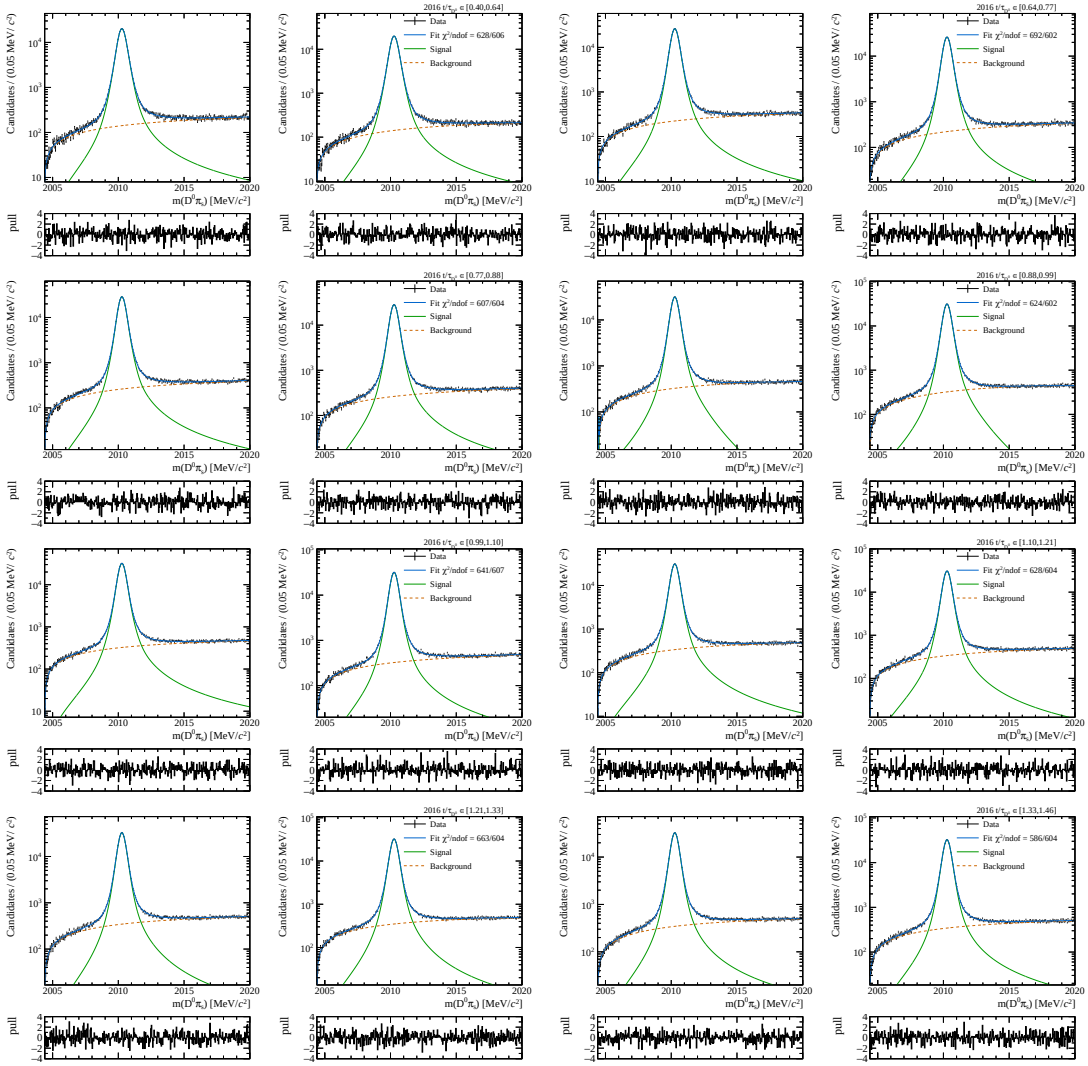

Figure G.1: Distributions of the $m(D^0\pi_s)_{\rm DTF}$ of $D^{*+} \to K^+K^-$ and $D^{*-} \to K^+K^-$ of some decay-time bin of the 2016 sample. Fit projection are superimposed.

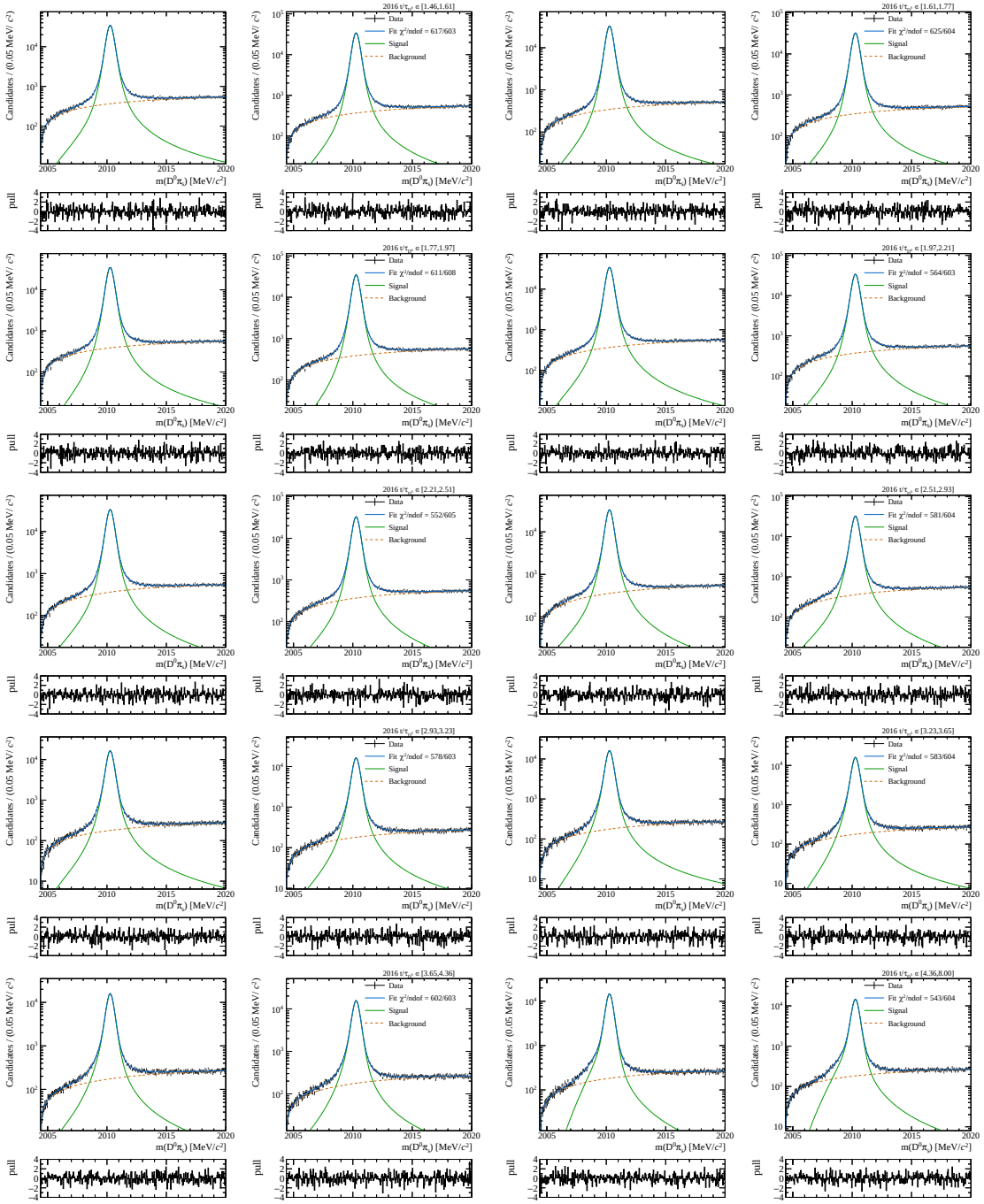

Figure G.2: Distributions of the $m(D^0\pi_s)_{\mathrm{DTF}}$ of $D^{*+} \to K^+K^-$ and $D^{*-} \to K^+K^-$ of some decay-time bin of the 2016 sample. Fit projection are superimposed.

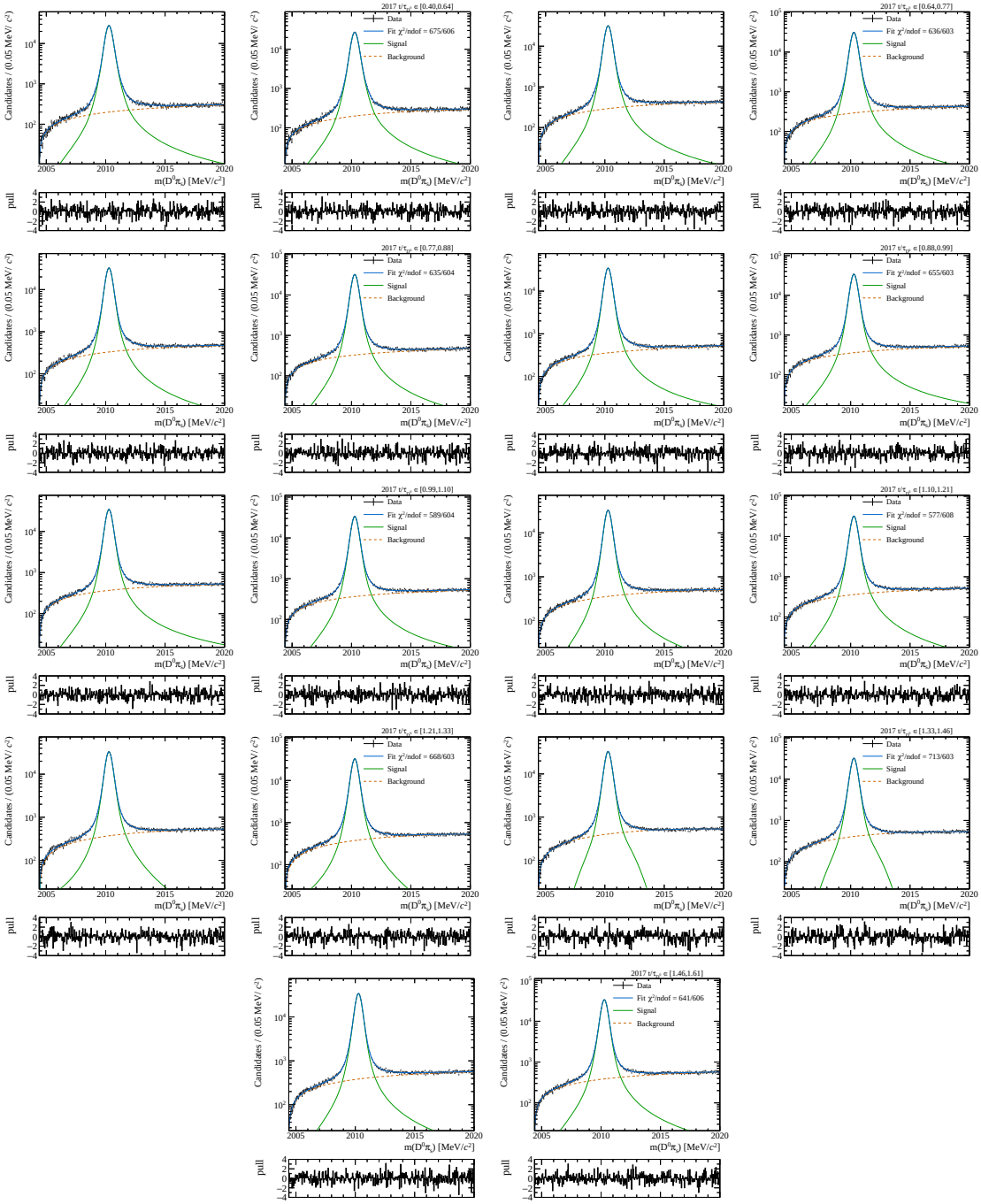

Figure G.3: Distributions of the $m(D^0\pi_s)_{\mathrm{DTF}}$ of $D^{*+} \to K^+K^-$ and $D^{*-} \to K^+K^-$ of some decay-time bin of the 2017 sample. Fit projection are superimposed.

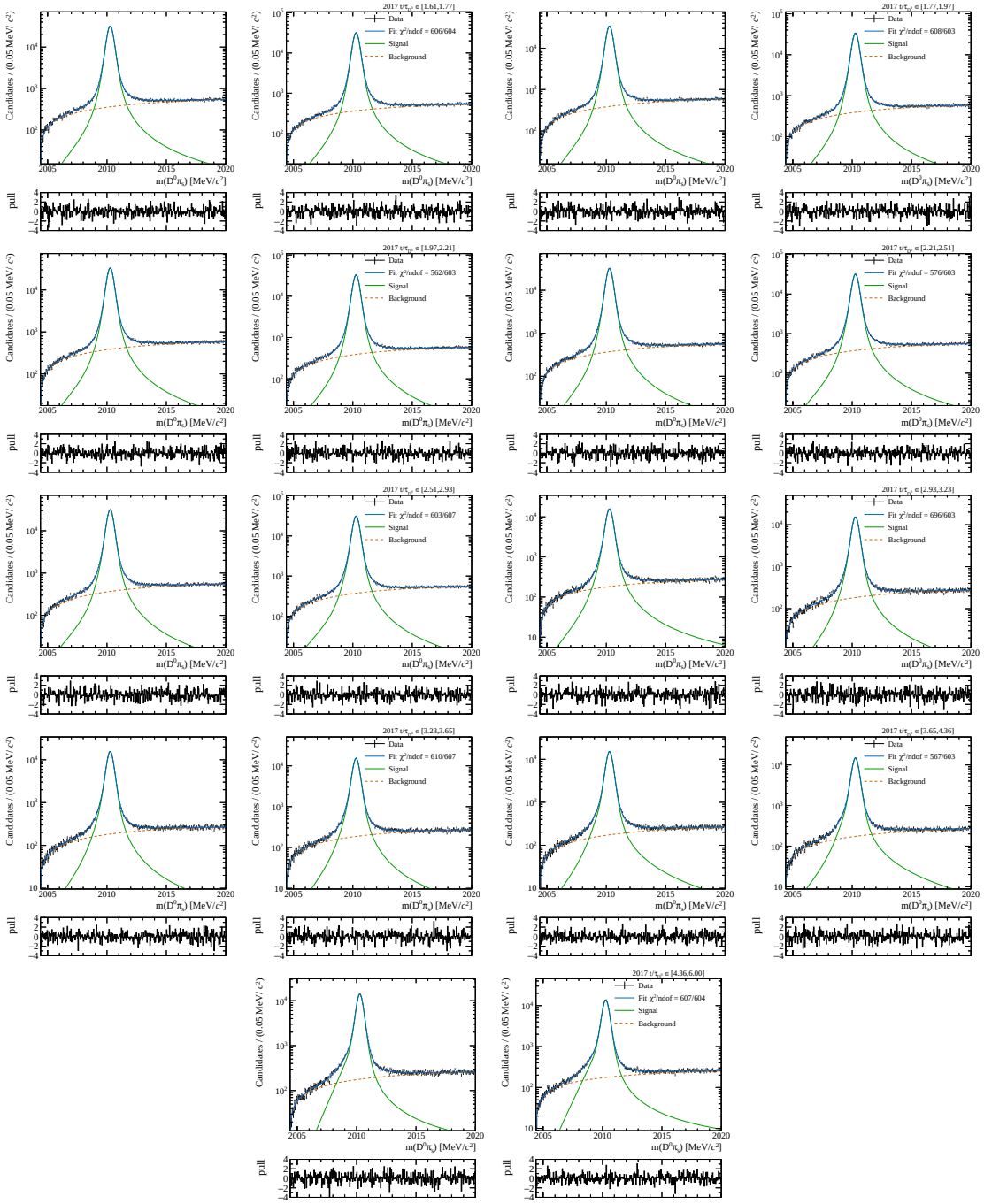

Figure G.4: Distributions of the $m(D^0\pi_s)_{\rm DTF}$ of $D^{*+} \to K^+K^-$ and $D^{*-} \to K^+K^-$ of some decay-time bin of the 2017 sample. Fit projection are superimposed.

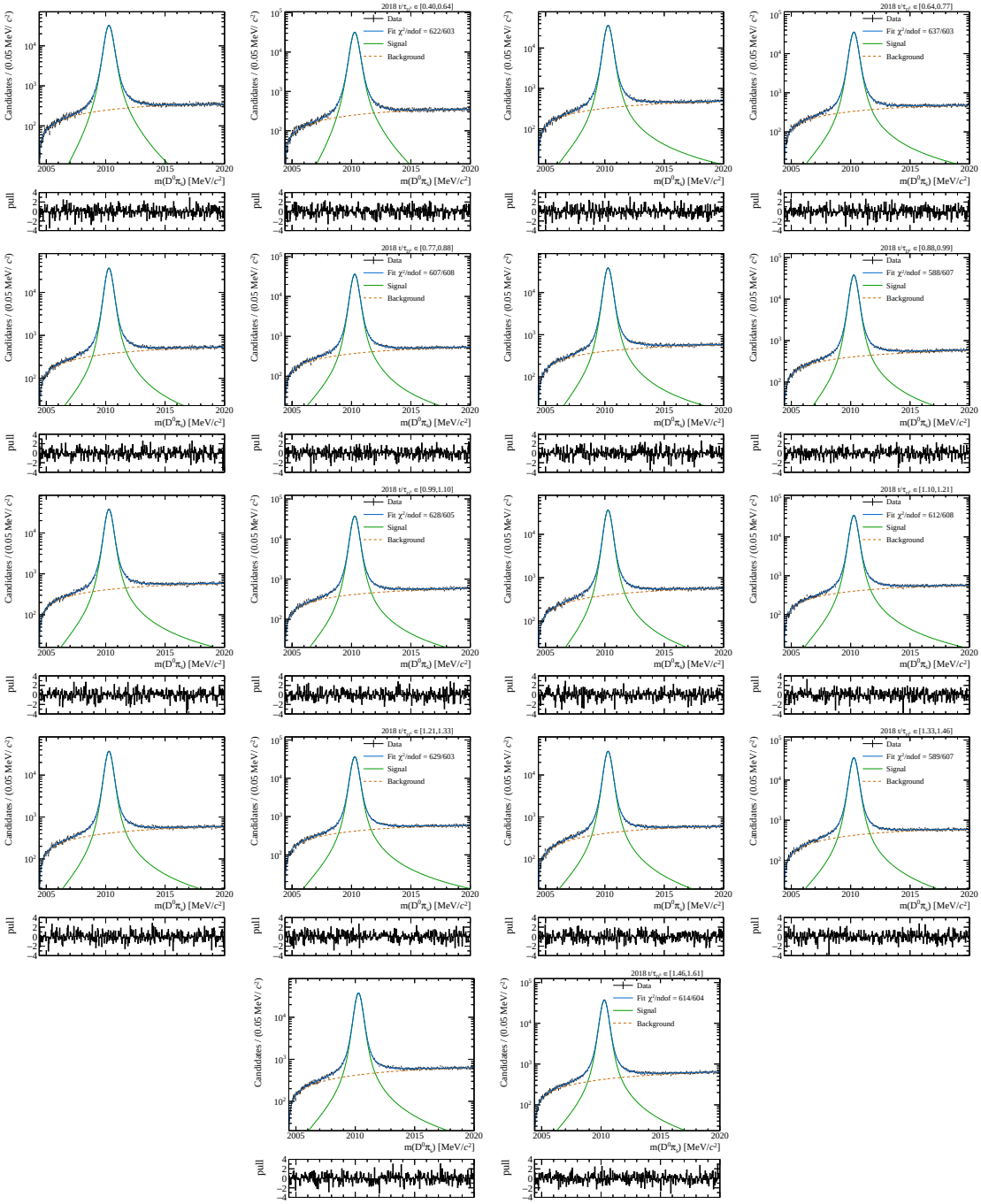

Figure G.5: Distributions of the $m(D^0\pi_s)_{\mathrm{DTF}}$ of $D^{*+} \to K^+K^-$ and $D^{*-} \to K^+K^-$ of some decay-time bin of the 2018 sample. Fit projection are superimposed.

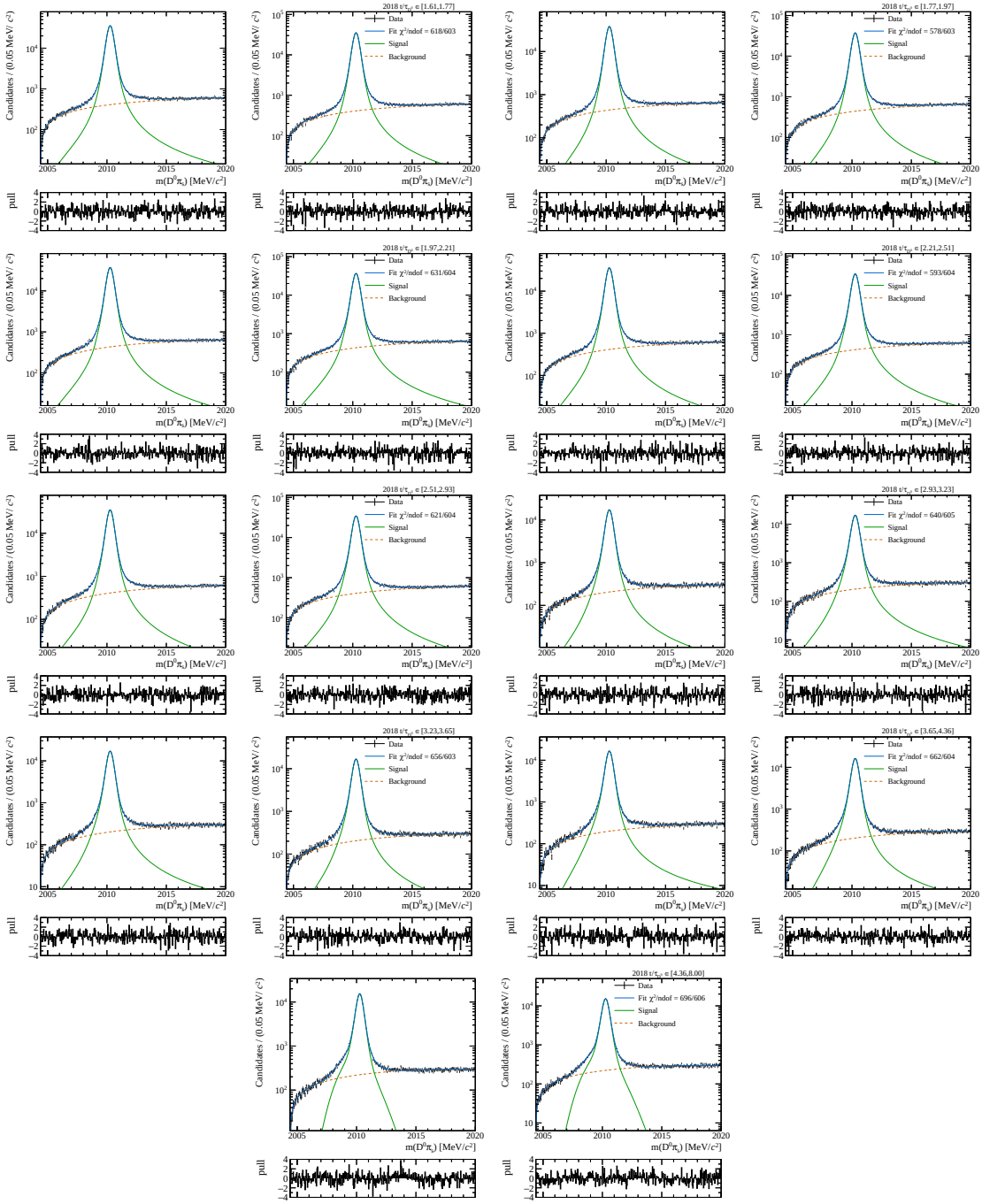

Figure G.6: Distributions of the $m(D^0\pi_s)_{\mathrm{DTF}}$ of $D^{*+} \to K^+K^-$ and $D^{*-} \to K^+K^-$ of some decay-time bin of the 2018 sample. Fit projection are superimposed.

Appendix $\mathcal{H}$

Mixing fit results

This appendix reports the results of the fit of the legacy Run 1+ 2 average in the old parametrization used in the previously published analysis. It follows the table of the results of the Run 2 fit for all the nuisance parameters in the CPV allowed scenario.

H.1 Alternative parametrization

No *CP* violation				
Parameters		Correlations		
		R_D	y'	x'^2
R_D	$(342.7 \pm 1.9)\times10^{-5}$	1	-92.7%	83.6%
y'	$(52.8 \pm 3.3)\times10^{-4}$		1	-96.2%
x'^2	$(2.0 \pm 1.7)\times10^{-5}$			1
χ^2/ndof	150.3 / 209	p-value	1.00	

Table H.1: Fit results in the old parametrization [10], not allowing for *CPV*, simultaneously fitting Run 1 and Run 2.

No *CP* violation			
Source	R_D $[10^{-5}]$	y' $[10^{-4}]$	x'^2 $[10^{-5}]$
Mass mismodeling	0.43	0.74	0.38
Ghost soft pions	0.48	0.94	0.50
Instrumental asymm.	< 0.01	< 0.01	< 0.01
$a^d_{K^+K^-}$ ext. input	< 0.01	< 0.01	< 0.01
ΔY ext. input	0.02	0.03	0.01
Doubly Mis-ID bkg.	0.10	0.04	0.02
Common removal	0.23	< 0.01	< 0.01
Decay-time bias	0.09	0.13	0.06
m_{D^0}, τ_{D^0} ext. inputs	< 0.01	0.10	< 0.01
Total syst. uncertainty	0.69	1.19	0.62
Statistical uncertainty	1.79	3.11	1.61
Total uncertainty	1.92	3.33	1.73

Table H.2: Summary of statistical and systematic uncertainties in the mixing fit with the old parametrization [10], not allowing for *CPV*, for the legacy Run 1 + Run 2 results.

No *CP* violation in the decay and in the mixing					
	Parameters	Correlations			
		R_D	y'^+	x'^2	y'^-
R_D	$(342.7 \pm 1.9)\times10^{-5}$	1	-91.4%	83.6%	-91.4%
y'^+	$(52.6 \pm 3.4)\times10^{-4}$		1	-94.9%	94.5%
x'^2	$(2.0 \pm 1.7)\times10^{-5}$			1	-94.9%
y'^-	$(53.0 \pm 3.4)\times10^{-4}$				1
χ^2/ndof	150.1 / 208	p-value	1.00		

Table H.3: Fit results in the old parametrization [10], allowing only *CPV* in the interference between mixing and decay, simultaneously fitting Run 1 and Run 2.

No *CP* violation in the decay and in the mixing				
Source	R_D $[10^{-5}]$	y'^{+} $[10^{-4}]$	x'^{2} $[10^{-5}]$	y'^{-} $[10^{-4}]$
Mass mismodeling	0.43	0.75	0.39	0.75
Ghost soft pions	0.48	0.96	0.50	0.96
Instrumental asymm.	< 0.01	0.13	< 0.01	0.12
$a^d_{K^+K^-}$ ext. input	< 0.01	0.25	< 0.01	0.23
ΔY ext. input	< 0.01	0.13	< 0.01	0.12
Doubly Mis-ID bkg.	0.11	0.07	0.04	0.07
Common removal	0.23	0.05	0.03	0.05
Decay-time bias	0.09	0.14	0.07	0.14
m_{D^0}, τ_{D^0} ext. inputs	< 0.01	0.10	0.01	0.10
Total syst. uncertainty	0.69	1.25	0.62	1.24
Statistical uncertainty	1.79	3.14	1.61	3.13
Total uncertainty	1.92	3.38	1.73	3.37

Table H.4: Summary of statistical and systematic uncertainties in the mixing fit with the old parametrization [10], allowing for *CPV* only in the interference between mixing and decay, for the legacy Run 1 + Run 2 results.

No *CP* violation in the decay						
Parameters		Correlations				
		R_D	y'^{+}	x'^{2+}	y'^{-}	x'^{2-}
R_D	$(342.7 \pm 1.9)\times10^{-5}$	1	-85.9%	72.4%	-86.1%	72.8%
y'^{+}	$(51.2 \pm 3.6)\times10^{-4}$		1	-94.3%	72.2%	-60.9%
x'^{2+}	$(3.2 \pm 2.0)\times10^{-5}$			1	-60.7%	51.0%
y'^{-}	$(54.4 \pm 3.6)\times10^{-4}$				1	-94.5%
x'^{2-}	$(0.8 \pm 2.0)\times10^{-5}$					1
χ^2/ndof	148.7 / 207	p-value	1.00			

Table H.5: Fit results in the old parametrization [10], allowing only *CPV* in the mixing and in the interference between mixing and decay, simultaneously fitting Run 1 and Run 2.

No *CP* violation in the decay					
Source	R_D [10^{-5}]	y'^{+} [10^{-4}]	x'^{2+} [10^{-5}]	y'^{-} [10^{-4}]	x'^{2-} [10^{-5}]
Mass mismodeling	0.43	0.79	0.43	0.79	0.44
Ghost soft pions	0.48	1.02	0.57	1.02	0.58
Instrumental asymm.	< 0.01	0.28	0.20	0.28	0.19
$a^d_{K^+K^-}$ ext. input	< 0.01	0.53	0.24	0.54	0.25
ΔY ext. input	< 0.01	0.10	< 0.01	0.11	< 0.01
Doubly Mis-ID bkg.	0.10	0.05	0.03	0.05	0.03
Common removal	0.22	< 0.01	< 0.01	< 0.01	< 0.01
Decay-time bias	0.09	0.14	0.07	0.14	0.07
m_{D^0}, τ_{D^0} ext. inputs	0.01	0.10	0.02	0.11	0.01
Total syst. uncertainty	0.69	1.41	0.77	1.41	0.78
Statistical uncertainty	1.79	3.29	1.82	3.30	1.84
Total uncertainty	1.92	3.58	1.98	3.59	2.00

Table H.6: Summary of statistical and systematic uncertainties in the mixing fit with the old parametrization [10], allowing for *CPV* only in the mixing and the interference between mixing and decay, for the legacy Run 1 + Run 2 results.

CP violation in the decay, mixing and interference							
Parameters		Correlations					
		R_D^+	y'^{+}	x'^{2+}	R_D^-	y'^{-}	x'^{2-}
R_D^+	$(340.4 \pm 2.8)\times10^{-5}$	1	-92.3%	83.4%	-2.8%	1.8%	-1.7%
y'^{+}	$(54.8 \pm 4.8)\times10^{-4}$		1	-96.3%	1.8%	-1.9%	1.9%
x'^{2+}	$(1.5 \pm 2.5)\times10^{-5}$			1	-1.7%	1.9%	-2.0%
R_D^-	$(345.0 \pm 2.7)\times10^{-5}$				1	-92.3%	83.1%
y'^{-}	$(50.8 \pm 4.7)\times10^{-4}$					1	-96.2%
x'^{2-}	$(2.5 \pm 2.4)\times10^{-5}$						1
χ^2/ndof	147.4 / 206	p-value	1.00				

Table H.7: Fit results in the old parametrization [10], allowing for *CPV* in the decay, in the mixing and the interference, simultaneously fitting Run 1 and Run 2.

CP violation in the decay, in the mixing and the interference						
Source	R_D^+ $[10^{-5}]$	y'^+ $[10^{-4}]$	x'^{2+} $[10^{-5}]$	R_D^- $[10^{-5}]$	y'^- $[10^{-4}]$	x'^{2-} $[10^{-5}]$
Mass mismodeling	0.61	1.06	0.55	0.61	1.05	0.54
Ghost soft pions	0.67	1.34	0.72	0.70	1.35	0.71
Instrumental asymm.	0.38	0.69	0.36	0.38	0.67	0.35
$a^d_{K^+K^-}$ ext. input	0.37	< 0.01	< 0.01	0.37	0.08	0.05
ΔY ext. input	< 0.01	0.10	0.01	0.04	0.12	0.04
Doubly Mis-ID bkg.	0.10	0.05	0.03	0.11	0.10	0.05
Common removal	0.23	0.08	0.04	0.23	0.10	0.05
Decay-time bias	0.09	0.14	0.07	0.10	0.17	0.08
m_{D^0}, τ_{D^0} ext. inputs	0.04	0.12	0.04	0.04	0.13	0.04
Total syst. uncertainty	1.07	1.81	0.96	1.08	1.81	0.94
Statistical uncertainty	2.54	4.42	2.30	2.52	4.36	2.26
Total uncertainty	2.75	4.78	2.49	2.74	4.72	2.45

Table H.8: Summary of statistical and systematic uncertainties in the mixing fit with the old parametrization [10], allowing for *CPV* in the decay, in the mixing, and interference, for the legacy Run 1 + Run 2 results.

H.2 Nuisance parameters

$p =$	$(2.0 \pm 1.0) \times 10^{-6}$	$c =$	$(1.3 \pm 0.6) \times 10^{-3}$		
$a^d_{KK} =$	$(4.5 \pm 5.3) \times 10^{-4}$	$\Delta Y =$	$(-8.9 \pm 11.3) \times 10^{-5}$	$s =$	1.000 ± 0.002
$\delta t_{0,16} =$	$(1.8 \pm 0.8) \times 10^{-2}$	$\delta t_{0,17} =$	$(1.6 \pm 0.7) \times 10^{-2}$	$\delta t_{0,18} =$	$(1.5 \pm 0.6) \times 10^{-2}$
$\delta t_{1,16} =$	$(2.0 \pm 0.6) \times 10^{-2}$	$\delta t_{1,17} =$	$(2.0 \pm 0.8) \times 10^{-2}$	$\delta t_{1,18} =$	$(2.1 \pm 0.4) \times 10^{-2}$
$\delta t_{2,16} =$	$(2.6 \pm 0.6) \times 10^{-2}$	$\delta t_{2,17} =$	$(2.5 \pm 0.3) \times 10^{-2}$	$\delta t_{2,18} =$	$(2.4 \pm 0.4) \times 10^{-2}$
$\delta t_{3,16} =$	$(2.9 \pm 0.5) \times 10^{-2}$	$\delta t_{3,17} =$	$(2.7 \pm 0.5) \times 10^{-2}$	$\delta t_{3,18} =$	$(3.0 \pm 0.3) \times 10^{-2}$
$\delta t_{4,16} =$	$(3.3 \pm 0.5) \times 10^{-2}$	$\delta t_{4,17} =$	$(3.2 \pm 0.5) \times 10^{-2}$	$\delta t_{4,18} =$	$(3.0 \pm 0.3) \times 10^{-2}$
$\delta t_{5,16} =$	$(3.6 \pm 0.5) \times 10^{-2}$	$\delta t_{5,17} =$	$(3.3 \pm 0.4) \times 10^{-2}$	$\delta t_{5,18} =$	$(3.3 \pm 0.3) \times 10^{-2}$
$\delta t_{6,16} =$	$(3.7 \pm 0.3) \times 10^{-2}$	$\delta t_{6,17} =$	$(3.8 \pm 0.3) \times 10^{-2}$	$\delta t_{6,18} =$	$(3.6 \pm 0.4) \times 10^{-2}$
$\delta t_{7,16} =$	$(4.2 \pm 0.2) \times 10^{-2}$	$\delta t_{7,17} =$	$(3.9 \pm 0.3) \times 10^{-2}$	$\delta t_{7,18} =$	$(3.9 \pm 0.2) \times 10^{-2}$
$\delta t_{8,16} =$	$(4.8 \pm 0.3) \times 10^{-2}$	$\delta t_{8,17} =$	$(4.3 \pm 0.3) \times 10^{-2}$	$\delta t_{8,18} =$	$(4.4 \pm 0.3) \times 10^{-2}$
$\delta t_{9,16} =$	$(4.8 \pm 0.2) \times 10^{-2}$	$\delta t_{9,17} =$	$(4.8 \pm 0.4) \times 10^{-2}$	$\delta t_{9,18} =$	$(4.9 \pm 0.3) \times 10^{-2}$
$\delta t_{10,16} =$	$(5.2 \pm 0.3) \times 10^{-2}$	$\delta t_{10,17} =$	$(5.3 \pm 0.2) \times 10^{-2}$	$\delta t_{10,18} =$	$(5.2 \pm 0.4) \times 10^{-2}$
$\delta t_{11,16} =$	$(5.8 \pm 0.3) \times 10^{-2}$	$\delta t_{11,17} =$	$(5.9 \pm 0.3) \times 10^{-2}$	$\delta t_{11,18} =$	$(5.7 \pm 0.4) \times 10^{-2}$
$\delta t_{12,16} =$	$(6.7 \pm 0.3) \times 10^{-2}$	$\delta t_{12,17} =$	$(6.4 \pm 0.3) \times 10^{-2}$	$\delta t_{12,18} =$	$(6.6 \pm 0.3) \times 10^{-2}$
$\delta t_{13,16} =$	$(7.4 \pm 0.3) \times 10^{-2}$	$\delta t_{13,17} =$	$(7.5 \pm 0.3) \times 10^{-2}$	$\delta t_{13,18} =$	$(7.7 \pm 0.3) \times 10^{-2}$
$\delta t_{14,16} =$	$(8.9 \pm 0.4) \times 10^{-2}$	$\delta t_{14,17} =$	$(8.6 \pm 0.3) \times 10^{-2}$	$\delta t_{14,18} =$	$(8.9 \pm 0.3) \times 10^{-2}$
$\delta t_{15,16} =$	$(0.98 \pm 0.03) \times 10^{-1}$	$\delta t_{15,17} =$	$(0.98 \pm 0.04) \times 10^{-1}$	$\delta t_{15,18} =$	$(1.00 \pm 0.03) \times 10^{-1}$
$\delta t_{16,16} =$	$(1.20 \pm 0.03) \times 10^{-1}$	$\delta t_{16,17} =$	$(1.26 \pm 0.04) \times 10^{-1}$	$\delta t_{16,18} =$	$(1.18 \pm 0.03) \times 10^{-1}$
$\delta t_{17,16} =$	$(2.26 \pm 0.08) \times 10^{-1}$	$\delta t_{17,17} =$	$(2.21 \pm 0.08) \times 10^{-1}$	$\delta t_{17,18} =$	$(2.26 \pm 0.06) \times 10^{-1}$
$\delta t^2_{0,16} =$	$(1.06 \pm 0.13) \times 10^{-2}$	$\delta t^2_{0,17} =$	$(1.01 \pm 0.11) \times 10^{-2}$	$\delta t^2_{0,18} =$	$(1.02 \pm 0.09) \times 10^{-2}$
$\delta t^2_{1,16} =$	$(1.52 \pm 0.13) \times 10^{-2}$	$\delta t^2_{1,17} =$	$(1.47 \pm 0.15) \times 10^{-2}$	$\delta t^2_{1,18} =$	$(1.39 \pm 0.06) \times 10^{-2}$
$\delta t^2_{2,16} =$	$(1.92 \pm 0.15) \times 10^{-2}$	$\delta t^2_{2,17} =$	$(1.76 \pm 0.07) \times 10^{-2}$	$\delta t^2_{2,18} =$	$(1.75 \pm 0.08) \times 10^{-2}$
$\delta t^2_{3,16} =$	$(2.26 \pm 0.12) \times 10^{-2}$	$\delta t^2_{3,17} =$	$(2.04 \pm 0.10) \times 10^{-2}$	$\delta t^2_{3,18} =$	$(2.08 \pm 0.08) \times 10^{-2}$
$\delta t^2_{4,16} =$	$(2.55 \pm 0.12) \times 10^{-2}$	$\delta t^2_{4,17} =$	$(2.37 \pm 0.14) \times 10^{-2}$	$\delta t^2_{4,18} =$	$(2.34 \pm 0.09) \times 10^{-2}$
$\delta t^2_{5,16} =$	$(2.92 \pm 0.15) \times 10^{-2}$	$\delta t^2_{5,17} =$	$(2.76 \pm 0.10) \times 10^{-2}$	$\delta t^2_{5,18} =$	$(2.71 \pm 0.07) \times 10^{-2}$
$\delta t^2_{6,16} =$	$(3.29 \pm 0.08) \times 10^{-2}$	$\delta t^2_{6,17} =$	$(3.23 \pm 0.10) \times 10^{-2}$	$\delta t^2_{6,18} =$	$(3.18 \pm 0.10) \times 10^{-2}$
$\delta t^2_{7,16} =$	$(3.74 \pm 0.06) \times 10^{-2}$	$\delta t^2_{7,17} =$	$(3.64 \pm 0.11) \times 10^{-2}$	$\delta t^2_{7,18} =$	$(3.61 \pm 0.06) \times 10^{-2}$
$\delta t^2_{8,16} =$	$(4.35 \pm 0.10) \times 10^{-2}$	$\delta t^2_{8,17} =$	$(4.15 \pm 0.10) \times 10^{-2}$	$\delta t^2_{8,18} =$	$(4.08 \pm 0.12) \times 10^{-2}$
$\delta t^2_{9,16} =$	$(4.97 \pm 0.09) \times 10^{-2}$	$\delta t^2_{9,17} =$	$(4.9 \pm 0.2) \times 10^{-2}$	$\delta t^2_{9,18} =$	$(4.78 \pm 0.11) \times 10^{-2}$
$\delta t^2_{10,16} =$	$(5.93 \pm 0.14) \times 10^{-2}$	$\delta t^2_{10,17} =$	$(5.79 \pm 0.12) \times 10^{-2}$	$\delta t^2_{10,18} =$	$(5.9 \pm 0.2) \times 10^{-2}$
$\delta t^2_{11,16} =$	$(7.11 \pm 0.12) \times 10^{-2}$	$\delta t^2_{11,17} =$	$(7.0 \pm 0.2) \times 10^{-2}$	$\delta t^2_{11,18} =$	$(6.7 \pm 0.2) \times 10^{-2}$
$\delta t^2_{12,16} =$	$(8.8 \pm 0.2) \times 10^{-2}$	$\delta t^2_{12,17} =$	$(8.7 \pm 0.2) \times 10^{-2}$	$\delta t^2_{12,18} =$	$(8.7 \pm 0.2) \times 10^{-2}$
$\delta t^2_{13,16} =$	$(1.14 \pm 0.02) \times 10^{-1}$	$\delta t^2_{13,17} =$	$(1.14 \pm 0.02) \times 10^{-1}$	$\delta t^2_{13,18} =$	$(1.13 \pm 0.02) \times 10^{-1}$
$\delta t^2_{14,16} =$	$(1.51 \pm 0.04) \times 10^{-1}$	$\delta t^2_{14,17} =$	$(1.48 \pm 0.03) \times 10^{-1}$	$\delta t^2_{14,18} =$	$(1.50 \pm 0.04) \times 10^{-1}$
$\delta t^2_{15,16} =$	$(1.86 \pm 0.04) \times 10^{-1}$	$\delta t^2_{15,17} =$	$(1.90 \pm 0.04) \times 10^{-1}$	$\delta t^2_{15,18} =$	$(1.95 \pm 0.03) \times 10^{-1}$
$\delta t^2_{16,16} =$	$(2.71 \pm 0.05) \times 10^{-1}$	$\delta t^2_{16,17} =$	$(2.89 \pm 0.07) \times 10^{-1}$	$\delta t^2_{16,18} =$	$(2.68 \pm 0.05) \times 10^{-1}$
$\delta t^2_{17,16} =$	$(8.2 \pm 0.3) \times 10^{-1}$	$\delta t^2_{17,17} =$	$(7.9 \pm 0.2) \times 10^{-1}$	$\delta t^2_{17,18} =$	$(8.2 \pm 0.2) \times 10^{-1}$
$a^{KK,\mathrm{wgt}}_{0,16} =$	$(-6.0 \pm 1.2) \times 10^{-3}$	$a^{KK,\mathrm{wgt}}_{0,17} =$	$(-6.9 \pm 1.1) \times 10^{-3}$	$a^{KK,\mathrm{wgt}}_{0,18} =$	$(-5.3 \pm 1.0) \times 10^{-3}$
$a^{KK,\mathrm{wgt}}_{1,16} =$	$(-3.3 \pm 1.1) \times 10^{-3}$	$a^{KK,\mathrm{wgt}}_{1,17} =$	$(-4.3 \pm 1.0) \times 10^{-3}$	$a^{KK,\mathrm{wgt}}_{1,18} =$	$(-7.7 \pm 1.0) \times 10^{-3}$
$a^{KK,\mathrm{wgt}}_{2,16} =$	$(-4.8 \pm 1.1) \times 10^{-3}$	$a^{KK,\mathrm{wgt}}_{2,17} =$	$(-7.1 \pm 1.0) \times 10^{-3}$	$a^{KK,\mathrm{wgt}}_{2,18} =$	$(-6.6 \pm 1.0) \times 10^{-3}$
$a^{KK,\mathrm{wgt}}_{3,16} =$	$(-5.7 \pm 1.0) \times 10^{-3}$	$a^{KK,\mathrm{wgt}}_{3,17} =$	$(-8.1 \pm 1.0) \times 10^{-3}$	$a^{KK,\mathrm{wgt}}_{3,18} =$	$(-6.0 \pm 1.0) \times 10^{-3}$
$a^{KK,\mathrm{wgt}}_{4,16} =$	$(-2.7 \pm 1.0) \times 10^{-3}$	$a^{KK,\mathrm{wgt}}_{4,17} =$	$(-8.5 \pm 1.0) \times 10^{-3}$	$a^{KK,\mathrm{wgt}}_{4,18} =$	$(-7.1 \pm 1.0) \times 10^{-3}$
$a^{KK,\mathrm{wgt}}_{5,16} =$	$(-5.7 \pm 1.0) \times 10^{-3}$	$a^{KK,\mathrm{wgt}}_{5,17} =$	$(-6.6 \pm 1.0) \times 10^{-3}$	$a^{KK,\mathrm{wgt}}_{5,18} =$	$(-7.2 \pm 1.0) \times 10^{-3}$
$a^{KK,\mathrm{wgt}}_{6,16} =$	$(-7.1 \pm 1.0) \times 10^{-3}$	$a^{KK,\mathrm{wgt}}_{6,17} =$	$(-6.2 \pm 1.0) \times 10^{-3}$	$a^{KK,\mathrm{wgt}}_{6,18} =$	$(-8.1 \pm 1.0) \times 10^{-3}$
$a^{KK,\mathrm{wgt}}_{7,16} =$	$(-2.0 \pm 1.0) \times 10^{-3}$	$a^{KK,\mathrm{wgt}}_{7,17} =$	$(-6.8 \pm 1.0) \times 10^{-3}$	$a^{KK,\mathrm{wgt}}_{7,18} =$	$(-7.3 \pm 1.0) \times 10^{-3}$
$a^{KK,\mathrm{wgt}}_{8,16} =$	$(-4.6 \pm 1.0) \times 10^{-3}$	$a^{KK,\mathrm{wgt}}_{8,17} =$	$(-7.6 \pm 1.0) \times 10^{-3}$	$a^{KK,\mathrm{wgt}}_{8,18} =$	$(-6.9 \pm 1.0) \times 10^{-3}$
$a^{KK,\mathrm{wgt}}_{9,16} =$	$(-2.4 \pm 1.0) \times 10^{-3}$	$a^{KK,\mathrm{wgt}}_{9,17} =$	$(-4.7 \pm 1.1) \times 10^{-3}$	$a^{KK,\mathrm{wgt}}_{9,18} =$	$(-6.3 \pm 1.0) \times 10^{-3}$
$a^{KK,\mathrm{wgt}}_{10,16} =$	$(-4.3 \pm 1.0) \times 10^{-3}$	$a^{KK,\mathrm{wgt}}_{10,17} =$	$(-7.7 \pm 1.0) \times 10^{-3}$	$a^{KK,\mathrm{wgt}}_{10,18} =$	$(-8.0 \pm 1.0) \times 10^{-3}$
$a^{KK,\mathrm{wgt}}_{11,16} =$	$(-5.1 \pm 1.0) \times 10^{-3}$	$a^{KK,\mathrm{wgt}}_{11,17} =$	$(-6.5 \pm 1.0) \times 10^{-3}$	$a^{KK,\mathrm{wgt}}_{11,18} =$	$(-6.6 \pm 1.0) \times 10^{-3}$
$a^{KK,\mathrm{wgt}}_{12,16} =$	$(-6.7 \pm 1.0) \times 10^{-3}$	$a^{KK,\mathrm{wgt}}_{12,17} =$	$(-8.1 \pm 1.1) \times 10^{-3}$	$a^{KK,\mathrm{wgt}}_{12,18} =$	$(-6.8 \pm 1.0) \times 10^{-3}$
$a^{KK,\mathrm{wgt}}_{13,16} =$	$(-6.3 \pm 1.0) \times 10^{-3}$	$a^{KK,\mathrm{wgt}}_{13,17} =$	$(-5.9 \pm 1.1) \times 10^{-3}$	$a^{KK,\mathrm{wgt}}_{13,18} =$	$(-5.9 \pm 1.0) \times 10^{-3}$
$a^{KK,\mathrm{wgt}}_{14,16} =$	$(-5.8 \pm 1.4) \times 10^{-3}$	$a^{KK,\mathrm{wgt}}_{14,17} =$	$(-10.0 \pm 1.5) \times 10^{-3}$	$a^{KK,\mathrm{wgt}}_{14,18} =$	$(-8.8 \pm 1.4) \times 10^{-3}$
$a^{KK,\mathrm{wgt}}_{15,16} =$	$(-4.9 \pm 1.4) \times 10^{-3}$	$a^{KK,\mathrm{wgt}}_{15,17} =$	$(-9.6 \pm 1.5) \times 10^{-3}$	$a^{KK,\mathrm{wgt}}_{15,18} =$	$(-6.0 \pm 1.4) \times 10^{-3}$
$a^{KK,\mathrm{wgt}}_{16,16} =$	$(-8.1 \pm 1.5) \times 10^{-3}$	$a^{KK,\mathrm{wgt}}_{16,17} =$	$(-8.5 \pm 1.5) \times 10^{-3}$	$a^{KK,\mathrm{wgt}}_{16,18} =$	$(-8.1 \pm 1.4) \times 10^{-3}$
$a^{KK,\mathrm{wgt}}_{17,16} =$	$(-4.8 \pm 1.5) \times 10^{-3}$	$a^{KK,\mathrm{wgt}}_{17,17} =$	$(-6.5 \pm 1.6) \times 10^{-3}$	$a^{KK,\mathrm{wgt}}_{17,18} =$	$(-5.7 \pm 1.5) \times 10^{-3}$

Table H.9: Fit results for nuisance parameters of the fit to the decay-time dependence of the WS-to-RS ratio performed in Sec. 9, iun the scenario that allow for *CPV* effects.

Bibliography

[1] LHCb collaboration, R. Aaij *et al.*, *Observation of cp violation in charm decays*, Phys. Rev. Lett. **122** (2019) 211803.

[2] LHCb, R. Aaij *et al.*, *Measurement of CP asymmetry in $D^0 \to K^0_S K^0_S$ decays*, Phys. Rev. D **104** (2021) L031102, arXiv:2105.01565.

[3] M. Bobrowski, A. Lenz, J. Riedl, and J. Rohrwild, *How Large Can the SM Contribution to CP Violation in $D^0 - \bar{D}^0$ Mixing Be?*, JHEP **03** (2010) 009, arXiv:1002.4794.

[4] Y. Grossman, A. L. Kagan, and Y. Nir, *New physics and CP violation in singly Cabibbo suppressed D decays*, Phys. Rev. **D75** (2007) 036008, arXiv:hep-ph/0609178.

[5] HFLAV Group, D. Asner *et al.*, *Averages of b-hadron, c-hadron, and τ-lepton properties*, arXiv:1010.1589.

[6] LHCb, R. Aaij *et al.*, *Model-independent measurement of charm mixing parameters in $B^- \to D0(\to KS0\pi+\pi-)\mu-\nu\,^-\mu X$ decays*, Phys. Rev. D **108** (2023) 052005, arXiv:2208.06512.

[7] LHCb collaboration, *Simultaneous determination of the CKM angle γ and parameters related to mixing and CP violation in the charm sector*, LHCb-CONF-2022-003, 2022.

[8] CLEO collaboration, D. M. Asner *et al.*, *Updated Measurement of the Strong Phase in $D^0 \to K^+\pi^-$ Decay Using Quantum Correlations in $e^+e^- \to D^0\bar{D}^0$ at CLEO*, Phys. Rev. **D86** (2012) 112001, arXiv:1210.0939.

[9] BESIII collaboration, M. Ablikim *et al.*, *Measurement of the $D \to K^-\pi^+$ strong phase difference in $\psi(3770) \to D^0\overline{D}^0$*, Phys. Lett. **B734** (2014) 227, arXiv:1404.4691.

[10] LHCb collaboration, R. Aaij *et al.*, *Updated determination of D^0-$\overline{D}^0$ mixing and CP violation parameters with $D^0 \to K^+\pi^-$ decays*, Phys. Rev. **D97** (2018) 031101, arXiv:1712.03220.

[11] Y. Nir, *CP violation in and beyond the standard model*, in *Proceedings, 27th SLAC Summer Institute on Particle Physics: CP Violation in and Beyond the Standard Model (SSI 99): Stanford, USA, July 7-16, 1999*, 165–243, 1999, arXiv:hep-ph/9911321.

[12] S. L. Glashow, *Partial Symmetries of Weak Interactions*, Nucl. Phys. **22** (1961) 579.

[13] S. Weinberg, *A model of leptons*, Phys. Rev. Lett. **19** (1967) 1264.

[14] A. Salam, *Elementary Particle Theory*, 1969.

[15] N. Cabibbo, *Unitary symmetry and leptonic decays*, Phys. Rev. Lett. **10** (1963) 531.

[16] M. Kobayashi and T. Maskawa, *CP-Violation in the Renormalizable Theory of Weak Interaction*, Progress of Theoretical Physics **49** (1973) 652, arXiv:http://oup.prod.sis.lan/ptp/article-pdf/49/2/652/5257692/49-2-652.pdf.

[17] L.-L. Chau and W.-Y. Keung, *Comments on the parametrization of the kobayashi-maskawa matrix*, Phys. Rev. Lett. **53** (1984) 1802.

[18] Z. Maki, M. Nakagawa, Y. Ohnuki, and S. Sakata, *A Unified Model for Elementary Particles:* , Progress of Theoretical Physics **23** (1960) 1174, arXiv:http://oup.prod.sis.lan/ptp/article-pdf/23/6/1174/5461148/23-6-1174.pdf.

[19] A. P. Serebrov *et al.*, *New measurements of the neutron electric dipole moment*, JETP Lett. **99** (2014) 4, arXiv:1310.5588.

[20] L. Wolfenstein, *Parametrization of the kobayashi-maskawa matrix*, Phys. Rev. Lett. **51** (1983) 1945.

[21] C. Jarlskog, *Commutator of the quark mass matrices in the standard electroweak model and a measure of maximal cp nonconservation*, Phys. Rev. Lett. **55** (1985) 1039.

[22] CKMfitter Group, J. Charles *et al.*, *Cp violation and the ckm matrix: Assessing the impact of the asymmetric b factories*, Eur. Phys. J. **C41** (2005) 1, arXiv:hep-ph/0406184, updated results and plots available at: http://ckmfitter.in2p3.fr.

[23] V. Weisskopf and E. Wigner, *Berechnung der natürlichen linienbreite auf grund der diracschen lichttheorie*, Zeitschrift für Physik **63** (1930) 54.

[24] Y. Grossman, Y. Nir, and G. Perez, *Testing New Indirect CP Violation*, Phys. Rev. Lett. **103** (2009) 071602, arXiv:0904.0305.

[25] A. L. Kagan and M. D. Sokoloff, *On Indirect CP Violation and Implications for D0 - anti-D0 and B(s) - anti-B(s) mixing*, Phys. Rev. D **80** (2009) 076008, arXiv:0907.3917.

[26] Particle Data Group, R. L. Workman and Others, *Review of Particle Physics*, PTEP **2022** (2022) 083C01.

[27] HFLAV Group, Y. Amhis *et al.*, *Averages of b-hadron, c-hadron, and τ-lepton properties as of summer 2016*, Eur. Phys. J. **C77** (2017) 895, arXiv:1612.07233, updated results and plots available at https://hflav.web.cern.ch/.

[28] CDF, A. Abulencia *et al.*, *Observation of $B_s^0 - \bar{B}_s^0$ Oscillations*, Phys. Rev. Lett. **97** (2006) 242003, arXiv:hep-ex/0609040.

[29] BaBar collaboration, B. Aubert *et al.*, *Evidence for $D^0 - \overline{D}^0$ Mixing*, Phys. Rev. Lett. **98** (2007) 211802, arXiv:hep-ex/0703020.

[30] Belle collaboration, M. Staric *et al.*, *Evidence for D^0 - $\bar{D}^0$ Mixing*, Phys. Rev. Lett. **98** (2007) 211803, arXiv:hep-ex/0703036, [,65(2007)].

[31] LHCb collaboration, R. Aaij *et al.*, *Measurement of D^0~$\bar{D}^0$ Mixing Parameters and Search for CP Violation Using $D^0 \to K^+\pi^-$ Decays*, Phys. Rev. Lett. **111** (2013) 251801, arXiv:1309.6534.

[32] S. L. Glashow, J. Iliopoulos, and L. Maiani, *Weak Interactions with Lepton-Hadron Symmetry*, Phys. Rev. D **2** (1970) 1285.

[33] M. S. Sozzi, *Discrete symmetries and CP violation: From experiment to theory*, 2008.

[34] F. Buccella, A. Paul, and P. Santorelli, *$SU(3)_F$ breaking through final state interactions and CP asymmetries in $D \to PP$ decays*, Phys. Rev. **D99** (2019) 113001, arXiv:1902.05564.

[35] A. Cerri *et al.*, *Opportunities in Flavour Physics at the HL-LHC and HE-LHC*, arXiv:1812.07638.

[36] CDF, D0 collaborations, C.-h. Chen, *Heavy flavor production at the Tevatron*, AIP Conf. Proc. **722** (2004) 67, arXiv:hep-ex/0401021.

[37] Belle-II, I. Adachi *et al.*, *Novel method for the identification of the production flavor of neutral charmed mesons*, Phys. Rev. D **107** (2023) 112010, arXiv:2304.02042.

[38] LHCb collaboration, R. Aaij *et al.*, *Observation of $D^0 - \overline{D}^0$ oscillations*, Phys. Rev. Lett. **110** (2013) 101802, arXiv:1211.1230.

[39] A. L. Kagan and L. Silvestrini, *Dispersive and absorptive CP violation in $D^0 - \overline{D^0}$ mixing*, Phys. Rev. D **103** (2021) 053008, arXiv:2001.07207.

[40] BESIII, M. Ablikim *et al.*, *Improved measurement of the strong-phase difference $\delta_D^{K\pi}$ in quantum-correlated $D\bar{D}$ decays*, Eur. Phys. J. C **82** (2022) 1009, arXiv:2208.09402.

[41] LHCb, R. Aaij *et al.*, *Measurement of the charm mixing parameter $y_{CP} - y_{CP}^{K\pi}$ using two-body D^0 meson decays*, Phys. Rev. D **105** (2022) 092013, arXiv:2202.09106.

[42] BaBar, B. Aubert *et al.*, *Improved measurement of the CKM angle γ in $B^\mp \to D^{(*)}K^{(*\mp)}$ decays with a Dalitz plot analysis of D decays to $K_S^0\pi^+\pi^-$ and $K_S^0K^+K^-$*, Phys. Rev. D **78** (2008) 034023, arXiv:0804.2089.

[43] CLEO, J. Libby *et al.*, *Model-independent determination of the strong-phase difference between D^0 and $\bar{D}^0 \to K_{S,L}^0 h^+h^-$ ($h = \pi, K$) and its impact on the measurement of the CKM angle γ/ϕ_3*, Phys. Rev. D **82** (2010) 112006, arXiv:1010.2817.

[44] Belle collaboration, U. Bitenc *et al.*, *Improved search for D0 - anti-D0 mixing using semileptonic decays at Belle*, Phys. Rev. **D77** (2008) 112003, arXiv:0802.2952.

[45] Y. Grossman, A. L. Kagan, and Y. Nir, *New physics and CP violation in singly Cabibbo suppressed D decays*, Phys. Rev. D **75** (2007) 036008, arXiv:hep-ph/0609178.

[46] LHCb collaboration, R. Aaij *et al.*, *Search for time-dependent CP violation in $D^0 \to K^+K^-$ and $D^0 \to \pi^+\pi^-$ decays*, Phys. Rev. **D104** (2021) 072010, arXiv:2105.09889.

[47] LHCb collaboration, R. Aaij *et al.*, *Model-independent measurement of mixing parameters in $D^0 \to K^0_S\pi^+\pi^-$ decays*, JHEP **04** (2016) 033, arXiv:1510.01664.

[48] E. Golowich, J. Hewett, S. Pakvasa, and A. A. Petrov, *Implications of D^0 - $\bar{D}^0$ Mixing for New Physics*, Phys. Rev. **D76** (2007) 095009, arXiv:0705.3650.

[49] Y. Nir, *Lessons from BaBar and Belle measurements of D0 - anti-D0 mixing parameters*, JHEP **05** (2007) 102, arXiv:hep-ph/0703235.

[50] W.-S. Hou, M. Nagashima, and A. Soddu, *Large time-dependent CP violation in B/s0 system and finite D^0 - $\bar{D}^0$ mass difference in four generation standard model*, Phys. Rev. **D76** (2007) 016004, arXiv:hep-ph/0610385.

[51] C. Alpigiani *et al.*, *Unitarity triangle analysis in the Standard Model and beyond*, arXiv:1710.09644.

[52] L. Wolfenstein, *Violation of CP Invariance and the Possibility of Very Weak Interactions*, Phys. Rev. Lett. **13** (1964) 562.

[53] Belle collaboration, B. R. Ko *et al.*, *Observation of $D^0 - \bar{D}^0$ Mixing in e^+e^- Collisions*, Phys. Rev. Lett. **112** (2014) 111801, arXiv:1401.3402, [Addendum: Phys. Rev. Lett.112,no.13,139903(2014)].

[54] CDF collaboration, T. A. Aaltonen *et al.*, *Observation of $D^0 - \overline{D}^0$ Mixing Using the CDF II Detector*, Phys. Rev. Lett. **111** (2013) 231802, arXiv:1309.4078.

[55] L. Evans and P. Bryant, *LHC machine*, Journal of Instrumentation **3** (2008) S08001.

[56] J. Haffner, *The CERN accelerator complex. Complexe des accélérateurs du CERN*, , General Photo.

[57] T. Sjostrand, S. Mrenna, and P. Z. Skands, *PYTHIA 6.4 Physics and Manual*, JHEP **05** (2006) 026, arXiv:hep-ph/0603175.

[58] LHCb collaboration, C. Elsasser, *$\bar{b}b$ production angle plots*, .

[59] LHCb collaboration, *LHCb reoptimized detector design and performance: Technical Design Report*, CERN-LHCC-2003-030, 2003.

[60] LHCb collaboration, P. R. Barbosa-Marinho *et al.*, *LHCb VELO (VErtex LOcator): Technical Design Report*, Technical Design Report LHCb, CERN, Geneva, 2001.

[61] LHCb collaboration, R. Aaij *et al.*, *LHCb detector performance*, Int. J. Mod. Phys. **A30** (2015) 1530022, arXiv:1412.6352.

[62] LHCb collaboration, P. R. Barbosa-Marinho *et al.*, *LHCb inner tracker: Technical Design Report*, Technical Design Report LHCb, CERN, Geneva, 2002. revised version number 1 submitted on 2002-11-13 14:14:34.

[63] LHCb Outer Tracker Group, R. Arink *et al.*, *Performance of the LHCb Outer Tracker*, JINST **9** (2014) P01002, arXiv:1311.3893.

[64] LHCb RICH Group, M. Adinolfi *et al.*, *Performance of the LHCb RICH detector at the LHC*, Eur. Phys. J. **C73** (2013) 2431, arXiv:1211.6759.

[65] E. P. Olloqui and the LHCb collaboration, *LHCb preshower(PS) and scintillating pad detector (SPD): Commissioning, calibration, and monitoring*, Journal of Physics: Conference Series **160** (2009) 012046.

[66] LHCb collaboration, S. Amato *et al.*, *LHCb calorimeters: Technical Design Report*, Technical Design Report LHCb, CERN, Geneva, 2000.

[67] I. M. and, *Current status and performance of the LHCb electromagnetic and hadron calorimeters*, Journal of Physics: Conference Series **293** (2011) 012052.

[68] A. A. Alves *et al.*, *Performance of the LHCb muon system*, Journal of Instrumentation **8** (2013) P02022.

[69] R. Aaij *et al.*, *Tesla : an application for real-time data analysis in High Energy Physics*, Comput. Phys. Commun. **208** (2016) 35, arXiv:1604.05596.

[70] LHCb collaboration, R. Aaij *et al.*, *LHCb Detector Performance*, Int. J. Mod. Phys. **A30** (2015) 1530022, arXiv:1412.6352.

[71] W. D. Hulsbergen, *Decay chain fitting with a kalman filter*, Nuclear Instruments and Methods in Physics Research Section A: Accelerators, Spectrometers, Detectors and Associated Equipment **552** (2005) 566.

[72] LHCb collaboration, R. Aaij *et al.*, *Measurement of the time-integrated CP asymmetry in $D^0 \to K^-K^+$ decays*, arXiv:2209.03179, submitted to PRL.

[73] M. De Cian, S. Farry, P. Seyfert, and S. Stahl, *Fast neural-net based fake track rejection in the LHCb reconstruction*, LHCb-PUB-2017-011. CERN-LHCb-PUB-2017-011, CERN, Geneva, 2017.

[74] V. V. Gligorov and M. Williams, *Efficient, reliable and fast high-level triggering using a bonsai boosted decision tree*, JINST **8** (2013) P02013, arXiv:1210.6861.

[75] M. Needham, *Clone Track Identification using the Kullback-Liebler Distance* , CERN, Geneva, 2008.

[76] T. Pajero and M. J. Morello, *Search for time-dependent CP violation in $D^0 \to K^+K^-$ and $D^0 \to \pi^+\pi^-$ decays*, LHCb-ANA-2020-040, 2020.

[77] M. Clemencic *et al.*, *The LHCb simulation application, gauss: Design, evolution and experience*, Journal of Physics: Conference Series **331** (2011) 032023.

[78] D. J. Lange, *The EvtGen particle decay simulation package*, Nucl. Instrum. Meth. A **462** (2001) 152.

[79] P. Golonka and Z. Was, *PHOTOS Monte Carlo: A Precision tool for QED corrections in Z and W decays*, Eur. Phys. J. C **45** (2006) 97, arXiv:hep-ph/0506026.

[80] GEANT4, S. Agostinelli *et al.*, *GEANT4–a simulation toolkit*, Nucl. Instrum. Meth. A **506** (2003) 250.

[81] N. L. Johnson, *Systems of frequency curves generated by methods of translation*, Biometrika **36** (1949) 149.

[82] A. Rogozhnikov, *Reweighting with Boosted Decision Trees*, J. Phys. Conf. Ser. **762** (2016) 012036, arXiv:1608.05806.

[83] A. Di Canto *et al.*, *Measurement of $D^0 - -\overline{D}^0$ mixing parameters and search for CP violation using $D^0 \to K^+\pi^-$ decay from Run 1 and 2 data*, LHCb-ANA-2017-016, 2018.

[84] T. Szumlak, S. Borghi, M. Smith, and C. Parkes, *Study of the VELO hit resolution in Run 1* , CERN, Geneva, 2015.

[85] H. Wouter, *Misalignment effects in $Z \to \mu\mu$ decays in Run 2*, , 2018.

[86] F. E. James, *Monte Carlo phase space*, (Geneva), 41 p, CERN, CERN, 1968. CERN, Geneva, 1 May 1968.

[87] R. J. Barlow and C. Beeston, *Fitting using finite Monte Carlo samples*, Comput. Phys. Commun. **77** (1993) 219.

[88] Belle-II, W. Altmannshofer *et al.*, *The Belle II Physics Book*, PTEP **2019** (2019) 123C01, arXiv:1808.10567, [Erratum: PTEP 2020, 029201 (2020)].

[89] T. Pajero and M. J. Morello, *Mixing and CP violation in $D^0 \to K^-\pi^+$ decays*, JHEP **03** (2022) 162, arXiv:2106.02014.